Transition Metal Complexes for Challenging Reductive Transformations: From Nitrogen Fixation Catalysts to Photoreductants

Thesis by

Javier Fajardo Jr.

In Partial Fulfillment of the Requirements for the Degree of

Doctor of Philosophy in Chemistry

CALIFORNIA INSTITUTE OF TECHNOLOGY

Pasadena, California

2020

(Defended June 2, 2020)

Javier Fajardo Jr.
ORCID: 0000-0003-0612-7953

To my family, friends, mentors, and all underrepresented minorities in STEM

ACKNOWLEDGEMENTS

My journey through graduate school at Caltech has been a rewarding, but difficult one. On the cusp of graduating and becoming the first member of my family to earn a doctorate degree, I now reflect on those last six years, which have at times seemed endless, and on other occasions seemed to pass by too quickly. Earning a Ph.D. is not something one can do alone- a lesson I have learned on several occasions- and there are a great number of people I must thank for both my professional and personal success while at Caltech. The acknowledgements I offer below as part of this thesis are only a starting point in this regard, as the positive impact they have had on me as a scientist and person is something I will appreciate for many years to come.

First and foremost, I would like to express my sincerest thanks to Harry Gray, who welcomed me into his research group in the late stages of my graduate school career and has served as my mentor the last two years. The opportunity to work with Harry, a remarkable scientist, and an equally amazing person, has been the highlight of my time at Caltech. As a member of the Gray group, Harry entrusted me with the scientific freedom and independence that allowed me to grow and flourish scientifically. I am deeply appreciative for his encouragement, kindness, patience, and steadfast support, both in times of productivity, and even more importantly, during times when research did not go as planned. Beyond his role as a scientific advisor, the genuine compassion and care Harry has for members of his group has also been a great source of inspiration. The ability to learn both scientifically and personally from him shaped me into the scientist I hoped to become, and I could not have asked for a better mentor.

Like Harry, Jay Winkler has also been a supportive and fantastic mentor. Jay has been instrumental

to my success in the Gray group- although I had the synthetic capabilities to prepare the compounds of interest, I knew very little when it came to the area of photophysics and photochemistry. His patience, time, input, and help has been invaluable in learning about these new fields, the advancement of our research, and my growth as a scientist. For that, I am deeply grateful.

I am also thankful to my thesis committee, Theo Agapie, Tom Miller, and Jonas Peters, which over the years have offered scientific guidance and support that has been important to my development. In particular, I would like to extend my deepest gratitude to Jonas, who served as my research advisor the first four years of my graduate career. A great portion of the scientific foundation that has enabled me to be successful in my research endeavors was acquired during my time in the Peters group. I became a significantly more thoughtful and careful scientist as a result of that experience. For the opportunity, the time Jonas invested in my education, and his continued support until the conclusion of my graduate studies, I am truly thankful.

I am enormously fortunate to have concluded my graduate residence as part of the Gray group, a collection of not only exceptional scientists, but also exceptional friends and people. The process of earning a Ph.D. is a challenging one, often involving many unsuccessful experiments, frustrations, and disappointments. The support of the Gray group during these difficult times has made getting to this point possible. I would like to thank Josef Schwan, who began the work on the third generation of tungsten arylisocyanides that would ultimately become my main research project. His initial contributions to this project, and numerous subsequent discussions, were invaluable to the progress made. In addition, Josef was a great friend and source of encouragement. Similarly, Brendon McNicholas has been an amazing friend throughout my years at Caltech, and an equally amazing

labmate. His support over the last couple of months as we have completed our graduation requirements made these stressful times much more manageable. In addition, I would like to thank Jill Clinton, who is one of the most wonderful, supportive, and positive people I have ever met. For their friendship, words of encouragement, and belief in me, I also extend my sincerest gratitude to Shabnam Hematian, Jieun Shin, Patrycja Kielb, Julian West, Wes Sattler, Dana Levine, Raheleh Ravanfar, Brian Sanders, Sarah Del Ciello, Wes Kramer, Maryann Morales, and Rick Jackson. Along with Katharina Brinkert, Cherish Nie, and Yuling Sheng, you all made the Gray group an absolute joy! I could not have asked for a better group!

In addition to those acknowledged above, a number of others have contributed to my progression as a scientist. To start, I would like to thank my undergraduate mentors, Vincent Lavallo, T. Don Tilley, Michael Lipschutz, and James Wright, for introducing me to research, inspiring me to pursue a Ph.D. in chemistry, and supporting me at the beginning of my journey. My synthetic skills, which have proven to be my most valuable asset over the course of my graduate research, can be traced back to their teaching. When I arrived at Caltech, Jonathan Rittle and Gaël Ung served as my mentors, and the success of my first research project is in large part due to their guidance. I also overlapped with many great scientists in the Peters and Agapie groups during my tenure here. I am particularly grateful to Matthew Chalkley, Meaghan Deegan, Nina Gu, Ryan Ribson, and Charlie Arnett, all exceptional chemists who have provided valuable scientific discussions and feedback over many years, and which contributed substantially to my improvement as a scientist and the advancement of my research.

The research I have conducted at Caltech has been made possible by an amazing group of people.

Thank you to the Peters, Agapie, Grubbs, Bercaw, Fu, Hadt, See, Reisman, Stoltz, and Tirrell groups, who have provided help in numerous ways, including insightful discussions, sharing of chemicals, and access to instrumentation. Mike Takase, Larry Henling, David VanderVelde, and Mona Shahgholi have been invaluable colleagues in the collection and interpretation of data necessary to move my projects forward. The administrative staff is also fantastic- they have always made me feel like an individual rather than a number. For making sure I fulfilled the degree requirements and kept on track to graduate, I am grateful to Alison Ross and Agnes Tong. And for their help and time scheduling committee meetings, especially in the whirlwind that is the last couple of months of the academic year, I greatly thank Priscilla Boon, Margarita Davis, Pat Anderson, and Julianne Just.

The challenges of graduate school extend well beyond the scientific realm, and I would like to express my thanks to the Caltech Center for Inclusion & Diversity, Diversity in Chemistry Initiative, Graduate Studies Office, Student Wellness Services, and Athletics for providing support outside of the lab environment. I am especially grateful to the mental health services facilities, which have helped me navigate both the personal and professional difficulties of graduate life at Caltech.

Finally, I would like to thank the friends and family without which I could not have made it to the end. For their unwavering support, conviction, and friendship throughout graduate school, especially in the daunting early years, I offer my deepest and sincerest thanks to Pablo Guzman, Trixia Buscagan, Miles Johnson, Matthew Chalkley, Gautam Stroscio, and Jeffrey Rosenberg. I also owe a tremendous debt of gratitude to Shabnam Hematian, who at one of the toughest junctures of my time at Caltech took the time to listen to my concerns, offered compassion and advice, and gave me

the courage necessary to transition to the Gray group. You all have been and continue to be an incredible source of inspiration and strength for me, both in terms of and beyond the confines of chemistry. This thesis is only a small portion of what you have helped me achieve.

Up until this point, I have lived within a 1 hour radius of my home in Southern California, and as a result have been fortunate enough to have an amazing support system close by. To my family, Javier, Silvia, Emily and Jesus, thank you for your endless support, love, and numerous trips from Moreno Valley to Pasadena. To Allen Chan and David Woen, my best friends since our time at UC Riverside, thank you for all the crazy adventures that served as much-needed getaways from the toils of graduate school. Moreover, having gone through the process of earning a chemistry Ph.D. yourselves, your support, encouragement, understanding, and advice has been invaluable. We did it fellas! Thank you to my best friend Trixia, who has played a large role in helping me overcome the daily struggles of research and graduate life (especially at an institution like Caltech). And to the baby dog Ollie, which Trixia and I raised together, there are literally no words I can write or say to thank him for his unconditional love and all the joy he has brought me over the difficult years in graduate school. But that has not stopped me from trying!

In addition to those listed above, I dedicate this thesis to all the underrepresented minorities in STEM who have served as role models and paved the way to make obtaining a doctorate degree from Caltech possible. And to URMs considering an education in STEM, I dedicate this thesis to you in hope it may somehow help and provide inspiration on your journey.

-JFJ

ABSTRACT

Transition metal complexes are routinely employed as catalysts for the reductive cleavage of a diverse array of strong chemical bonds. Two notable research areas that exemplify such utility are nitrogen fixation, involving cleavage of the notoriously unreactive triple bond of dinitrogen (N_2) to form ammonia (NH_3), and photoredox catalysis, wherein powerful photoreductants generated by visible light excitation facilitate challenging reduction steps in a host of synthetic organic transformations. This thesis focuses on a number of structure-function studies conducted on group 8 transition metal complexes that catalyze N_2-to-NH_3 conversion, commonly referred to as the nitrogen reduction reaction (N_2RR), and on homoleptic tungsten(0) arylisocyanides that, among their many attractive qualities, possess highly reducing electronically excited states. These comparative studies provide fundamental insight into critical design features which can guide efforts to improve existing N_2RR or photocatalysts or rationally tailor them for specific applications.

Chapter 2 details the effect apical Lewis acidic atom substitution in P_3^XFe platforms (X = B, Al, Ga) has on structure, bonding, and N_2RR activity. Structural, spectroscopic, electrochemical, and computational studies reveal that all three P_3^XFe systems possess similar electronic structures, degrees of N_2 activation, and geometric flexibility, but $P_3^{Al}Fe$ and $P_3^{Ga}Fe$ display significantly lower N_2RR efficiencies than P_3^BFe when treated with $HBAr^F_4/KC_8$ or $[H_2NPh_2][OTf]/Cp^*_2Co$ at –78 °C in Et_2O.

Chapter 3 reports on isostructural tris(phosphino)silyl Ru and Os complexes that mediate catalytic N_2RR. The study of the homologous, isostructural series of complexes $P_3^{Si}M$ (M = Fe, Ru, Os) helps delineate important factors for N_2RR catalyst design. Low-temperature protonation of $P_3^{Si}Os–N_2^-$ yields $P_3^{Si}Os{=}NNH_2^+$, representing the first instance of an Os–N_2 species being converted to a protonated Os–N_xH_y product.

Chapter 4 communicates a novel series of homoleptic tungsten(0) photoactive complexes supported by fused-ring (CN-1-(2-^{i}Pr)-Naph) or alkynyl-bridged (CNDipp^{CC}Ar) arylisocyanide ligands. Systematic studies establish facile electronic variation of the CNDipp^{CC}Ar platform as a straightforward method by which to rationally modulate the ground- and excited-state properties of W(CNDipp^{CC}Ar)$_6$ complexes. The photophysical properties of W(CN-1-(2-^{i}Pr)-Naph)$_6$ reveal potential benefits of utilizing fused-ring arylisocyanide ligands in the design of this class of photosensitizers.

PUBLISHED CONTENT AND CONTRIBUTIONS

Fajardo Jr., J.; Peters, J. C. Catalytic Nitrogen-to-Ammonia Conversion by Osmium and Ruthenium Complexes. *J. Am. Chem. Soc.* **2017**, *139* (45), 16105−16108. DOI: 10.1021/jacs.7b10204.

J.F.J. conceived the project, designed the research, performed all experiments, and participated in the writing of the manuscript.

TABLE OF CONTENTS

LIST OF FIGURES

Chapter I:

Chapter II:

LIST OF SCHEMES

LIST OF TABLES

Chapter II:

Chapter III:

LIST OF ABBREVIATIONS

Å	Angstrom
AltraPhos	[(*o*-$C_6H_4NCH_2P^iPr_2)_3N$]Al
Aq	Aqueous
Ar	Aryl group
atm	Atmosphere
Avg	Average
$BAr^F{}_4^-$	$[B(3,5\text{-}C_6H_3(CF_3)_2)_4]^-$, tetrakis(3,5-bis(trifluoromethyl)phenyl)borate
BDFE	Bond dissociation free energy
bpy	2,2´-bipyridine
br	Broad
ca.	Circa
Calcd	Calculated
cm^{-1}	Wavenumber or inverse centimeters
CNAr	Arylisocyanide ligand
CNPh	Phenylisocyanide
CNDipp	2,6-Diisopropylphenylisocyanide
CNDippAr	Oligoarylisocyanide ligand
CNDippPh	4-Phenyl-2,6-diisopropylphenylisocyanide
$CNDippPh^{OMe2}$	4-(3,5-Dimethoxyphenyl)-2,6-diisopropylphenylisocyanide
$CNDippPh^{OMe3}$	4-(3,4,5-Trimethoxyphenyl)-2,6-diisopropylphenylisocyanide
$CNDippPh^{Ph}$	4-(4-Biphenyl)-2,6-diisopropylphenylisocyanide

CNDipp^{CC}Ar	Alkynyl-bridged arylisocyanide ligand
CN-2-Naph	2-Naphthylisocyanide
CN-1-Naph	1-Naphthylisocyanide
CN-1-(2-^{i}Pr)-Naph	2-Isopropyl-1-naphthylisocyanide
CNMe	Methylisocyanide
CN^{Me}Ar$_3$NC	2,2´´-Diisocyano-3,5,3´´,5´´-tetramethyl-1,1´:3´,1´´-terphenyl
CN^{tBu}Ar$_3$NC	2,2´´-Diisocyano-3,5,3´´,5´´-tetra-*tert*-butyl-1,1´:3´,1´´-terphenyl
CO	Carbonyl
Cp	Cyclopentadienyl
Cp*	Pentamethylcyclopentadienyl
CV	Cyclic voltammetry or voltammogram
d	Doublet or deuterium
DCM	Dichloromethane
dd	Doublet of doublets
DFT	Density functional theory
Dipp	2,6-Diisopropylphenyl
DME	1,2-Dimethoxyethane
DMF	N,N-Dimethylformamide
DMSO	Dimethylsulfoxide
d_x	Compound with x deuterium atoms
e^-	Electron

E	Redox potential
E_{00}	Difference in energy between the zeroth vibrational levels of the ground and excited states
E_p	Peak potential
EPR	Electron paramagnetic resonance
Equiv	Equivalents
Et_2O	Diethyl ether
eV	Electron volt
Fc	Ferrocene
FWHM	Full-width at half-maximum
g	Gram
G	Gauss
GM	Goeppert-Mayer
GS	Ground state
$HCCl_3$	Chloroform
HER	Hydrogen evolution reaction
Hg	Mercury
HMDSO	Hexamethyldisiloxane
HOMO	Highest occupied molecular orbital
$h\nu$	Light
Hz	Hertz
I	Intensity
^{i}Pr	Isopropyl

IR	Infrared
ISC	Intersystem crossing
J	NMR coupling constant
K	Kelvin
KC_8	Potassium graphite
k_{nr}	Nonradiative decay rate constant
k_r	Radiative decay rate constant
L	Liter
LUMO	Lowest unoccupied molecular orbital
m	Multiplet
M	Molar
Me	Methyl
MHz	Megahertz
mL	Milliliter
MLCT	Metal-to-ligand charge transfer
mM	Millimolar
mm	Millimeter
mmol	Millimole
mol	Mole
mV	Millivolt
N_2RR	Nitrogen reduction reaction
^{n}Bu	*n*-Butyl

nm	Nanometer
NMR	Nuclear magnetic resonance
ns	Nanosecond
N_xH_y	Generic nitrogenous ligands with x N atoms and y H atoms
p-	Para
P_3^{Al}	(*o*-^{i}Pr$_2$PC$_6$H$_4$)$_3$Al, tris(*o*-diisopropylphosphinophenyl)alane
P_3^{B}	(*o*-^{i}Pr$_2$PC$_6$H$_4$)$_3$B, tris(*o*-diisopropylphosphinophenyl)borane
P_3^{C}	[(*o*-^{i}Pr$_2$PC$_6$H$_4$)$_3$C]$^-$, tris(*o*-diisopropylphosphinophenyl)methyl anion
P_3^{Ga}	(*o*-^{i}Pr$_2$PC$_6$H$_4$)$_3$Ga, tris(*o*-diisopropylphosphinophenyl)gallane
P_3^{In}	(*o*-^{i}Pr$_2$PC$_6$H$_4$)$_3$In, tris(*o*-diisopropylphosphinophenyl)indane
P_3^{Si}	[(*o*-^{i}Pr$_2$PC$_6$H$_4$)$_3$Si]$^-$, tris(*o*-diisopropylphosphinophenyl)silyl anion
Ph	Phenyl
ppm	Parts per million
ppy	2-Phenylpyridine
Py	Pyridine
q	Quartet
r	Ratio of a Y–X bond length to the sum of the respective covalent radii
R	Generic organic group or R-factor
RT	Room temperature
S	Spin quantum number
s	Singlet or second
SET	Single electron transfer

t	Triplet
^{t}Bu	*tert*-Butyl
o-	Ortho
OTf	Trifluoromethanesulfonate anion
THF	Tetrahydrofuran
UV	Ultraviolet
V	Volt
Vis	Visible
XRD	X-ray diffraction
°	Degree
°C	Degrees Celcius
δ	Chemical shift or two-photon absorption cross section
Σ	Summation
ε	Extinction coefficient
η^{x}	Hapticity of order x
λ	Wavelength
λ_{max}	Wavelength of local maximum intensity
μ-X	Bridging X ligand
μA	Microampere
μ_{B}	Bohr magneton
μ_{eff}	Effective magnetic moment
μL	Microliter

μs	Microsecond
ν(xy)	Vibrational frequency between atoms x and y
σ	Hammett parameter
τ	Lifetime
φ	Dihedral angle
ϕ_{PL}	Photoluminescence quantum yield
ϕ_{PS}	Photosubstitution quantum yield
*	Lowest energy excited state
2-MeTHF	2-Methyltetrahydrofuran
12-c-4	12-crown-4
^{1}H	Hydrogen-1
$\{^{1}H\}$	Proton-decoupled
^{13}C	Carbon-13
^{15}N	Nitrogen-15
^{31}P	Phosphorus-31

Chapter 1

Introduction

1.1. Opening Remarks

Transition metal complexes are routinely employed as catalysts for the reductive cleavage of a diverse array of strong chemical bonds. Two notable research areas that exemplify such utility are nitrogen fixation, involving cleavage of the notoriously unreactive triple bond of dinitrogen (N_2) to form ammonia (NH_3), and photoredox catalysis, wherein powerful photoreductants generated by visible light excitation facilitate challenging reduction steps in a host of synthetic organic transformations. These examples also illustrate the different roles transition metal catalysts can adopt. Whereas in the former the catalyst is responsible for binding and activating N_2 towards functionalization, in the latter the excited state of the photocatalyst is involved solely in outer-sphere single electron transfer (SET) events. Therefore, the design principles for developing the coordination compounds used in these contexts are inherently different. However, the ability to readily modulate the properties of transition metal complexes with molecular precision through judicious tuning of the supporting ligand platform or metal center makes structure-function studies a powerful tool to gain a better understanding of such principles.

This thesis focuses on a number of structure-function studies conducted on group 8 transition metal complexes that catalyze N_2-to-NH_3 conversion, commonly referred to as the nitrogen reduction reaction (N_2RR), and on homoleptic tungsten(0) arylisocyanides that, among their many attractive qualities, possess highly reducing electronically excited states. As is outlined in the following sections, and discussed in greater detail in the individual chapters, these comparative studies provide fundamental insight into critical design features which can guide efforts to improve existing N_2RR or photocatalysts or rationally tailor them for specific applications or transformations of interest.

1.2. Development of Group 8 N_2RR Catalysts

The first iron-based N_2-to-NH_3 conversion catalyst, $[Na(12\text{-crown-}4)_2][P_3^BFe–N_2]$ (P_3^B = $(o\text{-}^i Pr_2PC_6H_4)_3B$), was disclosed by Peters and co-workers in 2013 (Figure 1.1).[1] When reacted with 46 equiv of $[H(OEt_2)_2][BAr^F{}_4]$ ($HBAr^F{}_4$, $BAr^F{}_4^-$ = tetrakis(3,5-bis(trifluoromethyl)phenyl)borate) as the acid and 50 equiv of KC_8 as the reductant in diethyl ether (Et_2O) at –78 °C under an N_2 atmosphere, this tris(phosphine)borane N_2RR catalyst produces 7.0 ± 1.0 equiv of NH_3 per Fe, corresponding to an efficiency of 46 ± 7% based on acid.[1] Subsequent reports have since established that P_3^BFe-mediated N_2RR proceeds with greater selectivities for NH_3 when decamethylcobaltocene (Cp^*_2Co) is instead paired with anilinium triflate acids.[2] Notably, 12.8 ± 0.5 equiv of NH_3 per Fe (efficiency of 72 ± 3% based on electrons) are formed when $P_3^BFe^+$ is treated with 54 equiv of Cp^*_2Co and 108 equiv of $[H_2NPh_2][OTf]$ in Et_2O at –78 °C.[3]

Because of its early identification and success, P_3^BFe has been the subject of numerous mechanistic,[2-4] reactivity,[5-13] and computational studies[14-19] aimed at elucidating the pathway by which it mediates N_2-to-NH_3 conversion. These investigations have proven to be deeply informative about the design principles that are essential to the N_2RR performance of the P_3^BFe platform. Importantly, results suggest that the electronic and geometric flexibility of the Fe→B interaction is important for storing reducing equivalents in low-valent states that initially bind/activate π-acidic N_2 while also accommodating π-donating nitrogen fixation intermediates that form upon successive N_2 functionalization (Figure 1.2A). The ability of P_3^BFe complexes to adopt (relatively) stable electronic structures along this progression has been critical to the characterization of N_2 fixation intermediates and achievement of sufficiently strong $P_3^BFe–N_xH_y$

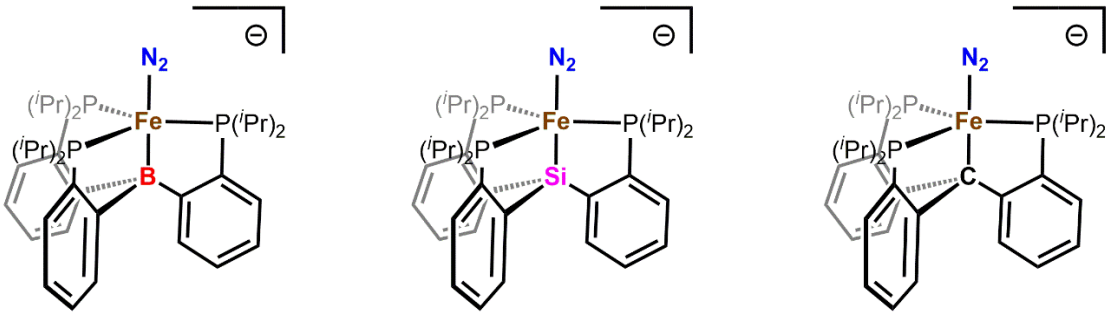

Figure 1.1. Previous isostructural $P_3^{X}Fe$ N_2RR catalysts reported by Peters and co-workers.

N–H bond dissociation free energies (BDFEs) in early intermediates to favor N_2RR over HER (hydrogen evolution reaction).

Equally important in establishing and validating these catalyst design principles have been parallel investigations on related $P_3^{Si}Fe$ (P_3^{Si} = $[(o\text{-}^{i}Pr_2PC_6H_4)_3Si]^-$) and $P_3^{C}Fe$ (P_3^{C} = $[(o\text{-}^{i}Pr_2PC_6H_4)_3C]^-$) systems, where the neutral Lewis acidic boron center has been replaced with an anionic silyl or alkyl donor, respectively (Figure 1.1). Indeed, explorations on $P_3^{Si}Fe$ preceded those of $P_3^{B}Fe$, and were crucial to the development of the latter. For instance, while early studies demonstrated that $P_3^{Si}Fe$ could bind/activate N_2, promote N_2 functionalization, and facilitate the late-stage N_2 fixation steps (e.g., reduction of $P_3^{Si}Fe–NH_3^+$ and $P_3^{Si}Fe–N_2H_4^+$ to release NH_3 and/or N_2H_4 and reform $P_3^{Si}Fe–N_2$),[20-22] treatment of $P_3^{Si}Fe–N_2$ with aryl azides led to the catalytic formation of N–N coupled azoarene products that proceeded through Fe-imido species that could only be observed as transients in frozen 2-MeTHF glasses at 77 K.[23] This was attributed to the rigidity of Si–Fe linkage, which enforces a trigonal bipyramidal environment at the Fe center and an associated electronic structure where the Fe–N antibonding $\pi^*(d_{xz},d_{yz})$ orbitals are occupied Figure 1.2B). Having previously demonstrated that Fe-imido groups could be stabilized in pseudotetrahedral coordination geometries in related tris(phosphine)borate systems,[24-26] and

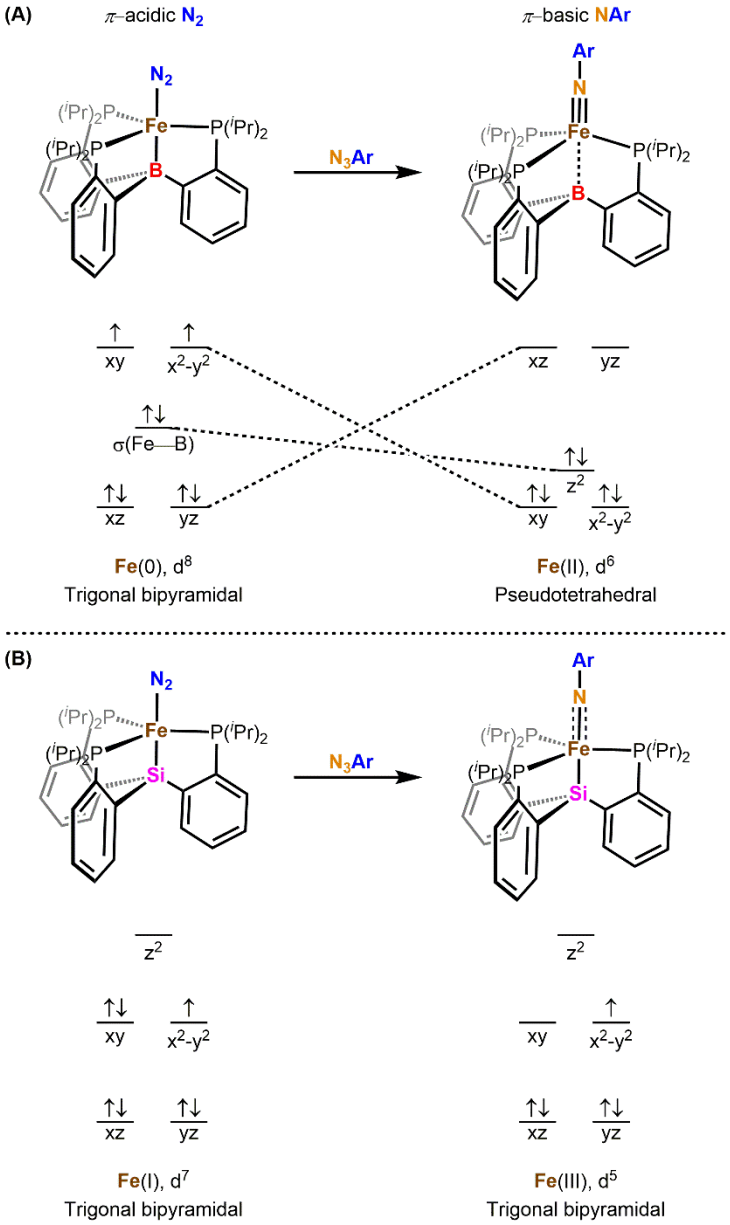

Figure 1.2. (A) Representative example demonstrating how the flexibility of the Fe–B linkage allows the $P_3{}^{B}Fe$ system to adopt more favorable geometries and electronic structures that can stabilize Fe–N multiply bonded species, in contrast to (B) the more rigid Fe–Si bond of $P_3{}^{Si}Fe$.

hypothesizing that such Fe–N multiply bonded species are likely intermediates of Fe-mediated N_2-to-NH_3 conversion that need to be stabilized to an appreciable extent, helped guide the design of

the P_3^BFe system. In contrast to $P_3^{Si}Fe$, the iron center in P_3^BFe can shuttle between pseudotetrahedral and trigonal bipyramidal geometries, and treatment of $P_3^BFe–N_2$ with organic azides yields stable and isolable Fe≡N–R imido complexes (Figure 1.2A).[5]

Further evidence in support of the importance of the hemilabile Fe–B linkage for efficient N_2-to-NH_3 conversion came from studies of the N_2RR catalytic activity of $P_3^{Si}Fe$ under conditions that proved fruitful for P_3^BFe. From these investigations, it was found that $P_3^{Si}Fe$ exhibits far greater selectivity for HER than N_2RR,[4] with reaction of $[Na(12\text{-crown-}4)_2][P_3^{Si}Fe–N_2]$ with 46 equiv of $HBAr^F_4$ and 50 equiv of KC_8 in Et_2O at –78 °C only producing 0.8 ± 0.5 equiv of NH_3 per Fe (efficiency of 5 ± 3%).[1] Similarly, treatment of $P_3^{Si}Fe–N_2$ with 54 equiv of Cp^*_2Co and 108 equiv of $[H_2NPh_2][OTf]$ in Et_2O at –78 °C yields 1.2 ± 0.1 equiv of NH_3 per Fe (efficiency of 6 ± 1%).[3]

Despite the underwhelming N_2RR selectivity of $P_3^{Si}Fe–N_2^-$, several notable observations suggested that $P_3^{Si}M$ may still be a promising platform to mediate N_2-to-NH_3 conversion. Most notably, upon substantially increasing the acid and reductant loading to 1500 equiv of $HBAr^F_4$ and 1800 equiv of KC_8, $P_3^{Si}Fe–N_2^-$ generates catalytic yields of NH_3 (3.8 ± 0.8 equiv per Fe), albeit with dismal efficiency (0.8 ± 0.2%; Figure 1.4A).[4] Isostructural $[K(OEt_2)_2][P_3^CFe–N_2]$ is also a competent N_2RR catalyst with a selectivity intermediary to that of $P_3^{Si}Fe–N_2^-$ and $P_3^BFe–N_2^-$ (4.6 ± 0.8 equiv NH_3 per Fe, 36 ± 6%, when reacted with 38 equiv of $HBAr^F_4$ and 40 equiv of KC_8).[27] Finally, $P_3^{Si}Fe–N_2^-$ can undergo productive protonation at low temperature with $HBAr^F_4$ or triflic acid (HOTf) to yield the isolable Fe-hydrazido(2–) complex $P_3^{Si}Fe{=}NNH_2^+$ (Figure 1.4A),[28] which features Fe–N multiple bond character and is analogous to the catalytically relevant $P_3^BFe{=}NNH_2^+$ distal nitrogen fixation intermediate.[9]

The collection of findings described above prompted further studies of the $P_3^{B}Fe$ and $P_3^{Si}M$ platforms in order to develop additional N_2RR catalyst design principles. Firstly, given the high N_2RR catalytic efficiencies boasted by $P_3^{B}Fe$, and the decreased performance of $P_3^{C}Fe$ and $P_3^{Si}Fe$ under analogous conditions, a logical extension of these comparative studies was the exploration of the related tris(phosphine)alane (P_3^{Al})[29] and tris(phosphine)gallane[30] Fe systems (Figure 1.3). Because all three $P_3^{X}Fe$ scaffolds (X = B, Al, Ga) feature a group 13 X(III) Lewis acidic center, systematic studies were anticipated to yield complementary findings to those of $P_3^{Si}Fe$ and $P_3^{C}Fe$, and thus aid in further discerning the effect of the apical atom on structure, bonding, and N_2RR activity. This forms the basis for the research described in Chapter 2 of this thesis.

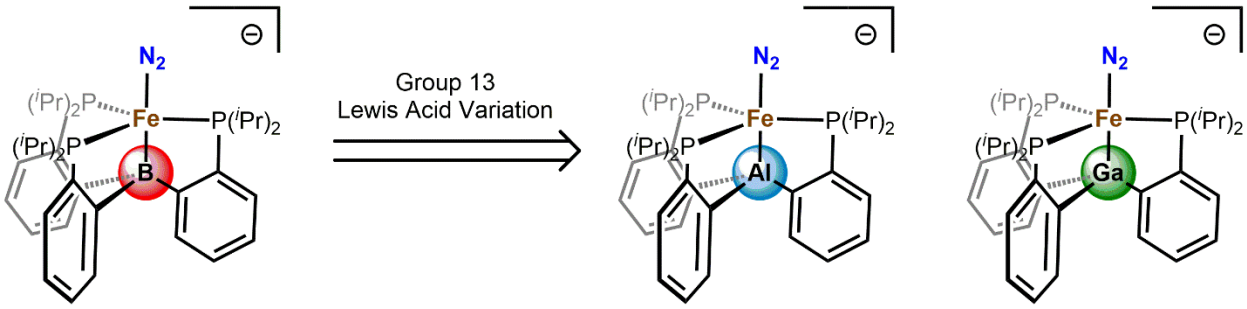

Figure 1.3. $P_3^{X}Fe$ (X = B, Al, Ga) platforms employed in the structure-function studies described in Chapter 2 to investigate the effect of the apical Lewis acidic atom on structure, bonding, and N_2RR activity.

The second set of structure-function studies conducted explored the effect of group 8 metal center variation on $P_3^{Si}M$-mediated N_2RR catalysis. In addition to the promising observations noted above for $P_3^{Si}Fe$ and $P_3^{C}Fe$, previous examinations of $P_3^{Si}Ru$ and $P_3^{Si}Os$ also indicated they might be active for N_2RR catalysis. Notably, like $P_3^{B}Fe$ and $P_3^{Si}Fe$, the $P_3^{Si}M$ (M = Ru, Os) systems

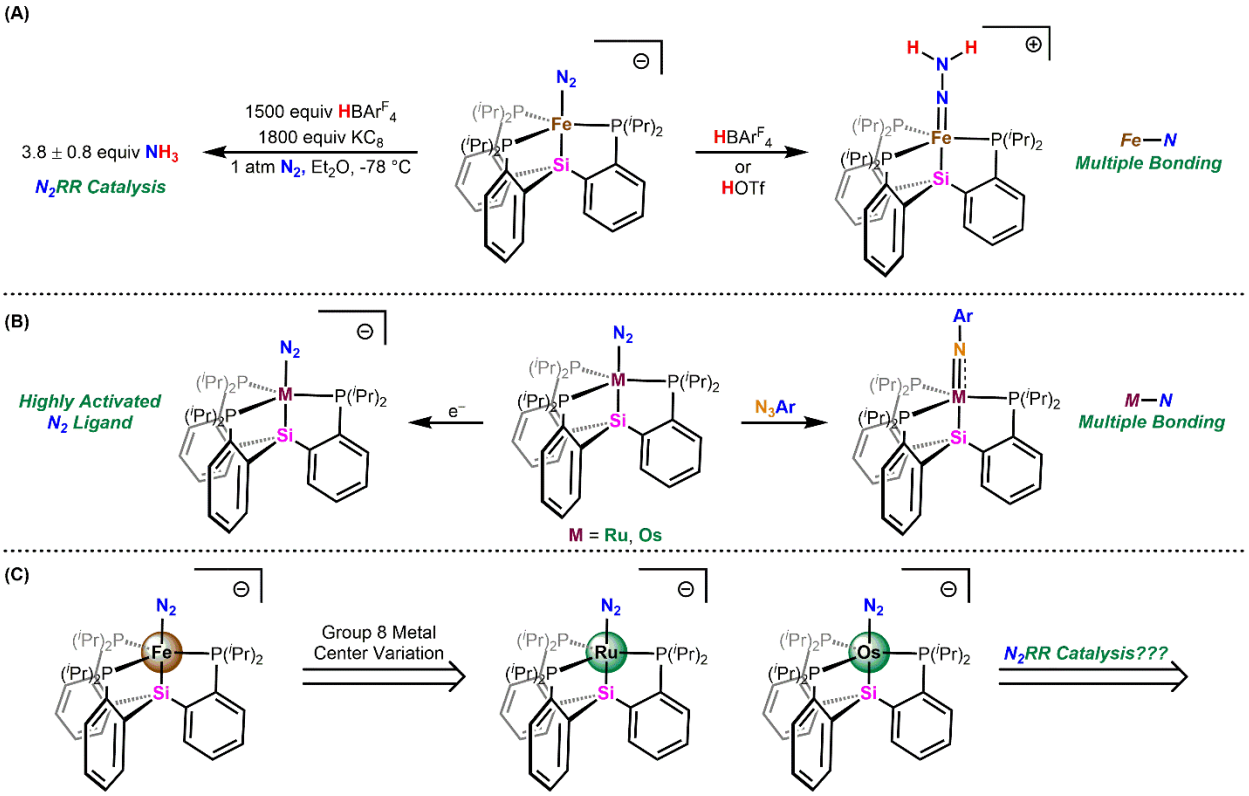

Figure 1.4. (A) Recent results suggesting $P_3^{Si}Fe$ can catalyze N_2RR and support Fe–N multiply bonded species, (B) previous studies on $P_3^{Si}Ru$ and $P_3^{Si}Os$ demonstrating that these platforms can bind/activate N_2 and support M–N multiply bonded species (M = Ru, Os), and (C) the structure-N_2RR activity studies on $P_3^{Si}M$ recapitulated in Chapter 3.

are capable of binding N_2 in multiple oxidation states, with $P_3^{Si}Ru–N_2^-$ and $P_3^{Si}Os–N_2^-$ displaying among the most activated dinitrogen ligands known for terminal N_2 complexes of Os(0) and Ru(0).[31] They also form stable $P_3^{Si}M$-imido species upon reaction with aryl azides, exemplifying their ability to stabilize M–N multiply bonded species (Figure 1.4B).[31,32] Interestingly, the reduction potentials of $P_3^{Si}Ru–N_2$ (E = –2.14 V vs $Fc^{[1+/0]}$)[31] and $P_3^{Si}Os–N_2$ (E = –1.94 V vs $Fc^{[1+/0]}$)[31] are anodically shifted from that of $P_3^{Si}Fe–N_2$ (E = –2.2 V vs $Fc^{[1+/0]}$)[22] and potentially accessible with Cp^*_2Co (E (Co^+/Co^0) = –1.96 V vs $Fc^{[1+/0]}$). Previous chemical and electrochemical

reactivity studies indicate that accessing the anionic dinitrogen complexes $P_3^BFe–N_2^-$ and $P_3^{Si}Fe–N_2^-$ is requisite for productive N_2 protonation.[2-4,9,22,28] Thus, $P_3^{Si}Ru$ and $P_3^{Si}Os$ could possibly provide the first examples of Ru- and Os-based N_2-to-NH_3 conversion catalysts (Figure 1.4C), catalyze N_2RR under the milder $[H_2NPh_2][OTf]/Cp^*_2Co$ conditions, and lend further evidence to the aforementioned design principles. Chapter 3 details the investigations of the N_2RR reactivity of $P_3^{Si}Ru–N_2^-$ and $P_3^{Si}Os–N_2^-$.

1.3. Group 6 Homoleptic Arylisocyanides: Powerful Photoreductants

Over the past decade, visible light photocatalysis has emerged as a powerful tool for synthetic chemists, enabling the discovery of novel chemical transformations and access to more efficient synthetic routes than those possible with traditional thermal methods.[33] However, the majority of these methodologies rely on $Ru(bpy)_3^{2+}$- or *fac*-$Ir(ppy)_3$-type complexes (bpy = 2,2´-bipyridine; ppy = 2-phenylpyridine) as the photoredox catalyst to perform demanding single electron oxidations or reductions.[34] While these robust, precious metal-based complexes offer long-lived, strongly luminescent, and highly reducing metal-to-ligand charge transfer (MLCT) [$d\pi(M) \rightarrow \pi^*$(ligand)] electronically excited states,[35] the development of earth-abundant photoredox catalysts with similarly favorable photophysical and photochemical properties is of great interest.[36,37]

In this regard, isoelectronic group 6 homoleptic arylisocyanide (CNAr) transition metal complexes represent an attractive alternative. First investigated by our group in the late 1970s, $M(CNAr)_6$ compounds (Figure 1.5A), employing monodentate monoarylisocyanide ligands, exhibit intense MLCT [$d\pi(M) \rightarrow \pi^*$(CNAr)] bands in the 400–500 nm visible region of their

electronic absorption spectra (M = Cr: λ_{max} = 475 nm, ε = 7.6 x 10^4 M^{-1} cm^{-1}; M = Mo: λ_{max} = 475 nm, ε = 7.2 x 10^4 M^{-1} cm^{-1}; M = W: λ_{max} = 465 nm, ε = 9.5 x 10^4 M^{-1} cm^{-1}).[38,39] These favorable spectroscopic properties arise from combining strong σ-donor and π-acceptor CNAr ligands with electron releasing M(0) centers to produce a large octahedral field splitting where the dσ-antibonding e_g* orbitals are highly destabilized. Importantly, the energy of the e_g* set resides significantly above that of the ligand-based π*(CNAr) orbital, which results from the interaction of the aryl group lowest unoccupied molecular orbital (LUMO) with the (originally degenerate) out-of-plane isocyanide C≡N π*-star orbital to give the energetically stabilized π^*_v orbital delocalized over the entire C≡N–Ar unit.[40,41] Thus, $M(CNAr)_6$ complexes possess the electronic structure shown in Figure 1.5B, and the MLCT transitions occur at relatively low energies.[38,39] For comparison, isoelectronic $M(CO)_6$ (M = Cr, Mo, W) and $Mn(CNMe)_6^+$ compounds, whose ligands

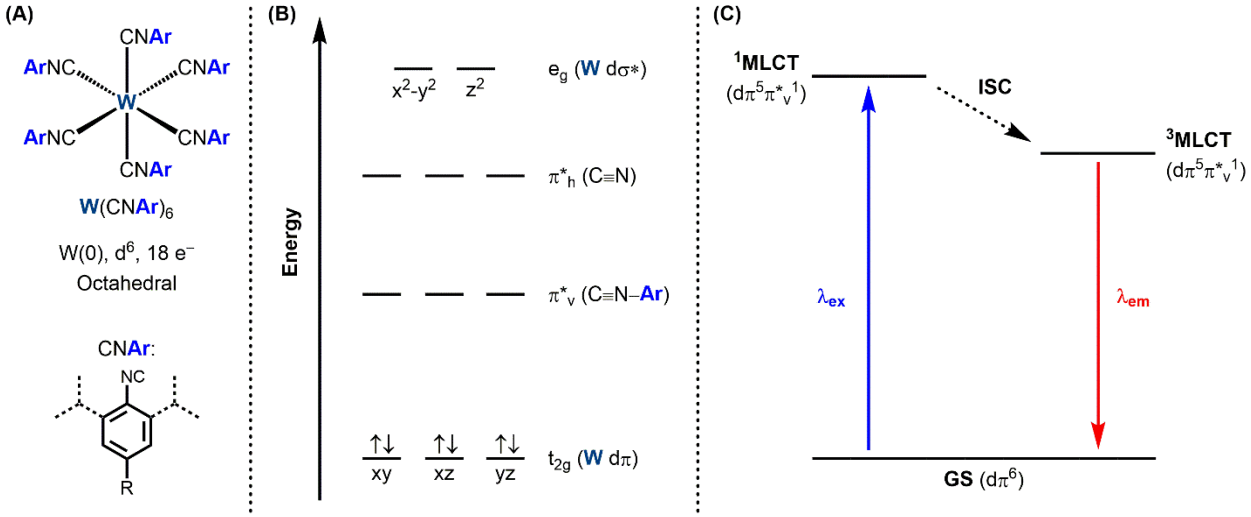

Figure 1.5. (A) Tungsten(0) hexakis(arylisocyanides) studied by our group, (B) a simplified molecular orbital diagram depicting their electronic structure, and (C) a simplified Jablonski diagram showing the dynamics that lead to population of their long-lived, luminescent, and highly reducing ^{3}MLCT state.

do not benefit from a similar type of stabilization as CNAr, undergo MLCT [dπ(M) → π*(ligand)] transitions at much higher energies.[42-44]

In accordance with their electronic structure, $Mo(CNPh)_6$ and $W(CNPh)_6$ (CNPh = phenylisocyanide) display ^{3}MLCT luminescence in 77 K solvent glasses and room temperature solutions (Figure 1.5C). However, in the latter, they are readily susceptible to photoinduced ligand substitution. For example, upon 436 nm irradiation of pyridine (Py) solutions of $M(CNPh)_6$ (M = Mo, W), $Mo(CNPh)_5(Py)$ and $W(CNPh)_5(Py)$ are obtained with photosubstitution quantum yields (ϕ_{PS}) of 0.055 and 0.011, respectively (Figure 1.6).[45,46] Alternatively, irradiation of $M(CNPh)_6$ in degassed chloroform ($HCCl_3$) solution leads to one-electron reduction of $HCCl_3$ and subsequent formation of seven-coordinate $[M(CNPh)_6(Cl)]^+$ (M = Mo, W).[45,46] Such structural changes are undesirable for photosensitizer and photoredox applications.

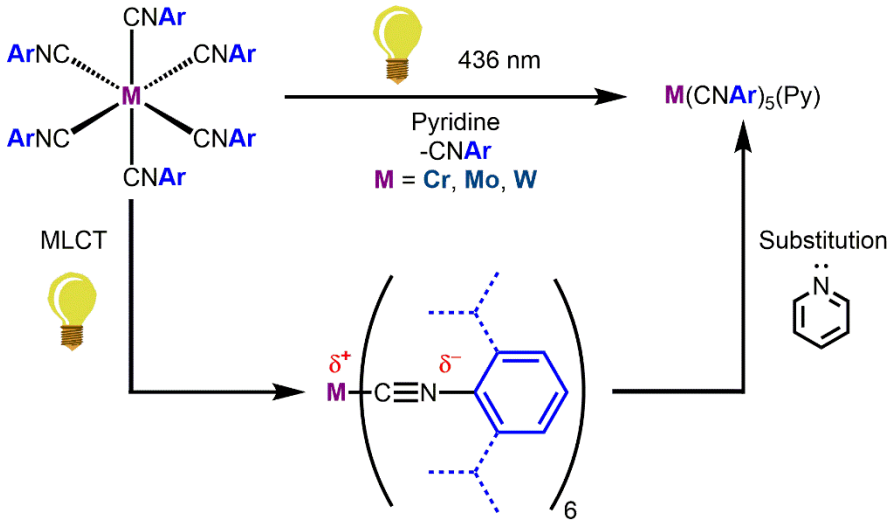

Figure 1.6. Protection of the metal center in $M(CNAr)_6$ by addition of *ortho* sterics leads to lower photosubstitution quantum yields for $M(CNDipp)_6$ versus $M(CNPh)_6$ (M = Mo, W).

Hypothesizing that the above reactions likely proceed through an associative rather than dissociative process because of the highly destabilized nature of the metal-centered (d-d) excited states (Figure 1.5B), our group then investigated analogous complexes bearing bulkier 2,6-diisopropylphenylisocyanide (CNDipp) ligands. Gratifyingly, the more sterically hindered $M(CNDipp)_6$ photoactive compounds feature substantially lower ϕ_{PS} in pyridine solution (M = Mo, 0.022; M = W, 0.0003; Figure 1.6), and only the one-electron oxidation product $M(CNDipp)_6^+$ is obtained upon photoexcitation in degassed $HCCl_3$.[45,46] Therefore, in addition to the use of arylisocyanides, a second critical design principle for developing photo-robust $M(CNAr)_6$ complexes (M = Mo, W) is the inclusion of *ortho* sterics to shield the formally oxidized metal center, that forms after excitation and/or SET, from attack by nucleophiles.

Despite these promising early findings by our group, this research area laid dormant for over three decades. However, a renewed interest in these comparatively earth-abundant photoactive complexes has led to significant advances over the last several years, and group 6 homoleptic arylisocyanides are now beginning to emerge as a privileged class of low-spin d^6 photosensitizers with photophysical and photochemical properties that rival those of Ru(II) and Ir(III) photoactive complexes.[47,48] Notably, Wenger and co-workers have employed chelating *meta*-terphenyl diisocyanides to prepare a number of remarkably photostable homoleptic complexes of the form $M(CNAr_3NC)_3$, which in addition to displaying long-lived luminescence in room temperature solution, possess ^{3}MLCT excited states that are far more reducing than that of *fac*-$Ir(ppy)_3$ (E ($Ir^{4+}/*Ir^{3+}$) = –2.1 V vs $Fc^{[1+/0]}$; * denotes the lowest energy excited state) and have been exploited in visible light photoredox catalysis (Figure 1.7). For example, $Mo(CN^{Me}Ar_3NC)_3$ ($CN^{Me}Ar_3NC$ = 2,2´´-diisocyano-3,5,3´´,5´´-tetramethyl-1,1´:3´,1´´-terphenyl), a Mo(0)

isocyanide analogue of $Ru(bpy)_3^{2+}$ with an excited-state reduction potential of E ($Mo^+/*Mo^0$) = –2.6 V (vs $Fc^{[1+/0]}$), can photocatalyze the rearrangement of acyl cyclopropanes to 2,3-dihydrofurans.[49] Alternatively, replacement of the methyl groups with more sterically demanding *tert*-butyl substituents yields $Mo(CN^{t\text{Bu}}Ar_3NC)_3$ (E ($Mo^+/*Mo^0$) = –2.7 V vs $Fc^{[1+/0]}$; $CN^{t\text{Bu}}Ar_3NC$ = 2,2´´-diisocyano-3,5,3´´,5´´-tetra-*tert*-butyl-1,1´:3´,1´´-terphenyl), whose significantly improved lifetime (τ), photoluminescence quantum yield (ϕ_{PL}), and photo-robustness enable it to catalyze the light-driven base-promoted homolytic aromatic substitution of aryl iodides.[50] Importantly, photoexcited *fac*-$Ir(ppy)_3$ is not a competent photoredox catalyst for either reaction.

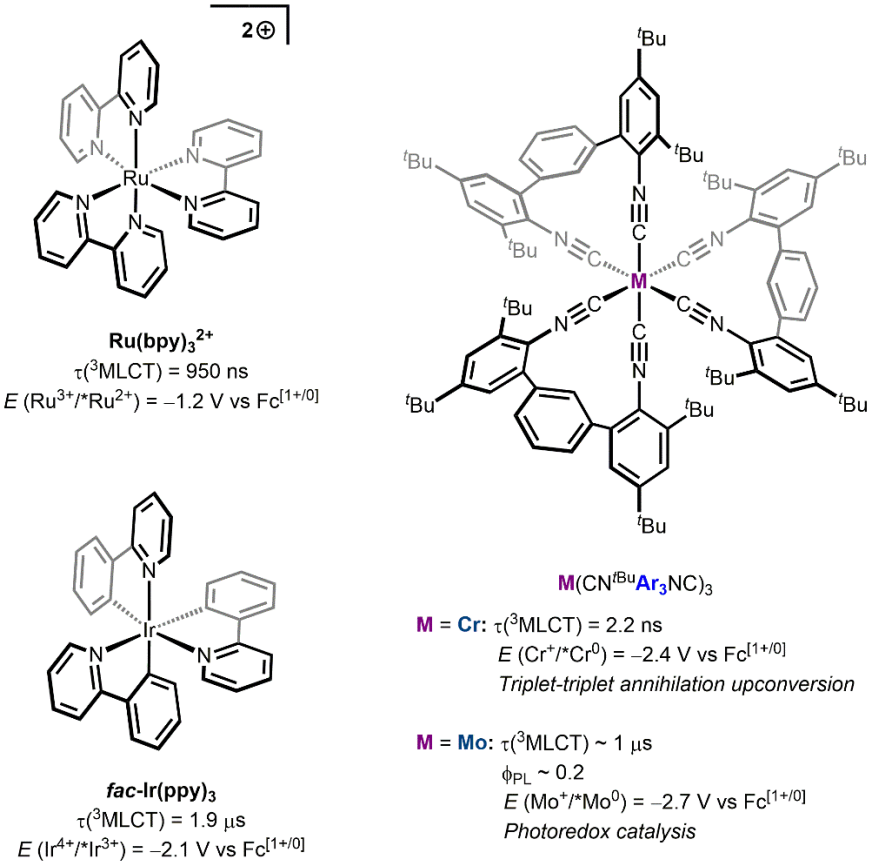

Figure 1.7. Comparison of the photophysical properties of $Ru(bpy)_3^{2+}$, *fac*-$Ir(ppy)_3$, and the group 6 tris(diisocyanides) $M(CN^{t\text{Bu}}Ar_3NC)_3$ (M = Cr, Mo).

The use of the sterically encumbered diisocyanide $CN^{tBu}Ar_3NC$ also proved to be instrumental for the construction of robust analogues of $Cr(CNAr)_6$ photoactive compounds. In contrast to $Cr(CNPh)_6$ and $Cr(CNDipp)_6$, which are nonemissive and only very weakly emissive in room temperature fluid solution, respectively,[45,46] $Cr(CN^{tBu}Ar_3NC)_3$ displays luminescence in deaerated room temperature THF solution with $\tau(^3MLCT) = 2.2$ ns (Figure 1.7), representing the first example of a $3d^6$ ^3MLCT room temperature photoluminescent analogue of $Fe(bpy)_3^{2+}$.[51] Furthermore, $Cr(CN^{tBu}Ar_3NC)_3$ is moderately photostable in weakly and noncoordinating solvents, whereas $Cr(CNPh)_6$ and $Cr(CNDipp)_6$ readily undergo dissociative ligand substitution upon photoexcitation (Figure 1.6). Although $Cr(CN^{tBu}Ar_3NC)_3$ has not been explored in photoredox applications, its favorable photophysical properties, photo-robustness, application in triplet-triplet annihilation upconversion, and comparable photoreducing power (E ($Cr^+/*Cr^0$) = –2.4 V vs $Fc^{[1+/0]}$) to $Mo(CN^RAr_3NC)_3$ (R = Me, ^{t}Bu) suggest it is a promising photocatalyst (Figure 1.7).[51]

Beginning in 2013, our group has conducted parallel investigations on the $W(CNDipp)_6$ system to further elaborate on its photophysical and photochemical properties. Like its tris(diisocyanide) congeners, $W(CNDipp)_6$ is relatively inert to photosubstitution (*vide supra*) and is a potent excited-state reductant (E ($W^+/*W^0$) = –2.8 V vs $Fc^{[1+/0]}$), capable of photoreducing anthracene, benzophenone, and cobaltocenium (as observed by transient absorption spectroscopy) upon visible light excitation (Figure 1.8A).[52] Lowering the energy of the π*(CNAr) orbital and its associated MLCT state through extension of the ligand aromatic π-system results in more intense and red-shifted MLCT absorption and emission profiles, longer $\tau(^3MLCT)$, and higher ϕ_{PL} for the complexes $W(CNDippPh)_6$ (CNDippPh = 4-phenyl-2,6-diisopropylphenylisocyanide),

$W(CNDippPh^{OMe2})_6$ ($CNDippPh^{OMe2}$ = 4-(3,5-dimethoxyphenyl)-2,6-diisopropylphenylisocyanide), $W(CNDippPh^{OMe3})_6$ ($CNDippPh^{OMe3}$ = 4-(3,4,5-trimethoxyphenyl)-2,6-diisopropylphenylisocyanide), and $W(CNDippPh^{Ph})_6$ ($CNDippPh^{Ph}$ = 4-(4-biphenyl)-2,6-diisopropylphenylisocyanide).[53] Importantly, these tungsten(0) oligoarylisocyanides $W(CNDippAr)_6$ retain comparable excited-state reduction potentials (Figure 1.8B) and are capable of reducing aryl alkyl ketone substrates, such as acetophenone (as judged by transient absorption spectroscopy), whose reductive functionalization is of interest to the organic community.[53]

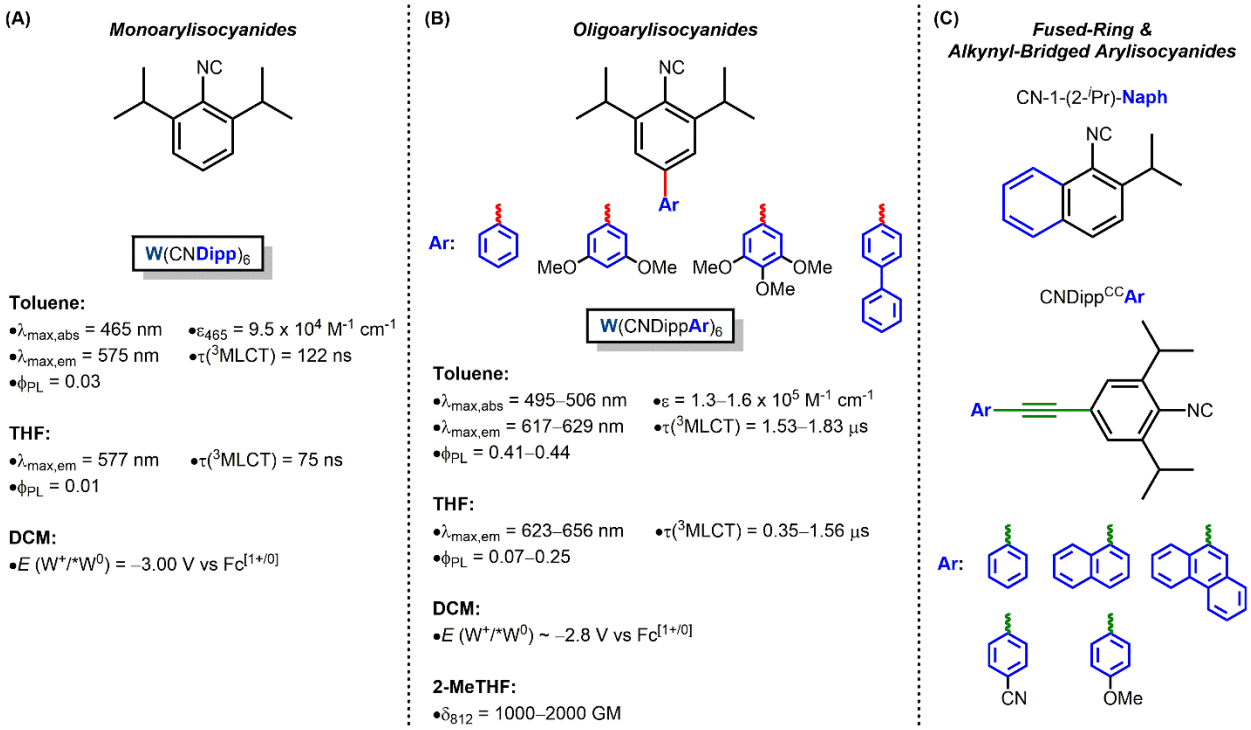

Figure 1.8. (A,B) Previous work demonstrating the enhancement of the photophysical properties of $W(CNAr)_6$ compounds upon moving from CNDipp to CNDippAr ligands and (C) the fused-ring and alkynyl-bridged arylisocyanide ligands explored in the structure-function studies of Chapter 4 to probe the effect of further extension of the ligand aromatic system.

In addition to giving rise to more favorable one-photon photophysical properties, another important consequence of moving from the use of monoarylisocyanides to oligoarylisocyanides is the enhancement of nonlinear optical properties of the corresponding tungsten compounds. For instance, while $W(CNDipp)_6$ does not have a detectable two-photon absorption (TPA) cross section at 812 nm (δ_{812}), $W(CNDippPh)_6$, $W(CNDippPh^{OMe2})_6$, and $W(CNDippPh^{Ph})_6$ possess exceptionally high δ_{812} = 1000–2000 GM (GM = Goeppert-Mayer; 1 GM = 10^{-50} cm^4 s $photon^{-1}$ $molecule^{-1}$; Figure 1.8B).[54] For comparison, $\delta_{812}(Ru(bpy)_3^{2+})$ = 7 GM and δ_{800}(*fac*-$Ir(ppy)_3$) = 20 GM are drastically smaller.[54,55] Because both one-photon and two-photon absorption by $W(CNDippAr)_6$ complexes leads to population of the same reactive ^{3}MLCT state,[54] this opens the possibility of triggering substrate photoreduction or photoredox catalysis using lower energy near infrared light.[56]

Motivated by these dramatic enhancements observed for $W(CNDippAr)_6$ complexes, we embarked on further studies to probe the effect of extension of the ligand aromatic system on the one- and two-photon photophysical properties of the resulting $W(CNAr)_6$ compounds. Guided by the design principles established up to this point (e.g., the importance of *ortho* sterics, etc.), we prepared a novel series of fused-ring (CN-1-(2-^{i}Pr)-Naph) and alkynyl-bridged ($CNDipp^{CC}Ar$) arylisocyanide ligands (Figure 1.8C). Through systematic variation of their electronics, we demonstrate that simple substitutions on the latter ligand platform provides a straightforward method by which to rationally modulate the photophysical properties of $W(CNDipp^{CC}Ar)_6$ complexes. We also establish other important considerations in the design of $W(CNAr)_6$ photosensitizers. The detailed results of these studies are presented in Chapter 4.

1.4. Overview of Individual Chapters

In Chapter 2, the results of structure-function studies designed to probe the effects of the apical Lewis acidic atom on structure, bonding, and N_2RR activity of P_3^XFe platforms (X = B, Al, Ga) are discussed. While structural, spectroscopic, electrochemical, and computational studies reveal that all three P_3^XFe systems possess similar electronic structures, degrees of N_2 activation, and geometric flexibility, $P_3^{Al}Fe$ and $P_3^{Ga}Fe$ display significantly lower N_2RR efficiencies than P_3^BFe when treated with $HBAr^F_4/KC_8$ or $[H_2NPh_2][OTf]/Cp^*_2Co$ at –78 °C in Et_2O. Preliminary reactivity studies confirm that all P_3^XFe frameworks are robust under these catalytic conditions employed, suggesting a greater selectivity for HER over N_2RR may be responsible for the attenuated NH_3 yields observed for $P_3^{Al}Fe$ and $P_3^{Ga}Fe$ relative to P_3^BFe.

Chapter 3 recapitulates a complementary set of structure-function studies on the homologous, isostructural series of complexes $P_3^{Si}M–N_2^-$ (M = Fe, Ru, Os) to (1) explore the viability of Ru- and Os-mediated N_2RR catalysis and (2) help delineate important factors for N_2RR catalyst design. Despite the critical role Ru and Os complexes have played in the development of transition metal dinitrogen chemistry, at the time of this work they had not been shown to mediate catalytic N_2RR. Moreover, molecular N_2RR catalysts based on metals other than Fe and Mo were limited to two cobalt systems. Results from this work establishes that both $P_3^{Si}Ru–N_2^-$ and $P_3^{Si}Os–N_2^-$ are competent N_2RR catalysts. The Os system is most active, and liberates more than 120 equiv NH_3 per Os center in a single batch experiment using Cp^*_2Co and $[H_2NPh_2][OTf]$ as reductant and acid source. Stoichiometric reactivity studies reveal that (1) Cp^*_2Co can competently reduce $P_3^{Si}Os–N_2$ to $P_3^{Si}Os–N_2^-$ at –78 °C, a step critical for productive N_2 functionalization, and (2) the dinitrogen ligand of $P_3^{Si}Os–N_2^-$ is sufficiently activated to be doubly protonated to afford

the structurally characterized hydrazido(2–) species $P_3^{Si}Os{=}NNH_2^+$. In addition to representing the first instance of an Os–N_2 species being converted to a protonated Os–N_xH_y product, $P_3^{Si}Os{=}NNH_2^+$ itself mediates NH_3 generation, suggesting it is a plausible intermediate of the catalysis. A systematic variation in the acid source of the N_2RR catalysis also suggests that the use of Et_2O-insoluble anilinium triflates is important in impeding the formation of Os-hydride species that form during catalysis as inactive species.

Finally, in Chapter 4 a novel series of homoleptic tungsten(0) photoactive complexes supported by fused-ring (CN-1-(2-^{i}Pr)-Naph) or alkynyl-bridged (CNDipp^{CC}Ar) arylisocyanide ligands is reported. Through systematic variation of the ligand electronics, we demonstrate that simple substitutions on the CNDipp^{CC}Ar platform provide a straightforward method by which to rationally modulate the ground- and excited-state properties of W(CNDipp^{CC}Ar)$_6$ complexes. Alternatively, study of the photophysical properties of W(CN-1-(2-^{i}Pr)-Naph)$_6$ reveals potential benefits of utilizing fused-ring arylisocyanide ligands in the design of this class of photosensitizers, such as increased steric protection and rigidity at the tungsten center that results in comparatively long lifetimes. The properties of these new photoactive compounds complement those of previously reported W(CNDippAr)$_6$ complexes.

1.5. References

(1) Anderson, J. S.; Rittle, J.; Peters, J. C. *Nature* **2013**, *501*, 84.

(2) Chalkley, M. J.; Del Castillo, T. J.; Matson, B. D.; Peters, J. C. *J. Am. Chem. Soc.* **2018**, *140*, 6122.

(3) Chalkley, M. J.; Del Castillo, T. J.; Matson, B. D.; Roddy, J. P.; Peters, J. C. *ACS Cent. Sci.* **2017**, *3*, 217.

(4) Del Castillo, T. J.; Thompson, N. B.; Peters, J. C. *J. Am. Chem. Soc.* **2016**, *138*, 5341.

(5) Moret, M.-E.; Peters, J. C. *Angew. Chem. Int. Ed.* **2011**, *50*, 2063.

(6) Moret, M.-E.; Peters, J. C. *J. Am. Chem. Soc.* **2011**, *133*, 18118.

(7) Anderson, J. S.; Moret, M.-E.; Peters, J. C. *J. Am. Chem. Soc.* **2013**, *135*, 534.

(8) Fong, H.; Moret, M.-E.; Lee, Y.; Peters, J. C. *Organometallics* **2013**, *32*, 3053.

(9) Anderson, J. S.; Cutsail, G. E.; Rittle, J.; Connor, B. A.; Gunderson, W. A.; Zhang, L.; Hoffman, B. M.; Peters, J. C. *J. Am. Chem. Soc.* **2015**, *137*, 7803.

(10) Buscagan, T. M.; Oyala, P. H.; Peters, J. C. *Angew. Chem. Int. Ed.* **2017**, *56*, 6921.

(11) Thompson, N. B.; Green, M. T.; Peters, J. C. *J. Am. Chem. Soc.* **2017**, *139*, 1531.

(12) Deegan, M. M.; Peters, J. C. *Chem. Sci.* **2018**, *9*, 6264.

(13) Nesbit, M. A.; Oyala, P. H.; Peters, J. C. *J. Am. Chem. Soc.* **2019**, *141*, 8116.

(14) Matson, B. D.; Peters, J. C. *ACS Catal.* **2018**, *8*, 1448.

(15) Thompson, N. B.; Oyala, P. H.; Dong, H. T.; Chalkley, M. J.; Zhao, J.; Alp, E. E.; Hu, M.; Lehnert, N.; Peters, J. C. *Inorg. Chem.* **2019**, *58*, 3535.

(16) Kaczmarek, M. A.; Malhotra, A.; Balan, G. A.; Timmins, A.; de Visser, S. P. *Chem. Eur. J.* **2018**, *24*, 5293.

(17) Lu, J.-B.; Ma, X.-L.; Wang, J.-Q.; Liu, J.-C.; Xiao, H.; Li, J. *J. Phys. Chem. A* **2018**, *122*, 4530.

(18) Jiang, Y.-F.; Ma, X.-L.; Lu, J.-B.; Wang, J.-Q.; Xiao, H.; Li, J. *Small Methods* **2019**, *3*, 1800340.

(19) Benedek, Z.; Papp, M.; Oláh, J.; Szilvási, T. *Inorg. Chem.* **2018**, *57*, 8499.

(20) Mankad, N. P.; Whited, M. T.; Peters, J. C. *Angew. Chem. Int. Ed.* **2007**, *46*, 5768.

(21) Whited, M. T.; Mankad, N. P.; Lee, Y.; Oblad, P. F.; Peters, J. C. *Inorg. Chem.* **2009**, *48*, 2507.

(22) Lee, Y.; Mankad, N. P.; Peters, J. C. *Nat. Chem.* **2010**, *2*, 558.

(23) Mankad, N. P.; Müller, P.; Peters, J. C. *J. Am. Chem. Soc.* **2010**, *132*, 4083.

(24) Brown, S. D.; Betley, T. A.; Peters, J. C. *J. Am. Chem. Soc.* **2003**, *125*, 322.

(25) Brown, S. D.; Peters, J. C. *J. Am. Chem. Soc.* **2005**, *127*, 1913.

(26) Mehn, M. P.; Peters, J. C. *J. Inorg. Biochem.* **2006**, *100*, 634.

(27) Creutz, S. E.; Peters, J. C. *J. Am. Chem. Soc.* **2014**, *136*, 1105.

(28) Rittle, J.; Peters, J. C. *J. Am. Chem. Soc.* **2016**, *138*, 4243.

(29) Sircoglou, M.; Saffon, N.; Miqueu, K.; Bouhadir, G.; Bourissou, D. *Organometallics* **2013**, *32*, 6780.

(30) Sircoglou, M.; Mercy, M.; Saffon, N.; Coppel, Y.; Bouhadir, G.; Maron, L.; Bourissou, D. *Angew. Chem. Int. Ed.* **2009**, *48*, 3454.

(31) Takaoka, A.; Gerber, L. C. H.; Peters, J. C. *Angew. Chem. Int. Ed.* **2010**, *49*, 4088.

(32) Takaoka, A.; Moret, M.-E.; Peters, J. C. *J. Am. Chem. Soc.* **2012**, *134*, 6695.

(33) Marzo, L.; Pagire, S. K.; Reiser, O.; König, B. *Angew. Chem. Int. Ed.* **2018**, *57*, 10034.

(34) Prier, C. K.; Rankic, D. A.; MacMillan, D. W. C. *Chem. Rev.* **2013**, *113*, 5322.

(35) Arias-Rotondo, D. M.; McCusker, J. K. *Chem. Soc. Rev.* **2016**, *45*, 5803.

(36) Larsen, C. B.; Wenger, O. S. *Chem. Eur. J.* **2018**, *24*, 2039.

(37) Hockin, B. M.; Li, C.; Robertson, N.; Zysman-Colman, E. *Catal. Sci. Technol.* **2019**, *9*, 889.

(38) Mann, K. R.; Cimolino, M.; Geoffroy, G. L.; Hammond, G. S.; Orio, A. A.; Albertin, G.; Gray, H. B. *Inorg. Chim. Acta* **1976**, *16*, 97.

(39) Kvapilová, H.; Sattler, W.; Sattler, A.; Sazanovich, I. V.; Clark, I. P.; Towrie, M.; Gray, H. B.; Záliš, S.; Vlček, A. *Inorg. Chem.* **2015**, *54*, 8518.

(40) Guy, M. P.; Guy, J. T.; Bennett, D. W. *J. Mol. Struct. (THEOCHEM)* **1985**, *122*, 95.

(41) Johnston, R. F.; Cooper, J. C. *J. Mol. Struct. (THEOCHEM)* **1991**, *236*, 297.

(42) Beach, N. A.; Gray, H. B. *J. Am. Chem. Soc.* **1968**, *90*, 5713.

(43) Rosa, A.; Baerends, E. J.; van Gisbergen, S. J. A.; van Lenthe, E.; Groeneveld, J. A.; Snijders, J. G. *J. Am. Chem. Soc.* **1999**, *121*, 10356.

(44) Fantucci, P. C.; Valenti, V.; Cariati, F. *Inorg. Chim. Acta* **1971**, *5*, 425.

(45) Mann, K. R.; Gray, H. B.; Hammond, G. S. *J. Am. Chem. Soc.* **1977**, *99*, 306.

(46) Gray, H. B.; Mann, K. R.; Lewis, N. S.; Thich, J. A.; Richman, R. M. *Inorganic and Organometallic Photochemistry* **1978**, *168*, 44.

(47) Büldt, L. A.; Wenger, O. S. *Dalton Trans.* **2017**, *46*, 15175.

(48) Büldt, L. A.; Wenger, O. S. *Angew. Chem. Int. Ed.* **2017**, *56*, 5676.

(49) Büldt, L. A.; Guo, X.; Prescimone, A.; Wenger, O. S. *Angew. Chem. Int. Ed.* **2016**, *55*, 11247.

(50) Herr, P.; Glaser, F.; Büldt, L. A.; Larsen, C. B.; Wenger, O. S. *J. Am. Chem. Soc.* **2019**, *141*, 14394.

(51) Büldt, L. A.; Guo, X.; Vogel, R.; Prescimone, A.; Wenger, O. S. *J. Am. Chem. Soc.* **2017**, *139*, 985.

(52) Sattler, W.; Ener, M. E.; Blakemore, J. D.; Rachford, A. A.; LaBeaume, P. J.; Thackeray, J. W.; Cameron, J. F.; Winkler, J. R.; Gray, H. B. *J. Am. Chem. Soc.* **2013**, *135*, 10614.

(53) Sattler, W.; Henling, L. M.; Winkler, J. R.; Gray, H. B. *J. Am. Chem. Soc.* **2015**, *137*, 1198.

(54) Takematsu, K.; Wehlin, S. A. M.; Sattler, W.; Winkler, J. R.; Gray, H. B. *Dalton Trans.* **2017**, *46*, 13188.

(55) Edkins, R. M.; Bettington, S. L.; Goeta, A. E.; Beeby, A. *Dalton Trans.* **2011**, *40*, 12765.

(56) Li, H.; Yang, Y.; He, C.; Zeng, L.; Duan, C. *ACS Catal.* **2019**, *9*, 422.

Chapter 2

A Comparative Study of Tripodal $P_3^XFe–N_2$ Complexes (X = B, Al, Ga): Effect of the Apical Atom on Bonding, Electronic Structure, and N_2-to-NH_3 Conversion

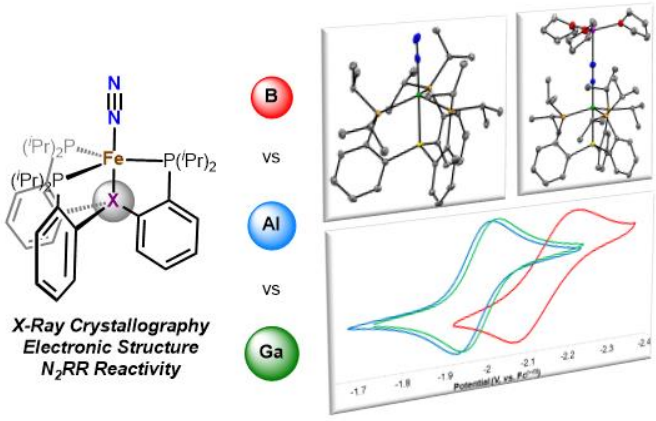

Abstract

Terminal dinitrogen complexes of iron ligated by tripodal, tetradentate P_3^X ligands (X = B, C, Si) have previously been shown to mediate catalytic N_2-to-NH_3 conversion (N_2RR) with external proton and electron sources. From this set of compounds, the tris(phosphino)borane (P_3^B) system is most active under all conditions canvassed thus far. To further probe the effects of the apical Lewis acidic atom on structure, bonding, and N_2RR activity, Fe–N_2 complexes supported by analogous group 13 tris(phosphino)alane (P_3^{Al}) and tris(phosphino)gallane (P_3^{Ga}) ligands are synthesized. The series of P_3^XFe–$N_2^{[0/1-]}$ compounds (X = B, Al, Ga) possess similar electronic structures and degrees of N_2 activation as determined from spectroscopic, structural, electrochemical, and computational (DFT) studies. However, treatment of [Na(12-crown-4)$_2$][P_3^XFe–N_2] (X = Al, Ga) with excess acid/reductant in the form of $HBAr^F{}_4$/KC_8 generates only 2.5 ± 0.1 and 2.7 ± 0.2 equiv of NH_3 per Fe, respectively. Similarly, the use of [H_2NPh_2][OTf]/$Cp^*{}_2Co$ leads to the production of 4.1 ± 0.9 (X = Al) and 3.6 ± 0.3 (X = Ga) equiv of NH_3. Preliminary reactivity studies confirming P_3^XFe framework stability under catalytic conditions suggest that a greater selectivity for hydrogen evolution versus N_2RR may be responsible for the attenuated yields of NH_3 observed for P_3^{Al}Fe and P_3^{Ga}Fe relative to P_3^BFe.

2.1. Introduction

While it was not long ago that well-defined molecular N_2-to-NH_3 conversion (N_2RR) catalysts were scarce and limited to Fe- and Mo-based transition metal complexes,[1-3] significant progress in the development of N_2RR catalysts in recent years has resulted in their increase in number, diversity, and efficiency.[4] These advancements have largely been made possible by a combination of systematic reactivity studies, in-depth mechanistic investigations, and structure-activity surveys.[4] Notably, the latter have been instrumental in optimizing the performance of Fe and Mo N_2RR catalysts, as well as the discovery of new catalytic systems based on other metals. For instance, inspired by their first report on (PNP)Mo-mediated N_2RR,[2] Nishibayashi and co-workers have performed systematic pincer ligand variations to develop a number of related (PXP)Mo complexes (X = N, P, C) capable of catalyzing N_2RR with more mild proton and electron sources, higher turnover numbers, and/or greater selectivities.[5] Similarly, metal center substitution of known Fe N_2-to-NH_3 conversion catalysts by V[6] or the nonbiologically relevant metals Co,[7] Ru,[8] and Os[8] has led to new catalytic systems supported by the same ligand platforms and featuring comparable N_2RR efficiencies. These systematic comparative studies are a critical component to gaining a better understanding of key N_2RR catalyst design principles.

In this context, extensive investigations carried out by our group on the dinitrogen coordination chemistry of and N_2RR catalysis by tripodal P_3^X ligated Fe complexes (P_3^B = (*o*-^{i}Pr$_2$PC$_6$H$_4$)$_3$B; P_3^C = [(*o*-^{i}Pr$_2$PC$_6$H$_4$)$_3$C]$^-$; P_3^{Si} = [(*o*-^{i}Pr$_2$PC$_6$H$_4$)$_3$Si]$^-$) have established that the identity of the apical atom (X) influences the observed N_2RR versus HER (hydrogen evolution reaction) selectivity.[3,9-13] Notably, from this series, the P_3^BFe system is the most efficient N_2RR catalyst under all conditions canvassed thus far, highlighting the privileged role of the group 13

Lewis acidic borane. This enhanced efficacy is in part attributed to the electron-accepting nature and geometric flexibility of the Fe→B interaction, which helps stabilize low-valent and Fe–N multiply bonded species proposed to be intermediates of a P_3^BFe-mediated nitrogen fixation cycle.[14-20]

Given the great importance of the boron center, we became interested in further probing the effect of X(III) apical atom substitution in the P_3^XFe framework on bonding, electronic structure, and N_2RR activity. To address this, herein we report the synthesis and characterization of the series of P_3^XFe–Br and P_3^XFe–$N_2^{[0/1-]}$ compounds supported by analogous group 13 tris(phosphino)alane (P_3^{Al} = (*o*-^{i}Pr$_2$PC$_6$H$_4$)$_3$Al)[21] and tris(phosphino)gallane (P_3^{Ga} = (*o*-^{i}Pr$_2$PC$_6$H$_4$)$_3$Ga)[22] ligands. Structural, spectroscopic, electrochemical, and computational studies reveal that all three P_3^XFe systems (X = B, Al, Ga) possess similar electronic structures, degrees of N_2 activation, and geometric flexibility. However, $P_3^{Al}Fe$ and $P_3^{Ga}Fe$ display significantly lower N_2RR efficiencies than P_3^BFe. Preliminary reactivity studies show that all P_3^XFe frameworks are robust under the catalytic conditions employed, suggesting a greater selectivity for competing HER may be responsible for the attenuated NH_3 yields observed.

2.2. Results and Discussion

2.2.1. Synthesis and Characterization of P_3^XFe–$N_2^{[0/1-]}$ Complexes

As an entry point into the desired dinitrogen chemistry, we sought to prepare an Fe(I) halide precursor similar to our approach in the related P_3^BFe system. Whereas P_3^BFe–Br (**2a**) can readily be prepared by heating a mixture of P_3^B (**1a**), Fe(0), and $FeBr_2$ to 90 °C in THF,[14] P_3^{Al} (**1b**) and P_3^{Ga} (**1c**) proved thermally unstable under these conditions. Instead, stirring **1b** and **1c** with $FeBr_2$

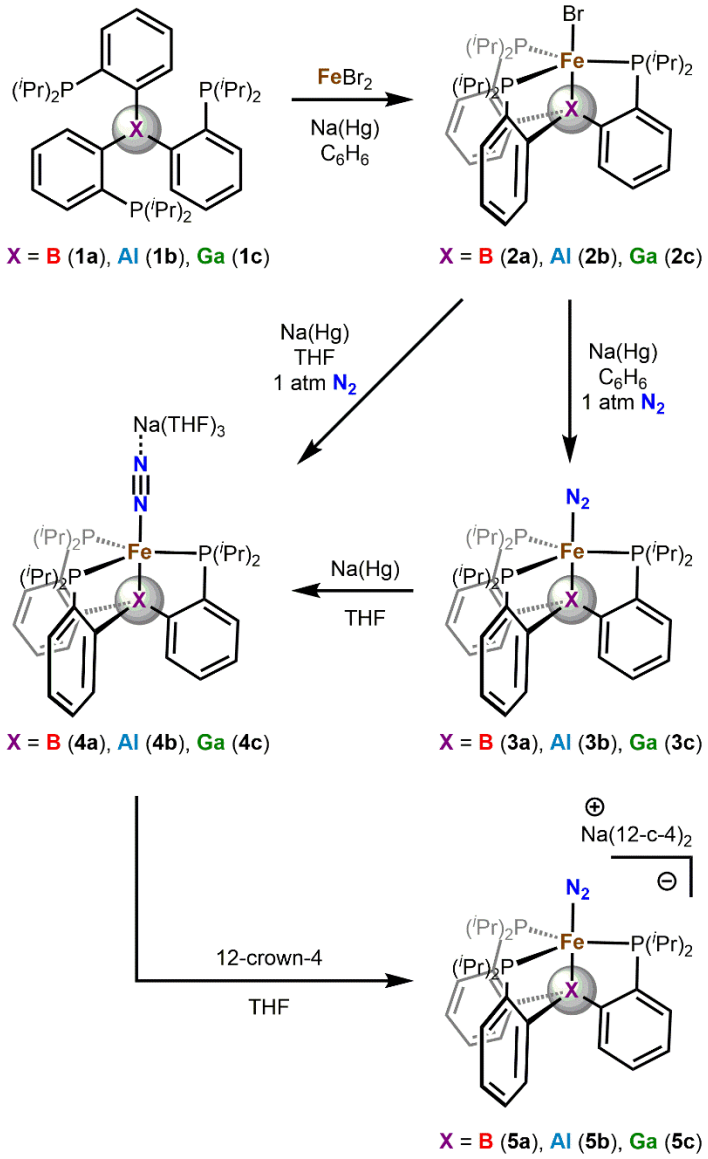

Scheme 2.1 Synthesis of $P_3^XFe–N_2^{[0/1-]}$ complexes.

in benzene, followed one-electron reduction with sodium amalgam (Na(Hg)), afforded the corresponding Fe(I) bromide complexes **2b** and **2c** as bright green solids in moderate isolated yield (Scheme 2.1). Both $P_3^XFe–Br$ derivatives feature paramagnetically shifted ^1H NMR resonances, solution magnetic moments of $\mu_{eff} = 4.3\mu_B$ (**2b**) and $\mu_{eff} = 4.2\mu_B$ (**2c**), and low-temperature rhombic EPR spectra (toluene glass, 10 K), consistent with an $S = 3/2$ ground state. The long Fe–P bond

lengths in the solid-state structures of **2b** (2.4603(3) Å) and **2c** (2.4690(3) Å) are also consistent with this high-spin configuration assignment (Figure 2.1). It is noteworthy that the Fe–Br bond in **2b** and **2c** remains intact, as previous examples of P_3^{Al} and P_3^{Ga} coordination to CuCl and AuCl(SMe$_2$) have instead yielded the zwitterionic complexes $P_3^{Al–Cl}$Cu and $P_3^{X–Cl}$Au (X = Al, Ga) resulting from halide abstraction by the apical X atom.[21,22] For comparison, reaction of P_3^{B} with these metal precursors instead yields P_3^{B}Cu–Cl and P_3^{B}Au–Cl.[23]

Reduction of **2b** and **2c** with Na(Hg) in benzene under a nitrogen atmosphere results in the formation of mononuclear dinitrogen complexes of the form P_3^{X}Fe–N$_2$ (X = Al (**3b**), X = Ga (**3c**)) (Scheme 2.1). **3b** and **3c** display intense, diagnostic infrared (IR) absorption bands at ν(NN) = 2003 and 1996 cm^{-1}, respectively, where the end-on N$_2$ ligand is only slightly more activated than in the related P_3^{B}Fe–N$_2$ (**3a**, 2011 cm^{-1})[14] and iron alumatrane (AltraPhos)Fe–N$_2$ (**6**, 2010 cm^{-1}, AltraPhos = Al[N(*o*-C$_6$H$_4$NCH$_2$P^{i}Pr$_2$)$_3$])[24] complexes and is moderately labile under vacuum.

The terminal nature of the N$_2$ moiety was further corroborated by X-ray diffraction (XRD) analysis of single crystals of **3b** and **3c** (Figure 2.1). The dinitrogen ligand in **3b** and **3c** exhibits a d(N–N) of 1.061 and 1.118 Å, consistent with minimal N$_2$ activation. In the solid state, **3b** and **3c** feature two short (**3b**: 2.3781(4), 2.3843(4) Å; **3c**: 2.3898(5), 2.3969(3) Å) and one comparable (**3b**: 2.4220(4) Å; **3c**: 2.4342(5) Å) Fe–P contact compared to **2b** and **2c**. This contraction in the Fe–P bonds is consistent with increased π-backdonation from the Fe center to the phosphines upon reduction, as well as the S = 1 ground state adopted by **3b** and **3c** in room temperature C$_6$D$_6$ solutions. XRD characterization of **3b** and **3c** allows for a structural comparison across the series of compounds **2**–**4** (*vide infra*) that span the formal oxidation states Fe(I) to Fe(–I). This contrasts with the P_3^{B}Fe system, where the XRD structure of **3a** could not be elucidated due to severe

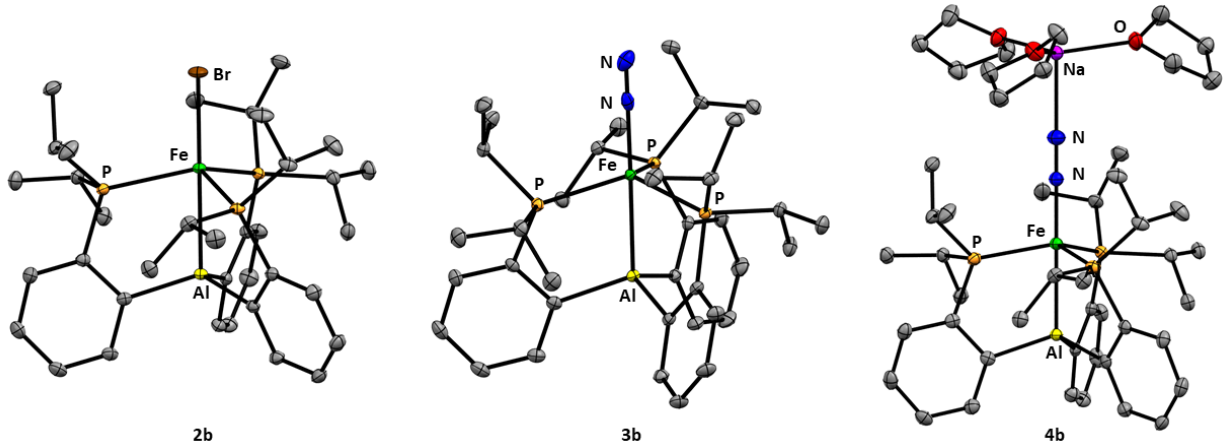

Figure 2.1. Solid-state structures of **2b**, **3b**, and **4b** with thermal ellipsoids set at 50% probability. Hydrogen atoms and co-crystallized solvents are omitted for clarity. The XRD structures of **2c**, **3c**, and **4c** are analogous and provided in the Experimental Section. See Table 2.1 for select structural data.

twinning.[14]

Treatment of $P_3^XFe–Br$ or $P_3^XFe–N_2$ with excess Na(Hg) in the more polar solvent THF leads exclusively to the anionic $S = ½$ complex $[Na(THF)_3][P_3^XFe–N_2]$ (X = Al (**4b**), X = Ga (**4c**)) (Scheme 2.1). Like $[Na(THF)_3][P_3^BFe–N_2]$ (**4a**), **4b** and **4c** feature a phase-dependent Lewis acid-base interaction between N_β and the Na^+ counterion that can be monitored by IR spectroscopy.

Whereas in the solid state **4b** and **4c** exhibit a single ν(NN) at 1883 and 1879 cm^{-1}, in THF two bands (**4b**: 1879, 1922 cm^{-1}; **4c**: 1878, 1920 cm^{-1}) are observed as a result of solvation of the Na^+ ion to yield some population of the free anion $P_3^XFe–N_2^-$.[14] Encapsulation of Na^+ by treatment of **4b** and **4c** with two equivalents of 12-crown-4 (12-c-4) yields $[Na(12\text{-c-}4)_2][P_3^{Al}Fe–N_2]$ (**5b**) and $[Na(12\text{-c-}4)_2][P_3^{Ga}Fe–N_2]$ (**5c**), respectively, which give rise to only the higher energy vibration. Compounds **4a** (1877, 1918 cm^{-1}),[14] **5a** (1918 cm^{-1}),[14] and the reduced iron alumatrane, [K(18-crown-6)][(AltraPhos)Fe–N_2] (**7**, 1925 cm^{-1}),[25] display similar degrees of N_2 activation to

5b and **5c**.

The intimate ion pair in salts **4b** and **4c** was also authenticated by their corresponding solid-state structure, where the capping Na^+ is coordinated by three additional THF molecules (Figure 2.1). As was the case in going from the formally Fe(I) to Fe(0) complexes, the Fe–P bond lengths in **4b** and **4c** are significantly contracted (**4b**: 2.2751(6) Å; **4c**: 2.2825(5) Å). Moreover, the N–N distances in **4a** (1.149(2) Å), **4b** (1.134(4) Å), and **4c** (1.142(4) Å) correlate well with their observed IR and electrochemical profiles (*vide infra*).

2.2.2. Electronic Structure and Bonding in P_3^XFe Systems

While isostructural alkyl (X = C),[9,10] silyl (X = Si),[10] and borane (X = B)[3,10,11,13] $P_3^XFe–N_2^-$ complexes have all demonstrated the capacity to facilitate catalytic N_2RR, the P_3^BFe system boasts the highest efficiencies under all conditions canvassed. This can be attributed in part to the greater electronic and geometric flexibility of the dative Fe→B interaction, which allows reduced $Fe–N_2$ and Fe–N multiply bonded species that may be traversed along an Fe-mediated N_2 fixation cycle to be stabilized by storing additional electron density in the Fe–B manifold and shuttling of the iron center between trigonal bipyramidal and pseudotetrahedral geometries.[14-20] Accordingly, the catalytically relevant intermediates $Fe–N_2^{[0/1-/2-]}$,[14,18] $Fe=NNR_2^{[1+/0]}$ (R = H, Me),[17,19] and $Fe≡N^{[1+]}$[18] have proven accessible on the P_3^B scaffold. Given the significant role of the Fe→B interaction in this respect, we sought to determine whether the Fe→Al and Fe→Ga bonds behave similarly.

The bonding and electronic structures of $P_3^BFe–N_2^{[0/1-]}$ and related, isoelectronic (AltraPhos)$Fe–N_2^{[0/1-]}$ and (AltraPhos)$Co–N_2$ have previously been elucidated through

spectroscopic and computational methods.[14,24,25] In short, the bonding in these complexes is best described as involving an Fe→X(III) dative interaction where the apical Lewis acidic atom remains redox innocent, but lowers the energy of the σ(Fe–X) orbital of Fe d_{z^2} and X p_z parentage below that of the $d_{xy,\ x^2-y^2}$ set in a typical trigonal bipyramidal orbital scheme. Therefore, reduction of **3** to **4** and **6** to **7** is Fe-centered, giving rise to formally Fe(–I) species with electronic configurations $(\sigma(Fe–X))^2(d_{xz,\ yz})^4(d_{xy,\ x^2-y^2})^3$.

A consequence of having three electrons in a set of degenerate orbitals of d_{xy} and $d_{x^2-y^2}$ parentage is the proclivity of these complexes to undergo Jahn-Teller distortion from C_3 symmetry. This is clearly reflected by the asymmetry of the P–Fe–P angles in the solid-state structures of **4a**, **5a**, and **7**; for **4a**, they are 107.3°, 110.3°, and 134.6°. In contrast, **4b** and **4c** crystallize in the trigonal space group R_3, being threefold symmetric about the apical axis defined by the X–Fe–N_2 unit. While this may suggest that **4b** and **4c** possess an electronic structure that differs from that of **4a**, DFT geometry optimization and single-point energy calculations on the anions $P_3^{Al}Fe–N_2^-$ and $P_3^{Ga}Fe–N_2^-$ reveal a relaxation to a Jahn-Teller distorted configuration with computed P–Fe–P angles of 111°, 112°, 125° and 111°, 112°, 126°, respectively. Corresponding spin density plots show that this distortion also arises from localization of the unpaired electron in an Fe-based d-orbital of *xy* symmetry (Figure 2.2, Mulliken spin density on Fe: **4b** = 1.09; **4c** = 1.10). X-band EPR spectra of **4b** and **4c** collected in 2-methyltetrahydrofuran glass (77 K) display axial signals with no discernible hyperfine coupling to ^{27}Al or $^{69/71}$Ga nuclei. Negligible spin leakage onto the Al and Ga atoms is detected computationally. In conjunction with the measured solution spin-states and computed frontier molecular orbital scheme (Figure 2.2), these data indicate that $P_3^XFe–N_2^{[0/1-]}$ (X = Al, Ga) possess electronic structures similar to those of $P_3^BFe–N_2^{[0/1-]}$ and

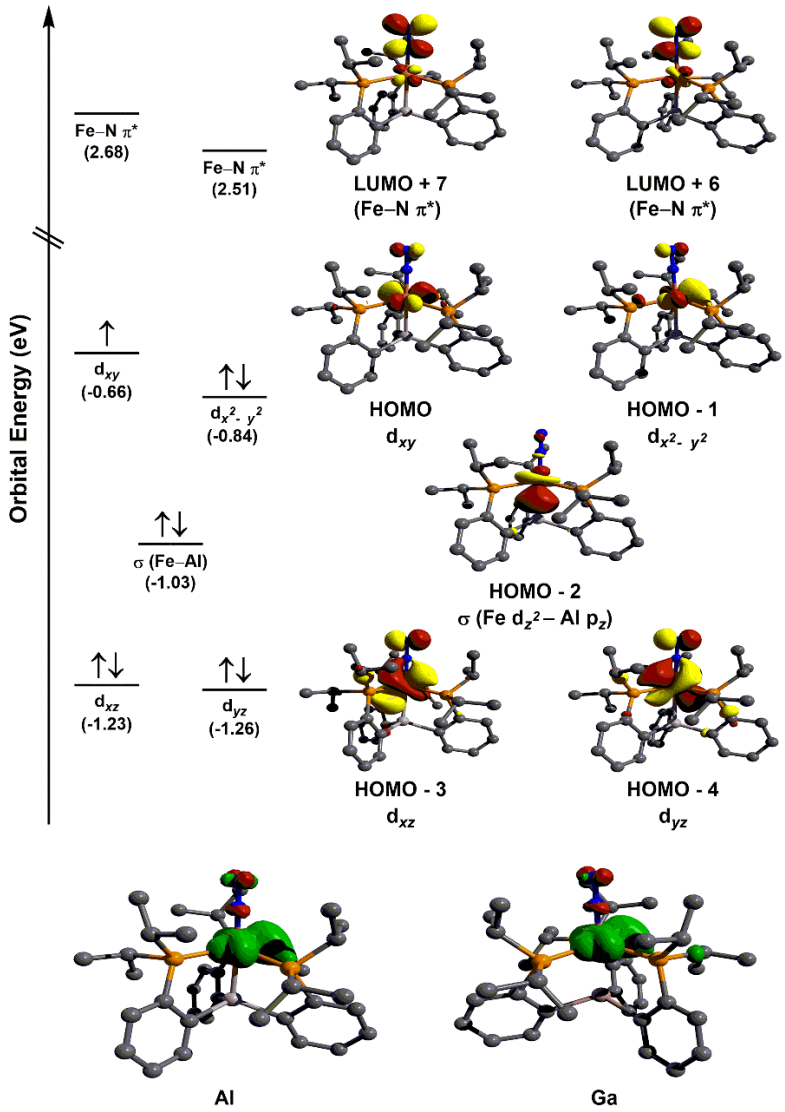

Figure 2.2. DFT-computed molecular orbital diagram (α-manifold, isovalue = 0.06 a.u.) for $P_3^{Al}Fe–N_2^-$ (top) and spin density plots (isovalue = 0.003 a.u.) for $P_3^{Al}Fe–N_2^-$ (bottom left) and $P_3^{Ga}Fe–N_2^-$ (bottom right). Hydrogen atoms are omitted for clarity.

(AltraPhos)Fe–$N_2^{[0/1-]}$.[14,25] The perfect trigonal symmetry exhibited by **4b** and **4c** in the solid-state is likely the result of crystal packing effects.

Having concluded that Fe→X σ-backdonation is operative in $P_3^{Al}Fe$ and $P_3^{Ga}Fe$, we next sought to determine the strength of this interaction relative to that in $P_3^{B}Fe$. To do so, we explored

the redox behavior of **3b** and **3c** by cyclic voltammetry (CV). **3b** and **3c** display reversible Fe–$N_2^{[0/1-]}$ redox couples centered at –1.97 V and –1.99 V (vs $Fc^{[1+/0]}$), respectively (Figure 2.3). Under identical conditions, the analogous redox event for **3a** occurs at the slightly more negative potential of –2.19 V.[14] Although the $Fe^{[1+/0]}$ redox couple of all three systems is irreversible, consistent with loss of the N_2 ligand upon oxidation, a similar trend is observed in their anodic peak potentials, with $E_{p,a}$(**3b**) = –0.92 V > $E_{p,a}$(**3c**) = –0.99 V > $E_{p,a}$(**3a**) = –1.5 V.

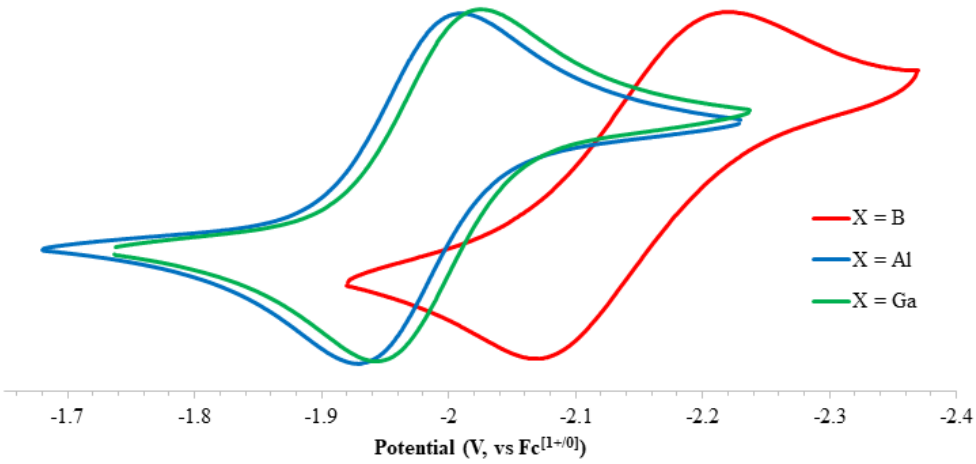

Figure 2.3. Cyclic voltammograms depicting the Fe–$N_2^{[0/1-]}$ redox couples of **3a** (red), **3b** (blue), and **3c** (green) at a scan rate of 40 mV/s in THF with 0.1 M [^{n}Bu$_4$N][PF_6] supporting electrolyte.

The ca. 200 mV anodic shift in the Fe–$N_2^{[0/1-]}$ reduction potential for **3b** and **3c** relative to **3a** suggests that exchange of the apical Lewis acidic element in the P_3^X scaffold results in only modest electronic perturbations at the iron center. This is in line with the ν(NN) vibrational data for P_3^XFe–$N_2^{[0/1-]}$ complexes, which reveal similar degrees of N_2 activation, as well as with electronic structure calculations, which show that the Fe→X interaction directly lowers the energy of Fe d_{z^2}, but only indirectly influences the energy of the highest occupied molecular orbital

(HOMO) through σ-inductive withdrawal of electron density from the Fe center. Interestingly, related (AltraPhos)Fe–N_2 **6** displays a reversible reduction feature at –2.08 V (vs $Fc^{[1+/0]}$),[24] suggestive of a weaker Fe→Al interaction than that of **3b**. We attribute this difference to competition between both Fe and N_{apical} for donation into the empty Al p_z orbital in the former.

To determine whether geometric flexibility is also conserved in the $P_3^{Al}Fe$ and $P_3^{Ga}Fe$ platforms, we turned our attention to the XRD structures of **2–4**. With the exception of the Fe→X interaction, all isostructural complexes exhibit comparable bond distances and angles, irrespective of the identity of the apical Lewis acidic atom (Table 2.5). However, inspection of the Fe–X distances reveals that all three systems possess similar degrees of fluxionality (Table 2.1). The overall changes in these axial bond lengths upon reduction of $P_3^{X}Fe$–Br to $[Na(THF)_3][P_3^{X}Fe–N_2]$ are 0.147 Å (X = B), 0.177 Å (X = Al), and 0.177 Å (X = Ga). Moreover, the values calculated for the ratio (*r*) of the Fe–X bond length to the sum of the respective covalent radii,[26] which accounts for the differing sizes of B, Al, and Ga, bare an overall net difference of $\Delta r = 0.7$ for each system. Therefore, the Fe–X bond is equally flexible in all three systems.

The decreasing values of *r* in the order **2** > **3** > **4** are also indicative of a stronger Fe–X bond upon reduction. As expected, such an increase in the dative interaction is accompanied by a greater pyramidalization at the X(III) apical atom and more trigonal planar geometry about Fe (Table 2.1). Interestingly, while the *r* values of $P_3^{Al}Fe$ and $P_3^{Ga}Fe$ are consistently lower than those of $P_3^{B}Fe$, alluding to a stronger Fe→Al and Fe→Ga interaction relative to Fe→B, the more pyramidalized geometry about boron across the series would seem to imply it forms the strongest Fe–X bond. This discrepancy likely stems from the difference in atomic sizes, with smaller boron being able to achieve a closer contact and consequently a more tetrahedral geometry. Such a cage

Table 2.1. Select structural data for complexes **2–4**, **6**, and **7**.

Complex	Fe–X[a]	ΣC–X–C[b]	ΣP– Fe–P[b]	*r*[c]
2a[d]	2.458	341.8	342.7	1.14
3a[e]	2.417	332.8	345.8	1.12
4a[d]	2.309	330.1	352.3	1.07
2b	2.662	340.8	344.8	1.05
3b	2.539	336.2	347.8	1.00
4b	2.485	334.8	349.6	0.98
2c	2.666	341.9	345.8	1.05
3c	2.544	337.8	348.7	1.00
4c	2.489	335.8	350.4	0.98
6[f]	2.809	351.6	335.0	1.11
7[g]	2.574	344.4	350.1	1.02

[a]Units of Å. [b]Units of °. [c]Ratio of the Fe–X bond length to the sum of the covalent radii (Fe: 1.32 Å; B: 0.84 Å; Al: 1.21 Å; Ga: 1.22 Å). [d]From ref. 14. [e]Values obtained from DFT geometry optimized structure. [f]From ref. 24. In solution, the terminal dinitrogen species (AltraPhos)Fe–N_2 is believed to be in equilibrium with its dinitrogen-bridged analogue, [(AltraPhos)Fe]$_2$(μ-N_2). The structural data presented here is for the latter complex. [g]From ref. 25.

structure steric constraint has also been observed in the related P_3^XPd compounds (X = B, In), where the larger size of In prevents pyramidalization that accurately reflects the strength of the donor-acceptor interaction. For instance, while computations and the smaller r = 0.93 value of P_3^{In}Pd indicate it has a stronger Pd→X interaction than P_3^BPd (r = 1.01), the indium center is in a less pyramidalized environment than boron (ΣC–In–C = 354.9°; ΣC–In–C = 341.8°).[23,27] Therefore, in accord with their electrochemical data, we favor a bonding scheme where the Fe→X donor-acceptor interaction is stronger for X = Al, Ga than for X = B. This assignment is also validated computationally, where normalized (with respect to the corresponding Fe–B bond) Löwdin bond orders of 1.08, 1.05, 1.05, and 1.02 are calculated for **3b**, **3c**, P_3^{Al}Fe–N_2^-, and P_3^{Ga}Fe–

N_2^-, respectively.

2.2.3. N_2RR Activity

Having concluded that the P_3^XFe platforms (X = B, Al, Ga) exhibit similar flexibilities, degrees of N_2 activation, and electronic structures, we reasoned that **5b** and **5c** might function as competent catalysts for N_2RR. Thus, we subjected these compounds to the catalytic conditions that have proved most fruitful for the P_3^BFe system, namely treatment with excess $[H(OEt_2)_2][BAr^F{}_4]$ ($HBAr^F{}_4$, $BAr^F{}_4^-$ = tetrakis(3,5-bis(trifluoromethyl)phenyl)borate)/KC_8[3,10] or $[H_2NPh_2][OTf]$/$Cp^*{}_2Co$[11] as the acid/reductant source at –78 °C in diethyl ether (Et_2O). Under the former conditions, **5b** and **5c** generate 2.5 ± 0.1 (17 ± 1% selectivity based on H^+) and 2.7 ± 0.2 (17 ± 1% efficiency) equiv of NH_3 per Fe, respectively (Table 2.2, entries 2 and 3). Moving to the

Table 2.2. N_2RR mediated by $[Na(12\text{-c-}4)_2][P_3^XFe–N_2]$ complexes.[a]

Entry	Catalyst	Acid (equiv)	Reductant (equiv)	NH_3/Fe (equiv)	Yield NH_3/H^+ (%)
1[b]	**5a**	46[d]	50[e]	7.0 ± 1.0	46 ± 7
2	**5b**	46[d]	50[e]	2.5 ± 0.1	17 ± 1
3	**5c**	46[d]	50[e]	2.7 ± 0.2	17 ± 1
4[c]	**5a**	54[f]	108[g]	12.8 ± 0.5	72 ± 3
5	**5b**	46[f]	50[g]	4.1 ± 0.9	27 ± 6
6	**5c**	46[f]	50[g]	3.6 ± 0.3	24 ± 2

[a]Catalyst, acid, reductant, and Et_2O sealed in a Schlenk tube at –196 °C under an N_2 atmosphere, warmed to –78 °C, and stirred. For runs utilizing $HBAr^F{}_4$, reactions were stirred at –78 °C for 1 hour, followed by stirring at room temperature for 45 minutes. For other runs, reactions were allowed to stir and warm to room temperature overnight. Yields are reported as an average of 3 runs. [b]From ref. 3. [c]From ref. 11. $P_3^BFe^+$ was used as the precatalyst. [d]$HBAr^F{}_4$. [e]KC_8. [f]$[H_2NPh_2][OTf]$. [g]$Cp^*{}_2Co$.

$[H_2NPh_2][OTf]/Cp^*_2Co$ combination, which is in the activity regime with the highest N_2-to-NH_3 selectivity observed for P_3^BFe,[13] results in only modest improvements, with **5b** and **5c** producing 4.1 ± 0.9 (27 ± 6% based on acid) and 3.6 ± 0.3 (24 ± 2% efficiency) equiv of NH_3 per Fe (Table 2.2, entries 5 and 6). Hydrazine is not detected under either set of conditions. These efficiencies are notably lower than those of P_3^BFe under similar conditions (Table 2.2, entries 1 and 4),[3,11] and suggest that in addition to the extent of N_2 activation and flexibility of the Fe–X linkage, other properties imparted by the identity of the apical atom in the P_3^X scaffold play an influential role in the nitrogen fixation process.

In order to discern whether the divergent N_2RR catalytic profiles of **5a–c** are a consequence of catalyst deactivation/decomposition, the Fe speciation present after exposure of the complexes to 10 equiv of acid and 12 equiv of reductant was examined. P_3^BFe is known to be remarkably robust under both sets of catalytic conditions, with substantial active (pre)catalyst remaining at the conclusion of the reaction as evidenced by Mössbauer spectroscopic studies and substrate reloading experiments.[10,11] Indeed, NMR and IR analysis of the post-reaction of **5a** with $HBAr^F_4/KC_8$ reveals $[M(solv)_x][P_3^BFe–N_2]$ (solv = solvent) and $(P_3^B)(\mu\text{-}H)Fe(L)(H)$ (L = H_2, N_2) as the major Fe-containing products (see Experimental Section). Similarly, $P_3^BFe–N_2$ and $(P_3^B)(\mu\text{-}H)Fe(L)(H)$ are obtained when $[H_2NPh_2][OTf]/Cp^*_2Co$ are employed. Free P_3^B ligand is not observed in either instance. It is worth noting that while the hydride-borohydride complex $(P_3^B)(\mu\text{-}H)Fe(N_2)(H)$ is an off-path species of P_3^BFe-mediated N_2RR catalysis, in the presence of protons and electrons it can revert back to $P_3^BFe–N_2^-$ and serve as a competent precatalyst.[10]

Analogous experiments utilizing **5b** and **5c** yield slightly different results depending on the conditions. In the case of reaction with 10 equiv of $HBAr^F_4$ and 12 equiv of KC_8,

$[M(solv)_x][P_3^XFe–N_2]$ (X = Al, Ga) is the major terminal Fe-containing product, with very little ligand decomposition observed by $^{31}P\{^1H\}$ NMR spectroscopy. On the other hand, the use of $[H_2NPh_2][OTf]$ and Cp^*_2Co yields a mixture of compounds that includes $P_3^XFe–N_2$ (X = Al, Ga) and products of ligand decomposition.

While the observation of substantially more ligand decomposition when **5b** and **5c** are reacted with $[H_2NPh_2][OTf]/Cp^*_2Co$ appears to be at odds with the milder nature of these reagents and higher NH_3 yields relative to $HBAr^F_4/KC_8$, this can be rationalized by the differing strength of the reductants and reactivity of $P_3^XFe–N_2$ species with H_2. Because of the highly reducing nature of KC_8 ($E \leq$ –3.0 V vs $Fc^{[1+/0]}$) and its slight excess in the reactions, after complete acid consumption, any residual KC_8 is expected to reduce $P_3^XFe–N_2$ to $[K(solv)_x][P_3^XFe–N_2]$, which is unreactive towards H_2. Additionally, conversion of $(P_3^B)(\mu\text{-}H)Fe(N_2)(H)$ to $P_3^BFe–N_2^-$ is viable under the $HBAr^F_4/KC_8$ conditions.[10] In contrast, the reduction potential of Cp^*_2Co (E = –1.96 V vs $Fc^{[1+/0]}$) is very close to that of the $P_3^XFe–N_2^{[0/1-]}$ couples (X = B, Al, Ga). While Cp^*_2Co is capable of reducing $P_3^BFe–N_2$ to $P_3^BFe–N_2^-$ at –78 °C,[11] reaction of $P_3^BFe–N_2$ with excess Cp^*_2Co at room temperature does not produce $P_3^BFe–N_2^-$ (as judged by IR spectroscopy). Such observations are consistent with a temperature-dependent redox equilibrium analogous to that reported for the related $P_3^{Si}Os$ system possessing a $P_3^{Si}Os–N_2^{[0/1-]}$ couple at –1.97 V (vs $Fc^{[1+/0]}$).[8] As a consequence, upon allowing the catalyst speciation reactions to warm and stir at room temperature (see Experimental Section for full procedures), $P_3^XFe–N_2$ (rather than $[M(solv)_x][P_3^XFe–N_2]$) is expected to be the dominant species in solution when Cp^*_2Co is the reductant.

Reaction of $P_3^XFe–N_2$ with H_2 formed from background and/or catalyzed HER gives rise

to the remaining products observed in the reaction of **5a–c** with $[H_2NPh_2][OTf]/Cp^*_2Co$. $P_3^BFe–N_2$ is known to react with H_2 cleanly to generate $(P_3^B)(\mu\text{-}H)Fe(L)(H)$ (L = H_2, N_2),[28] species that can re-enter the N_2RR catalytic cycle.[10] Treatment of $P_3^{Al}Fe–N_2$ and $P_3^{Ga}Fe–N_2$ with H_2 instead results in a mixture of products, including ligand decomposition, whose profile matches that observed at the end of catalyst speciation reactions (see Experimental Section). Attempts to separate and isolate the products cleanly have been unsuccessful. Taken together, this accounts for the different products observed under the two sets of pseudocatalytic conditions.

The above results suggest that $P_3^{Al}Fe$ and $P_3^{Ga}Fe$ platforms are relatively robust under both sets of N_2RR catalytic conditions explored. Although minor catalyst decomposition/deactivation does occur, this does not correlate well with the dramatically lower N_2RR efficiencies of $P_3^{Al}Fe$ and $P_3^{Ga}Fe$ versus P_3^BFe, or with the higher NH_3 yields obtained with the $[H_2NPh_2][OTf]/Cp^*_2Co$ conditions. Instead, our observations are more consistent with $P_3^{Al}Fe$ and $P_3^{Ga}Fe$ exhibiting a greater selectivity for HER versus N_2RR. Bimolecular coupling of $Fe{=}NNH_2^{[1+/0]}$ N_2RR intermediates featuring weak N–H bonds is predicted to be an operative unproductive HER pathway on the P_3^BFe system.[12] In this respect, it is worth noting that Fe-imido (Fe≡N–R; R = adamantly,[17] *p*-methoxyphenyl[14]) and Fe-disilylhydrazido ($Fe{=}NNSi_2$)[15,25] complexes that are accessible and stable on the P_3^BFe and (AltraPhos)Fe platforms could not be isolated with the P_3^{Al} and P_3^{Ga} scaffolds.

2.3. Conclusion

In summary, the series of $P_3^{Al}Fe$ and $P_3^{Ga}Fe$ complexes **2–5** spanning the formal oxidation states Fe(I) to Fe(–I) have been synthesized and structurally characterized. While these compounds

exhibit a similar degree of flexibility, N_2 activation, and overall electronic structure to those of the P_3^BFe system, **5b** and **5c** display significantly attenuated yields of ammonia under analogous N_2RR catalytic conditions. Preliminary reactivity studies confirm that $P_3^{Al}Fe$ and $P_3^{Ga}Fe$ are relatively robust under the catalytic conditions, suggesting that the lower turnover numbers observed are likely the result of greater HER versus N_2RR selectivity rather than differences in core framework stability. Future work will focus on corroborating this hypothesis.

2.4. Experimental Section

2.4.1. Experimental Methods

General Considerations

All manipulations were carried out using standard Schlenk or glovebox techniques under an N_2 atmosphere. Solvents were deoxygenated and dried by thoroughly sparging with N_2 gas followed by passage through an activated alumina column in the solvent purification system by SG Water, USA LLC. Non-halogenated solvents were tested with sodium benzophenone ketyl in tetrahydrofuran (THF) in order to confirm effective oxygen and moisture removal. Deuterated solvents were purchased from Cambridge Isotope Laboratories, Inc., degassed, and dried over activated 3 Å molecular sieves prior to use.

P_3^{Al} (**1b**)[21] and P_3^{Ga} (**1c**)[22] were synthesized from a modified literature procedure. $[H(OEt_2)_2][BAr^F{}_4]$ ($HBAr^F{}_4$, $BAr^F{}_4^-$ = tetrakis(3,5-bis(trifluoromethyl)phenyl)borate),[29] KC_8,[30] $[H_2NPh_2][OTf]$,[11,31] and $Cp^*{}_2Co$[32] were prepared according to literature methods. All other reagents were purchased from commercial vendors and used without further purification unless otherwise stated. Diethyl ether (Et_2O) used for NH_3 generation experiments was stirred over Na/K (≥ 1 hour) and filtered before use.

NMR Spectroscopy

NMR measurements were obtained on Varian 300, 400, or 500 MHz spectrometers. ^1H NMR chemical shifts are reported in ppm relative to tetramethylsilane, using residual protio solvent as an internal standard. ^{31}P NMR chemical shifts were externally referenced to 85% H_3PO_4 in H_2O.

Solution phase magnetic measurements were performed by the method of Evans.[33]

EPR Spectroscopy

X-band EPR spectra were obtained on a Bruker EMX spectrometer.

IR Spectroscopy

IR measurements were obtained as solutions or thin films formed by evaporation of solutions using a Bruker Alpha Platinum ATR spectrometer with OPUS software in a glovebox under an N_2 atmosphere.

UV-Visible Spectroscopy

Optical spectroscopy measurements were collected with a Cary 50 UV-visible spectrophotometer using a 1 cm path length quartz cuvette. All samples had a blank sample background subtraction applied.

Electrochemistry

Electrochemical measurements were carried out in a glovebox under an N_2 atmosphere in a one compartment cell using a CH Instruments 600B electrochemical analyzer. A glassy carbon electrode was used as the working electrode and platinum wire was used as the auxiliary electrode. A silver pseudoreference electrode was used with the ferrocene couple ($Fc^{[1+/0]}$) as an internal reference. THF solutions of electrolyte (0.1 M [^{n}Bu$_4$][PF_6]) and analyte (ca. 1 mM) were also prepared under an N_2 atmosphere.

Elemental Analysis

Elemental analyses were performed by Midwest Microlab, LLC (Indianapolis, IN) or by the Caltech Division of Chemistry and Chemical Engineering X-ray Crystallography Facility on a PerkinElmer 2400 Series II CHN Elemental Analyzer.

X-ray Crystallography

XRD studies were carried out at the Caltech Division of Chemistry and Chemical Engineering X-ray Crystallography Facility on a Bruker three-circle SMART diffractometer with a SMART 1K CCD detector or Bruker Kappa Apex II diffractometer. Data was collected at 100 K using Mo Kα radiation (λ = 0.71073 Å). Using OLEX2,[34] structures were solved with the XT[35] structure solution program using Direct Methods and refined with the XL[36] refinement package using Least Squares minimization. All non-hydrogen atoms were refined anisotropically. All hydrogen atoms were placed at geometrically calculated positions and refined using a riding model. The isotropic displacement parameters of all hydrogen atoms were fixed at 1.2 (1.5 for methyl groups) times the U_{eq} of the atoms to which they are bonded.

Computational Methods

All calculations were carried out using version 3.0.3 of the ORCA package.[37] The calculations were performed on the full $P_3{}^XFe$ scaffolds using DFT-D_3 (Grimmes D_3 dispersion correction[38]) with a TPSS functional,[39] a def2-TZVPP[40] basis set on Fe, P, N, B, Al, Ga atoms, and a def2-SVP[40] basis set on C, H atoms. Frequency calculations were performed on the geometry optimized structures to ensure a true minimum.

2.4.2. Synthetic Details and Characterization Data

Tris(2-(diisopropylphosphino)phenyl)alane (P_3^{Al}) (1b). This compound was synthesized according to a modified literature procedure as follows.[21] 3.4335 g (3.00 equiv, 12.6 mmol) of (2-bromophenyl)diisopropylphosphine was dissolved in Et_2O (30 mL) and cooled to –78 °C. 7.9 mL of *n*-BuLi (1.6 M in hexanes, 3.00 equiv, 12.6 mmol) was then added dropwise via a syringe. The reaction was allowed to stir for 30 minutes at –78 °C, followed by 30 minutes at room temperature.

Following removal of the Et_2O *in vacuo*, the remaining yellow-orange residue was dissolved in toluene (15 mL) and cooled to –78 °C in a glovebox coldwell. The solution was then transferred to a cooled (–78 °C) suspension of $AlCl_3$ (1.00 equiv, 4.19 mmol, 0.5587 g) in toluene. The vial was subsequently transferred from the coldwell to the freezer (–32 °C) and stored overnight.

After stirring the reaction mixture for 1 hour at room temperature, it was filtered through celite to remove the LiCl byproduct. Concentrating the yellow toluene solution under vacuum and triturating with pentane (3 x 20 mL) yielded **1b** as an off-white powder (2.4133 g, 95%). The ligand was stored in the freezer (–32 °C) and used without further purification.

^{1}H NMR (400 MHz, C_6D_6, 25 °C): δ(ppm) 8.41 (d, 3H, Ar–*H*), 7.40 (t, 3H, Ar–*H*), 7.26 (d, 3H, Ar–*H*), 7.20 (t, 3H, Ar–*H*), 2.01 (m, 6H, C*H*$(CH_3)_2$), 1.05 (q, 18H, CH(C*H*$_3)_2$), 0.88 (q, 18H, CH(C*H*$_3)_2$).

^{31}P{^{1}H} NMR (121 MHz, C_6D_6, 25 °C): δ(ppm) 15.2 (s).

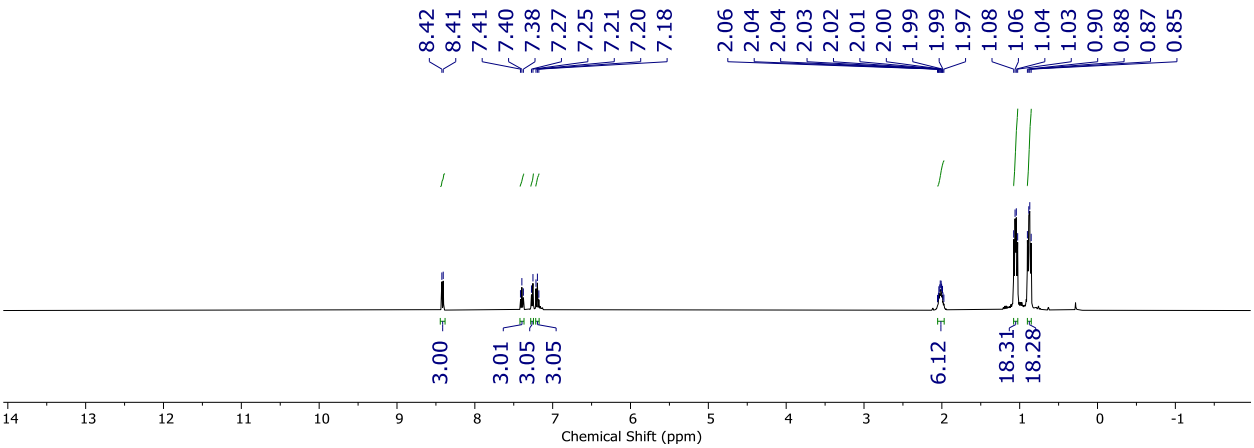

Figure 2.4. ^{1}H NMR spectrum (400 MHz, C_6D_6, 25 °C) of P_3^{Al} (**1b**).

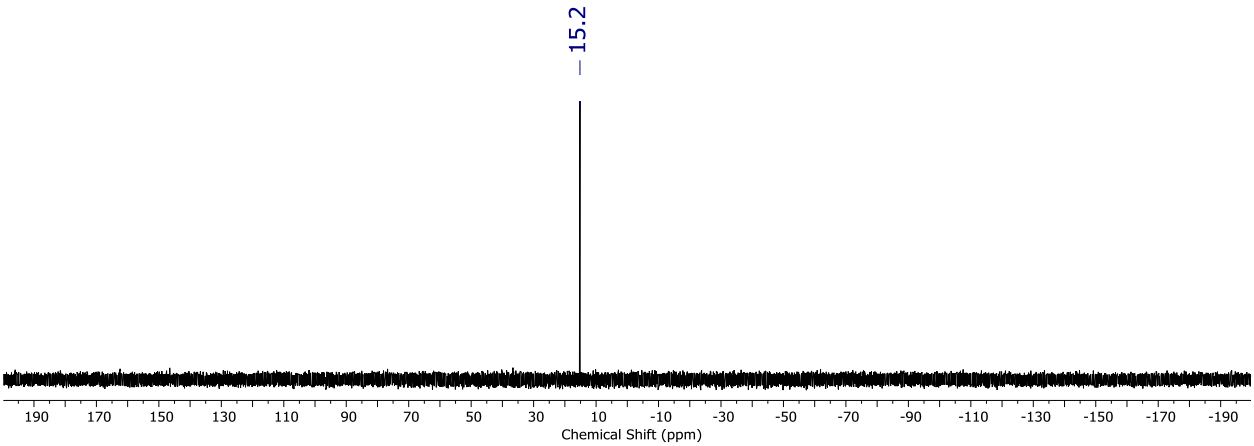

Figure 2.5. $^{31}P\{^{1}H\}$ NMR spectrum (121 MHz, C_6D_6, 25 °C) of P_3^{Al} (**1b**).

Tris(2-(diisopropylphosphino)phenyl)gallane (P_3^{Ga}) (1c). This compound was synthesized according to a modified literature procedure as follows.[22] 5.0953 g (3.00 equiv, 18.7 mmol) of (2-bromophenyl)diisopropylphosphine was dissolved in Et_2O (40 mL) and cooled to –78 °C. 11.7 mL of *n*-BuLi (1.6 M in hexanes, 3.00 equiv, 18.7 mmol) was then added dropwise via a syringe. The reaction was allowed to stir for 30 minutes at –78 °C, followed by 30 minutes at room temperature.

Following removal of the Et_2O *in vacuo*, the remaining yellow-orange residue was dissolved in toluene (15 mL) and cooled to –78 ºC in a glovebox coldwell. While stirring, a cooled (–78 ºC) toluene solution of $GaCl_3$ (1.00 equiv, 6.22 mmol, 1.0950 g) was added dropwise via pipette. After a few moments, the mixture became cloudy with the formation of LiCl. The vial was transferred from the coldwell to the freezer (–32 ºC) and stored overnight.

After stirring the reaction mixture for 10 minutes at room temperature, it was filtered through celite to remove the salt byproduct. Concentrating the yellow toluene solution under vacuum and triturating with pentane (3 x 20 mL) yielded **1c** as a white powder (3.8665 g, 96%). The ligand was stored in the freezer (–32 ºC) and used without further purification.

^{1}H NMR (400 MHz, C_6D_6, 25 ºC): δ(ppm) 8.42 (d, 3H, Ar–*H*), 7.40 (t, 3H, Ar–*H*), 7.26 (d, 3H, Ar–*H*), 7.18 (t, 3H, Ar–*H*), 1.99 (m, 6H, C*H*$(CH_3)_2$), 1.05 (q, 18H, CH(C*H*$_3)_2$), 0.88 (q, 18H, CH(C*H*$_3)_2$).

^{31}P{^{1}H} NMR (121 MHz, C_6D_6, 25 ºC): δ(ppm) 16.9 (s).

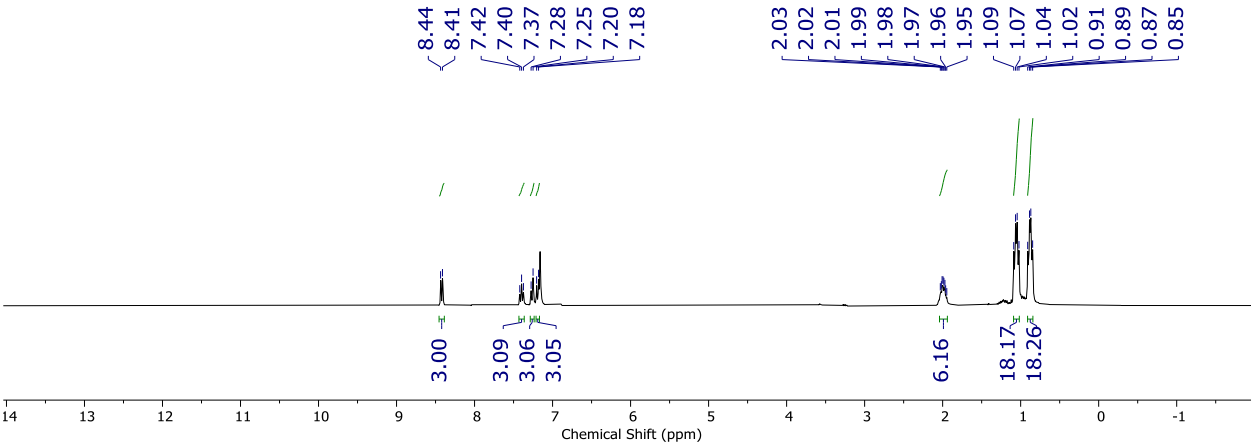

Figure 2.6. ^{1}H NMR spectrum (400 MHz, C_6D_6, 25 °C) of P_3^{Ga} (**1c**).

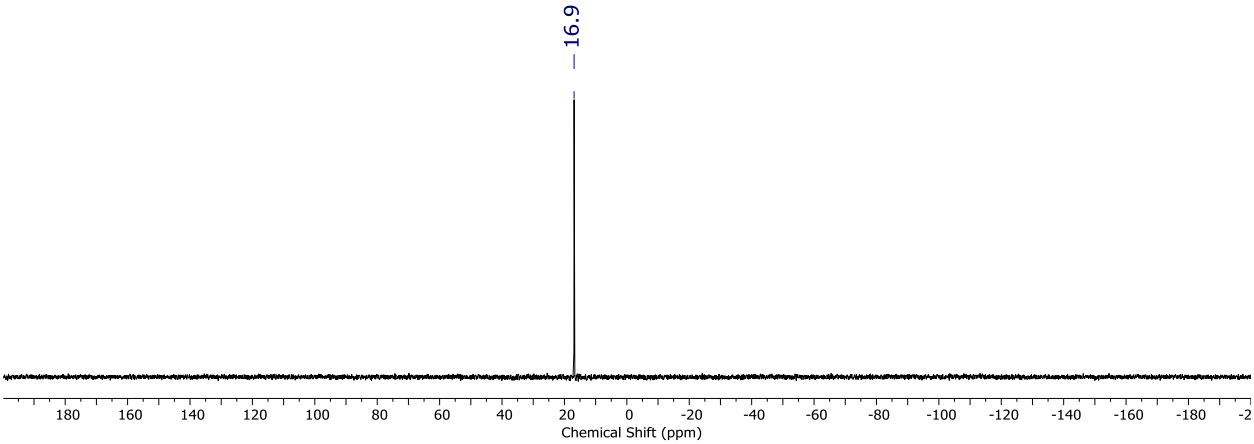

Figure 2.7. ^{31}P{^{1}H} NMR spectrum (121 MHz, C_6D_6, 25 °C) of P_3^{Ga} (**1c**).

P_3^{Al}Fe–Br (2b). 0.1313 g (1.00 equiv, 0.609 mmol) of $FeBr_2$ was stirred vigorously in benzene for 2 hours to give a fine suspension. **1b** (1.00 equiv, 0.609 mmol, 0.3695 g) was then added as a benzene solution to the suspension and stirred at room temperature for an additional 2 hours. Finally, Na(Hg) (Na: 1.06 equiv, 0.648 mmol, 0.0149 g) was added to the reaction mixture and stirred vigorously for 15 hours.

After allowing the precipitate to settle, the green supernatant was decanted from Hg and filtered through celite. Lyophilization of the solution gave a green residue that was washed with HMDSO (3 x 15 mL) on a coarse frit packed with celite. The remaining bright green solid was filtered through the celite using toluene and then concentrated under vacuum. Layering the concentrated toluene solution with pentane and storing at –32 °C overnight afforded **2b** as green needles (0.2319 g, 51%). Subsequent recrystallization of the mother liquor afforded another 0.0718 g of product (total yield = 67%). Crystals suitable for XRD were obtained by slow concentration of a THF solution of **2b** in a closed vessel containing HMDSO.

^{1}H NMR (400 MHz, C_6D_6, 25 °C): δ(ppm) 8.30, 7.42, 5.65, 0.35, –0.71, –5.06.

μ_{eff} (Evans Method, C_6D_6, 25 °C): 4.3 μ_B.

UV-visible (THF, 25 °C, nm {M^{-1} cm^{-1}}): 641 {71}, 784 {200}, 1056 {220}.

Anal. Calcd. for $C_{36}H_{54}AlBrFeP_3 \bullet C_6H_6$: C, 61.48; H, 7.37. Found: C, 61.20; H, 7.41.

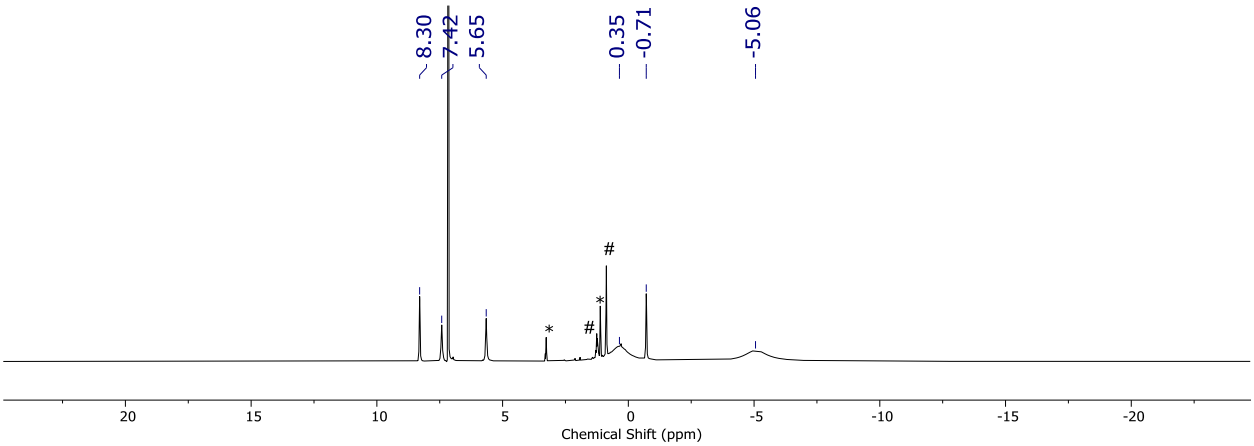

Figure 2.8. ^{1}H NMR spectrum (400 MHz, C_6D_6, 25 °C) of $P_3^{Al}Fe–Br$ (**2b**) (*Et_2O, $^{\#}$pentane).

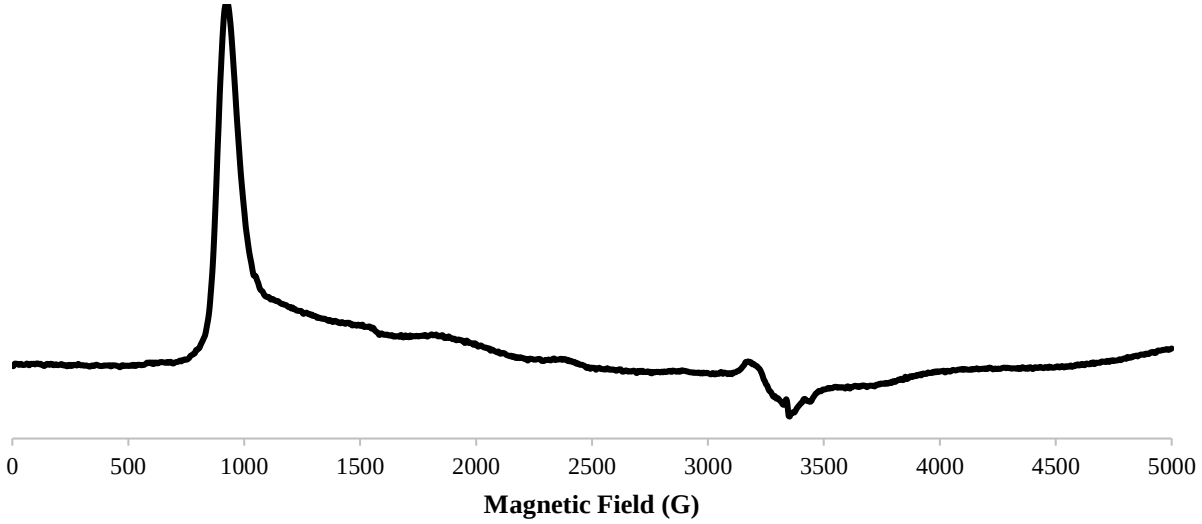

Figure 2.9. X-band EPR spectrum of $P_3^{Al}Fe–Br$ (**2b**) in toluene at 10 K.

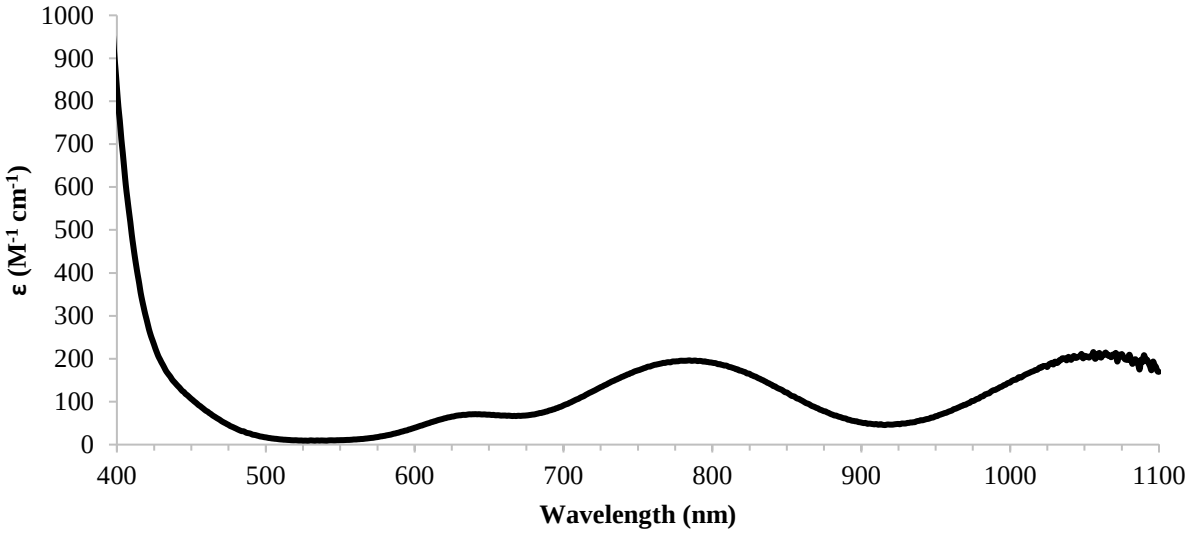

Figure 2.10. UV-visible spectrum of $P_3^{Al}Fe–Br$ (**2b**) in THF.

P_3^{Ga}Fe–Br (2c). 0.1339 g (1.00 equiv, 0.621 mmol) of $FeBr_2$ was stirred vigorously in benzene for 2 hours to give a fine suspension. **1c** (1.00 equiv, 0.621 mmol, 0.4031 g) was then added as a benzene solution to the suspension and stirred at room temperature for an additional 2 hours. Finally, Na(Hg) (Na: 1.07 equiv, 0.666 mmol, 0.0153 g) was added to the reaction mixture and stirred vigorously for 18 hours.

After allowing the precipitate to settle, the dark olive-green supernatant was decanted from Hg and filtered through celite. Lyophilization of the solution then gave a green residue that was washed with HMDSO (3 x 15 mL) on a coarse frit packed with celite. The remaining bright green solid was filtered through the celite using toluene and then concentrated under vacuum. Layering the concentrated toluene solution with pentane and storing at –32 ^{o}C overnight afforded **2c** as green needles (0.2778 g, 57%). Subsequent recrystallization of the mother liquor afforded another 0.0319

g of product (total yield = 64%). Crystals suitable for XRD were obtained by slow concentration of a THF solution of **2c** in a closed vessel containing HMDSO.

^{1}H NMR (400 MHz, C_6D_6, 25 ^{o}C): δ(ppm) 8.50, 7.94, 0.26, –3.12, –4.68, –5.30.

μ_{eff} (Evans Method, C_6D_6, 25 ^{o}C): 4.2 μ_B.

UV-visible (THF, 25 ^{o}C, nm {M^{-1} cm^{-1}}): 643 {73}, 802 {190}, 1064 {210}.

Anal. Calcd. For $C_{36}H_{54}GaBrFeP_3 \bullet C_6H_6$: C, 58.43; H, 7.01. Found: C, 58.05; H, 7.24.

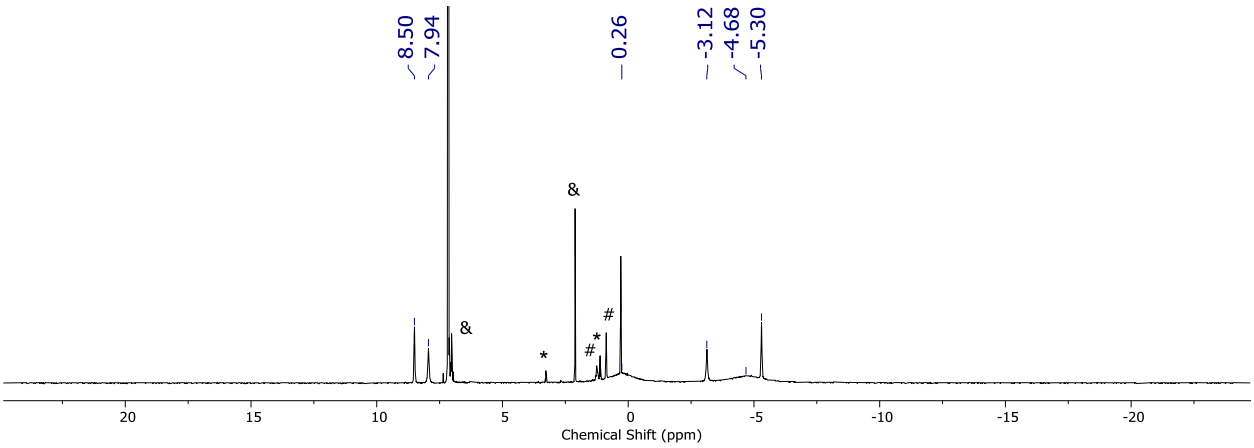

Figure 2.11. ^{1}H NMR spectrum (400 MHz, C_6D_6, 25 °C) of $P_3{}^{Ga}Fe$–Br (**2c**) (*Et_2O, $^{\#}$pentane, $^{\&}$toluene).

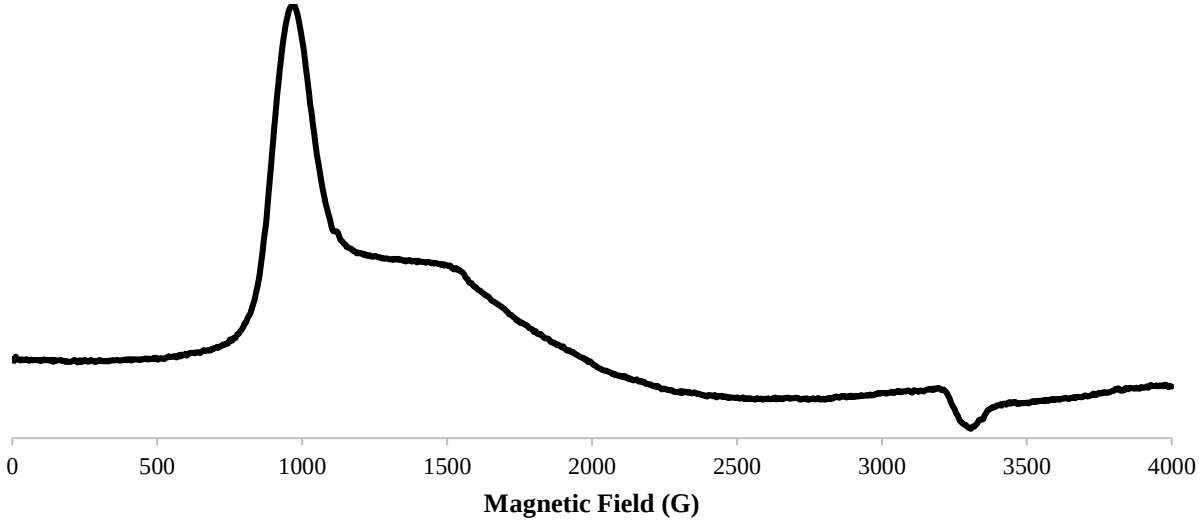

Figure 2.12. X-band EPR spectrum of $P_3^{Ga}Fe–Br$ (**2c**) in toluene at 10 K.

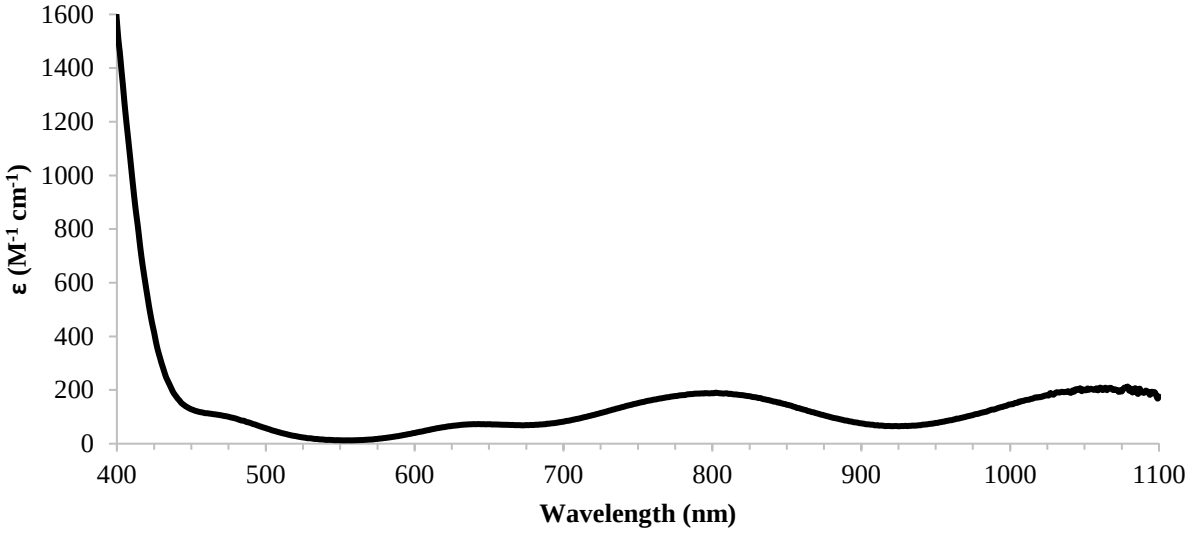

Figure 2.13. UV-visible spectrum of $P_3^{Ga}Fe–Br$ (**2c**) in THF.

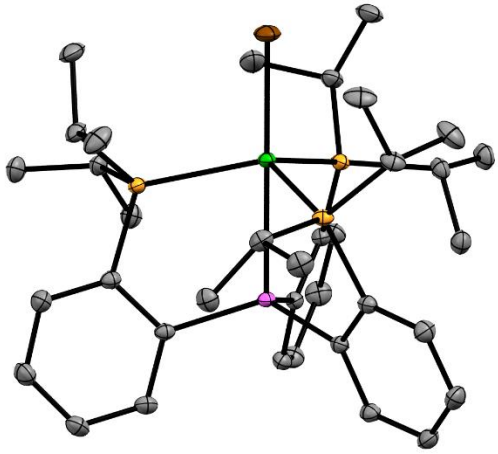

Figure 2.14. XRD structure of $P_3^{Ga}Fe–Br$ (**2c**) with thermal ellipsoids set at 50% probability. Hydrogen atoms and a co-crystallized HMDSO solvent molecule are omitted for clarity. Color code: Fe = green, P = orange, Ga = pink, Br = brown, C = gray.

$P_3^{Al}Fe–N_2$ (3b). 0.0534 g (1.00 equiv, 0.0719 mmol) of **2b** was dissolved in benzene (10 mL) to give a green solution. Excess Na(Hg) (Na: 7.62 equiv, 0.548 mmol, 0.0126 g) was then added and the reaction was stirred vigorously for 20 hours. Decanting the supernatant from Hg and filtering through celite yielded a dark yellow solution. Lyophilization of the solution afforded a brown solid that was washed with pentane (2 x 4 mL) to give **3b** (0.0375 g, 76%). Crystals suitable for XRD were obtained by slow concentration of an Et_2O solution of **3b** in a closed vessel containing toluene.

^{1}H NMR (300 MHz, C_6D_6, 25 ^{o}C): δ(ppm) 8.88, 8.63, 8.44, 3.48, –1.11, –4.59.

μeff (Evans Method, C_6D_6, 25 ^{o}C): 3.1 μ_B.

IR (thin film from C_6D_6): ν(NN) = 2003 cm^{-1}.

IR (THF): ν(NN) = 2006 cm^{-1}.

UV-visible (THF, 25 °C, nm {M^{-1} cm^{-1}}): 942 {530}.

E.A.: No combustion analysis data was obtained due to the lability of the dinitrogen ligand under vacuum.

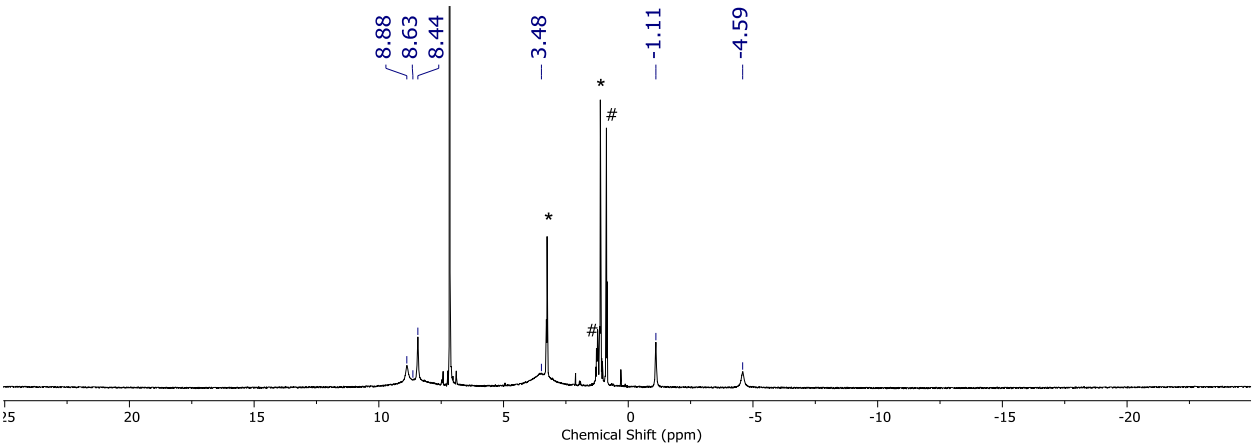

Figure 2.15. ^{1}H NMR spectrum (300 MHz, C_6D_6, 25 °C) of $P_3^{Al}Fe–N_2$ (**3b**) (*Et_2O, #pentane).

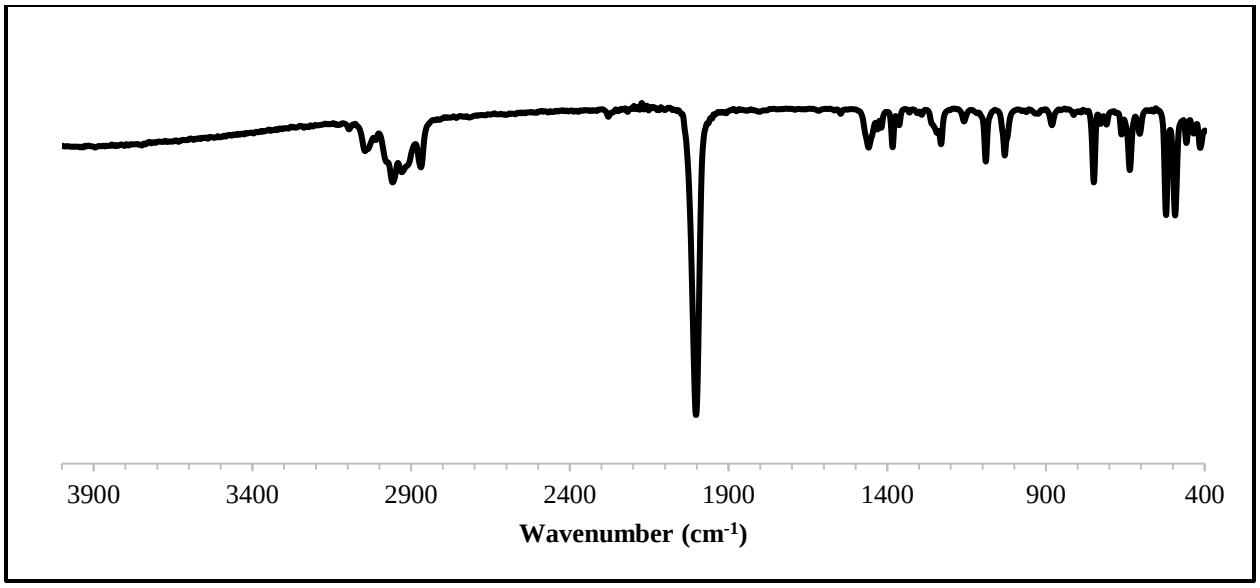

Figure 2.16. IR spectrum of $P_3^{Al}Fe–N_2$ (**3b**) deposited as a thin film from C_6D_6.

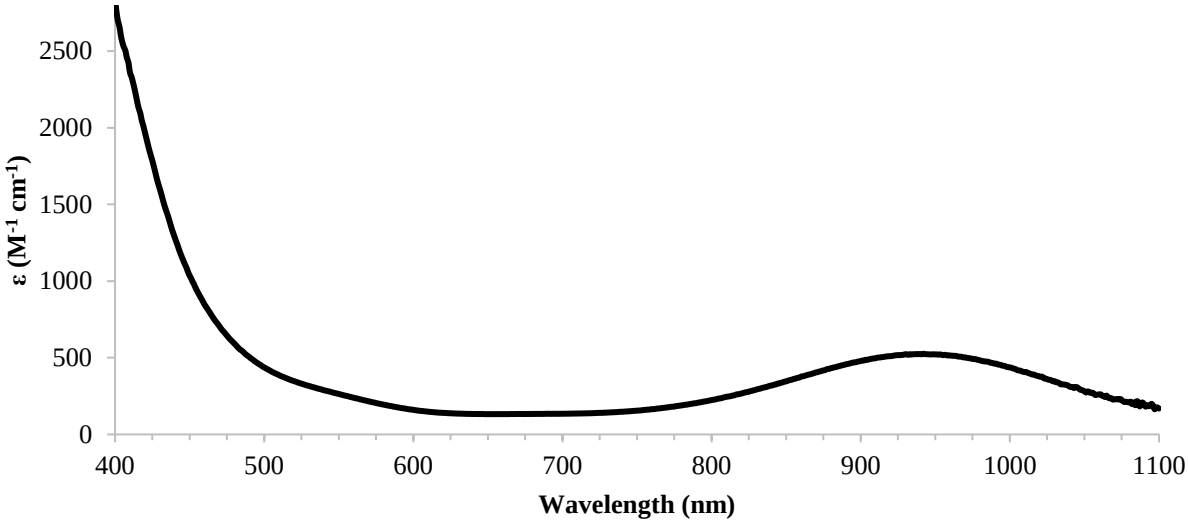

Figure 2.17. UV-visible spectrum of $P_3^{Al}Fe–N_2$ (**3b**) in THF.

$P_3^{Ga}Fe–N_2$ (3c). 0.0471 g (1.00 equiv, 0.0600 mmol) of **2c** was dissolved in benzene (10 mL) to give a green solution. Excess Na(Hg) (Na: 7.47 equiv, 0.448 mmol, 0.0103 g) was then added and

the reaction was stirred vigorously for 20 hours. Decanting the supernatant from Hg and filtering through celite yielded a yellow solution. Lyophilization of the solution, followed by washing of the remaining residue with pentane (2 x 4 mL), afforded **3c** as a yellow solid (0.0364 g, 83%). Crystals suitable for XRD were obtained by slow concentration of an Et_2O solution of **3c** in a closed vessel containing toluene.

^{1}H NMR (400 MHz, C_6D_6, 25 ^{o}C): δ(ppm) 11.15, 10.64, 9.08, 3.89, –4.76, –13.35.

μ_{eff} (Evans Method, C_6D_6, 25 ^{o}C): 2.8 μ_B.

IR (thin film from C_6D_6): ν(NN) = 1997 cm^{-1}.

IR (THF): ν(NN) = 1996 cm^{-1}.

UV-visible (THF, 25 ^{o}C, nm {M^{-1} cm^{-1}}): 924 {440}.

E.A.: No combustion analysis data was obtained due to the lability of the dinitrogen ligand under vacuum.

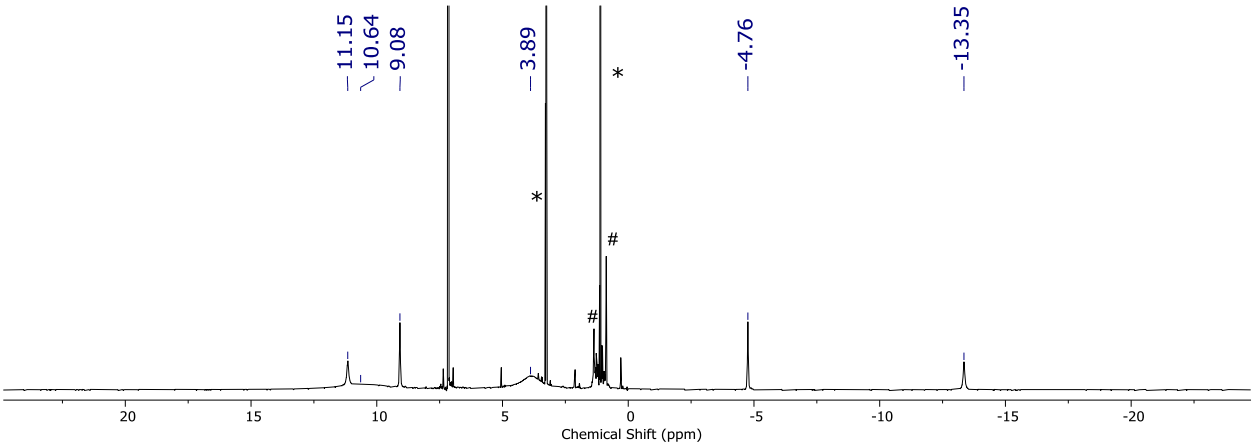

Figure 2.18. ^{1}H NMR spectrum (400 MHz, C_6D_6, 25 °C) of $P_3{}^{Ga}Fe–N_2$ (**3c**) (*Et_2O, $^{\#}$pentane).

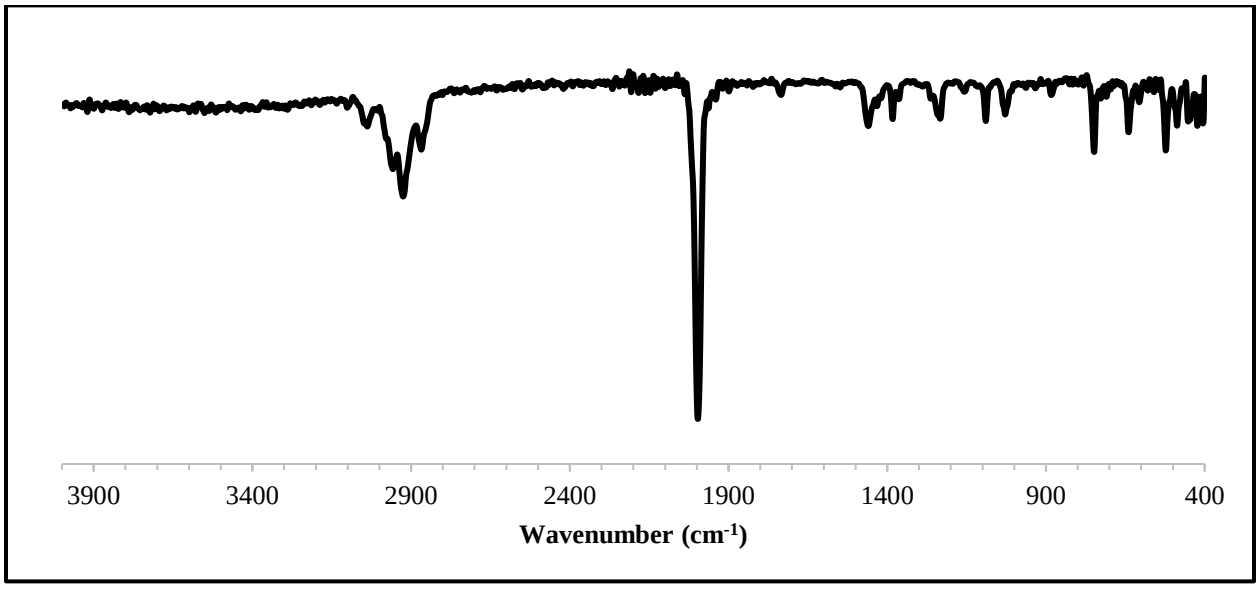

Figure 2.19. IR spectrum of $P_3{}^{Ga}Fe–N_2$ (**3c**) deposited as a thin film from C_6D_6.

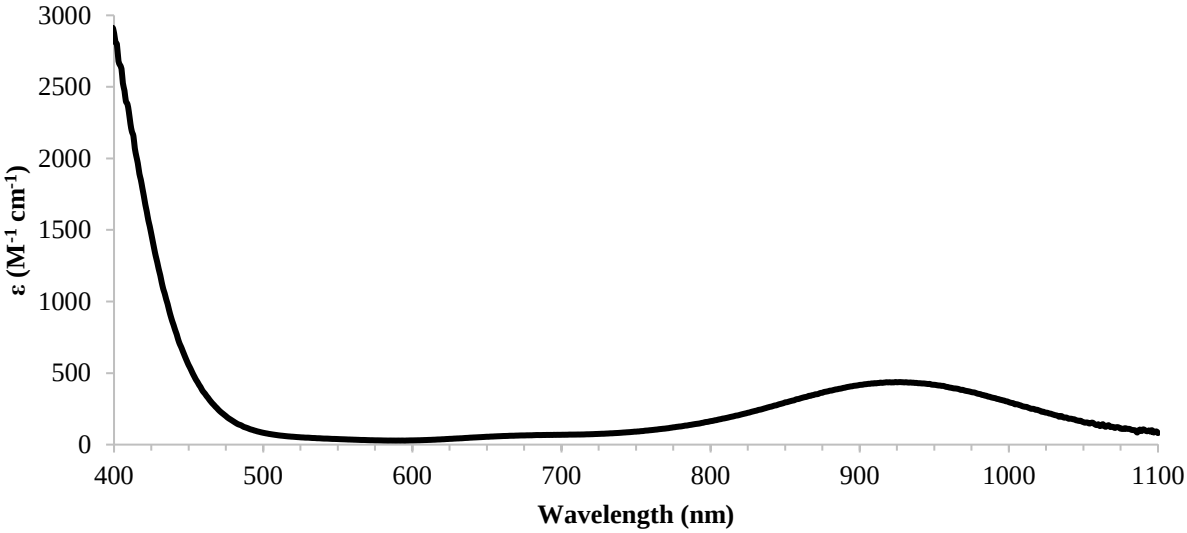

Figure 2.20. UV-visible spectrum of $P_3^{Ga}Fe–N_2$ (**3c**) in THF.

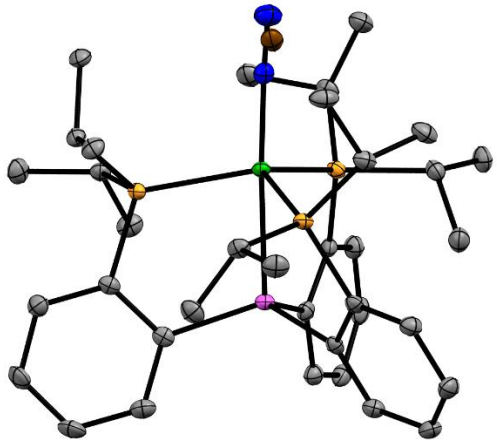

Figure 2.21. XRD structure of $P_3^{Ga}Fe–N_2$ (**3c**) with thermal ellipsoids set at 50% probability. Hydrogen atoms are omitted for clarity. In addition to **3c**, the crystal for which data was collected contained **2c** as a minor component (shown above). Color code: Fe = green, P = orange, Ga = pink, N = blue, Br = brown, C = gray.

[Na(THF)$_3$][$P_3^{Al}Fe–N_2$] (4b). 0.0496 g (1.00 equiv, 0.0668 mmol) of **2b** was dissolved in THF (5 mL) to give a green solution. Excess Na(Hg) (Na: 7.68 equiv, 0.513 mmol, 0.0118 g) was then

added and the reaction was stirred for 4 hours. After a few minutes, a color change from green to dark red was observed. Decanting the supernatant from Hg, followed by filtering through celite, yielded a red solution. Concentrating *in vacuo*, layering with pentane, and storing at –32 °C overnight yielded **4b** as a red solid (0.0515 g, 83%). Crystals suitable for XRD were grown by allowing pentane to slowly diffuse into a concentrated solution of **4b** in THF at –32 °C.

^{1}H NMR (400 MHz, THF-d_8, 25 °C): δ(ppm) 8.08, 7.77, 6.10, 4.41, 1.43, –2.34.

μ_{eff} (Evans Method, THF-d_8, 25 °C): 2.1 μ_B.

IR (thin film from THF): ν(NN) = 1883 cm^{-1}.

IR (THF): ν(NN) = 1879, 1922 cm^{-1}.

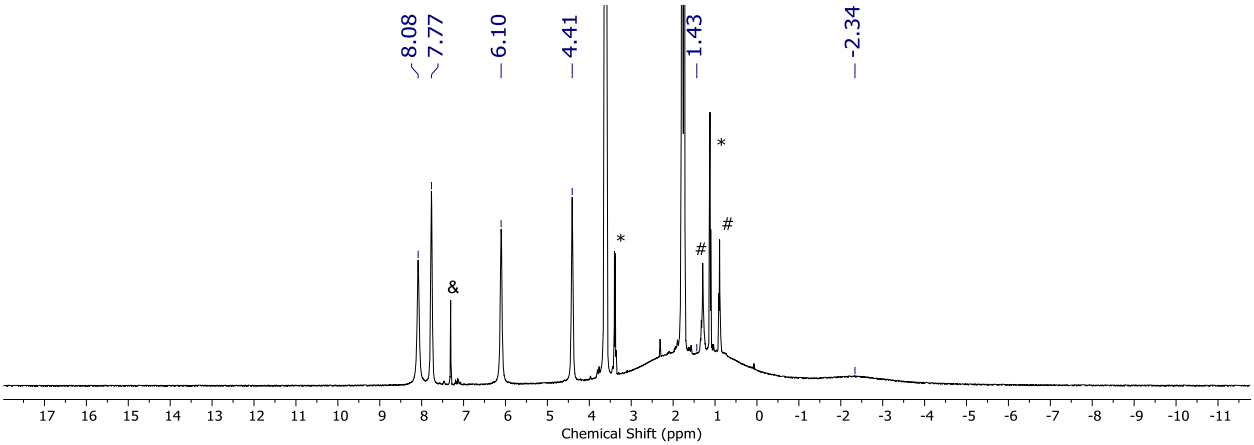

Figure 2.22. ^{1}H NMR spectrum (400 MHz, THF-d_8, 25 °C) of [Na(THF)$_3$][P$_3^{Al}$Fe–N$_2$] (**4b**) (*Et$_2$O, $^{\#}$pentane, $^{\&}$benzene).

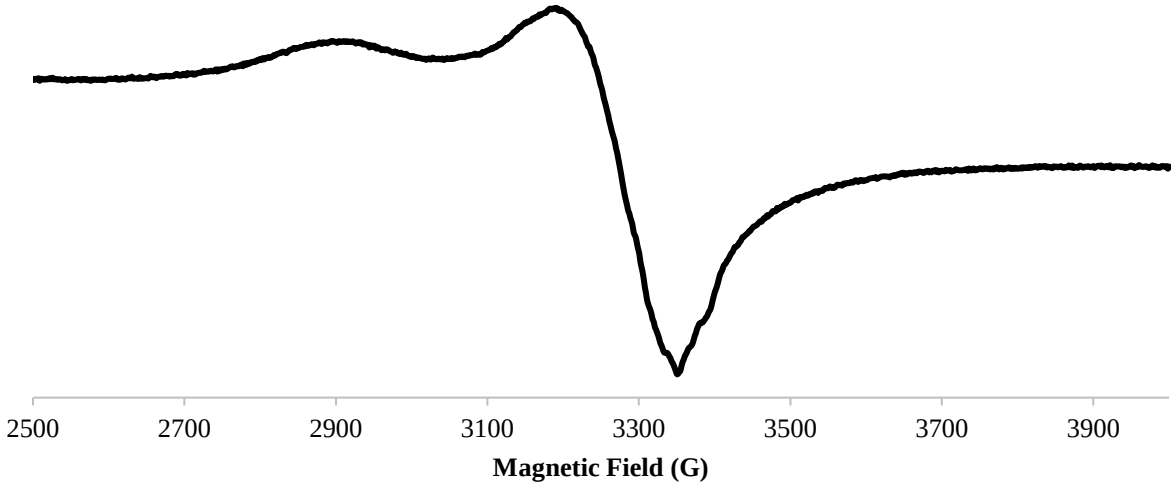

Figure 2.23. X-band EPR spectrum of $[Na(THF)_3][P_3^{Al}Fe–N_2]$ (**4b**) in 2-MeTHF at 77 K.

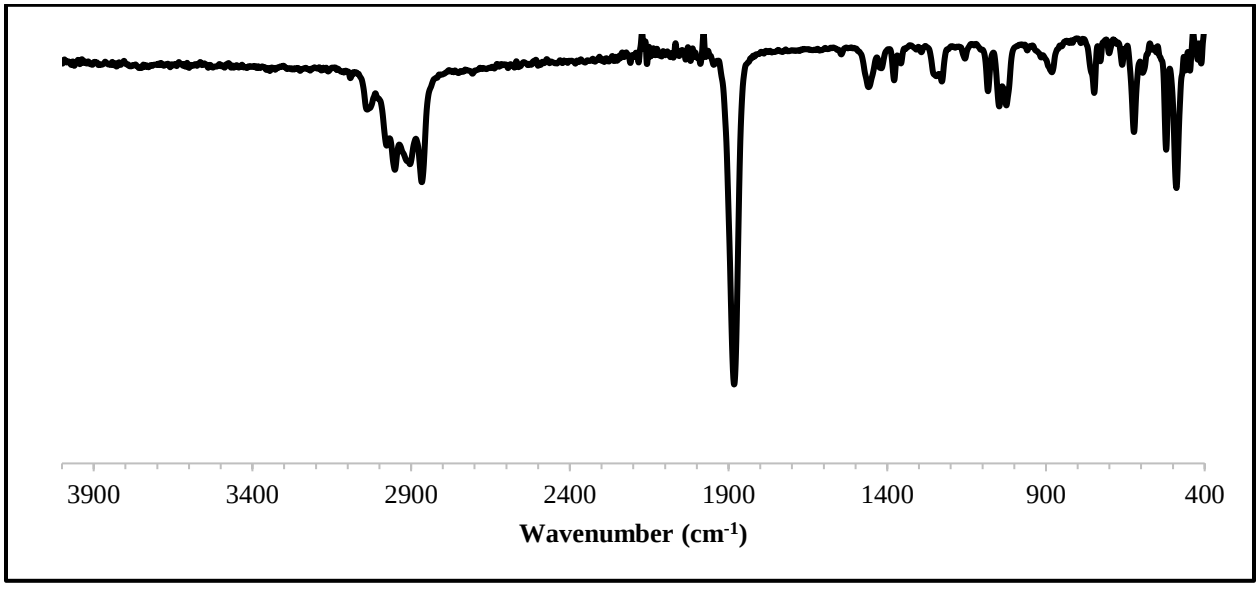

Figure 2.24. IR spectrum of $[Na(THF)_3][P_3^{Al}Fe–N_2]$ (**4b**) deposited as a thin film from THF.

$[Na(THF)_3][P_3^{Ga}Fe–N_2]$ (4c). 0.0766 g (1.00 equiv, 0.0976 mmol) of **2c** was dissolved in THF (5 mL) to give a green solution. Excess Na(Hg) (Na: 7.18 equiv, 0.700 mmol, 0.0161 g) was then

added and the reaction was stirred for 4 hours. After a few minutes, a color change from green to dark red was observed. Decanting the supernatant from Hg, followed by filtering through celite, yielded a red solution. Concentrating *in vacuo*, layering with pentane, and storing at –32 °C overnight yielded **4c** as a red solid (0.0824 g, 87%). Crystals suitable for XRD were grown by allowing pentane to slowly diffuse into a concentrated solution of **4c** in THF at –32 °C.

^{1}H NMR (400 MHz, THF-d_8, 25 °C): δ(ppm) 7.92, 6.84, 6.63, 3.46, 1.45, –5.23.

μ_{eff} (Evans Method, THF-d_8, 25 °C): 2.4 μ_B.

IR (thin film from THF): ν(NN) = 1879 cm^{-1}.

IR (THF): ν(NN) = 1879, 1920 cm^{-1}.

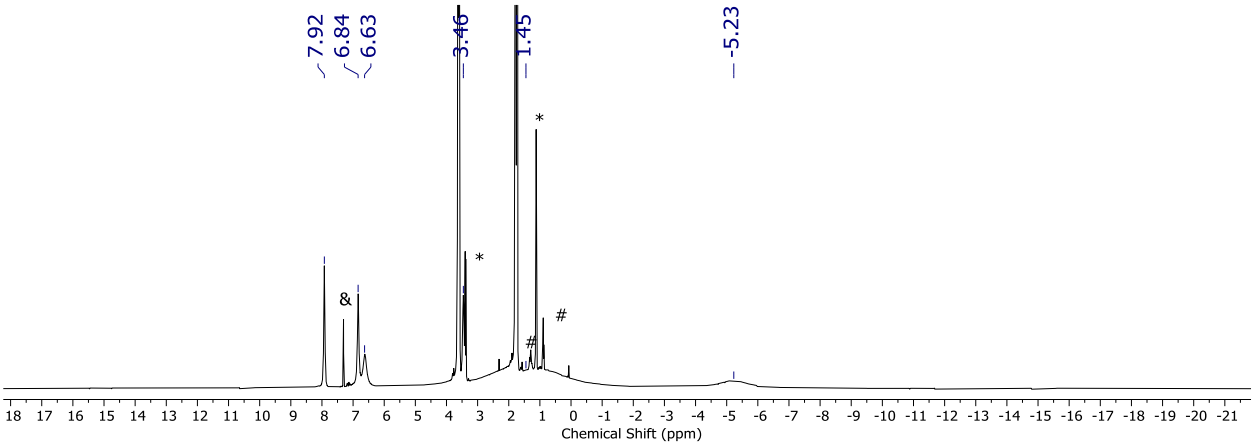

Figure 2.25. ^{1}H NMR spectrum (400 MHz, THF-d_8, 25 °C) of [Na(THF)$_3$][P$_3^{Ga}$Fe–N$_2$] (**4c**) (*Et$_2$O, $^{\#}$pentane, $^{\&}$benzene).

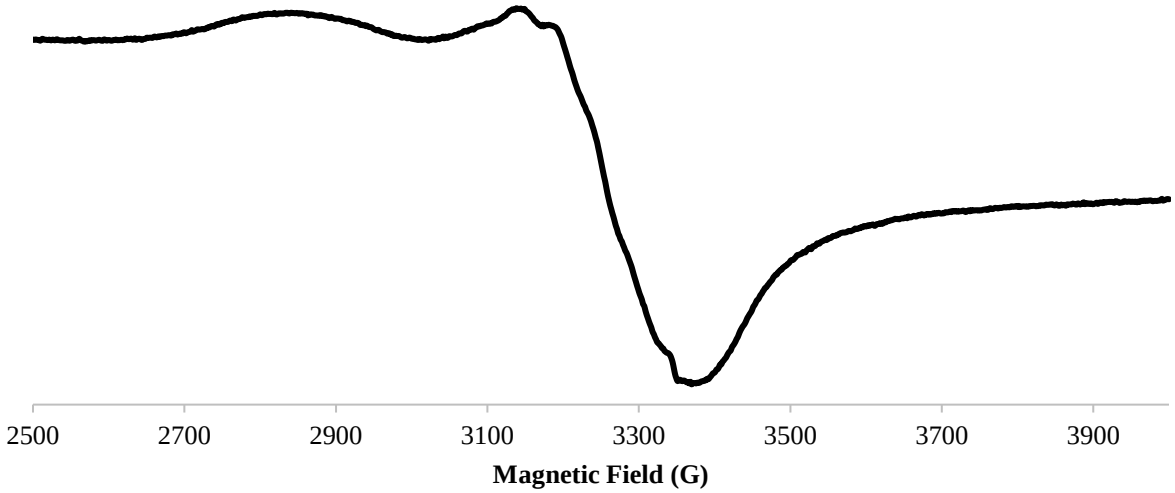

Figure 2.26. X-band EPR spectrum of $[Na(THF)_3][P_3^{Ga}Fe–N_2]$ (**4c**) in 2-MeTHF at 77 K.

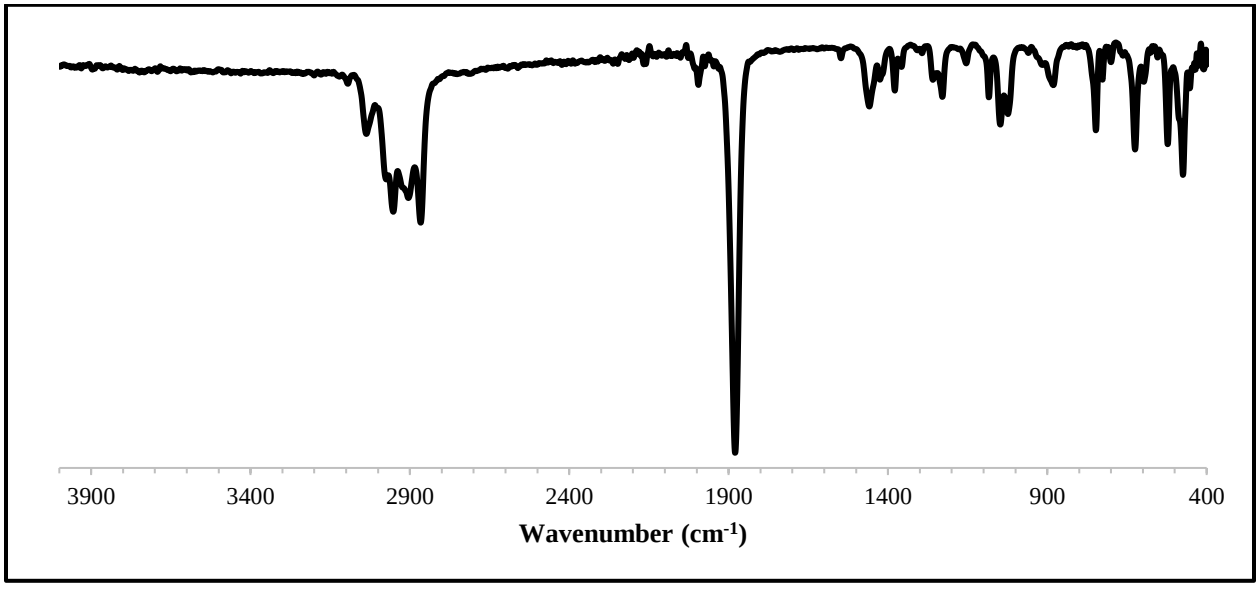

Figure 2.27. IR spectrum of $[Na(THF)_3][P_3^{Ga}Fe–N_2]$ (**4c**) deposited as a thin film from THF.

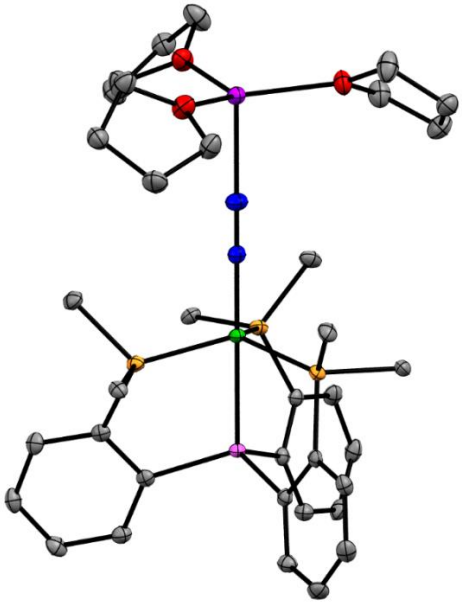

Figure 2.28. XRD structure of $[Na(THF)_3][P_3^{Ga}Fe–N_2]$ (**4c**) with thermal ellipsoids set at 50% probability. For clarity, the isopropyl groups have been truncated and hydrogen atoms have been omitted. Color code: Fe = green, P = orange, Ga = pink, N = blue, Na = purple, O = red, C = gray.

$[Na(12\text{-}c\text{-}4)_2][P_3^{Al}Fe–N_2]$ (5b). 0.0406 g (1.00 equiv, 0.0437 mmol) of **4b** was dissolved in THF (4 mL). 12-crown-4 (3.19 equiv, 0.139 mmol, 0.0245 g) was then added as a THF solution (2 mL) and the reaction was stirred at room temperature for 2 hours. Removing the THF *in vacuo*, washing the remaining residue with Et_2O (3 x 6 mL), and drying under vacuum afforded **5b** as a dark red solid (0.0423 g, 91%).

IR (thin film from THF): ν(NN) = 1914 cm^{-1}.

IR (THF): ν(NN) = 1922 cm^{-1}.

Anal. Calcd. for $C_{52}H_{86}AlFeN_2NaO_8P_3$: C, 58.59; H, 8.13; N, 2.63. Found: C, 58.23; H, 7.90; N, 2.37.

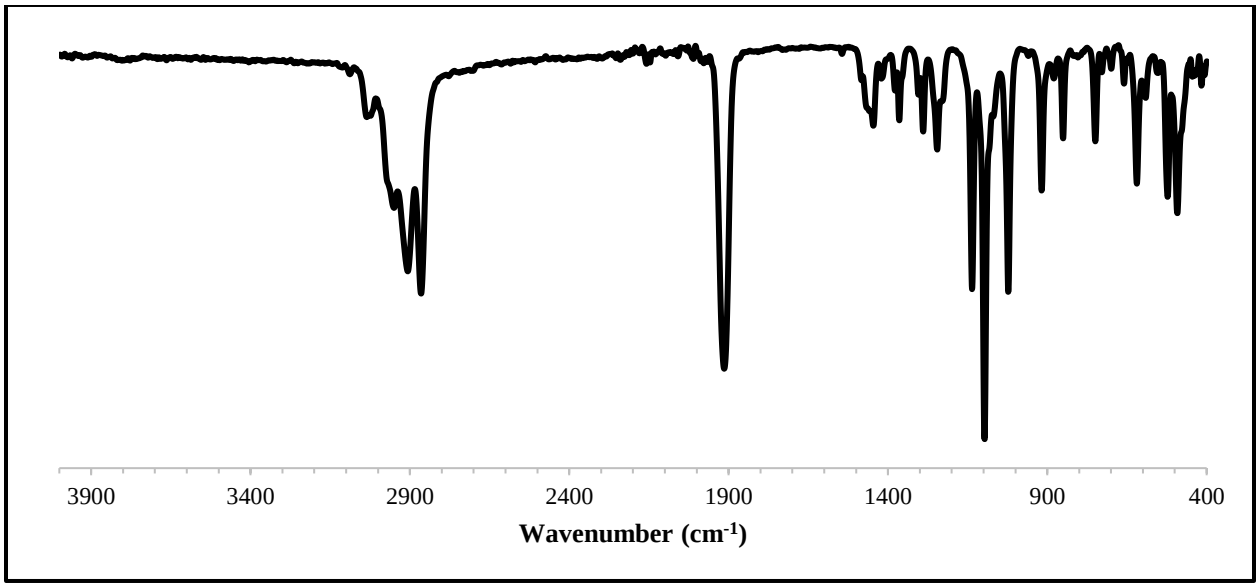

Figure 2.29. IR spectrum of $[Na(12\text{-c-}4)_2][P_3{}^{Al}Fe–N_2]$ (**5b**) deposited as a thin film from THF.

$[Na(12\text{-c-}4)_2][P_3{}^{Ga}Fe–N_2]$ (5c). 0.0501 g (1.00 equiv, 0.0515 mmol) of **4c** was dissolved in THF (4 mL). 12-crown-4 (3.58 equiv, 0.184 mmol, 0.0325 g) was then added as a THF solution (2 mL) and the reaction was stirred at room temperature for 2 hours. Removing the THF *in vacuo*, washing the remaining residue with Et_2O (3 x 6 mL), and drying under vacuum afforded **5c** as a dark red solid (0.0548 g, 96%).

IR (thin film from THF): ν(NN) = 1912 cm^{-1}.

IR (THF): ν(NN) = 1920 cm^{-1}.

Anal. Calcd. for $C_{52}H_{86}FeGaN_2NaO_8P_3$: C, 56.33; H, 7.82; N, 2.53. Found: C, 56.38; H, 7.60; N, 2.36.

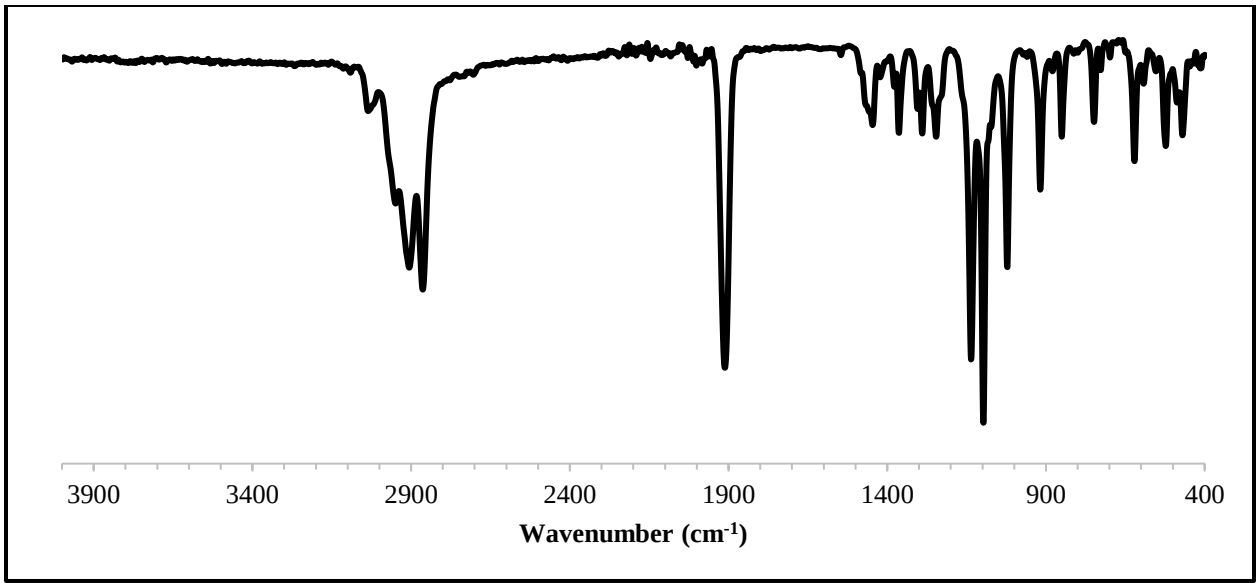

Figure 2.30. IR spectrum of $[Na(12\text{-c-}4)_2][P_3^{Ga}Fe–N_2]$ (**5c**) deposited as a thin film from THF.

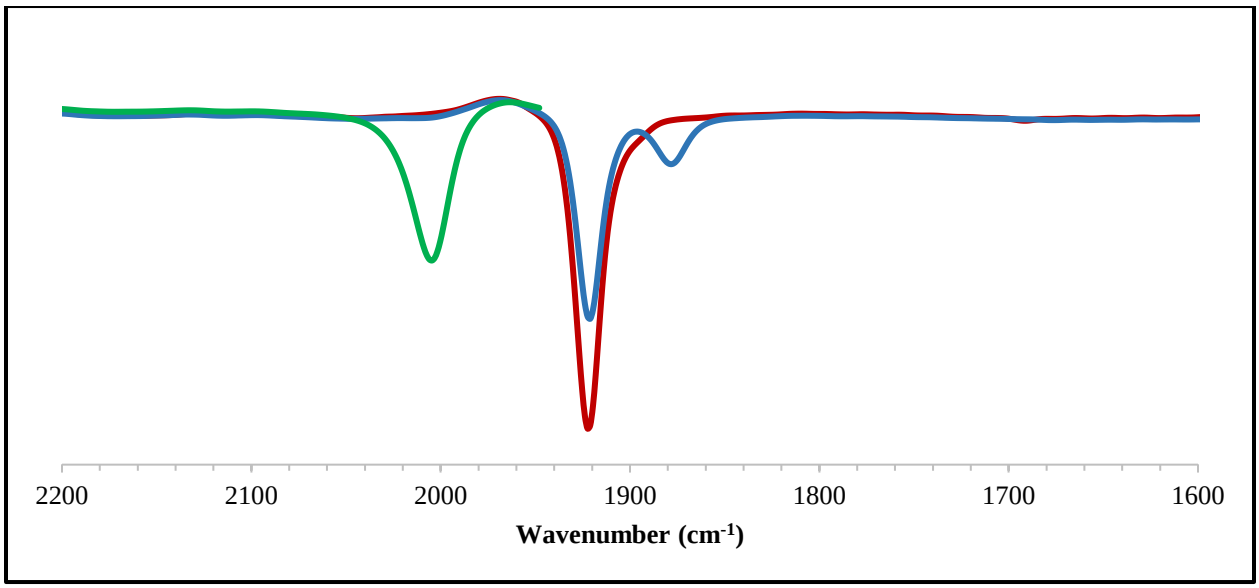

Figure 2.31. THF solution IR spectra of $P_3^{Al}Fe–N_2$ (**3b**, green), $[Na(THF)_3][P_3^{Al}Fe–N_2]$ (**4b**, blue), and $[Na(12\text{-c-}4)_2][P_3^{Al}Fe–N_2]$ (**5b**, red) in the region 1600–2200 cm^{-1}.

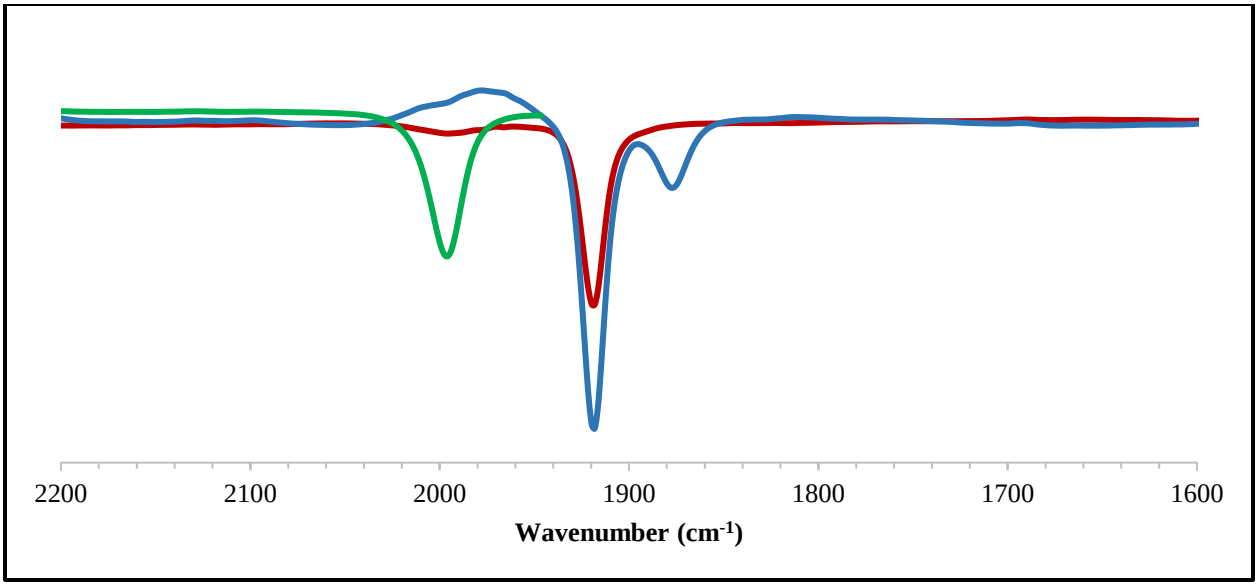

Figure 2.32. THF solution IR spectra of $P_3^{Ga}Fe–N_2$ (**3c**, green), $[Na(THF)_3][P_3^{Ga}Fe–N_2]$ (**4c**, blue), and $[Na(12\text{-c-}4)_2][P_3^{Ga}Fe–N_2]$ (**5c**, red) in the region 1600–2200 cm^{-1}.

2.4.3. Ammonia Production and Quantification Studies

Standard NH_3 Generation Reaction Procedure

All solvents were stirred with Na/K for ≥ 1 hour and filtered prior to use. In a nitrogen-filled glovebox, the precatalyst (ca. 2.0 μmol) was weighed into a vial. The precatalyst was then transferred quantitatively into a Schlenk tube as a suspension in Et_2O. The Et_2O was then evaporated to provide a solid layer of precatalyst at the bottom of the Schlenk tube. The acid and reductant were then added as solids and the tube was equipped with a stir bar. The tube was then cooled to 77 K in the coldwell. To the cold tube was added 2.0 mL of Et_2O. The temperature of the system was allowed to equilibrate for 5 minutes and then the tube was sealed with a Teflon screw-valve. This tube was passed out of the box into a liquid nitrogen bath and transported to a fume hood. The tube was then transferred to a dry ice/acetone bath (–78 °C) where it thawed and

was allowed to stir at –78 °C. For runs utilizing $HBAr^F_4$, reactions were stirred at –78 °C for 1 hour, followed by stirring at room temperature for 45 minutes. For all other runs, reactions were allowed to stir and gradually warm to room temperature overnight. To ensure reproducibility, all experiments were conducted in 200 mL Schlenk tubes (51 mm OD) using 25 mm stir bars, and stirring was conducted at ~900 rpm.

Ammonia and Hydrazine Quantification

The catalytic reaction mixture was cooled to 77 K and allowed to freeze. The reaction vessel was then opened to atmosphere and to the frozen solution was added an excess (with respect to acid) solution of a NaO^tBu solution in MeOH (0.25 mM) dropwise over 1–2 minutes. This solution was allowed to freeze, then the headspace of the tube was evacuated and the tube was sealed. The tube was then allowed to warm to room temperature and stirred at room temperature for at least 10 minutes. An additional Schlenk tube was charged with HCl (3 mL of a 2.0 M solution in Et_2O, 6 mmol) to serve as a collection flask. The volatiles of the reaction mixture were vacuum transferred at room temperature into this collection flask. After completion of the vacuum transfer, the collection flask was sealed and warmed to room temperature. Solvent was removed *in vacuo*, and the remaining residue dissolved in 1 mL of DI H_2O. A 20 µL aliquot of this solution was then analyzed for the presence of NH_3 (present as $[NH_4][Cl]$) by the indophenol method.[41] Quantification was performed with UV-visible spectroscopy by analyzing the absorbance at 635 nm. A further aliquot of this solution was analyzed for the presence of N_2H_4 (present as $[N_2H_5][Cl]$) by a standard colorimetric method.[42] Quantification was performed with UV-visible spectroscopy by analyzing the absorbance at 458 nm.

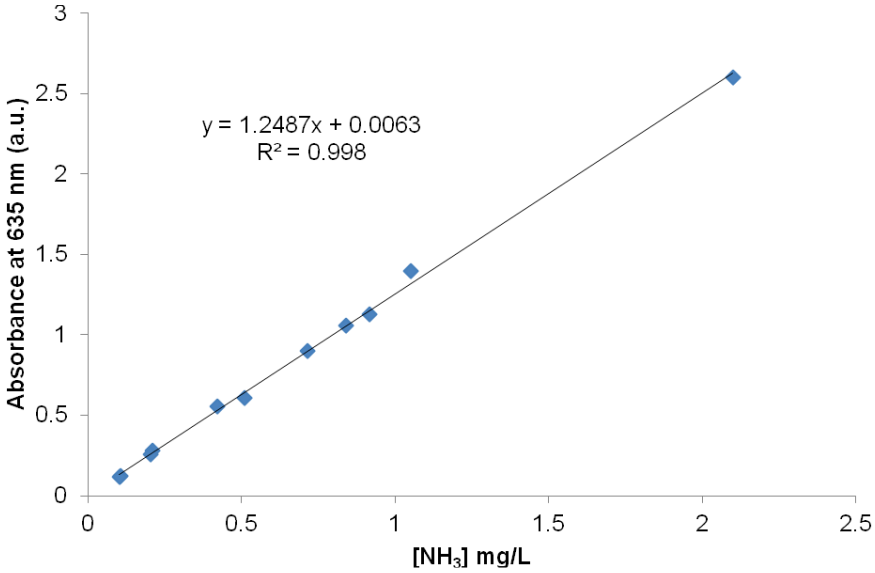

Figure 2.33. Calibration curve used for NH_3 quantification.

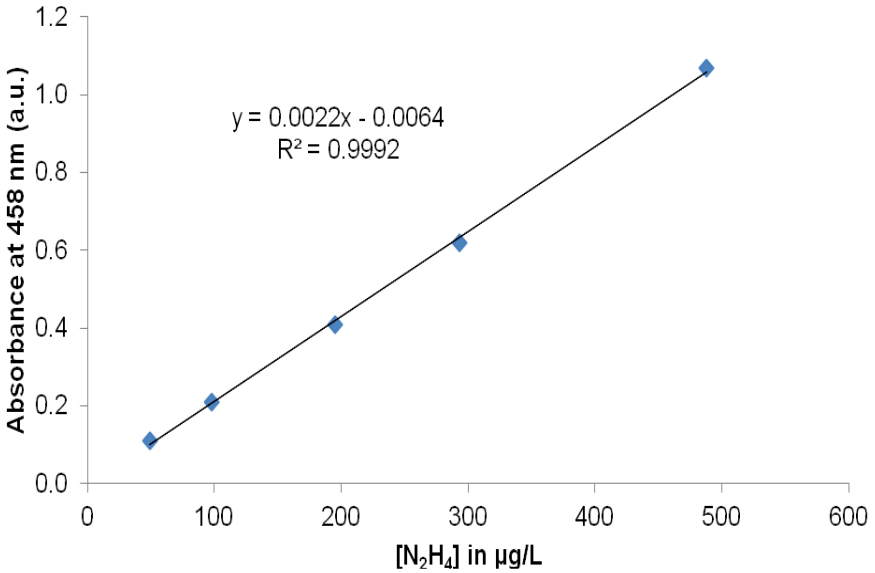

Figure 2.34. Calibration curve used for N_2H_4 quantification.

Table 2.3. UV-visible quantification results for standard NH_3 generation experiments with [Na(12-c-4)$_2$][P_3^{Al}Fe–N_2] (**5b**).

Entry	Total volume of Et_2O (mL)	Fe (μmol)	Acid (equiv)	Reductant (equiv)	NH_4Cl (μmol)	NH_3/Fe (equiv)	Yield NH_3/H^+ (%)
A	2.0	2.0	46[a]	50[b]	5.0	2.5	16
B	2.0	2.0	46[a]	50[b]	5.0	2.5	17
C	2.0	2.0	46[a]	50[b]	5.1	2.6	17
Avg.						2.5 ± 0.1	17 ± 1
D	2.0	2.0	46[c]	50[d]	6.3	3.2	21
E	2.0	2.1	46[c]	50[d]	8.5	4.1	27
F	2.0	2.0	46[c]	50[d]	10	5.1	33
Avg.						4.1 ± 0.9	27 ± 6

[a]$HBAr^F_4$. [b]KC_8. [c]$[H_2NPh_2][OTf]$. [d]Cp^*_2Co.

*N_2H_4 was not detected in the catalytic runs.

Table 2.4. UV-visible quantification results for standard NH_3 generation experiments with [Na(12-c-4)$_2$][P_3^{Ga}Fe–N_2] (**5c**).

Entry	Total volume of Et_2O (mL)	Fe (μmol)	Acid (equiv)	Reductant (equiv)	NH_4Cl (μmol)	NH_3/Fe (equiv)	Yield NH_3/H^+ (%)
A	2.0	2.0	46[a]	50[b]	5.0	2.5	16
B	2.0	2.0	46[a]	50[b]	5.2	2.6	17
C	2.0	1.9	46[a]	50[b]	5.5	2.9	19
Avg.						2.7 ± 0.2	17 ± 1
D	2.0	2.0	46[c]	50[d]	6.8	3.4	22
E	2.0	2.0	46[c]	50[d]	6.9	3.5	23
F	2.0	2.0	46[c]	50[d]	7.7	3.9	25
Avg.						3.6 ± 0.3	24 ± 2

[a]$HBAr^F_4$. [b]KC_8. [c]$[H_2NPh_2][OTf]$. [d]Cp^*_2Co.

*N_2H_4 was not detected in the catalytic runs.

2.4.4. Cyclic Voltammetry

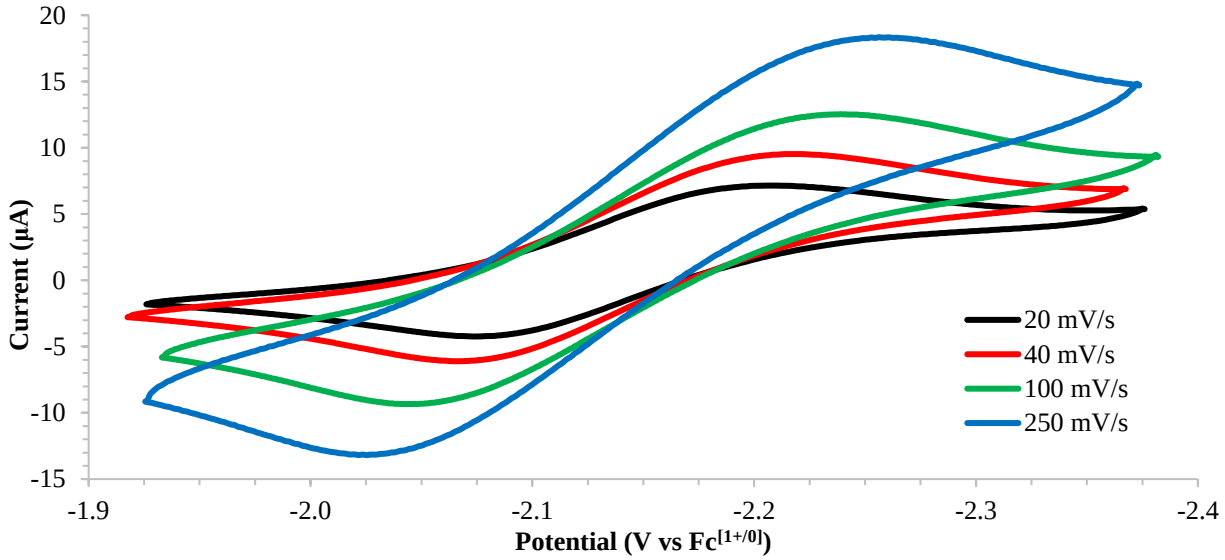

Figure 2.35. Cyclic voltammograms of $P_3{}^BFe–N_2$ (**3a**) in 0.1 M THF solution of [^{n}Bu$_4$][PF$_6$] at different scan rates.

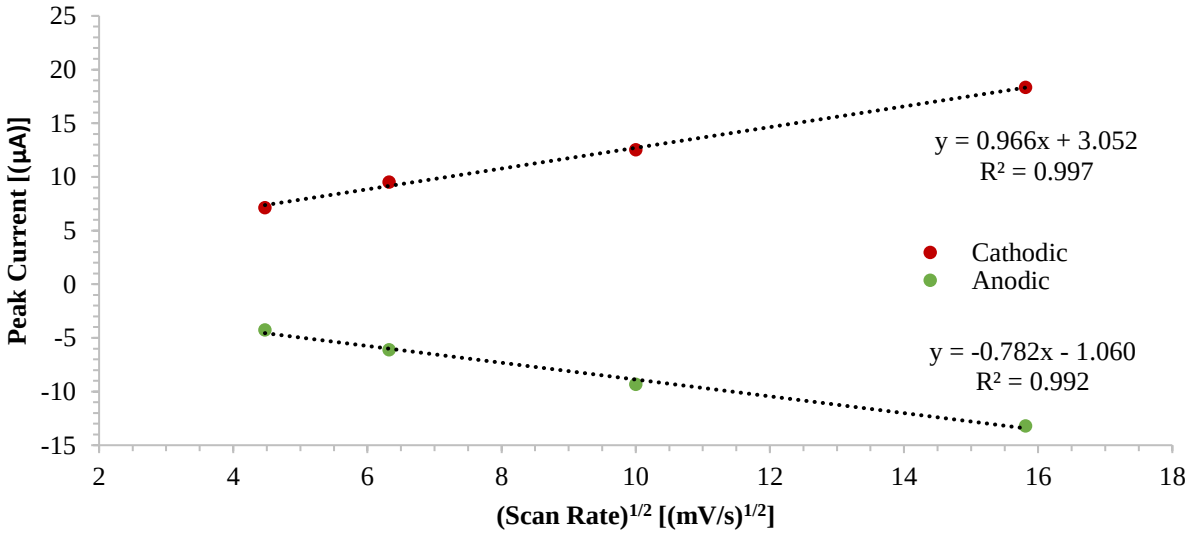

Figure 2.36. Plot of the cathodic/anodic peak current versus the square root of scan rate for $P_3{}^BFe–N_2$ (**3a**) in 0.1 M THF solution of [^{n}Bu$_4$][PF$_6$] at different scan rates.

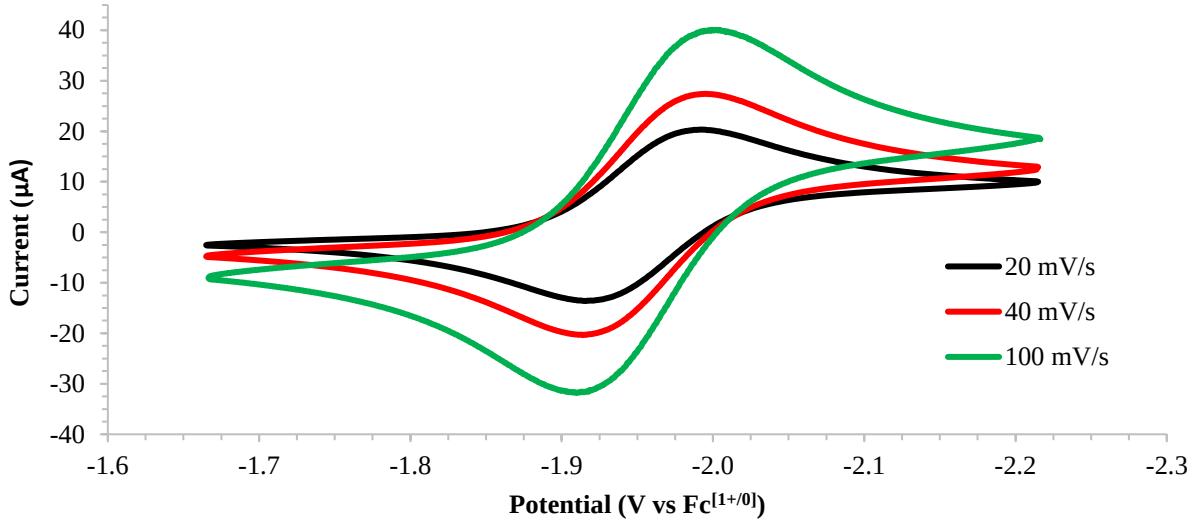

Figure 2.37. Cyclic voltammograms of $P_3^{Al}Fe–N_2$ (**3b**) in 0.1 M THF solution of [^{n}Bu$_4$][PF$_6$] at different scan rates.

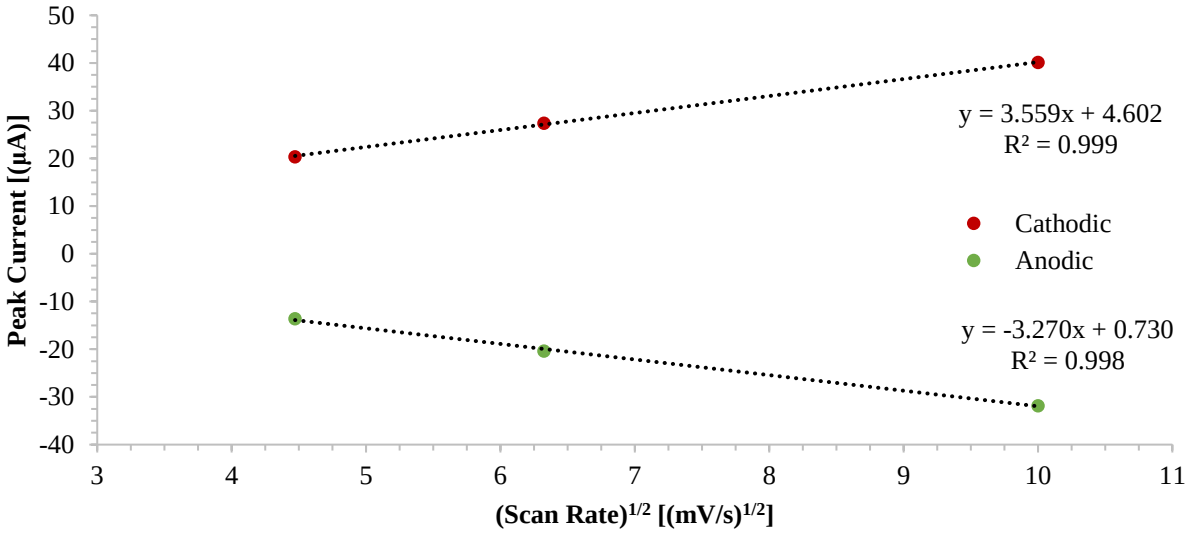

Figure 2.38. Plot of the cathodic/anodic peak current versus the square root of scan rate for $P_3^{Al}Fe–N_2$ (**3b**) in 0.1 M THF solution of [^{n}Bu$_4$][PF$_6$] at different scan rates.

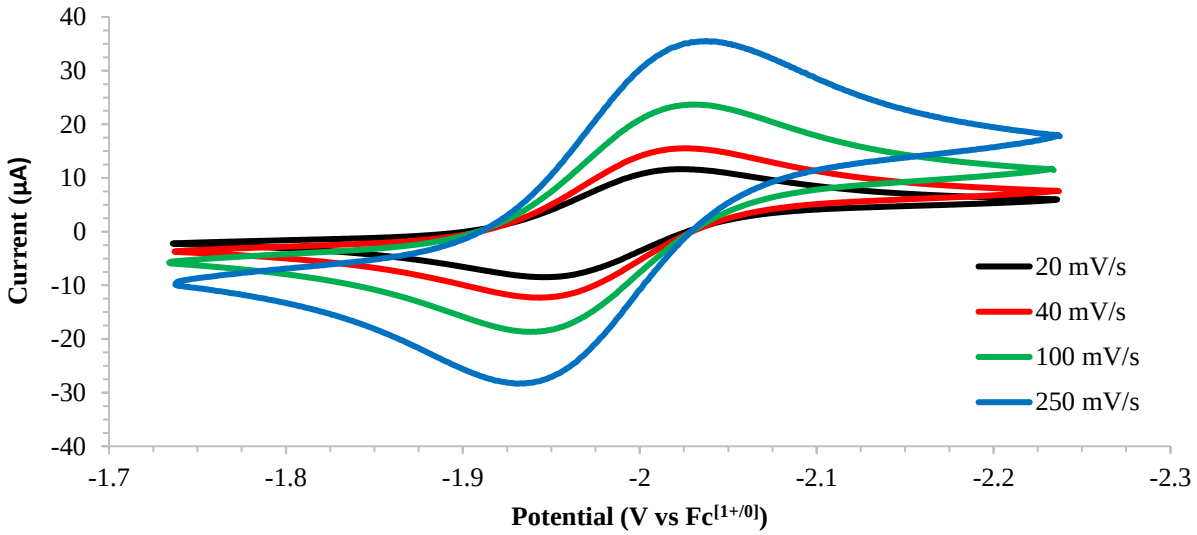

Figure 2.39. Cyclic voltammograms of $P_3^{Ga}Fe–N_2$ (**3c**) in 0.1 M THF solution of [^{n}Bu$_4$][PF$_6$] at different scan rates.

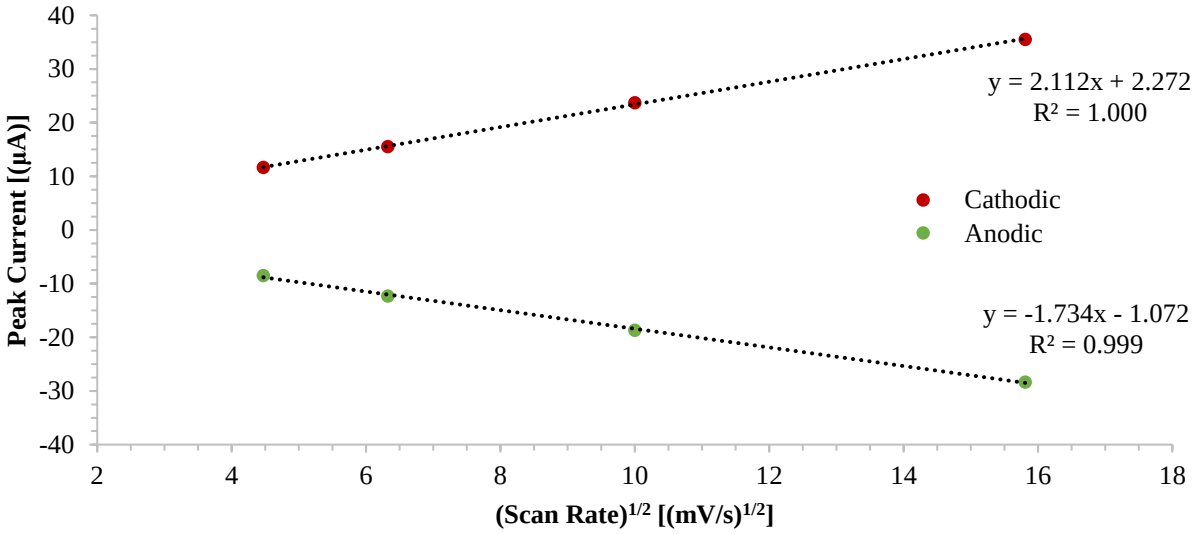

Figure 2.40. Plot of the cathodic/anodic peak current versus the square root of scan rate for $P_3^{Ga}Fe–N_2$ (**3c**) in 0.1 M THF solution of [^{n}Bu$_4$][PF$_6$] at different scan rates.

2.4.5. Miscellaneous Experiments

Treatment of [Na(12-c-4)$_2$][P$_3^X$Fe–N$_2$] (5a–c) with 10 equiv of HBAr$^F_4$ and 12 equiv of KC$_8$

In the glovebox, [Na(12-c-4)$_2$][P$_3^X$Fe–N$_2$] (**5**, 9.3 x 10^{-3} mmol) was weighed out into a 20 mL scintillation vial, equipped with a stir bar, and suspended in 1.5 mL of Et$_2$O. In a separate 4 mL vial, HBAr$^F_4$ (10 equiv, 0.093 mmol) was dissolved in 0.5 mL of Et$_2$O. Finally, in another 4 mL vial, KC$_8$ (12 equiv, 0.11 mmol) was suspended in 1 mL of Et$_2$O. All three vials were cooled to –78 °C for 30 minutes in the glovebox coldwell equipped with an external dry ice/acetone bath.

After the temperature had equilibrated, the HBAr$^F_4$ solution was added dropwise inside the –78 °C glovebox coldwell to the stirring vial containing **5**. Residual HBAr$^F_4$ was transferred using 0.5 mL of pre-chilled Et$_2$O. The reaction was stirred at –78 °C for 5 minutes before similarly delivering the KC$_8$ suspension. Residual KC$_8$ was transferred using 0.5 mL of pre-chilled Et$_2$O. The reaction vial was then capped and stirred for 1 hour at –78 °C followed by 20 minutes at room temperature. The reaction mixture was then filtered through glass filter paper into a 20 mL vial, concentrated to ½ the original volume, transferred to an NMR tube, and analyzed by ^{31}P{^{1}H} NMR and IR spectroscopies. For **5a**, [M(solv)$_x$][P$_3^B$Fe–N$_2$] (solv = solvent) and (P$_3^B$)(μ-H)Fe(L)(H) (L = H$_2$, N$_2$) were the Fe-containing products present. For **5b** and **5c**, analysis of the Et$_2$O filtrate revealed the presence of both [M(solv)$_x$][P$_3^X$Fe–N$_2$] and free phosphine resulting from ligand decomposition.

In addition to the Et$_2$O filtrate, the residue remaining in the original reaction vessel and the pipet filter was extracted with a minimal amount of THF. The resulting dark red solution was also analyzed by ^{31}P{^{1}H} NMR (silent; no signals) and IR spectroscopies. For **5a–c**, [M(solv)$_x$][P$_3^X$Fe–N$_2$] was

the only Fe-containing species observed. This was further confirmed by addition of 12-crown-4 to the THF solution, causing a shift in the *v*(NN) to higher wavenumbers and matching that reported for $[Na(12\text{-c-}4)_2][P_3^XFe–N_2]$.

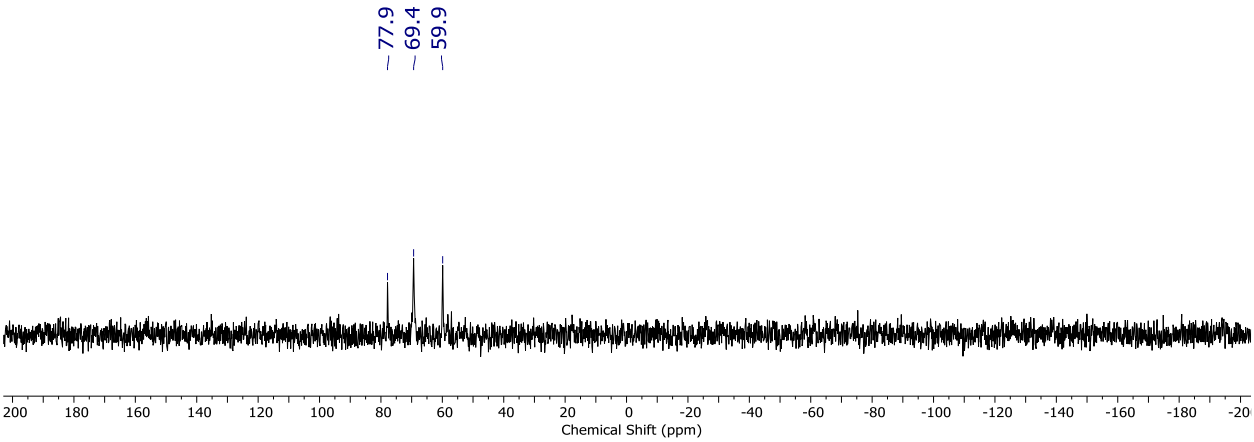

Figure 2.41. $^{31}P\{^1H\}$ NMR spectrum (162 MHz, Et_2O, 25 °C) for the addition of 10 equiv $HBAr^F_4$ and 12 equiv KC_8 to $[Na(12\text{-c-}4)_2][P_3^BFe–N_2]$ (**5a**).

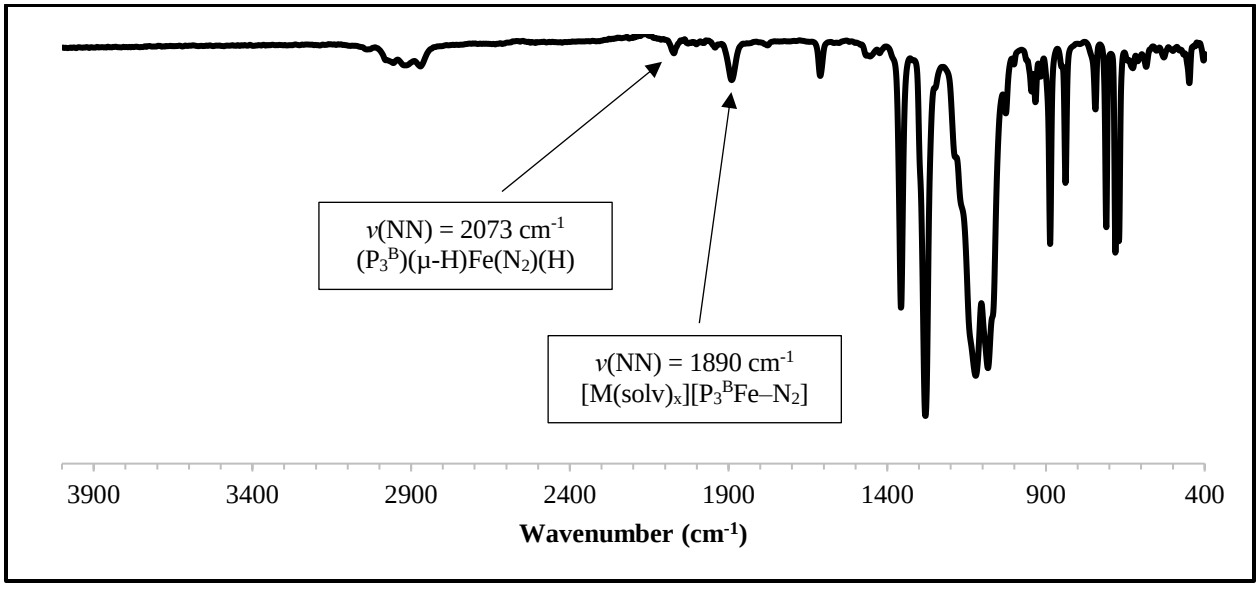

Figure 2.42. IR spectrum for the addition of 10 equiv $HBAr^F_4$ and 12 equiv KC_8 to $[Na(12\text{-c-}4)_2][P_3^BFe–N_2]$ (**5a**) from the Et_2O filtrate; deposited as a thin film from Et_2O.

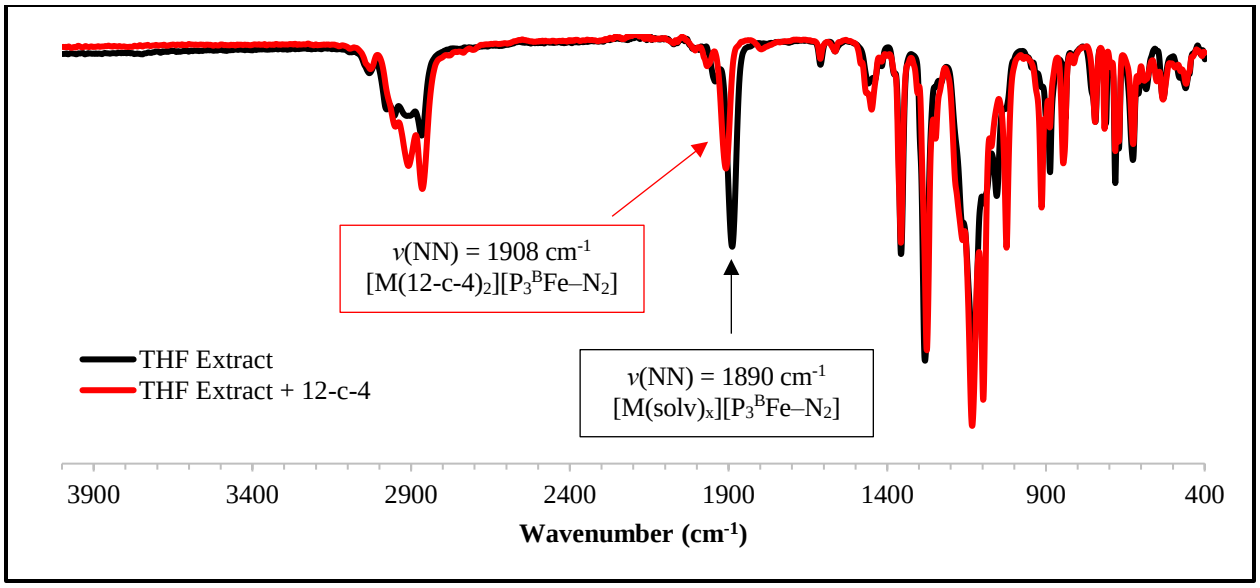

Figure 2.43. IR spectra for the addition of 10 equiv $HBAr^{F}_{4}$ and 12 equiv KC_8 to $[Na(12\text{-c-}4)_2][P_3{}^{B}Fe–N_2]$ (**5a**) from the THF extract before (black) and after (red) addition of 12-crown-4; deposited as a thin film from THF.

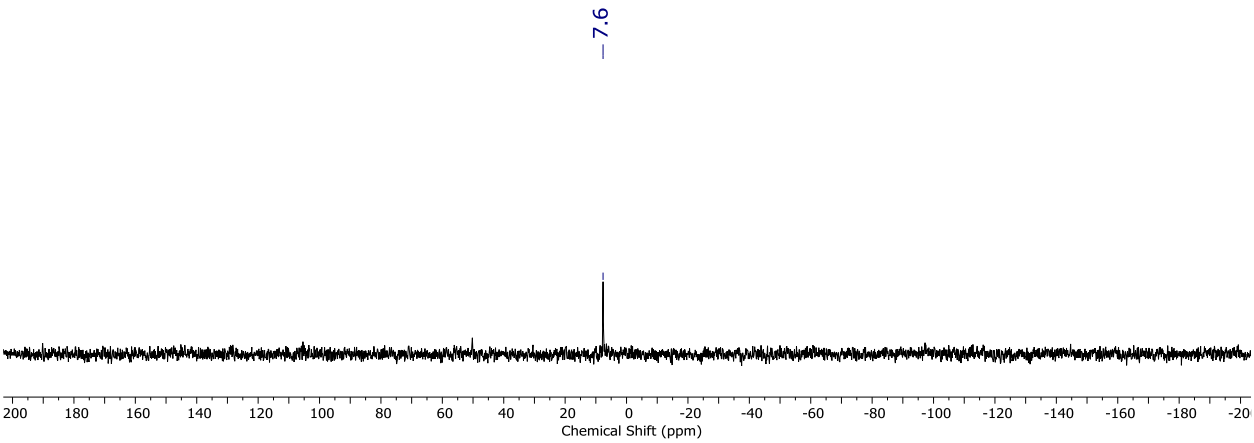

Figure 2.44. $^{31}P\{^{1}H\}$ NMR spectrum (162 MHz, Et_2O, 25 °C) for the addition of 10 equiv $HBAr^{F}_{4}$ and 12 equiv KC_8 to $[Na(12\text{-c-}4)_2][P_3{}^{Al}Fe–N_2]$ (**5b**).

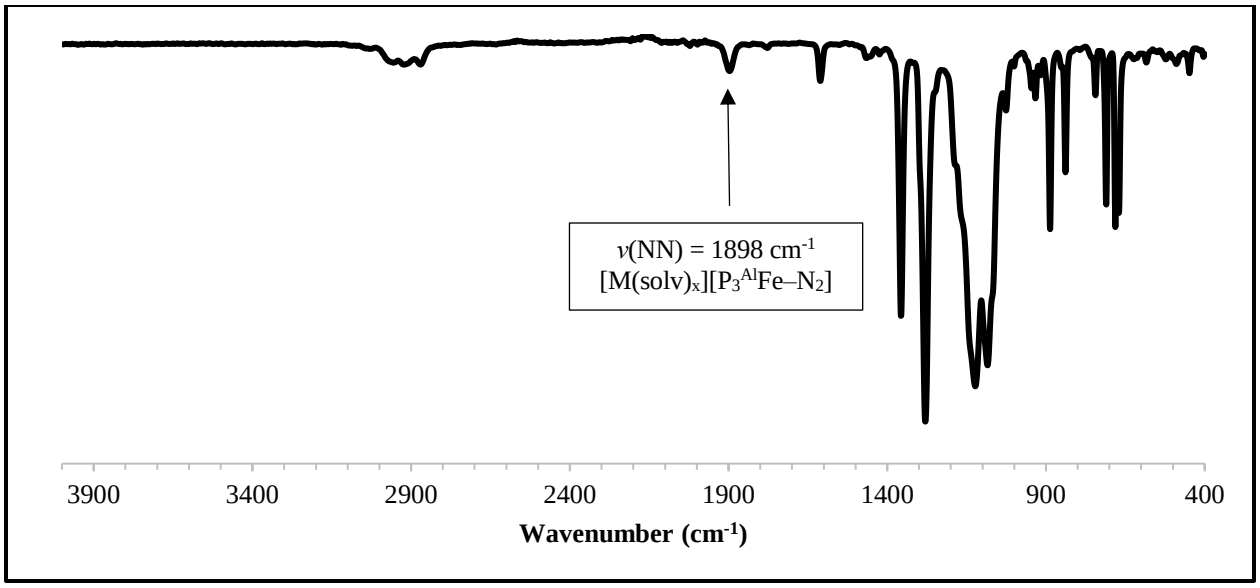

Figure 2.45. IR spectrum for the addition of 10 equiv $HBAr^{F}_{4}$ and 12 equiv KC_8 to $[Na(12\text{-c-}4)_2][P_3^{Al}Fe–N_2]$ (**5b**) from the Et_2O filtrate; deposited as a thin film from Et_2O.

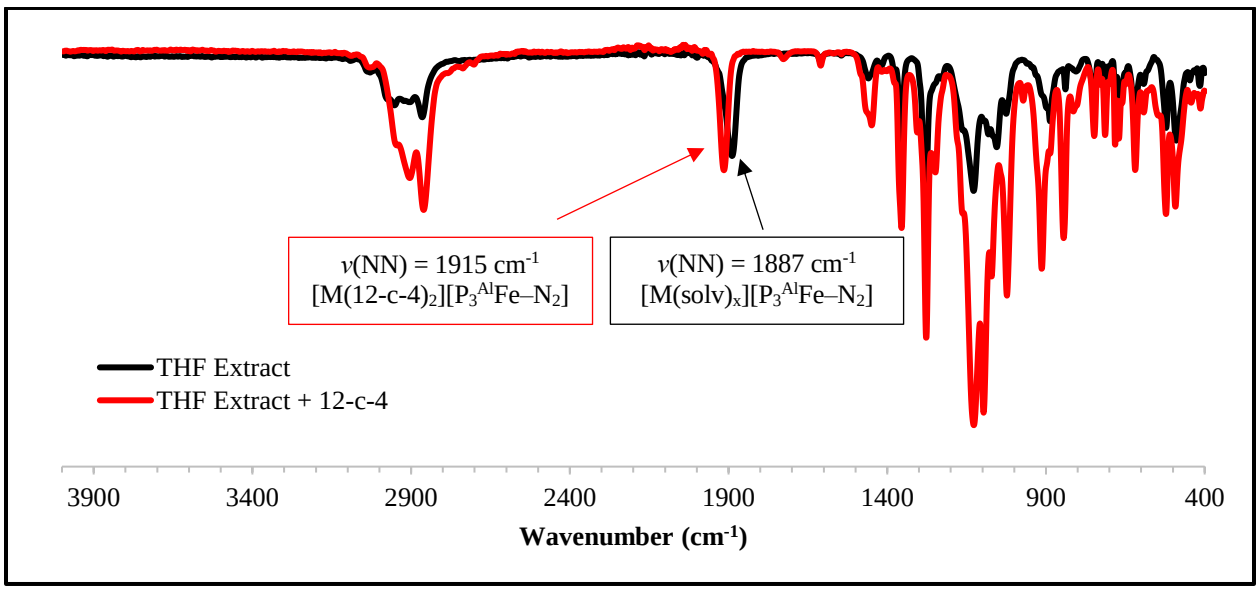

Figure 2.46. IR spectra for the addition of 10 equiv $HBAr^{F}_{4}$ and 12 equiv KC_8 to $[Na(12\text{-c-}4)_2][P_3^{Al}Fe–N_2]$ (**5b**) from the THF extract before (black) and after (red) addition of 12-crown-4; deposited as a thin film from THF.

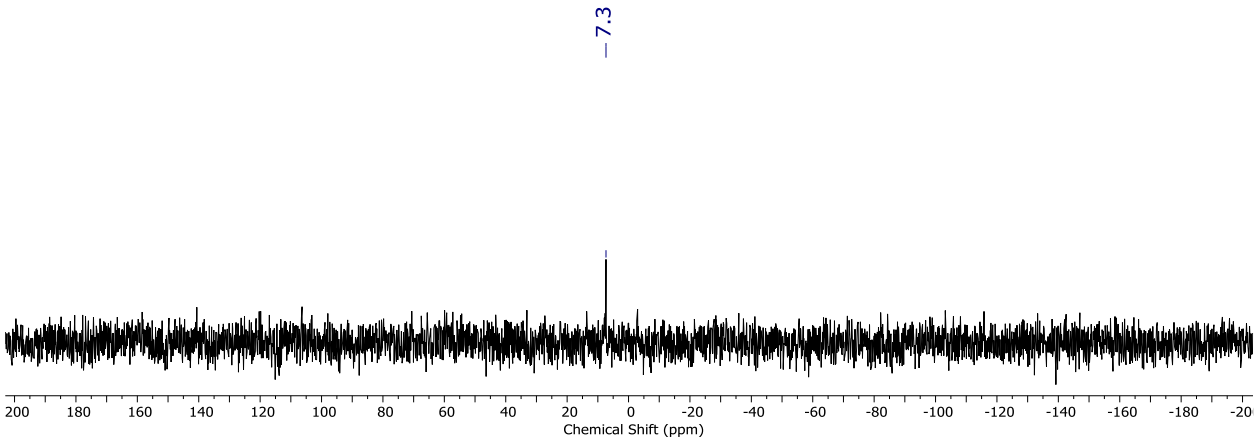

Figure 2.47. $^{31}P\{^{1}H\}$ NMR spectrum (162 MHz, Et_2O, 25 °C) for the addition of 10 equiv $HBAr^F_4$ and 12 equiv KC_8 to $[Na(12\text{-}c\text{-}4)_2][P_3{}^{Ga}Fe\text{–}N_2]$ (**5c**).

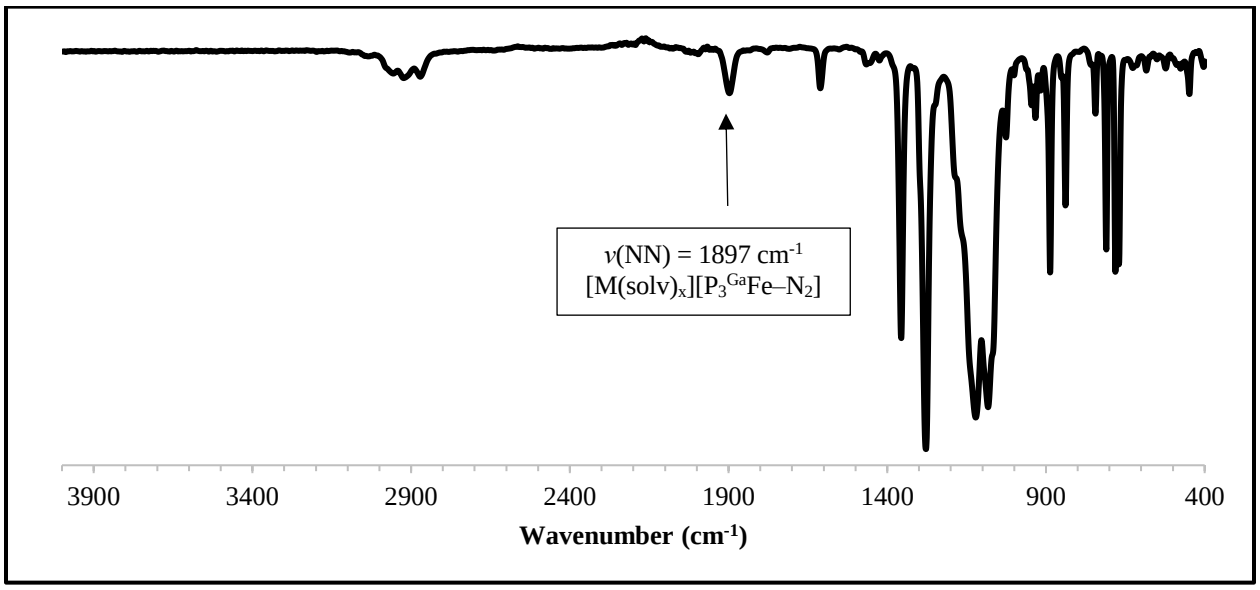

Figure 2.48. IR spectrum for the addition of 10 equiv $HBAr^F_4$ and 12 equiv KC_8 to $[Na(12\text{-}c\text{-}4)_2][P_3{}^{Ga}Fe\text{–}N_2]$ (**5c**) from the Et_2O filtrate; deposited as a thin film from Et_2O.

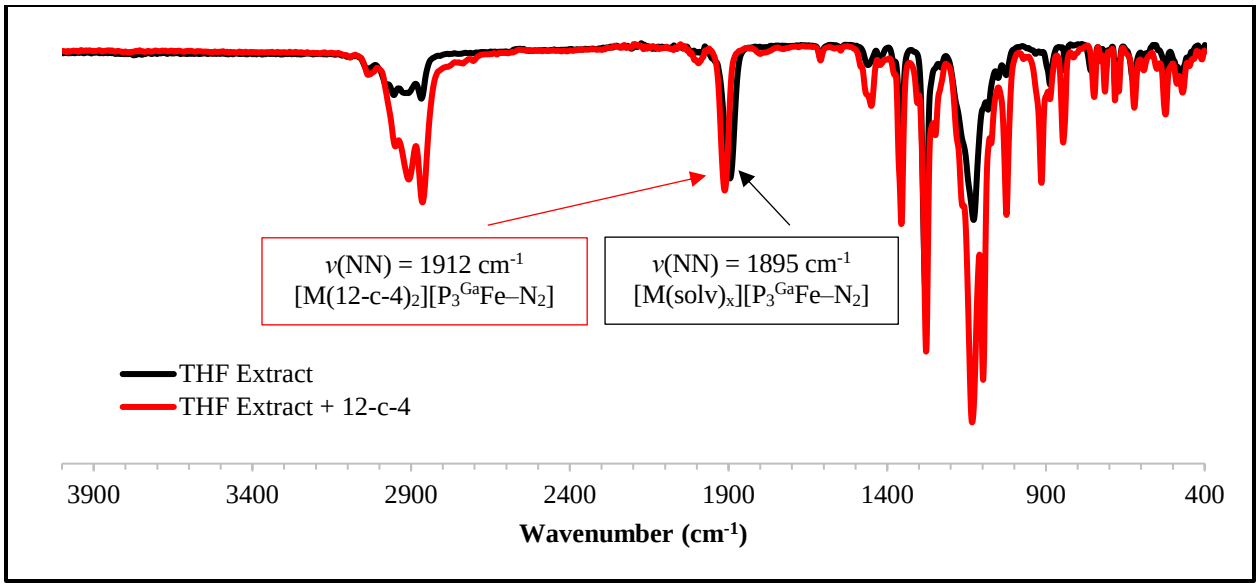

Figure 2.49. IR spectra for the addition of 10 equiv $HBAr^{F}_{4}$ and 12 equiv KC_8 to $[Na(12\text{-}c\text{-}4)_2][P_3^{Ga}Fe\text{–}N_2]$ (**5c**) from the THF extract before (black) and after (red) addition of 12-crown-4; deposited as a thin film from THF.

Treatment of $[Na(12\text{-}c\text{-}4)_2][P_3^{X}Fe\text{–}N_2]$ (5a–c) with 10 equiv $[H_2NPh_2][OTf]$ and 12 equiv Cp^*_2Co

In the glovebox, $[Na(12\text{-}c\text{-}4)_2][P_3^{X}Fe\text{–}N_2]$ (**5**, 9.3 x 10^{-3} mmol) was weighed out into a 20 mL scintillation vial, equipped with a stir bar, and suspended in 1.5 mL of Et_2O. In a separate 4 mL vial, $[H_2NPh_2][OTf]$ (10 equiv, 0.093 mmol) was suspended in 0.5 mL of Et_2O. Finally, in another 4 mL vial, Cp^*_2Co (12 equiv, 0.11 mmol) was suspended in 1 mL of Et_2O. All three vials were cooled to –78 °C for 30 minutes in the glovebox coldwell equipped with an external dry ice/acetone bath.

After the temperature had equilibrated, the suspension of Cp^*_2Co was added dropwise inside the –78 °C glovebox coldwell to the stirring vial containing **5**. Residual Cp^*_2Co was transferred using 0.5 mL of pre-chilled Et_2O. The reaction was stirred at –78 °C for 5 minutes before similarly delivering

the $[H_2NPh_2][OTf]$ suspension. Residual $[H_2NPh_2][OTf]$ was transferred using 0.5 mL of pre-chilled Et_2O. The reaction vial was then capped and stirred for 3 hours at –78 °C followed by 30 minutes at room temperature. The reaction mixture was then filtered through glass filter paper into a 20 mL vial, concentrated to ½ the original volume, transferred to an NMR tube, and analyzed by $^{31}P\{^1H\}$ NMR and IR spectroscopies. For **5a**, $P_3^BFe–N_2$ and $(P_3^B)(\mu\text{-}H)Fe(N_2)(H)$ were the Fe-containing products present. For **5b** and **5c**, analysis of the Et_2O filtrate revealed a mixture of compounds that included $P_3^XFe–N_2$ and free phosphine resulting from ligand decomposition.

Further extraction of the reaction residue with THF did not reveal the presence of any P_3^XFe compounds upon analysis.

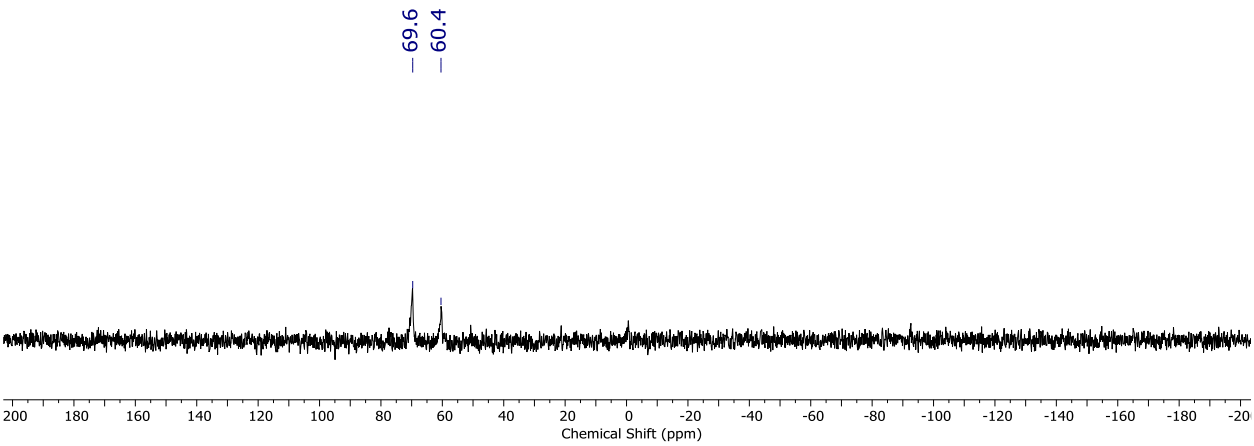

Figure 2.50. $^{31}P\{^1H\}$ NMR spectrum (162 MHz, Et_2O, 25 °C) for the addition of 10 equiv $[H_2NPh_2][OTf]$ and 12 equiv Cp^*_2Co to $[Na(12\text{-}c\text{-}4)_2][P_3^BFe–N_2]$ (**5a**).

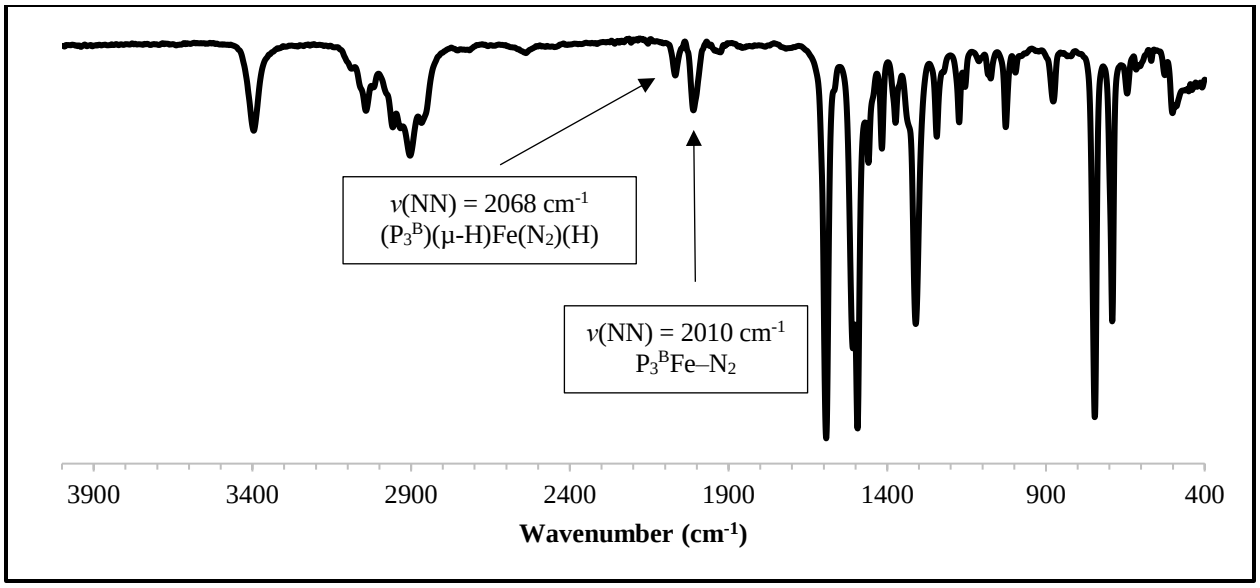

Figure 2.51. IR spectrum for the addition of 10 equiv $[H_2NPh_2][OTf]$ and 12 equiv Cp^*_2Co to $[Na(12\text{-c-}4)_2][P_3^BFe–N_2]$ (**5a**) from the Et_2O filtrate; deposited as a thin film from Et_2O.

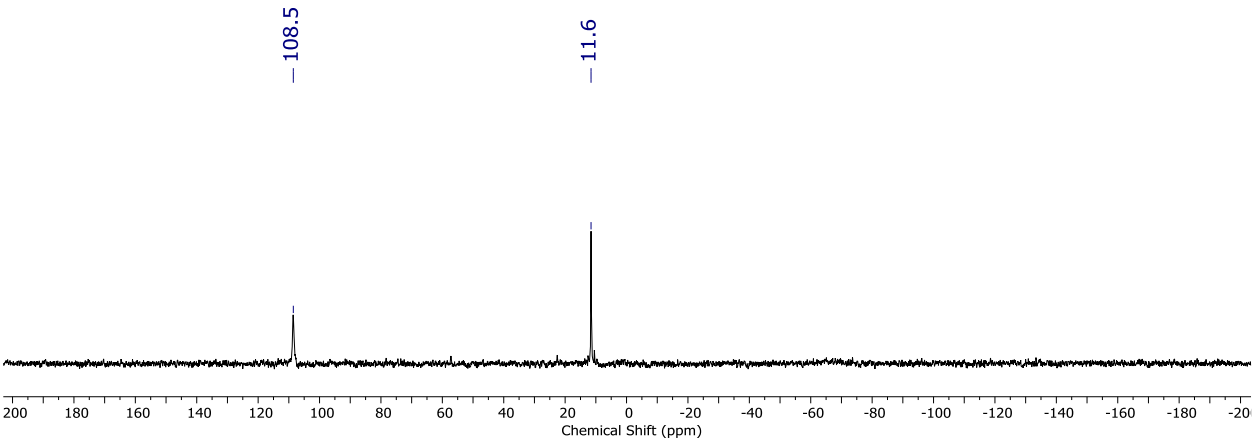

Figure 2.52. $^{31}P\{^1H\}$ NMR spectrum (162 MHz, Et_2O, 25 °C) for the addition of 10 equiv $[H_2NPh_2][OTf]$ and 12 equiv Cp^*_2Co to $[Na(12\text{-c-}4)_2][P_3^{Al}Fe–N_2]$ (**5b**).

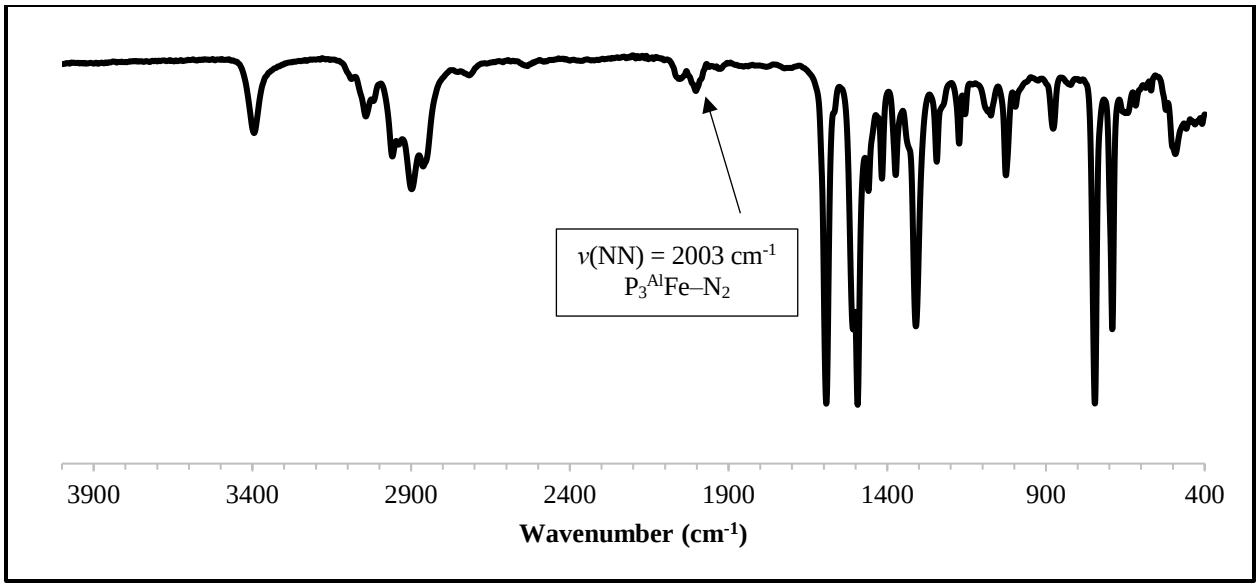

Figure 2.53. IR spectrum for the addition of 10 equiv $[H_2NPh_2][OTf]$ and 12 equiv Cp^*_2Co to $[Na(12\text{-c-}4)_2][P_3^{Al}Fe–N_2]$ (**5b**) from the Et_2O filtrate; deposited as a thin film from Et_2O.

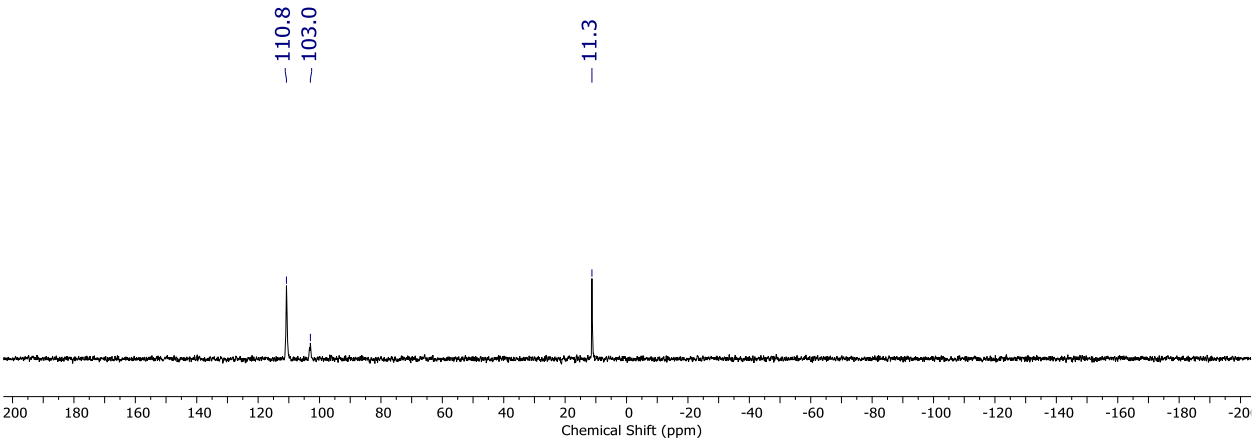

Figure 2.54. $^{31}P\{^1H\}$ NMR spectrum (162 MHz, Et_2O, 25 °C) for the addition of 10 equiv $[H_2NPh_2][OTf]$ and 12 equiv Cp^*_2Co to $[Na(12\text{-c-}4)_2][P_3^{Ga}Fe–N_2]$ (**5c**).

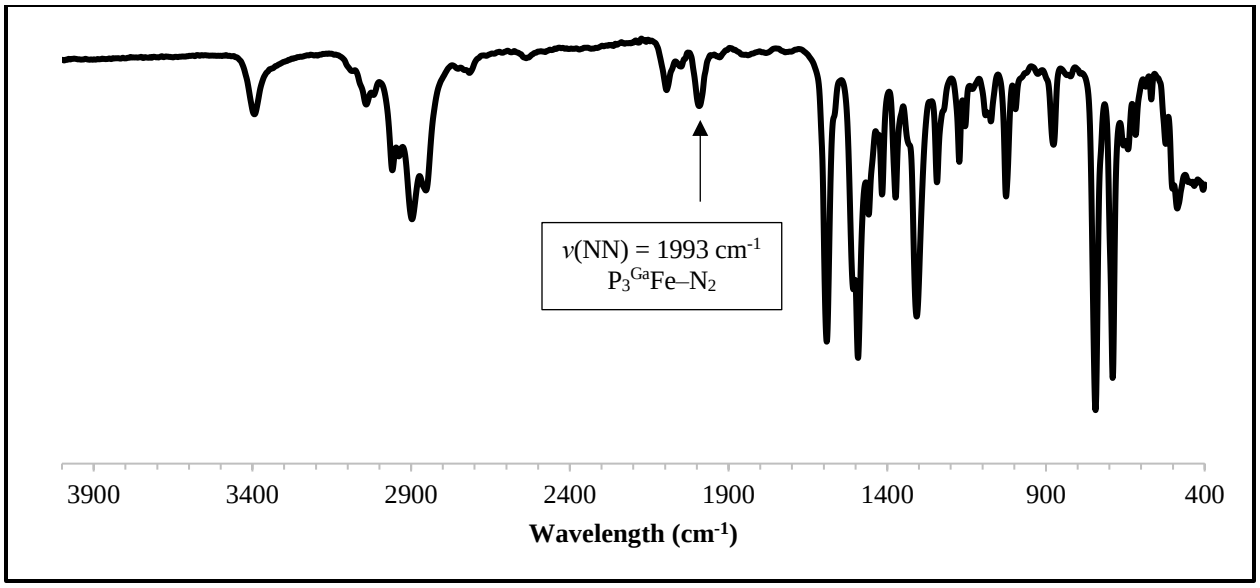

Figure 2.55. IR spectrum for the addition of 10 equiv $[H_2NPh_2][OTf]$ and 12 equiv Cp^*_2Co to $[Na(12\text{-c-}4)_2][P_3^{Ga}Fe–N_2]$ (**5c**) from the Et_2O filtrate; deposited as a thin film from Et_2O.

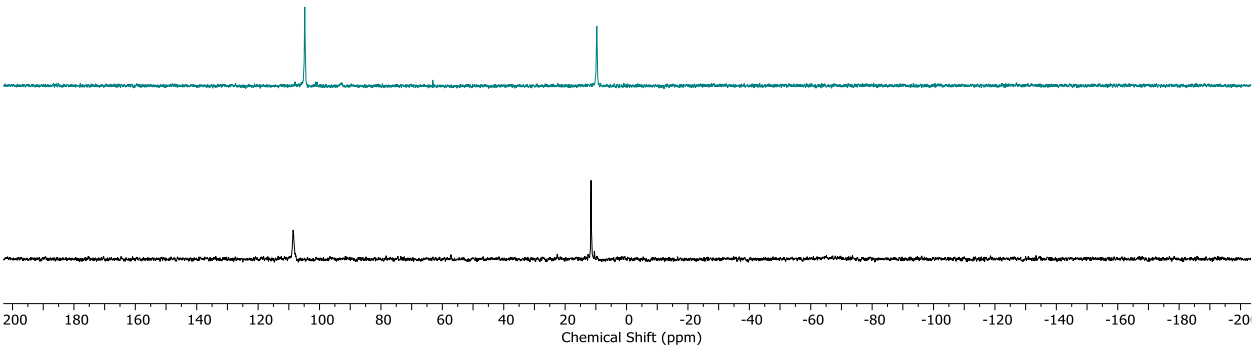

Figure 2.56. Stacked $^{31}P\{^1H\}$ NMR spectra (162 MHz, 25 °C) for the addition of 10 equiv $[H_2NPh_2][OTf]$ and 12 equiv Cp^*_2Co to $[Na(12\text{-c-}4)_2][P_3^{Al}Fe–N_2]$ (**5b**) (bottom, Et_2O) and the reaction of $P_3^{Al}Fe–N_2$ (**3b**) with 1 atm of H_2 at room temperature, followed by freeze-pump thawing and storing under an atmosphere of N_2 for 3 days (top, C_6D_6).

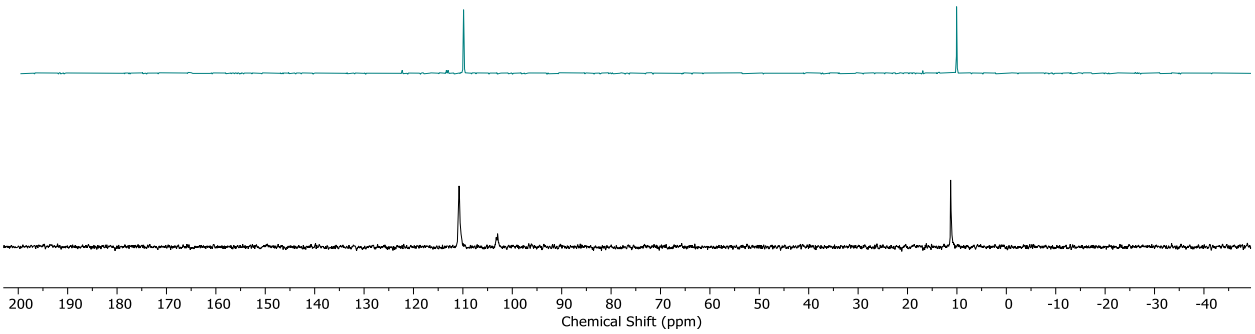

Figure 2.57. Stacked $^{31}P\{^{1}H\}$ NMR spectra (162 MHz, 25 °C) for the addition of 10 equiv $[H_2NPh_2][OTf]$ and 12 equiv Cp^*_2Co to $[Na(12\text{-}c\text{-}4)_2][P_3^{Ga}Fe\text{–}N_2]$ (**5c**) (bottom, Et_2O) and the reaction of $P_3^{Ga}Fe\text{–}N_2$ (**3c**) with 1 atm of H_2 at room temperature, followed by freeze-pump thawing and storing under an atmosphere of N_2 for 3 days (top, C_6D_6).

2.4.6. X-Ray Data Tables

Table 2.5. Structural comparison of P_3^XFe complexes.

Metric	$P_3^XFe–Br$			$P_3^XFe–N_2$			$[Na(THF)_3][P_3^XFe–N_2]$		
X	B	Al	Ga	B*	Al	Ga	B‡	Al	Ga
Fe–X[a]	2.458	2.662	2.666	2.417	2.539	2.544	2.311, 2.306	2.485	2.489
Fe–P[a]	2.383	2.460	2.469	2.306	2.378	2.390	2.232, 2.225	2.275	2.282
	2.403			2.312	2.384	2.397	2.240, 2.263		
	2.435			2.404	2.422	2.434	2.307, 2.291		
Fe–Br[a]	2.414	2.409	2.416	-----	-----	-----	-----	-----	-----
Fe–N[a]	-----	-----	-----	1.844	1.888	1.846	1.776, 1.773	1.769	1.759
N–N[a]	-----	-----	-----	1.129	1.061	1.118	1.149, 1.148	1.134	1.141
P–Fe–P[b]	106.8	114.9	115.3	109.9	113.6	113.7	107.3, 113.4	116.5	116.8
	113.8			111.4	114.6	114.7	110.3, 114.1		
	122.1			124.5	119.7	120.4	134.6, 124.7		
ΣP–Fe–P[b]	342.7	344.8	345.8	345.8	347.8	348.7	352.3, 352.3	349.6	350.4
C–X–C[b]	112.0	113.6	114.0	107.6	107.8	108.3	106.9, 107.6	111.6	111.9
	114.8			111.2	113.5	114.1	109.7, 110.6		
	115.0			114.0	115.0	115.4	113.2, 112.1		
ΣC–X–C[b]	341.8	340.8	341.9	332.8	336.2	337.8	329.8, 330.3	334.8	335.8
X–Fe–Br[b]	173.7	180.0	180.0	-----	-----	-----	-----	-----	-----
X–Fe–N[b]	-----	-----	-----	174.2	176.6	177.0	173.9, 178.8	180.0	180.0
Fe–N–N[b]	-----	-----	-----	177.0	177.6	177.4	175.9, 179.8	180.0	180.0
r	1.14	1.05	1.05	1.12	1.00	1.00	1.07, 1.07	0.98	0.98

[a]Units of Å. [b]Units of °. *From DFT optimized structure. ‡Two independent molecules present in the asymmetric unit.

Table 2.6. Crystal data and structure refinement for **2b**, **3b**, and **4b**.

Compound	**2b**	**3b**	**4b**
Empirical formula	$C_{39}H_{63}AlBrFeO_{0.5}P_3Si$	$C_{36}H_{54}AlFeN_2P_3$	$C_{48}H_{78}AlFeN_2NaO_3P_3$
Formula weight	823.63	690.55	929.85
Temperature [K]	100	100	100
Crystal system	Trigonal	Orthorhombic	Trigonal
Space group	$P\bar{3}$	Pbca	R3
a [Å]	15.4455(5)	16.0945(17)	18.0659(3)
b [Å]	15.4455(5)	17.2155(18)	18.0659(13)
c [Å]	10.2238(4)	25.795(3)	12.9769(5)
α [°]	90	90	90
β [°]	90	90	90
γ [°]	120	90	120
Volume [$Å^3$]	2112.26(16)	7147.1(13)	3667.9(2)
Z	2	8	3
ρ_{calc} [g/cm^3]	1.295	1.284	1.263
μ [mm^{-1}]	1.493	0.608	0.475
F (000)	868.0	2944.0	1497.0
Radiation	MoKα (λ = 0.71073)	MoKα (λ = 0.71073)	MoKα (λ = 0.71073)
Reflections collected	37355	133330	23224
Unique reflections	6489	16490	4266
Data/restraints/parameters	6489/0/146	16490/0/400	4266/1/182
R(int)	0.0457	0.0809	0.0476
R_1 ($I > 2\sigma(I)$)	0.0361	0.0453	0.0262
wR_2 (all data)	0.0789	0.0898	0.0583
GOOF	1.019	1.028	1.036

Table 2.7. Crystal data and structure refinement for **2c**, **3c**, and **4c**.

Compound	**2c**	**3c**	**4c**
Empirical formula	$C_{39}H_{63}BrFeGaO_{0.46}P_3Si_{0.94}$	$C_{48}H_{72}Br_{0.09}Ga_{1.33}Fe_{1.33}N_{2.5}P_4$	$C_{48}H_{78}FeGaN_2NaO_3P_3$
Formula weight	864.04	982.13	972.59
Temperature [K]	100	100	100
Crystal system	Trigonal	Orthorhombic	Trigonal
Space group	$P\bar{3}$	Pbca	R3
a [Å]	15.4998(10)	16.0652(9)	18.0650(6)
b [Å]	15.4998(10)	17.1911(9)	18.0650(6)
c [Å]	10.2411(8)	25.8976(16)	12.9480(5)
α [°]	90	90	90
β [°]	90	90	90
γ [°]	120	90	120
Volume [$Å^3$]	2130.7(3)	7152.4(7)	3659.4(3)
Z	2	6	3
ρ_{calc} [g/cm^3]	1.347	1.368	1.324
μ [mm^{-1}]	2.076	1.392	0.998
F (000)	902.0	3099.0	1551.0
Radiation	MoKα (λ = 0.71073)	MoKα (λ = 0.71073)	MoKα (λ = 0.71073)
Reflections collected	44998	70848	14861
Unique reflections	7570	7690	4777
Data/restraints/parameters	7570/0/160	7690/12/410	4777/1/182
R(int)	0.0399	0.0569	0.0278
R_1 ($I > 2\sigma(I)$)	0.0226	0.0279	0.0244
wR_2 (all data)	0.0472	0.0579	0.0488
GOOF	0.931	1.038	0.992

2.4.7. DFT Calculations

Table 2.8. Optimized coordinates [Å] for $P_3{}^BFe–N_2$ (**3a**) (Charge = 0, *S* = 1).

Fe	2.70616	3.79764	2.47086
P	4.27362	4.83320	3.97078
P	0.52514	4.50167	2.16771
P	3.67546	3.33833	0.42933
N	2.49594	2.20005	3.36777
C	4.68707	4.77245	-0.05521
C	4.25825	5.97881	0.55535
C	3.74100	6.57077	4.00421
C	2.69847	2.93605	-1.14467
H	1.97296	2.16455	-0.82721
C	1.64746	7.45552	-0.30846
H	2.60656	7.83181	-0.68076
C	1.63672	6.45850	0.69493
C	2.61797	8.32077	2.78714
H	2.10358	8.68703	1.89234
C	4.08049	4.24207	5.74709
H	4.61598	4.98008	6.37090
C	3.10421	6.99038	2.80533
C	-0.82530	6.53022	0.62000
H	-1.79596	6.18394	0.98941
C	0.05393	1.75929	1.42624
H	-0.16455	1.43960	2.45886
H	1.13989	1.65610	1.26759
H	-0.45808	1.06038	0.74061
C	6.17438	4.90086	3.89130
H	6.47084	3.83724	3.84135
C	4.85990	1.88458	0.51339
H	5.44243	1.87095	-0.42598
C	3.37999	8.73711	5.05998
H	3.47150	9.39843	5.92891
C	3.87846	7.42927	5.11377
H	4.34934	7.07398	6.03674
C	1.92546	4.16638	-1.64400
H	2.61929	4.96929	-1.94558
H	1.26154	4.58788	-0.87770
H	1.31212	3.89298	-2.52209
C	6.69657	5.61735	2.64052
H	6.35709	6.66539	2.61965
H	6.36260	5.14297	1.70963
H	7.80192	5.61458	2.64985

C	0.37447	5.97048	1.10300
C	5.80477	4.73563	-0.91362
H	6.14331	3.79010	-1.35064
C	-1.95471	3.28091	1.20735
H	-2.38434	2.56253	0.48516
H	-2.33645	4.27773	0.93775
H	-2.34800	3.01631	2.20402
C	6.51515	5.91232	-1.18657
H	7.39616	5.88474	-1.83753
C	-0.59694	4.89840	3.60770
H	-1.58270	5.13226	3.16206
B	2.95849	6.00245	1.51256
C	-0.41936	3.19602	1.15378
H	-0.10653	3.46171	0.12830
C	0.45944	7.98110	-0.83211
H	0.49895	8.75262	-1.61074
C	6.09654	7.12274	-0.60947
H	6.65273	8.04463	-0.81575
C	2.75102	9.18049	3.88663
H	2.34969	10.19914	3.83299
C	-0.76093	3.70758	4.56481
H	0.21039	3.38420	4.97065
H	-1.21891	2.83615	4.06853
H	-1.40626	3.98768	5.41723
C	2.61347	4.24834	6.18798
H	2.01143	3.56265	5.57184
H	2.17318	5.25554	6.10861
H	2.52943	3.92122	7.24052
C	4.98729	7.15032	0.24653
H	4.69698	8.09659	0.71875
C	3.55187	2.37396	-2.29701
H	2.89838	2.16870	-3.16474
H	4.06909	1.43389	-2.04615
H	4.30663	3.11056	-2.62128
C	5.83298	2.06947	1.68548
H	5.28104	2.12926	2.64136
H	6.42524	2.99194	1.57340
H	6.53364	1.21650	1.74809
N	2.31263	1.23848	3.93008
C	6.83271	5.54057	5.13106
H	7.93015	5.52685	4.99619
H	6.61443	5.01625	6.07508
H	6.52946	6.59637	5.23773
C	-0.07690	6.16610	4.30860

H	-0.70078	6.40079	5.18989
H	-0.09037	7.03342	3.62833
H	0.96470	6.03944	4.64593
C	4.08499	0.56102	0.64272
H	4.79195	-0.28633	0.71116
H	3.42044	0.37192	-0.21677
H	3.46688	0.55536	1.55534
C	-0.78380	7.54001	-0.34912
H	-1.71379	7.96997	-0.73642
C	4.73878	2.86646	5.96237
H	4.58321	2.53770	7.00646
H	5.82583	2.88837	5.77933
H	4.30236	2.09865	5.30455

Table 2.9. Optimized coordinates [Å] for $P_3{}^BFe–N_2^-$ (Charge = –1, S = ½).

Fe	-0.05319	-0.07911	-0.95871
P	2.16865	-0.57042	-0.69356
P	-1.96310	-1.10661	-0.54662
P	-0.43042	2.05641	-0.50154
N	-0.11336	-0.11189	-2.74703
C	0.39487	2.43226	1.09530
C	0.59932	1.26177	1.87566
C	2.18470	-1.65435	0.78428
C	-2.14552	2.86748	-0.19897
H	-2.75635	2.52382	-1.05454
C	-1.66170	-0.30022	3.38891
H	-0.92234	0.21293	4.01576
C	-1.37458	-0.51235	2.01889
C	0.97990	-2.24682	2.78882
H	0.14564	-2.09729	3.48398
C	2.85759	-1.69363	-2.05206
H	3.79874	-2.12557	-1.66570
C	1.09601	-1.39249	1.66411
C	-3.58527	-1.58221	1.82366
H	-4.34062	-2.09287	1.21733
C	-3.26616	0.27114	-2.68381
H	-3.00877	-0.46543	-3.46334
H	-2.41422	0.96314	-2.59972
H	-4.15425	0.83639	-3.02952
C	3.73372	0.51299	-0.45670
H	3.72250	1.17569	-1.34022
C	0.27583	3.33068	-1.70645

H	0.20830	4.33034	-1.23784
C	2.94257	-3.53462	2.14494
H	3.63623	-4.36783	2.31333
C	3.09491	-2.70305	1.02456
H	3.90878	-2.90360	0.31760
C	-2.78409	2.33828	1.09430
H	-2.19647	2.64398	1.97739
H	-2.84354	1.24241	1.11480
H	-3.80839	2.74305	1.20631
C	3.65801	1.38037	0.80405
H	3.59347	0.75221	1.70803
H	2.78498	2.04414	0.80604
H	4.56864	2.00592	0.88467
C	-2.38874	-1.11948	1.23974
C	0.83875	3.69452	1.53561
H	0.70218	4.58186	0.90614
C	-4.77640	-1.33885	-1.46521
H	-5.64914	-0.76441	-1.83446
H	-5.07296	-1.79950	-0.50997
H	-4.59247	-2.14991	-2.19124
C	1.50398	3.82053	2.76554
H	1.87486	4.79896	3.09467
C	-2.07766	-2.94645	-0.94114
H	-3.08453	-3.27785	-0.62217
B	0.06237	-0.17233	1.32380
C	-3.55868	-0.40575	-1.33511
H	-3.82124	0.38718	-0.61078
C	-2.86948	-0.71452	3.96745
H	-3.06254	-0.52543	5.03162
C	1.70649	2.67987	3.55902
H	2.23480	2.76838	4.51705
C	1.87812	-3.29805	3.02865
H	1.74152	-3.94562	3.90503
C	-1.91261	-3.21584	-2.44392
H	-0.96381	-2.79681	-2.81507
H	-2.72141	-2.76037	-3.03960
H	-1.90986	-4.30400	-2.64940
C	1.90503	-2.85805	-2.34248
H	0.92503	-2.48653	-2.67776
H	1.74425	-3.47603	-1.44376
H	2.31878	-3.50705	-3.13920
C	1.25651	1.42612	3.11715
H	1.45831	0.53807	3.73001
C	-2.17951	4.40655	-0.16481

H	-3.21612	4.74923	0.02489
H	-1.84815	4.87884	-1.10421
H	-1.55470	4.79659	0.65799
C	1.75219	3.03278	-1.99033
H	1.85932	2.01570	-2.40616
H	2.35514	3.09142	-1.06944
H	2.16530	3.75432	-2.72194
N	-0.15887	-0.17196	-3.88795
C	5.07344	-0.24838	-0.44047
H	5.89980	0.47842	-0.31554
H	5.27692	-0.81544	-1.36376
H	5.12118	-0.94632	0.41428
C	-1.02917	-3.68878	-0.09669
H	-1.00189	-4.76386	-0.35957
H	-1.24255	-3.59504	0.98088
H	-0.02438	-3.26394	-0.25849
C	-0.53649	3.32935	-3.01500
H	-0.13159	4.08176	-3.71988
H	-1.60234	3.56591	-2.85182
H	-0.48162	2.34401	-3.50570
C	-3.83057	-1.38029	3.18892
H	-4.77046	-1.72453	3.63782
C	3.17903	-0.88921	-3.32471
H	3.54660	-1.56668	-4.11986
H	3.95907	-0.12813	-3.14933
H	2.28312	-0.37743	-3.70952

Table 2.10. Optimized coordinates [Å] for $P_3^{Al}Fe–N_2$ (**3b**) (Charge = 0, *S* = 1).

Fe	2.72247	3.78850	2.43793
P	4.11750	4.93616	4.03355
P	0.54835	4.55294	2.04060
P	3.85029	3.31554	0.46463
N	2.48348	2.20010	3.35261
C	4.95798	4.60654	-0.22825
C	4.53768	5.93436	0.05261
C	3.64616	6.69671	4.19683
C	2.82270	2.89767	-1.07199
H	2.04701	2.20284	-0.70264
C	1.12587	7.89664	-0.21975
H	1.99049	8.41573	-0.65448
C	1.33134	6.75048	0.58095
C	2.93817	8.66513	2.99059

H	2.62785	9.16304	2.06282
C	3.98422	4.23084	5.77703
H	4.50523	4.95704	6.42591
C	3.28037	7.29450	2.96262
C	-1.10722	6.63211	0.90280
H	-1.98962	6.17417	1.36143
C	0.13205	1.80710	1.26670
H	-0.17336	1.47414	2.27201
H	1.22711	1.70336	1.20201
H	-0.31799	1.11564	0.53184
C	6.01403	5.04573	3.91863
H	6.33878	3.99099	3.86909
C	4.94303	1.80019	0.64371
H	5.53350	1.71635	-0.28641
C	3.29573	8.78412	5.39263
H	3.28627	9.35384	6.32894
C	3.65973	7.43073	5.40128
H	3.93906	6.95849	6.34937
C	2.14005	4.16331	-1.61883
H	2.88132	4.83664	-2.08199
H	1.62861	4.74317	-0.83440
H	1.39474	3.88856	-2.38681
C	6.48651	5.75897	2.64780
H	6.08221	6.78362	2.58964
H	6.18191	5.22816	1.73851
H	7.58949	5.82605	2.64909
C	0.18722	6.10193	1.10465
C	6.09641	4.34487	-1.01902
H	6.42796	3.31904	-1.21375
C	-1.85828	3.32972	0.93357
H	-2.24652	2.57727	0.22253
H	-2.21732	4.31323	0.59687
H	-2.30685	3.11147	1.91833
C	6.83248	5.41267	-1.55124
H	7.72938	5.21338	-2.14848
C	-0.55099	4.78836	3.53731
H	-1.55116	5.03512	3.13437
Al	3.03658	6.08305	1.36937
C	-0.32301	3.24591	0.96904
H	0.04936	3.51733	-0.03470
C	-0.15854	8.40246	-0.46318
H	-0.29545	9.29536	-1.08492
C	6.41794	6.73366	-1.31614
H	6.99368	7.56701	-1.73551

C	2.93880	9.40364	4.18376
H	2.64505	10.45990	4.17922
C	-0.68196	3.52529	4.39940
H	0.30164	3.15275	4.72311
H	-1.18559	2.70723	3.85823
H	-1.27493	3.74238	5.30642
C	2.53302	4.14359	6.26298
H	1.94159	3.45888	5.63686
H	2.04015	5.12873	6.25153
H	2.50487	3.76102	7.29975
C	5.28327	6.98290	-0.52839
H	4.99429	8.02518	-0.33658
C	3.61176	2.21125	-2.20106
H	2.93565	2.02462	-3.05538
H	4.04496	1.24179	-1.90643
H	4.42712	2.86212	-2.56159
C	5.90826	2.00668	1.82014
H	5.34293	2.13937	2.76120
H	6.54067	2.89799	1.67167
H	6.57158	1.13076	1.94187
N	2.25224	1.24732	3.91030
C	6.66289	5.71184	5.14793
H	7.75784	5.74547	4.99984
H	6.47745	5.17577	6.09292
H	6.31069	6.75124	5.26316
C	-0.03492	6.00834	4.32143
H	-0.63424	6.15984	5.23686
H	-0.08661	6.92681	3.71351
H	1.01840	5.87677	4.61514
C	4.11733	0.51398	0.81571
H	4.79255	-0.35844	0.88941
H	3.43170	0.33392	-0.02904
H	3.51519	0.54650	1.73663
C	-1.27599	7.77925	0.11755
H	-2.28031	8.18779	-0.04149
C	4.71361	2.87995	5.90313
H	4.56905	2.47128	6.92041
H	5.79846	2.97475	5.73422
H	4.32546	2.13620	5.18980

Table 2.11. Optimized coordinates [Å] for $P_3{}^{Al}Fe–N_2^-$ (Charge = –1, S = ½).

Fe	-0.02207	0.02174	-1.07949

P	-2.05990	-0.83060	-0.71872
Al	-0.03626	-0.20269	1.38407
N	-0.01424	0.29080	-2.84380
N	-0.01612	0.43587	-3.97899
C	-3.62210	-3.29849	-0.79420
H	-4.10105	-3.07574	0.17562
H	-3.58651	-4.40048	-0.90128
H	-4.27439	-2.91046	-1.59442
C	-1.94175	-0.47429	2.00184
C	-2.46888	-0.36806	3.30702
H	-1.78240	-0.26032	4.15893
C	-3.85177	-0.35175	3.55191
H	-4.23340	-0.23903	4.57543
C	-3.42713	-0.36813	-1.94728
H	-4.38020	-0.77940	-1.56374
C	-2.19108	-2.73366	-0.83813
H	-1.74630	-2.96104	-1.82397
C	-3.55848	1.15667	-2.03703
H	-3.81391	1.60004	-1.06047
H	-4.34954	1.43918	-2.75882
H	-2.60547	1.59715	-2.37765
C	-2.87247	-0.60679	0.93415
C	-4.75115	-0.45457	2.47920
H	-5.83336	-0.42460	2.66043
C	-1.34254	-3.41354	0.24230
H	-0.29752	-3.07940	0.21123
H	-1.35871	-4.51228	0.10830
H	-1.72647	-3.18397	1.25135
C	-3.16508	-0.97104	-3.33900
H	-2.19880	-0.63188	-3.74285
H	-3.95577	-0.64887	-4.04434
H	-3.16094	-2.07486	-3.32815
C	-4.26288	-0.59427	1.17094
H	-4.97786	-0.67793	0.34364
P	1.92298	-1.07750	-0.69824
C	4.82982	-1.30697	-0.47933
H	4.78231	-1.99557	0.38226
H	5.78352	-0.74845	-0.40322
H	4.87742	-1.91091	-1.40082
C	1.14568	-1.77210	1.85541
C	1.14810	-2.55992	3.02715
H	0.55675	-2.23641	3.89538
C	1.84765	-3.77535	3.10540
H	1.80699	-4.38187	4.02013

C	2.30938	-2.23223	-2.15000
H	3.09028	-2.93930	-1.81397
C	3.65573	-0.31363	-0.45496
H	3.75529	0.37015	-1.31522
C	1.05986	-3.04428	-2.51885
H	0.71714	-3.65762	-1.66888
H	1.26992	-3.72200	-3.36863
H	0.23528	-2.37078	-2.81107
C	1.92569	-2.23369	0.75916
C	2.57976	-4.23072	1.99727
H	3.10775	-5.19129	2.03911
C	3.71944	0.51143	0.83647
H	2.95797	1.30197	0.86234
H	4.71453	0.98620	0.93396
H	3.55558	-0.12765	1.72129
C	2.85035	-1.45435	-3.36225
H	2.14253	-0.67581	-3.68668
H	3.00679	-2.14374	-4.21443
H	3.81851	-0.96916	-3.14930
C	2.63069	-3.45361	0.82932
H	3.20908	-3.82060	-0.02676
P	0.12637	2.18848	-0.44325
C	-1.11999	4.80662	0.04768
H	-0.54778	4.96179	0.97934
H	-2.07825	5.35143	0.15382
H	-0.56327	5.28090	-0.77758
C	0.74170	1.49491	2.14510
C	1.27323	1.69463	3.43770
H	1.13732	0.91615	4.20242
C	2.01480	2.84083	3.76849
H	2.44064	2.95628	4.77384
C	1.07967	3.31663	-1.63232
H	1.26480	4.26400	-1.09189
C	-1.40464	3.31012	-0.17626
H	-1.97049	3.19530	-1.11685
C	2.43920	2.69535	-1.97792
H	3.05243	2.55465	-1.07233
H	3.00099	3.34625	-2.67626
H	2.30033	1.70959	-2.45456
C	0.94929	2.52519	1.18718
C	2.23337	3.83136	2.79805
H	2.82869	4.72085	3.04024
C	-2.27077	2.79023	0.97667
H	-2.54577	1.73683	0.84047

H	-3.20327	3.38064	1.05408
H	-1.73591	2.86639	1.93994
C	0.27980	3.65010	-2.90488
H	0.04946	2.74560	-3.48692
H	0.87328	4.32515	-3.55275
H	-0.67185	4.16058	-2.68037
C	1.68949	3.68108	1.51287
H	1.86827	4.46477	0.76739

Table 2.12. Optimized coordinates [Å] for $P_3^{Ga}Fe–N_2$ (**3c**) (Charge = 0, *S* = 1).

Fe	2.72596	3.80343	2.43712
P	4.11595	4.93887	4.05084
P	0.53314	4.53458	2.02381
P	3.85460	3.32180	0.45868
N	2.48677	2.21779	3.34083
C	4.96413	4.61211	-0.23492
C	4.55844	5.94057	0.04638
C	3.66007	6.70481	4.21189
C	2.81854	2.91229	-1.07351
H	2.05275	2.20558	-0.70581
C	1.12031	7.91359	-0.19036
H	1.98896	8.45273	-0.59013
C	1.31615	6.75976	0.59756
C	2.97575	8.68487	3.00559
H	2.67477	9.18498	2.07635
C	3.97709	4.24170	5.79568
H	4.49896	4.96696	6.44517
C	3.30357	7.31355	2.98451
C	-1.12049	6.58968	0.84393
H	-2.00772	6.11027	1.26963
C	0.13324	1.78518	1.27437
H	-0.15437	1.45655	2.28640
H	1.22870	1.69603	1.19613
H	-0.31733	1.08216	0.55085
C	6.01127	5.03497	3.92946
H	6.32803	3.97762	3.88201
C	4.94470	1.80455	0.62871
H	5.53785	1.72213	-0.29981
C	3.33103	8.79670	5.40857
H	3.32752	9.36525	6.34553
C	3.68003	7.43915	5.41614
H	3.95414	6.96352	6.36399

C	2.11835	4.17561	-1.60242
H	2.85210	4.87505	-2.03793
H	1.58192	4.72490	-0.81420
H	1.39228	3.90237	-2.38926
C	6.48237	5.74049	2.65393
H	6.08781	6.76882	2.59630
H	6.16488	5.21117	1.74834
H	7.58605	5.79594	2.64685
C	0.17610	6.08001	1.08052
C	6.09930	4.34863	-1.02961
H	6.42438	3.32180	-1.22948
C	-1.88165	3.27766	0.95953
H	-2.26930	2.51012	0.26452
H	-2.26125	4.25060	0.61550
H	-2.31216	3.06618	1.95365
C	6.84012	5.41422	-1.56011
H	7.73373	5.21160	-2.16101
C	-0.55842	4.78953	3.52222
H	-1.56020	5.03757	3.12391
Ga	3.05151	6.10628	1.37155
C	-0.34468	3.21583	0.97264
H	0.00889	3.48311	-0.03912
C	-0.16603	8.39803	-0.46682
H	-0.30043	9.29704	-1.08017
C	6.43467	6.73648	-1.31833
H	7.01410	7.56849	-1.73528
C	2.98249	9.42151	4.20030
H	2.70063	10.48105	4.19564
C	-0.68491	3.53505	4.39760
H	0.30120	3.16460	4.71641
H	-1.19385	2.71225	3.86885
H	-1.26964	3.76222	5.30748
C	2.52285	4.16137	6.27446
H	1.93410	3.47415	5.64830
H	2.03221	5.14760	6.25407
H	2.48746	3.78489	7.31323
C	5.30351	6.99048	-0.52641
H	5.01910	8.03200	-0.32696
C	3.60693	2.24500	-2.21446
H	2.92479	2.05083	-3.06225
H	4.05987	1.28176	-1.92899
H	4.40730	2.91136	-2.57998
C	5.90712	2.00494	1.80888
H	5.33927	2.13763	2.74844

H	6.54327	2.89427	1.66460
H	6.56689	1.12635	1.93062
N	2.27084	1.26355	3.90329
C	6.66935	5.70048	5.15406
H	7.76431	5.72281	5.00355
H	6.48034	5.17072	6.10191
H	6.32732	6.74376	5.26504
C	-0.02942	6.01368	4.29149
H	-0.62059	6.17684	5.21020
H	-0.08022	6.92713	3.67593
H	1.02546	5.87774	4.57841
C	4.11522	0.51985	0.79445
H	4.78808	-0.35383	0.87434
H	3.43676	0.34072	-0.05623
H	3.50536	0.55424	1.71043
C	-1.28784	7.74418	0.06881
H	-2.29489	8.13445	-0.11619
C	4.69913	2.88743	5.92786
H	4.55094	2.48359	6.94653
H	5.78472	2.97559	5.75996
H	4.30746	2.14317	5.21694

Table 2.13. Optimized coordinates [Å] for $P_3{}^{Ga}Fe–N_2^-$ (Charge = –1, *S* = ½).

Ga	0.04761	-0.20997	1.33001
Fe	0.01185	0.04111	-1.13410
P	-1.94450	-1.06259	-0.76543
C	-4.84853	-1.28552	-0.51312
H	-4.91097	-1.87369	-1.44383
H	-4.79162	-1.98850	0.33617
H	-5.79885	-0.72476	-0.41446
C	-3.67097	-0.29659	-0.48922
H	-3.77936	0.40011	-1.33792
C	-1.10805	-3.01444	-2.61030
H	-0.28045	-2.34351	-2.89914
H	-0.76428	-3.64061	-1.77014
H	-1.32803	-3.68016	-3.46710
C	-1.82522	-3.82130	2.99755
H	-1.77350	-4.44405	3.90081
C	-2.57563	-4.25339	1.89261
H	-3.10799	-5.21182	1.92512
C	-2.35026	-2.19893	-2.22383
H	-3.13313	-2.90499	-1.89055

C	-1.12254	-2.60665	2.93165
H	-0.51774	-2.29756	3.79532
C	-1.13890	-1.80313	1.77338
C	-3.71322	0.50967	0.81489
H	-3.53632	-0.14227	1.68762
H	-2.95075	1.29901	0.83968
H	-4.70638	0.98351	0.93476
C	-2.63918	-3.45557	0.73908
H	-3.23154	-3.80547	-0.11459
C	-1.93007	-2.23760	0.67819
C	-2.89553	-1.40371	-3.42299
H	-3.85635	-0.91085	-3.19475
H	-2.18323	-0.62934	-3.74757
H	-3.06792	-2.08312	-4.28005
N	-0.00820	0.30260	-2.89210
N	-0.01444	0.44850	-4.02763
P	2.06683	-0.80093	-0.81239
C	3.61641	-3.27344	-0.92329
H	4.26906	-2.87492	-1.71808
H	4.09762	-3.06816	0.04924
H	3.57618	-4.37339	-1.04808
C	2.18790	-2.70197	-0.95661
H	1.74042	-2.91230	-1.94535
C	3.55360	1.20037	-2.11638
H	2.59800	1.64385	-2.44578
H	3.81474	1.63237	-1.13626
H	4.33984	1.49215	-2.83967
C	3.89554	-0.37999	3.45128
H	4.28650	-0.27987	4.47262
C	4.78458	-0.46989	2.36906
H	5.86841	-0.44315	2.54036
C	3.42434	-0.32582	-2.04397
H	4.38026	-0.74017	-1.67089
C	2.50998	-0.39389	3.21992
H	1.82933	-0.29855	4.07743
C	1.97802	-0.48346	1.91794
C	1.33647	-3.39176	0.11503
H	1.71728	-3.17223	1.12742
H	0.29193	-3.05694	0.08404
H	1.35342	-4.48918	-0.02978
C	4.28374	-0.59268	1.06367
H	4.99100	-0.66730	0.22897
C	2.89162	-0.60084	0.83822
C	3.15647	-0.91194	-3.44190

H	3.14720	-2.01579	-3.44364
H	2.19126	-0.56358	-3.84068
H	3.94804	-0.58546	-4.14427
P	-0.13544	2.20655	-0.49153
C	1.11677	4.81753	0.02229
H	0.55669	5.30263	-0.79449
H	0.54964	4.96240	0.95870
H	2.07662	5.35927	0.13021
C	1.39762	3.32377	-0.22217
H	1.95624	3.22056	-1.16833
C	-2.45817	2.72490	-2.00192
H	-2.32220	1.74106	-2.48361
H	-3.06558	2.58027	-1.09301
H	-3.02424	3.37837	-2.69438
C	-2.00263	2.82333	3.73866
H	-2.42514	2.93052	4.74636
C	-2.22322	3.82185	2.77720
H	-2.81652	4.71003	3.02858
C	-1.09616	3.34448	-1.66259
H	-1.27676	4.29083	-1.11879
C	-1.26208	1.67926	3.39695
H	-1.12151	0.89355	4.15265
C	-0.73822	1.49649	2.10125
C	2.27111	2.78623	0.91709
H	1.74364	2.85091	1.88521
H	2.54201	1.73405	0.76464
H	3.20575	3.37331	0.99537
C	-1.68380	3.68129	1.48883
H	-1.86420	4.47138	0.75055
C	-0.94628	2.52782	1.14910
C	-0.30251	3.67726	-2.93924
H	0.64882	4.19036	-2.71895
H	-0.07206	2.77118	-3.51927
H	-0.89964	4.34908	-3.58708

2.5. References

(1) Yandulov, D. V.; Schrock, R. R. *Science* **2003**, *301*, 76.

(2) Arashiba, K.; Miyake, Y.; Nishibayashi, Y. *Nat. Chem.* **2011**, *3*, 120.

(3) Anderson, J. S.; Rittle, J.; Peters, J. C. *Nature* **2013**, *501*, 84.

(4) For a recent review, see: Chalkley, M. J.; Drover, M. W.; Peters, J. C. *Chem. Rev.* **2020**. DOI: 10.1021/acs.chemrev.9b00638.

(5) For representative examples, see: (a) Tanaka, H.; Arashiba, K.; Kuriyama, S.; Sasada, A.; Nakajima, K.; Yoshizawa, K.; Nishibayashi, Y. *Nat. Commun.* **2014**, *5*, 3737. (b) Kuriyama, S.; Arashiba, K.; Nakajima, K.; Tanaka, H.; Kamaru, N.; Yoshizawa, K.; Nishibayashi, Y. *J. Am. Chem. Soc.* **2014**, *136*, 9719. (c) Arashiba, K.; Kinoshita, E.; Kuriyama, S.; Eizawa, A.; Nakajima, K.; Tanaka, H.; Yoshizawa, K.; Nishibayashi, Y. *J. Am. Chem. Soc.* **2015**, *137*, 5666. (d) Eizawa, A.; Arashiba, K.; Tanaka, H.; Kuriyama, S.; Matsuo, Y.; Nakajima, K.; Yoshizawa, K.; Nishibayashi, Y. *Nat. Commun.* **2017**, *8*, 14874. (e) Arashiba, K.; Eizawa, A.; Tanaka, H.; Nakajima, K.; Yoshizawa, K.; Nishibayashi, Y. *Bull. Chem. Soc. Jpn.* **2017**, *90*, 1111. (f) Itabashi, T.; Mori, I.; Arashiba, K.; Eizawa, A.; Nakajima, K.; Nishibayashi, Y. *Dalton Trans.* **2019**, *48*, 3182. (g) Ashida, Y.; Arashiba, K.; Nakajima, K.; Nishibayashi, Y. *Nature* **2019**, *568*, 536.

(6) Sekiguchi, Y.; Arashiba, K.; Tanaka, H.; Eizawa, A.; Nakajima, K.; Yoshizawa, K.; Nishibayashi, Y. *Angew. Chem. Int. Ed.* **2018**, *57*, 9064.

(7) Kuriyama, S.; Arashiba, K.; Tanaka, H.; Matsuo, Y.; Nakajima, K.; Yoshizawa, K.; Nishibayashi, Y. *Angew. Chem. Int. Ed.* **2016**, *55*, 14291.

(8) Fajardo Jr., J.; Peters, J. C. *J. Am. Chem. Soc.* **2017**, *139*, 16105.

(9) Creutz, S. E.; Peters, J. C. *J. Am. Chem. Soc.* **2014**, *136*, 1105.

(10) Del Castillo, T. J.; Thompson, N. B.; Peters, J. C. *J. Am. Chem. Soc.* **2016**, *138*, 5341.

(11) Chalkley, M. J.; Del Castillo, T. J.; Matson, B. D.; Roddy, J. P.; Peters, J. C. *ACS Cent. Sci.* **2017**, *3*, 217.

(12) Matson, B. D.; Peters, J. C. *ACS Catal.* **2018**, *8*, 1448.

(13) Chalkley, M. J.; Del Castillo, T. J.; Matson, B. D.; Peters, J. C. *J. Am. Chem. Soc.* **2018**, *140*, 6122.

(14) Moret, M.-E.; Peters, J. C. *Angew. Chem. Int. Ed.* **2011**, *50*, 2063.

(15) Moret, M.-E.; Peters, J. C. *J. Am. Chem. Soc.* **2011**, *133*, 18118.

(16) Anderson, J. S.; Moret, M.-E.; Peters, J. C. *J. Am. Chem. Soc.* **2013**, *135*, 534.

(17) Anderson, J. S.; Cutsail, G. E.; Rittle, J.; Connor, B. A.; Gunderson, W. A.; Zhang, L.; Hoffman, B. M.; Peters, J. C. *J. Am. Chem. Soc.* **2015**, *137*, 7803.

(18) Thompson, N. B.; Green, M. T.; Peters, J. C. *J. Am. Chem. Soc.* **2017**, *139*, 1531.

(19) Thompson, N. B.; Oyala, P. H.; Dong, H. T.; Chalkley, M. J.; Zhao, J.; Alp, E. E.; Hu, M.; Lehnert, N.; Peters, J. C. *Inorg. Chem.* **2019**, *58*, 3535.

(20) Nesbit, M. A.; Oyala, P. H.; Peters, J. C. *J. Am. Chem. Soc.* **2019**, *141*, 8116.

(21) Sircoglou, M.; Saffon, N.; Miqueu, K.; Bouhadir, G.; Bourissou, D. *Organometallics* **2013**, *32*, 6780.

(22) Sircoglou, M.; Mercy, M.; Saffon, N.; Coppel, Y.; Bouhadir, G.; Maron, L.; Bourissou, D. *Angew. Chem. Int. Ed.* **2009**, *48*, 3454.

(23) Sircoglou, M.; Bontemps, S.; Bouhadir, G.; Saffon, N.; Miqueu, K.; Gu, W.; Mercy, M.; Chen, C.-H.; Foxman, B. M.; Maron, L.; Ozerov, O. V.; Bourissou, D. *J. Am. Chem. Soc.* **2008**, *130*, 16729.

(24) Rudd, P. A.; Liu, S.; Gagliardi, L.; Young, V. G.; Lu, C. C. *J. Am. Chem. Soc.* **2011**, *133*, 20724.

(25) Rudd, P. A.; Planas, N.; Bill, E.; Gagliardi, L.; Lu, C. C. *Eur. J. Inorg. Chem.* **2013**, *2013*, 3898.

(26) Cordero, B.; Gómez, V.; Platero-Prats, A. E.; Revés, M.; Echeverría, J.; Cremades, E.; Barragán, F.; Alvarez, S. *Dalton Trans.* **2008**, 2832.

(27) Derrah, E. J.; Sircoglou, M.; Mercy, M.; Ladeira, S.; Bouhadir, G.; Miqueu, K.; Maron, L.; Bourissou, D. *Organometallics* **2011**, *30*, 657.

(28) Fong, H.; Moret, M.-E.; Lee, Y.; Peters, J. C. *Organometallics* **2013**, *32*, 3053.

(29) Brookhart, M.; Grant, B.; Volpe, A. F. *Organometallics* **1992**, *11*, 3920.

(30) Weitz, I. S.; Rabinovitz, M. *J. Chem. Soc., Perkin Trans. 1* **1993**, 117.

(31) Vicente, J.; Chicote, M.-T.; Guerrero, R.; Jones, P. G. *J. Chem. Soc., Dalton Trans.* **1995**, 1251.

(32) Robbins, J. L.; Edelstein, N.; Spencer, B.; Smart, J. C. *J. Am. Chem. Soc.* **1982**, *104*, 1882.

(33) Evans, D. F. *J. Chem. Soc.* **1959**, 2003.

(34) Dolomanov O. V.; Bourhis, L. J.; Gildea, R. J.; Howards, J. A. K.; Puschmann, H. *J. Appl. Cryst.* **2009**, *42*, 339.

(35) Sheldrick, G. M. *Acta Cryst. A.* **2015**, *71*, 3.

(36) Sheldrick, G. M. *Acta Cryst. A.* **2008**, *64*, 112.

(37) Neese, F. *Wiley Interdiscip. Rev.: Comput. Mol. Sci.* **2012**, *2*, 73.

(38) Grimme, S.; Antony, J.; Ehrlich, S.; Krieg, H. *J. Chem. Phys.* **2010**, *132*, 154104.

(39) Tao, J.; Perdew, J. P.; Staroverov, V. N.; Scuseria, G. E. *Phys. Rev. Lett.* **2003**, *91*, 146401.

(40) Weigend, F.; Ahlrichs, R. *Phys. Chem. Chem. Phys.* **2005**, *7*, 3297.

(41) Weatherburn, M. W. *Anal. Chem.* **1967**, *39*, 971.

(42) Watt, G.W.; Crisp, J. D. *Anal Chem.* **1952**, *24*, 2006.

Chapter 3

Catalytic Nitrogen-to-Ammonia Conversion by Osmium and Ruthenium Complexes

Reproduced with permission from:

Fajardo Jr., J.; Peters, J. C. Catalytic Nitrogen-to-Ammonia Conversion by Osmium and Ruthenium Complexes. *J. Am. Chem. Soc.* **2017**, *139* (45), 16105−16108. DOI: 10.1021/jacs.7b10204.

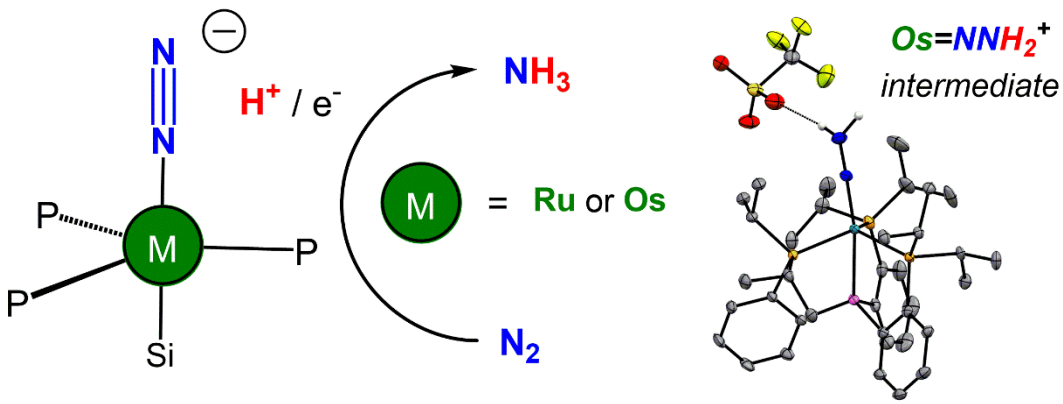

Abstract

Despite the critical role Ru and Os complexes have played in the development of transition metal dinitrogen chemistry, they have not been shown to mediate catalytic N_2-to-NH_3 conversion (N_2RR), nor have M–N_xH_y complexes been derived from protonation of their M–N_2 precursors. To help delineate factors for N_2RR catalysis, we report on isostructural tris(phosphino)silyl Ru and Os complexes that mediate catalytic N_2RR, and compare their activities with an isostructural Fe complex. The Os system is most active, and liberates more than 120 equiv NH_3 per Os center in a single batch experiment using Cp^*_2Co and $[H_2NPh_2][OTf]$ as reductant and acid source. Isostructural Ru and Fe complexes generate little NH_3 under the same conditions. Protonation of **[Os]**–N_2^- affords a structurally characterized **[Os]**=NNH_2^+ hydrazido species that mediates NH_3 generation, suggesting it is a plausible intermediate of the catalysis. Inactive Os hydrides are characterized that form during catalysis.

3.1. Introduction

Synthetic Mo and Fe model systems have been identified as catalysts for N_2-to-NH_3 conversion (N_2RR).[1,2] The development of these catalytic systems has in part been motivated by the role(s) these metals may play in biological nitrogen fixation, and the desire to test various mechanistic hypotheses using well defined inorganic model complexes.[3] In contrast, synthetic models based on metals other than Fe or Mo that display efficacy for catalytic N_2RR are limited to two cobalt systems; both use a combination of strong acid and reductant in the form of $[H(OEt_2)_2][BAr^F{}_4]$ ($HBAr^F{}_4$, $BAr^F{}_4{}^-$ = tetrakis(3,5-bis-(trifluoromethyl)phenyl)borate) and KC_8.[4]

The heavier group 8 elements Ru and Os have played a significant role in the history and development of ammonia synthesis and M–N_2 model chemistry. For example, an active heterogeneous Ru catalyst is used in the Kellog Advanced Ammonia Process (KAAP),[5] and the first metal-dinitrogen complex discovered featured ruthenium ($((NH_3)_5Ru–N_2{}^{2+}$).[6] Achievements in Ru and Os model chemistry have included (1) demonstration of terminal nitride ($M{\equiv}N^{[3/2+]}$) coupling to form (isolable or transient) N_2-bridged bimetallics of the type $L_nM–N_2–ML_n{}^{[6/5/4+]}$ (M = Ru or Os);[7,8] (2) photochemically induced homolytic N_2 cleavage to generate terminal Os≡N products;[9] (3) selective protonation and hydrogenation of terminal osmium nitrides to generate NH_3;[10] and (4) stepwise NH_3 oxidation to N_2 via diimide (HN=NH) and hydrazine (N_2H_4) intermediates at cofacial Ru porphyrins.[11]

Despite these advances, there remain no examples of synthetic Ru or Os complexes that demonstrate stepwise protonation of M–N_2 to generate M–N_xH_y species, or that catalyze N_2RR.[12] The study of a homologous, isostructural series of complexes (Fe, Ru, Os) will help to delineate important factors for N_2RR catalyst design.

A limitation with respect to achieving N_2RR catalysis by either Ru or Os is that low-valent redox states (< 2+) can be difficult to access for these metals.[13] In systems where such states may be accessed, it is common for the electron(s) to be ligand- rather than metal-localized; this is especially true of d^7 systems.[14] For M–N_2 species, this should in turn lead to a less activated, and thereby less readily functionalized, N_2 ligand. One notable exception are **[M]**–$N_2^{[0/1-]}$ redox pairs (M = Ru, Os; Figure 3.1) reported by our group, where utilization of a rigid, chelating tris(phosphine)silyl ligand permits access to low-valent M(I) and M(0) terminal dinitrogen compounds.[14a] These species exhibit *ν*(NN) stretching frequencies suggestive of highly activated, terminally bonded N_2 ligands. To our knowledge, [K(THF)$_2$][P_3^{Si}Os–N_2] (abbreviated hereafter as **[Os]**–N_2^-) exhibits the lowest *ν*(NN) stretching frequency (1931 cm^{-1}) known for a terminal N_2 adduct of Ru or Os (Figure 3.1).[14a]

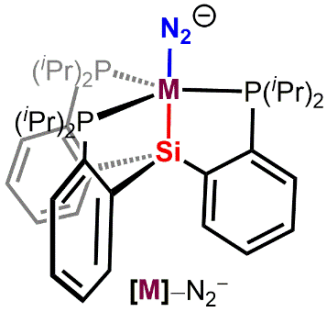

M	ν(NN) (cm^{-1})	*E* (V)
Os	1931	-1.94
Ru	1960	-2.14
Fe	1920	-2.2
		(vs $Fc^{[1+/0]}$)

Figure 3.1. Ruthenium and osmium N_2RR catalysts studied herein and the pertinent physical data from refs 14a and 18.

Herein, we establish that [K(THF)$_2$][P_3^{Si}Ru–N_2] (**[Ru]**–N_2^-) and **[Os]**–N_2^- complexes mediate catalytic N_2RR. **[Os]**–N_2^- is especially competent in the presence of Cp*$_2$Co and mild acids. Moreover, the N_2 ligand of **[Os]**–N_2^- can be protonated to afford a structurally characterized **[Os]**=NNH_2^+ hydrazido complex, a likely intermediate by analogy to related **[Fe]**=NNH_2^+ species

implicated as intermediates of N_2RR by our lab.[15] Catalytically inactive Os-hydride species are characterized that appear to form as thermodynamic sinks of the spent catalyst system.

3.2. Results and Discussion

The N_2RR performance of **[Ru]**–N_2^- and **[Os]**–N_2^- was initially canvassed under conditions similar to those studied in the context of N_2RR by related iron systems (46 equiv $HBAr^F_4$, 50 equiv KC_8, 1 atm N_2, Et_2O, −78 °C).[2a-d] **[Os]**–N_2^- affords 1.6 ± 0.3 equiv of NH_3 (Table 3.1, entry 1) under these conditions, exceeding that observed for [Na(12-crown-4)$_2$][P_3^{Si}Fe–N_2] (**[Fe]**–N_2^-; entry 2). **[Ru]**–N_2^- performs better under these conditions (entry 3), affording 4.3 ± 0.3 equiv of NH_3 (28% selectivity for NH_3 based on H^+), confirming N_2RR catalysis with Ru is viable. Related tripodal, tetra(phosphine) Ru(0) dinitrogen complexes have not shown selective reactivity at the coordinated N_2 ligand; the weak acids canvassed (e.g., 2,6-lutidinium tetrafluoroborate) tend to react at the metal center to yield oxidized $[Ru(N_2)(H)]^+$ products, whereas stronger acids (e.g., HCl, HOTf) protonate at the phosphine ligand.[16]

With these results in hand, we next canvassed milder reagents.[2f,17] Thus, treatment of a suspension of **[Os]**–N_2^- in Et_2O at −78 °C with 46 equiv of $[H_2NPh_2]$[OTf] and 50 equiv of Cp^*_2Co results in the generation of 7.1 ± 0.6 equiv of NH_3 per Os (Table 3.1, entry 6; 46% based on acid). An identical catalytic run performed under an $^{14}N_2$ atmosphere using $[H_2{}^{15}NPh_2]$[OTf] yields only $[^{14}NH_4]$[Cl], confirming NH_3 formed is derived from the N_2 atmosphere. Attempts to use either $[(\eta^6\text{-}C_6H_6)Os(Cl)(\mu\text{-}Cl)]_2$ or **[Os]**–Cl as the (pre)catalyst generates only < 0.1 and 2.5 equiv of NH_3, respectively. For comparison, **[Fe]**–N_2^-, whose **[Fe]**–$N_2^{[0/1-]}$ redox couple (−2.2 V vs $Fc^{[1+/0]}$) is shifted ∼220 mV cathodically from that of $Cp^*_2Co^{[1+/0]}$,[18] generates only stoichiometric

quantities of NH_3 under analogous conditions (entry 4); likewise, **[Ru]**–N_2^- (E = −2.14 V vs $Fc^{[1+/0]}$, Figure 3.1)[14a] shows poor N_2RR performance (entry 5).

Os-catalyzed N_2RR proceeded in the presence of correspondingly weaker and stronger anilinium acids with unperturbed yields for NH_3 production. For example, replacing

Table 3.1. N_2RR mediated by **[M]**–N_2^- complexes.[a]

Entry	Catalyst	Acid (equiv)	Reductant (equiv)	NH_3/M (equiv)	Yield NH_3/H^+ (%)
1[b]	**[Fe]**−N_2^-	46[c]	50[d]	0.8 ± 0.5	4.7 ± 2.9
2	**[Ru]**−N_2^-	46[c]	50[d]	4.3 ± 0.3	28 ± 2
3	**[Os]**−N_2^-	46[c]	50[d]	1.6 ± 0.3	10 ± 2
4	**[Fe]**−N_2^-	46[e]	50[f]	1.4 ± 0.3	9.3 ± 1.8
5	**[Ru]**−N_2^-	46[e]	50[f]	0.8 ± 0.5	4.9 ± 3.5
6	**[Os]**−N_2^-	46[e]	50[f]	7.1 ± 0.6	46 ± 4
7	**[Os]**−N_2^-	150[e]	180[f]	18 ± 1	35 ± 1
8	**[Os]**−N_2^-	500[e]	600[f]	50 ± 3	30 ± 2
9	**[Os]**−N_2^-	800[e]	960[f]	86 ± 5	32 ± 2
10	**[Os]**−N_2^-	1500[e]	1800[f]	120 ± 11	24 ± 2
11	**[Os]**−N_2^-	46[g]	50[f]	7.9 ± 0.3	52 ± 2
12	**[Os]**−N_2^-	46[h]	50[f]	7.9	52
13	**[Os]**−N_2^-	46[i]	50[f]	6.3 ± 0.5	41 ± 3
14	**[Os]**−N_2^-	46[j]	50[f]	0.1 ± 0.1	0.8 ± 0.2
15	**[Os]**−N_2^-	46[k]	50[f]	1.2 ± 0.1	7.6 ± 0.8
16	**[Os]**−N_2^-	46[l]	50[f]	0.7 ± 0.1	4.6 ± 0.7

[a]Catalyst, acid, reductant, and Et_2O sealed in a Schlenk tube at −196°C under an N_2 atmosphere, warmed to −78 °C, and stirred. For runs utilizing $HBAr^F_4$, reactions were stirred at −78 °C for 1 hour, followed by stirring at room temperature for 45 minutes. For other runs, reactions were allowed to stir and warm to room temperature overnight. [b]From ref 2a. [c]$HBAr^F_4$. [d]KC_8. [e]$[H_2NPh_2][OTf]$. [f]Cp^*_2Co. [g]$[H_3NPh][OTf]$. [h]$[H_3N\text{-}2,5\text{-}Cl_2C_6H_3][OTf]$. [i][*N*-Me-$H_2NPh$][OTf]. [j]$[H_2NPh_2][BAr^F_4]$. [k]$[H_3NPh][BAr^F_4]$. [l]HOTf.

$[H_2NPh_2][OTf]$ with either $[H_3NPh][OTf]$ or $[H_3N\text{-}2,5\text{-}Cl_2C_6H_3][OTf]$ affords 7.9 equiv of NH_3 per Os, respectively (Table 3.1, entries 11 and 12). [*N*-Me-$H_2NPh][OTf]$ gives a diminished yield (6.3 ± 0.5 equiv of NH_3 per Os; entry 13). These observations contrast with $P_3^BFe{-}N_2^-$, where selectivity is diminished when using $[H_3NPh][OTf]$ compared to $[H_2NPh_2][OTf]$.[2f]

Attempts to replace Cp^*_2Co with weaker metallocene reductants, such as cobaltocene (Cp_2Co) or decamethylchromocene (Cp^*_2Cr), did not yield detectable NH_3. Similarly, Et_2O soluble acids $[H_2NPh_2][BAr^F_4]$ and $[H_3NPh][BAr^F_4]$ furnished lower yields of NH_3 relative to their triflate counterparts (Table 3.1, entries 14 and 15), presumably due to increasing background HER and possibly promoting catalyst deactivation (*vide infra*). Ether-miscible HOTf displays similar behavior (entry 16).

To explore the effect of increasing acid/reductant loading with **[Os]**–N_2^-, we tested 150 equiv of $[H_2NPh_2][OTf]$ and 180 equiv of Cp^*_2Co and detected 18 ± 1 equiv of NH_3 per Os (Table 3.1, entry 7), only a modestly diminished yield (35% based on H^+) relative to the lower loading. Increasing substrate loading leads to further increases in total yield of NH_3, again with little impact on efficiency for NH_3 with respect to acid (entries 8 and 9). Reloading an 800 equiv acid run after stirring for 3 hours at −78 °C (1600 equiv total) affords a total of 122 equiv of NH_3, suggesting a substantial amount of active catalyst is present at the end of the first run.

In a single run at the highest loading tested, 1500 equiv of $[H_2NPh_2][OTf]$ and 1800 equiv of Cp^*_2Co, a yield of 120 ± 11 equiv of NH_3 per Os (24 ± 2% for NH_3; entry 10) is observed. This total turnover number exceeds that of reported Fe catalysts, regardless of protocol,[19] and also exceeds TON data for most Mo catalysts.[1] Noteworthy exceptions concern Mo catalysts supported by pincer-phosphine ligands, shown to be both active and selective for NH_3 generation under

certain conditions.[1d,f]

For a direct single-run comparison under the present conditions, we tested the best known Fe catalyst, [Na(12-crown-4)$_2$][P_3^BFe–N_2],[2d,f] at 1500 equiv of [H_2NPh_2][OTf] and 1800 equiv of Cp*$_2$Co; only 22 ± 5 equiv of NH_3 are produced (average of two runs). This P_3^BFe–N_2^- catalyst performs more efficiently than **[Os]**–N_2^- at lower substrate loading, however.[2f] The single-run TON value for **[Os]**–N_2^- is hence noteworthy, despite its modest selectivity for NH_3 relative to H_2 overall.

With respect to formation of inactive osmium hydrides, we comment for comparison that **[Fe]**–N_2^- reacts with stoichiometric acid (e.g., $HBAr^F_4$) to liberate 0.5 equiv of H_2 and its one-electron oxidized derivative, **[Fe]**–N_2, presumably via a diazenido intermediate, **[Fe]**–N=NH, that releases H_2 bimolecularly;[20] none of the thermally stable, and catalytically inactive, hydride product, **[Fe]**(N_2)(H),[21] is observed. By contrast, exposing **[Os]**–N_2^- to stoichiometric $HBAr^F_4$ in THF-d_8 solution at −78 °C affords a mixture of the hydride products **[Os]**(N_2)(H) (major) and

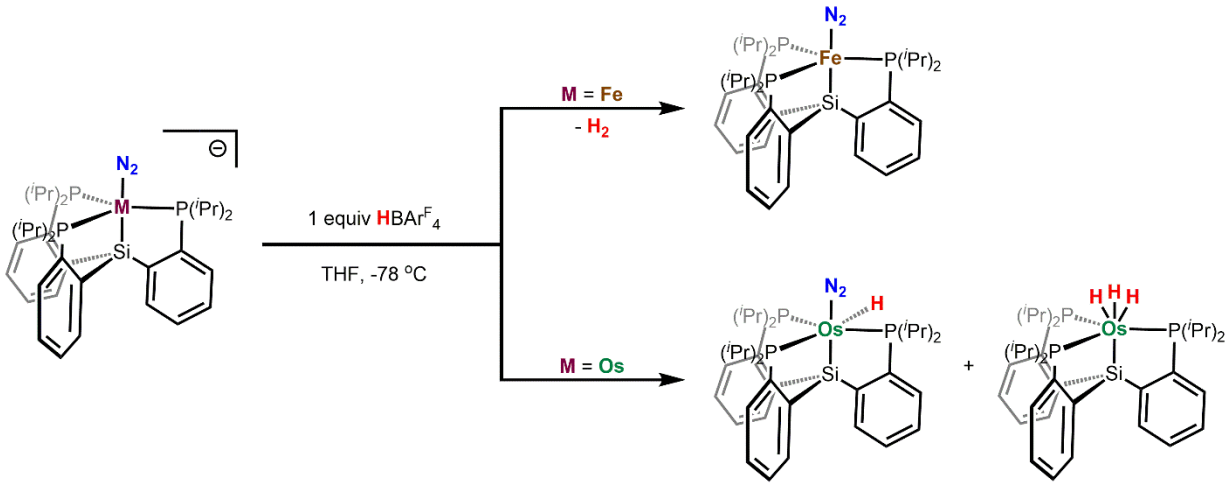

Scheme 3.1. Formation of Os-hydride species at −78 °C.

[Os]H_3 (minor), as determined by variable temperature NMR spectroscopy (Scheme 3.1).[22] On warming, **[Os]**–N_2 is also observed as a byproduct.

[Os]H_3 can be synthesized independently by reacting **[Os]**–Cl with $LiEt_3BH$, or by exposing either **[Os]**$(N_2)(H)$ or **[Os]**–N_2 to an atmosphere of H_2. Subjecting **[Os]**$(N_2)(H)$ or **[Os]**H_3 to 46 equiv of acid ($HBAr^F_4$ or $[H_2NPh_2][OTf]$) and 50 equiv of reductant (KC_8 or Cp^*_2Co; 1 atm N_2, Et_2O, −78 °C) does not furnish detectable NH_3. Examination of the Os speciation after treatment of **[Os]**–N_2^- with 10 equiv of acid and 12 equiv of reductant reveals **[Os]**$(N_2)(H)$ ($HBAr^F_4/KC_8$: 32%; $[H_2NPh_2][OTf]/Cp^*_2Co$: 0%) and **[Os]**H_3 ($HBAr^F_4/KC_8$: 48%; $[H_2NPh_2][OTf]/Cp^*_2Co$: 62%) as the only observable products by NMR and IR spectroscopies, providing evidence these inactive Os-hydride species form during catalytic reactions. For the $P_3^BFe–N_2^-$ catalyst system using $[H_2NPh_2][OTf]/Cp^*_2Co$, off-path hydrides are not observed;[2f] they are observed, however, when using $HBAr^F_4/KC_8$.[2d]

We hypothesized access to zerovalent **[Os]**–N_2^- is critical for productive N_2 functionalization, presumably proceeding via an initial **[Os]**–N=NH intermediate formed via the first protonation step. The **[Os]**–$N_2^{[0/1-]}$ redox couple is −1.94 V (vs $Fc^{[1+/0]}$, Figure 3.1),[14a] suggesting Cp^*_2Co should be a sufficiently strong reductant to (re)generate the **[Os]**–N_2^- state during catalysis. By analogy, access to anionic $P_3^EFe–N_2^-$ (E = B, C, Si) states has been shown to be chemically and electrochemically correlated with N_2RR catalysis.[2d,f] Invoking **[Os]**–N_2^- as "on path" for catalysis helps rationalize the poor N_2-to-NH_3 conversion exhibited by the osmium catalyst when Cp^*_2Co is replaced by either Cp_2Co (E = −1.33 vs $Fc^{[1+/0]}$, THF) or Cp^*_2Cr (E = −1.55 vs $Fc^{[1+/0]}$, THF); these reagents cannot regenerate **[Os]**–N_2^-.

To gauge whether Cp^*_2Co can competently reduce **[Os]**–N_2 to generate **[Os]**–N_2^-, a green

Et_2O solution of **[Os]**–N_2 was treated with 5 equiv of Cp^*_2Co at room temperature. Surprisingly, analysis of the reaction mixture by ^{31}P NMR and IR spectroscopies, monitoring over several hours with vigorous stirring, shows none of the expected **[Os]**–N_2^- species.

An analogous experiment, performed in THF-d_8 and monitored by ^1H and ^{31}P NMR spectroscopies at room temperature, shows only unreacted **[Os]**–N_2 and Cp^*_2Co. However, upon cooling this mixture to −78 °C, resonances consistent with the formation of **[Os]**–N_2^- appear.[23] Accordingly, a color change from green-brown to red is observed within seconds, indicating a temperature-dependent redox process. This is monitored as a function of temperature by optical spectroscopy; a gradual decrease in the absorption bands at λ = 670 nm and λ = 1000 nm corresponding to **[Os]**–N_2 is observed, with a simultaneous increase in a feature attributable to **[Os]**–N_2^- near λ = 550 nm (Figure 3.2). Variable temperature cycling confirms a temperature-dependent redox equilibrium.

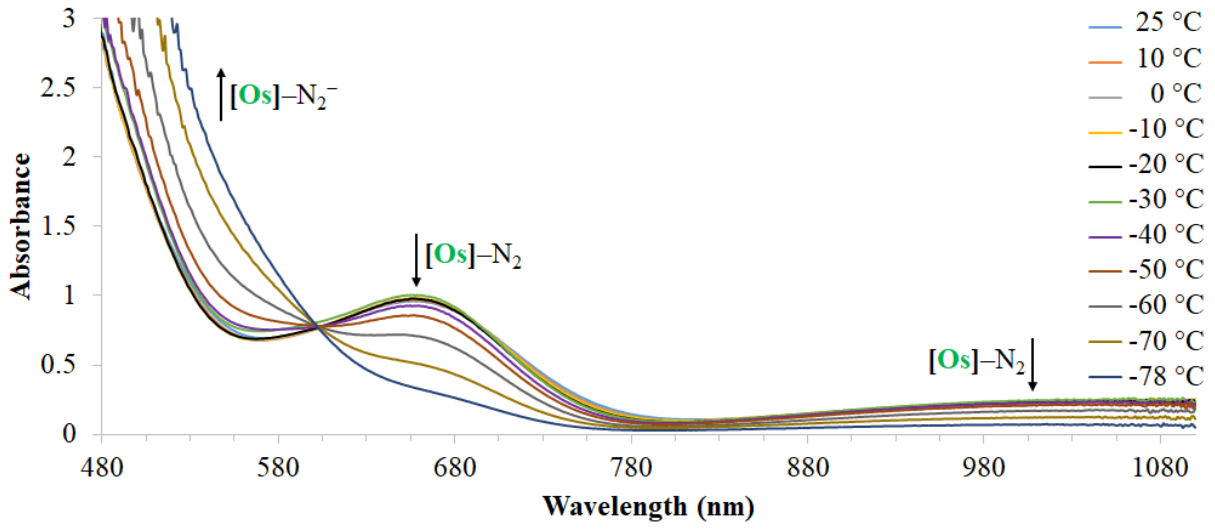

Figure 3.2. UV-visible absorbance spectra for reaction of **[Os]**–N_2 (1.2 mM) and 5 equiv of Cp^*_2Co (6.0 mM) in THF at listed temperature.

We conclude that, at the catalytically relevant temperature of −78 °C, Cp^*_2Co is capable of reducing **[Os]**–N_2 to **[Os]**–N_2^-, a step that may be entropically driven via formation of {**[Os]**–N_2}{Cp^*_2Co}. The VT optical data suggest an observable population of **[Os]**–N_2^- can be generated at temperatures as high as −40 °C. Accordingly, a catalytic run carried-out at −40 °C (46 equiv $[H_2NPh_2][OTf]$ and 50 equiv Cp^*_2Co) produces 6.2 equiv NH_3.[24] By contrast, neither **[Ru]**–N_2^- nor **[Fe]**–N_2^- can be competently generated using Cp^*_2Co,[23] consistent with their comparatively poor performance.

We next probed the reactivity of **[Os]**–N_2^- with protons. Tripodal tris(phosphine) hydrazido $P_3^EFe{=}NNH_2^+$ complexes have been spectroscopically (E = B)[15a] and structurally characterized (E = Si),[15b] generated via double protonation of $P_3^EFe–N_2^-$ at low temperature. Similarly, reaction of **[Os]**–N_2^- with 3 equiv of HOTf in thawing 2-MeTHF (−135 °C) produces an orange mixture, from which pale orange {**[Os]**=NNH_2}{OTf} can be isolated upon precipitation (Scheme 3.2). Spectroscopic features of this diamagnetic hydrazido complex include a ν(NH) stretch centered at 3232 cm^{-1} and a diagnostic ^{1}H NMR resonance (THF-d_8) at δ = 10.0 ppm.[15b]

X-ray diffraction analysis of {**[Os]**=NNH_2}{OTf} locates two protons bound to the sp^2-hybridized β N atom (N2) with H-bonding to the triflate anion (Scheme 3.2). The *Os–N–*NH_2 unit is linear (∠ (Os–N1–N2) = 176°), the N1–N2 distance is 1.271(5) Å, and the Os–N1 distance is short (1.815(3) Å), in accord with a hydrazido(2−) featuring substantial Os–N multiple bond character. The Os–N and N–N distances in **[Os]**=NNH_2^+ are within the range observed for structurally characterized linear and bent hydrazido(2−) complexes of osmium,[25] prepared by trapping Os(IV)-imido intermediates[26] or by the reaction between Os-nitride complexes with

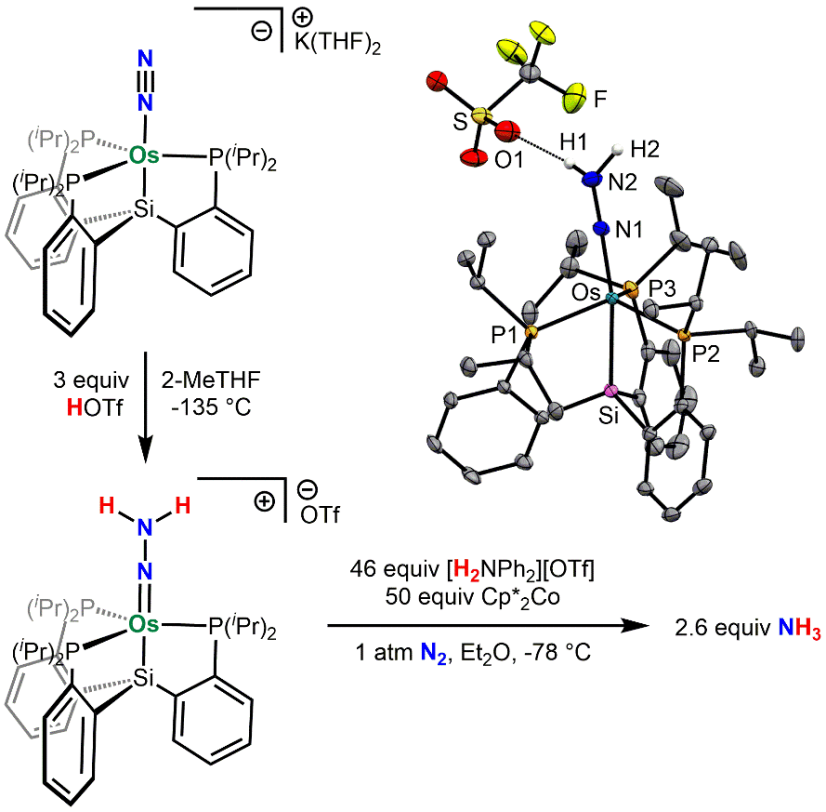

Scheme 3.2. Synthesis, XRD structure, and reactivity of the Os-hydrazido(2−) complex {**[Os]**=NNH_2}{OTf}. For the XRD structure, thermal ellipsoids set at 50% probability and hydrogen atoms (except for N–H's) are omitted for clarity.

secondary ammines.[27] A related osmium-imide complex prepared by our lab, **[Os]**=N–Ar (Ar = *p*-trifluoromethylphenyl),[14a] displays similar structural parameters to **[Os]**=NNH_2^+, including comparable Os–N bond lengths, Os–P bond lengths, and degrees of pyramidalization at the Si and Os atoms (Table 3.2). **[Os]**=NNH_2^+ represents the first instance of an Os–N_2 species to be converted to a protonated Os–N_xH_y product.

To assess the possible intermediacy of **[Os]**=NNH_2^+ in the Os-mediated N_2RR catalysis described herein, **[Os]**=NNH_2^+ was treated with 46 equiv of [H_2NPh_2][OTf] and 50 equiv of Cp^*_2Co at low temperature, generating greater-than-stoichiometric quantities of NH_3 (ca. 2.6

equiv; no hydrazine detected; Scheme 3.2). **[Os]**=NNH_2^+ and its one-electron reduced state, **[Os]**=NNH_2, should be active toward bimolecular proton-coupled-electron transfer (PCET) steps to generate inactive hydrides (or competing H_2) owing to very weak N–H bonds.[2f,15c,20] Such reactivity likely explains the poor catalytic performance of isolated **[Os]**=NNH_2^+; catalysis should be more efficient when such hydrazido species are formed in lower concentration *in situ* during catalysis. Combined with the observation that Cp^*_2Co can reduce **[Os]**–N_2 to **[Os]**–N_2^- at low temperature, and that **[Os]**–N_2^- can be protonated to yield **[Os]**=NNH_2^+, the observation that **[Os]**=NNH_2^+ can facilitate NH_3 formation lends support to an electron transfer-proton transfer N_2RR pathway that proceeds, initially at least, via a distal pathway.

3.3. Conclusion

To conclude, we have shown for the first time both Ru and Os coordination complexes can serve as catalysts for N_2RR in the presence of reductant and acid sources under ambient pressure at low temperature. The tris(phosphine)silyl Os system is most active, displaying high turnover at high loadings of Cp^*_2Co and $[H_2NPh_2][OTf]$. Access to zerovalent **[Os]**–N_2^- appears critical for N_2 functionalization, and a bona fide **[Os]**=NNH_2^+ hydrazido complex can be generated via protonation of **[Os]**–N_2^- and is shown to facilitate NH_3 generation. Os-hydrides, including **[Os]**(N_2)(H) and **[Os]**H_3, form during the catalysis as catalytically inactive states. That a tris(phosphine)silyl ligand proves so effective for osmium-mediated N_2RR catalysis, but is largely ineffective for the isostructural **[Fe]**–N_2^- and **[Ru]**–N_2^- systems using Cp^*_2Co and $[H_2NPh_2][OTf]$, underscores the value in comparatively exploring related systems for N_2RR. In this case, the key **[Os]**–$N_2^{[0/1-]}$ redox couple is accessible with Cp^*_2Co, but only at low

temperature, whereas a stronger reductant is needed to drive the **[Fe]**–$N_2^{[0/1-]}$ and **[Ru]**–$N_2^{[0/1-]}$ reductions.

3.4. Experimental Section

3.4.1. Experimental Methods

General Considerations

All manipulations were carried out using standard Schlenk or glovebox techniques under an N_2 atmosphere. Solvents were deoxygenated and dried by thoroughly sparging with N_2 gas followed by passage through an activated alumina column in the solvent purification system by SG Water, USA LLC. Non-halogenated solvents were tested with sodium benzophenone ketyl in tetrahydrofuran (THF) in order to confirm effective oxygen and moisture removal. Deuterated solvents were purchased from Cambridge Isotope Laboratories, Inc., degassed, and dried over activated 3 Å molecular sieves prior to use.

$[H_2NPh_2][BAr^F{}_4]$ and $[H_3NPh][BAr^F{}_4]$ were synthesized from a modified literature procedure.[17] $P_3{}^{Si}Os–Cl$,[14a] $P_3{}^{Si}Os–N_2$,[14a] $[K(THF)_2][P_3{}^{Si}Os–N_2]$,[14a] $P_3{}^{Si}Ru–Cl$,[14a] $P_3{}^{Si}Ru–N_2$,[14a] $[K(THF)_2][P_3{}^{Si}Ru–N_2]$,[14a] $P_3{}^{Si}Fe–N_2$,[30] $[Na(12\text{-crown-}4)_2][P_3{}^{Si}Fe–N_2]$,[18] $[Na(12\text{-crown-}4)_2][P_3{}^{B}Fe–N_2]$,[28] $[H(OEt_2)_2][BAr^F{}_4]$ ($HBAr^F{}_4$, $BAr^F{}_4{}^-$ = tetrakis(3,5-bis(trifluoromethyl)phenyl)borate),[29] KC_8,[30] $[H_2NPh_2][OTf]$,[2f,31] $[H_2{}^{15}NPh_2][OTf]$,[31,32] $[H_3NPh][OTf]$,[2f] [*N*-Me-H_2NPh][OTf],[2f] and $Cp^*{}_2Co$[33] were prepared according to literature methods. $H_2{}^{15}NPh$ was obtained from Sigma-Aldrich, Inc., degassed, and dried over activated 3 Å molecular sieves prior to use**.** All other reagents were purchased from commercial vendors and used without further purification unless otherwise stated. Diethyl ether (Et_2O) and THF used for NH_3 generation experiments were stirred over Na/K (≥ 1 hour) and filtered before use. *Note:* $P_3{}^{Si}M$ is equivalent to the abbreviated **[M]** notation in the main text.

NMR Spectroscopy

NMR measurements were obtained on Varian 300, 400, or 500 MHz spectrometers. ^{1}H NMR chemical shifts are reported in ppm and referenced to residual protio solvent. ^{31}P NMR chemical shifts were externally referenced to 85% H_3PO_4 in H_2O.

IR Spectroscopy

IR measurements were obtained as solids or thin films formed by evaporation of solutions using a Bruker Alpha Platinum ATR spectrometer with OPUS software.

UV-Visible Spectroscopy

Optical spectroscopy measurements were collected with a Cary 50 UV-visible spectrophotometer using a 1 cm path length quartz cuvette. Variable temperature measurements were collected with a Unisoku CoolSpek cryostat mounted within the Cary spectrophotometer. All samples had a blank sample background subtraction applied. Density corrections were applied using literature temperature versus density data available for THF.[34]

X-ray Crystallography

XRD studies were carried out at the Caltech Division of Chemistry and Chemical Engineering X-ray Crystallography Facility on a Bruker three-circle SMART diffractometer with a SMART 1K CCD detector or Bruker Kappa Apex II diffractometer. Data was collected at 100 K using Mo Kα radiation ($\lambda = 0.71073$ Å). Using OLEX2,[35] structures were solved with the XT[36] structure solution program using Direct Methods and refined with the XL[37] refinement package using Least Squares

minimization. All non-hydrogen atoms were refined anisotropically. All hydrogen atoms were placed at geometrically calculated positions and refined using a riding model. The isotropic displacement parameters of all hydrogen atoms were fixed at 1.2 (1.5 for methyl groups) times the U_{eq} of the atoms to which they are bonded.

3.4.2. Synthetic Details and Characterization Data

$[H_2NPh_2][BAr^F{}_4]$. This compound was synthesized from a modified literature procedure as follows.[17] Inside the glovebox, $HNPh_2$ (0.0855 g, 0.504 mmol) was weighed out into a 20 mL scintillation vial, equipped with a stir bar, and dissolved in 5 mL of Et_2O. While stirring at room temperature, an $HBAr^F{}_4$ (1.00 equiv, 0.504 mmol, 0.5107 g) solution in Et_2O (5 mL) was added dropwise. The reaction was allowed to stir at room temperature for 1 hour before concentrating the volume of the solution to 2 mL, layering with pentane, and cooling to –30 °C. The white crystals obtained from the crystallization were dried under vacuum to yield $[H_2NPh_2][BAr^F{}_4]$ in quantitative yield.

$[H_3NPh][BAr^F{}_4]$. $[H_3NPh][BAr^F{}_4]$ was prepared from H_2NPh via a procedure analogous to that for $[H_2NPh_2][BAr^F{}_4]$.

$[P_3{}^{Si}Os{=}NNH_2][OTf]$. This compound was synthesized from a modified literature procedure as follows.[15b] Inside the glovebox, $[K(THF)_2][P_3{}^{Si}Os{-}N_2]$ (0.0574 g, 0.0569 mmol) was dissolved in 2 mL of 2-MeTHF, filtered through glass filter paper into a 20 mL scintillation vial, and frozen inside the coldwell chilled with an external liquid nitrogen bath. A second vial containing a

solution of HOTf acid (3.02 equiv, 0.172 mmol, 15.2 µL) in 1 mL of 2-MeTHF was similarly frozen. In addition, a pair of large forceps, a spatula, two pipets, and a vial containing 15 mL of pentane were cooled inside the coldwell.

After freezing and allowing the temperature to equilibrate, the acid solution was briefly thawed by elevating it off the floor of the coldwell with the forceps. Using the pre-chilled pipet, the acid solution was layered dropwise on top of the frozen solution of $[K(THF)_2][P_3{}^{Si}Os–N_2]$. Following the refreezing of the solutions, the two layers were combined by first elevating the vial off the coldwell floor with the forceps until the solutions thawed to a viscous mixture, and then stirring mechanically with the pre-chilled spatula. (*Note:* It is critical to combine the layers as soon as the solvent glass melts and while the solution remains rather viscous.) The two layers were mixed in this fashion for ca. 10 minutes, at which point the reaction mixture had changed color from dark red to orange.

Upon completion of mixing, the reaction mixture was allowed to glass. While still at 77 K, it was layered with 15 mL of pre-chilled pentane using a pre-chilled pipet. (*Note:* The pentane was added in small fractions and allowed to freeze in between so as not to allow the reaction layer to thaw). The contents of the vial were then allowed to freeze and equilibrate at 77 K for 10 minutes. During this time, a vial containing 20 mL of pentane, two pipets, a 50 mL filter flask, and a M-porosity frit were similarly cooled to 77 K inside the glovebox coldwell.

The coldwell bath was then switched from a liquid nitrogen bath to a dry ice/acetone bath (–78 °C),

and the pentane-layered reaction was allowed to thaw for 1 hour. The layers were further mixed with a pre-chilled pipet to give a cloudy orange mixture that was vacuum filtered through the M-frit inside the glovebox coldwell. While still at –78 °C, the collected pale orange solid was rinsed with pre-chilled pentane. Transferring the solid to a tared vial and drying under vacuum thus afforded 0.0518 g (< 93% yield) of $[P_3^{Si}Os{=}NNH_2][OTf]$ as a pale orange solid. Crystals suitable for XRD were obtained by vapor diffusion of pentane into a concentrated THF solution of $[P_3^{Si}Os{=}NNH_2][OTf]$ at room temperature.

********Note:* $[P_3^{Si}Os{=}NNH_2][OTf]$ prepared in this manner contains variable amounts of KOTf.

^{1}H NMR (500 MHz, THF-d_8, 25 ^{o}C): δ(ppm) 9.87 (s, 2H, NNH_2), 8.17 (d, J = 7.2 Hz, 3H, Ar–H), 7.60 (d, J = 7.6 Hz, 3H, Ar–H), 7.40 (t, J = 7.4 Hz, 3H, Ar–H), 7.27 (t, J = 7.4 Hz, 3H, Ar–H), 2.70 (br s, 6H, CH(CH_3)$_2$), 1.10–1.04 (br m, 18H, CH(CH_3)$_2$), 0.69 (br s, 18H, CH(CH_3)$_2$).

^{31}P{^{1}H} NMR (202 MHz, THF-d_8, 25 ^{o}C): δ(ppm) 56.5 (s).

^{19}F NMR (376 MHz, THF-d_8, 25 ^{o}C): δ(ppm) –82.2 (s).

IR (solid-state): ν(NH) = 3232 cm^{-1}.

E.A.: No combustion analysis data was obtained due to the presence of KOTf salts that could not be separated from the $[P_3^{Si}Os{=}NNH_2][OTf]$ product.

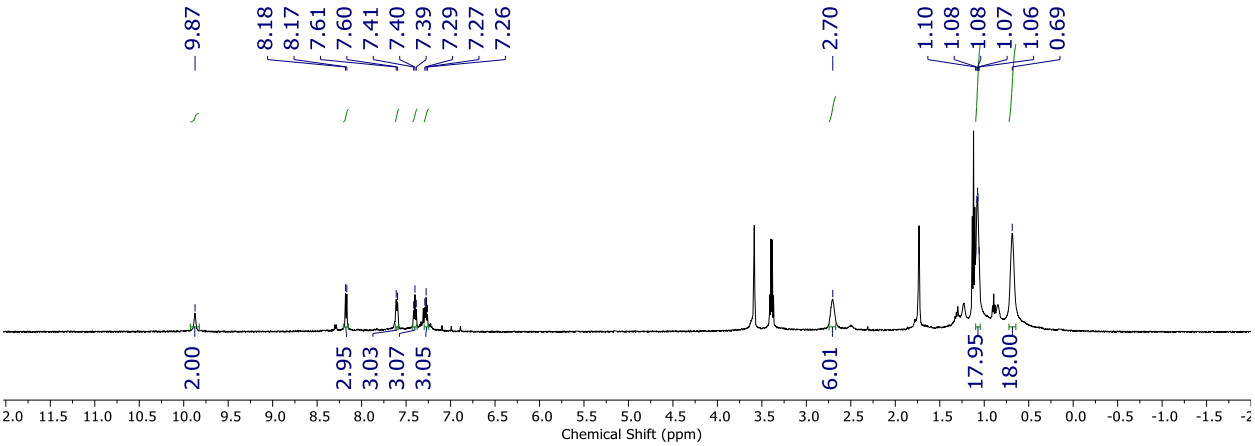

Figure 3.3. ^{1}H NMR spectrum (500 MHz, THF-d_8, 25 °C) of [P_3^{Si}Os=NNH_2][OTf].

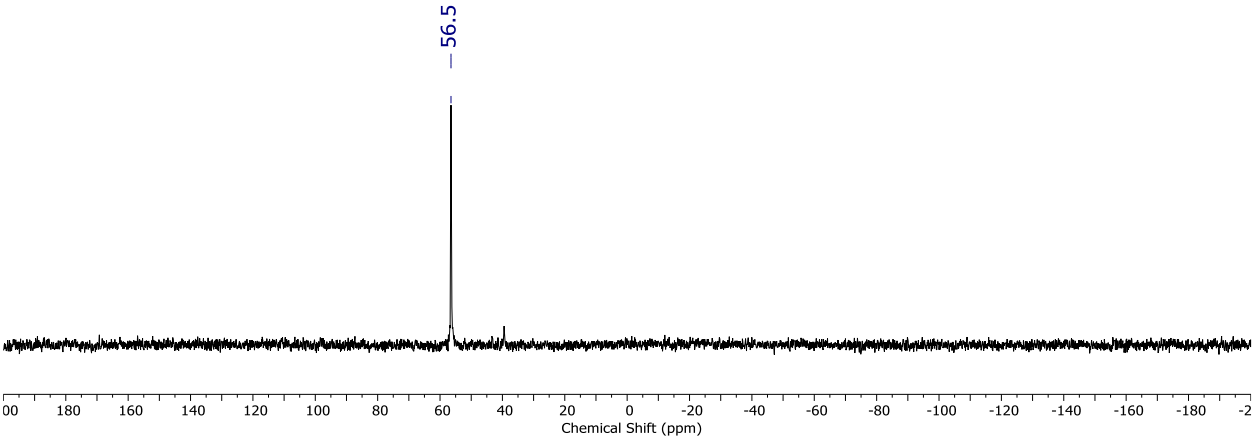

Figure 3.4. ^{31}P{^{1}H} NMR spectrum (202 MHz, THF-d_8, 25 °C) of [P_3^{Si}Os=NNH_2][OTf].

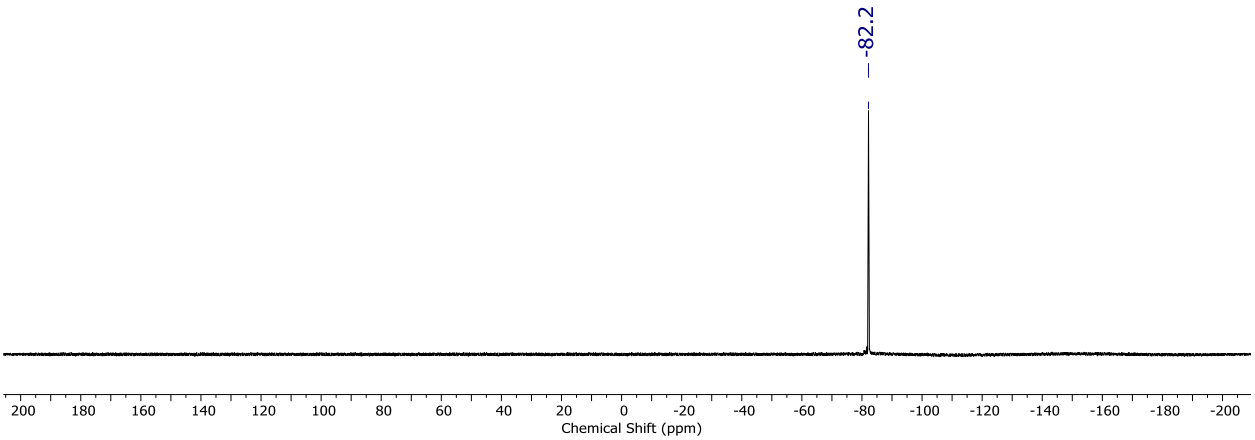

Figure 3.5. ^{19}F NMR spectrum (376 MHz, THF-d_8, 25 °C) of $[P_3^{Si}Os{=}NNH_2][OTf]$.

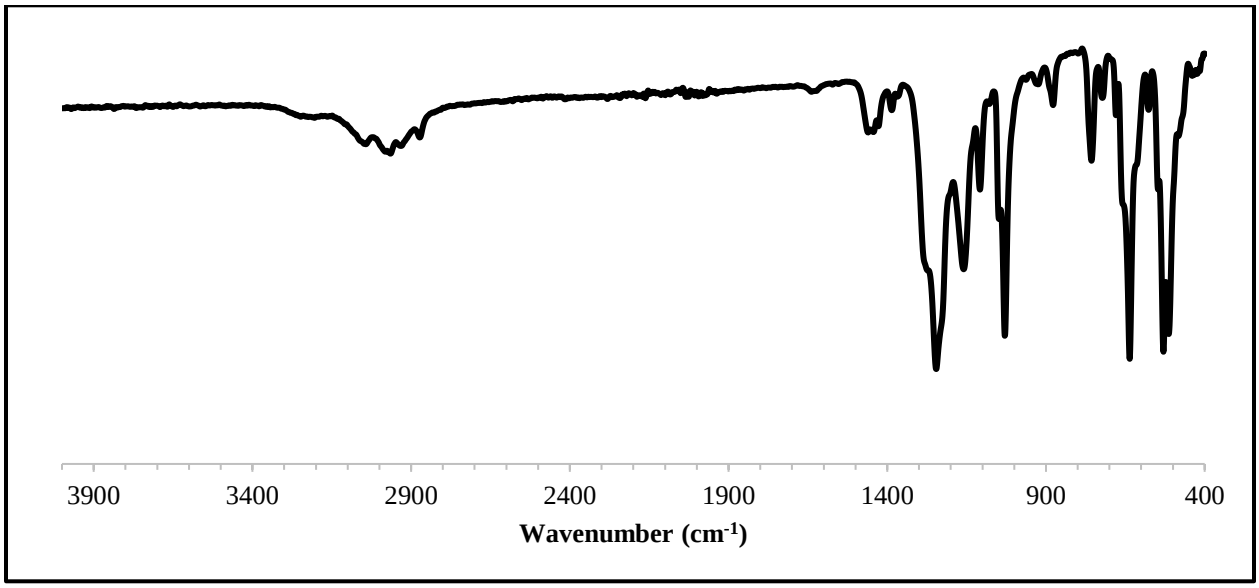

Figure 3.6. Solid-state IR spectrum of $[P_3^{Si}Os{=}NNH_2][OTf]$.

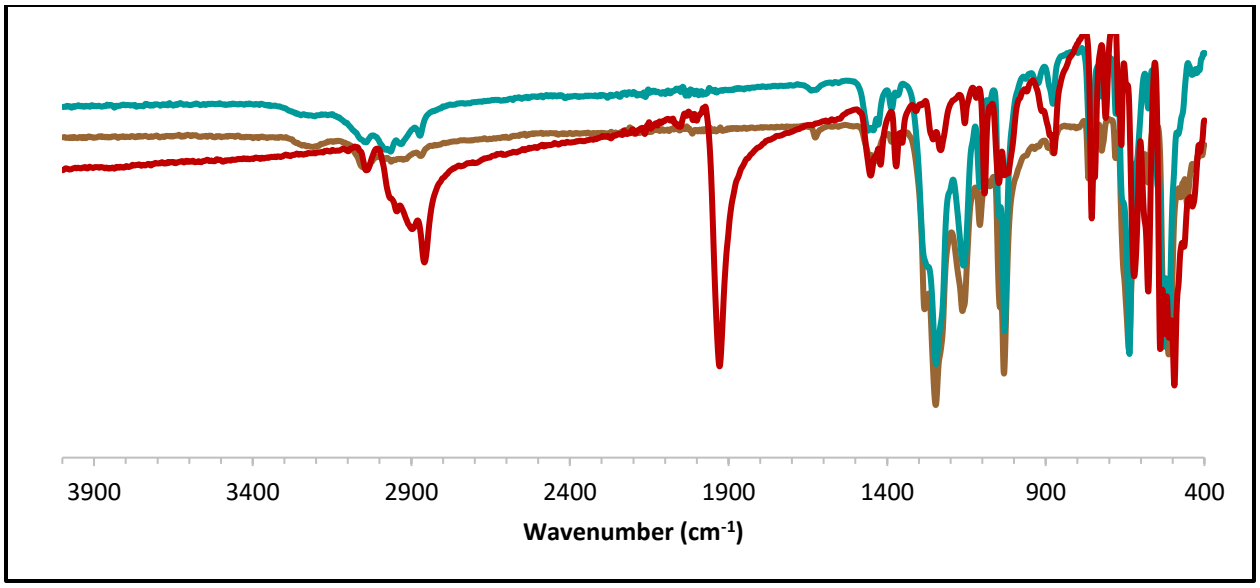

Figure 3.7. Overlaid solid-state IR spectra of $[K(THF)_2][P_3^{Si}Os–N_2]$ (red), $[P_3^{Si}Os=NNH_2][OTf]$ (teal), and $[P_3^{Si}Fe=NNH_2][OTf]$ (brown).

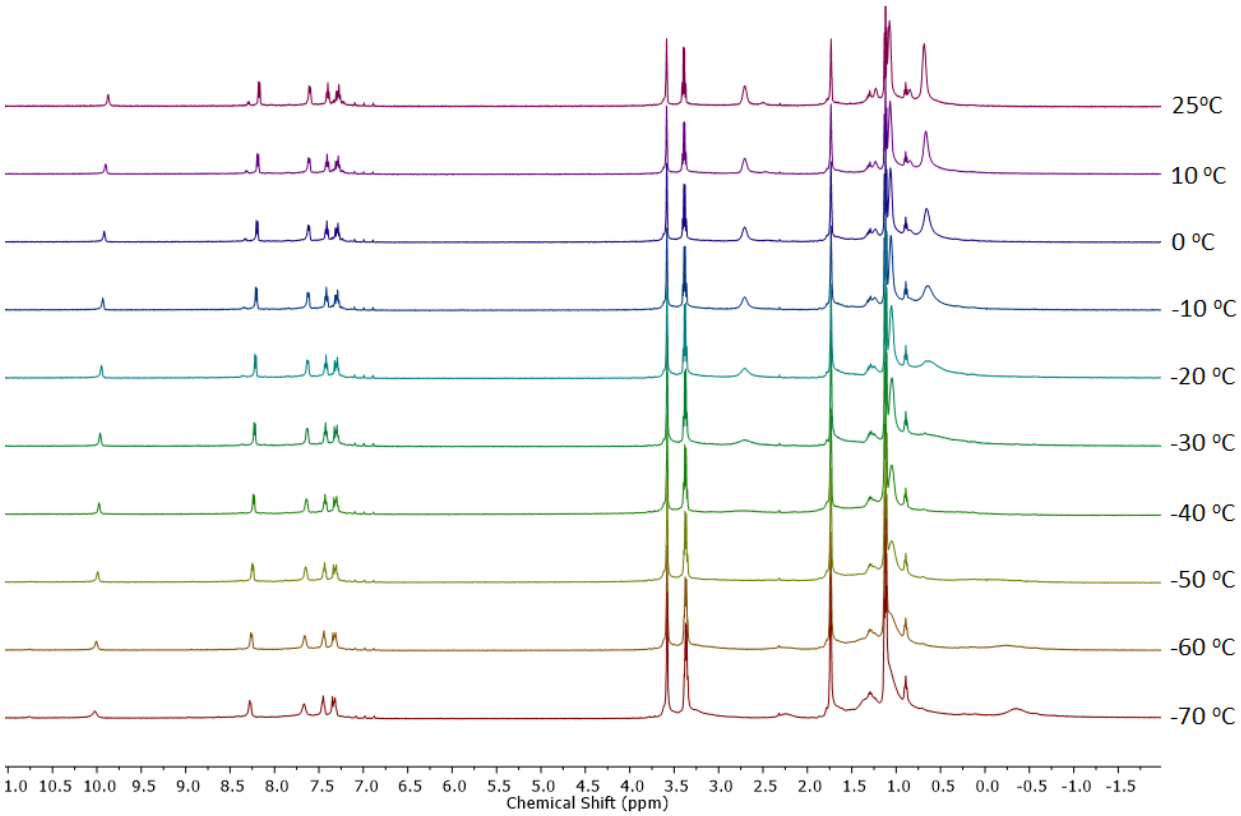

Figure 3.8. Variable temperature ^{1}H NMR spectra (500 MHz, THF-d_8) of $[P_3{}^{Si}Os{=}NNH_2][OTf]$.

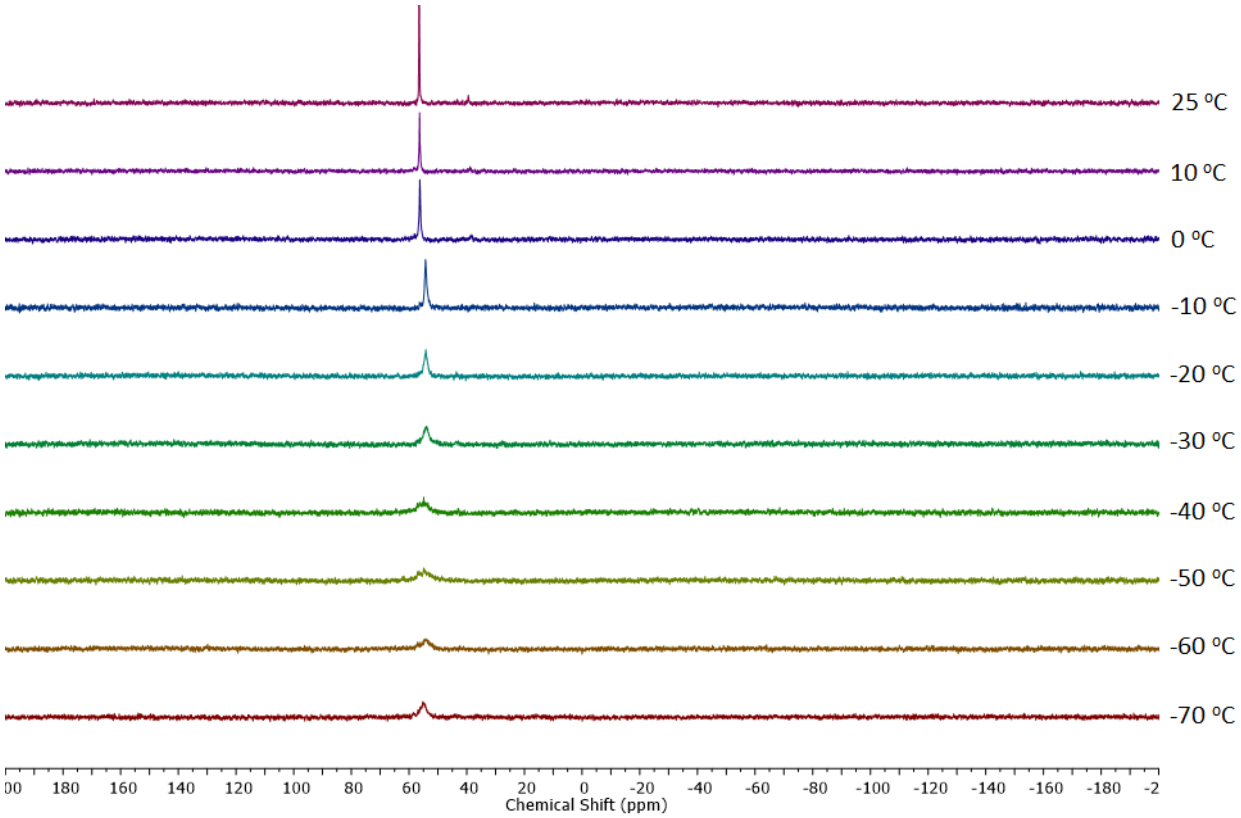

Figure 3.9. Variable temperature $^{31}P\{^{1}H\}$ NMR spectra (202 MHz, THF-d_8) of $[P_3{}^{Si}Os{=}NNH_2][OTf]$.

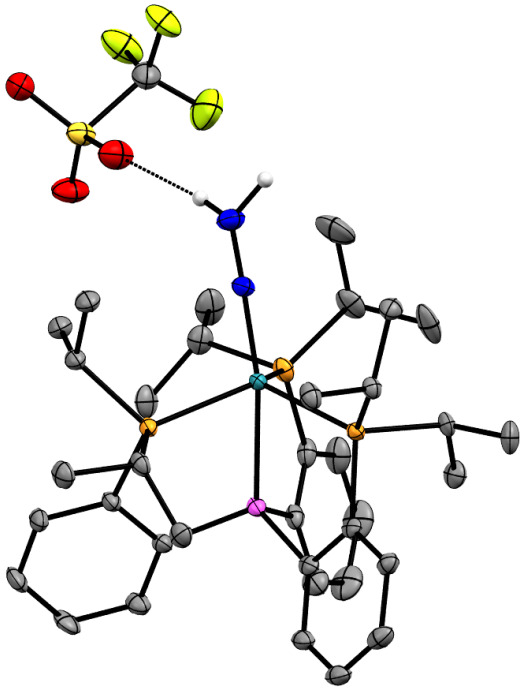

Figure 3.10. XRD structure of $[P_3^{Si}Os{=}NNH_2][OTf]$ with thermal ellipsoids set at 50% probability. Hydrogen atoms (except N–H's) are omitted for clarity. Color code: Os = teal, S = yellow, P = orange, Si = pink, F = green-yellow, O = red, N = blue, C = gray, H = white.

Table 3.2. Comparison of the structural data of $[P_3^{Si}Os{=}NNH_2][OTf]$ with that of $[K(THF)_2][P_3^{Si}Os{-}N_2]$, $[P_3^{Si}Fe{=}NNH_2][OTf]$, and $P_3^{Si}Os{=}N{-}Ar$ (Ar = *p*-trifluoromethylphenyl).

Metric	**[Os]–N_2^-**	**[Os]=NNH_2^+**	**[Fe]=NNH_2^+**	**[Os]=N–Ar**
M–N1	1.965	1.815	1.668	1.859
N1–N2	1.136	1.271	1.273	-----
M–Si	2.339	2.440	2.344	2.408
∠Si–M–N1	179	168	171	162
∠M–N1–N2	178	176	175	-----
Σ∠P–M–P	352	346	350	346
Σ∠C–Si–C	321	324	325	323
Σ∢Nβ	-----	358	359	-----

$P_3^{Si}Os(N_2)(H)$. $P_3^{Si}Os{-}N_2$ (0.0145 g, 0.0176 mmol) was dissolved in 4 mL of Et_2O to give a green solution. While stirring vigorously, 166 µL of an N_2H_4 stock solution in Et_2O (10.0 µL of anhydrous N_2H_4 in 3 mL of Et_2O; 0.106 M, 1.15 equiv, 0.0202 mmol) was delivered via micropipette. After a few moments, the color of the reaction gradually changed from green to orange. The reaction was then stirred vigorously at room temperature for 1 hour before removing the Et_2O under vacuum. The remaining residue was extracted into C_6H_6, filtered through celite, and lyophilized to yield $P_3^{Si}Os(N_2)(H)$ as an aqua solid (0.0135 g, ca. 90% $P_3^{Si}Os(N_2)(H)$ as determined by ^1H and ^{31}P NMR spectroscopies).

******Note:*** $P_3^{Si}Os(N_2)(H)$ prepared in this fashion contains a small amount of $P_3^{Si}OsH_3$ as an impurity. Attempts to purify $P_3^{Si}Os(N_2)(H)$ were unsuccessful due to the similar solubility

properties of the compounds. Other reaction conditions canvassed afforded a similar distribution of products.

^{1}H NMR (400 MHz, C_6D_6, 25 ^{o}C): δ(ppm) 8.25 (d, *J* = 7.4 Hz, 2H, Ar–*H*), 8.06 (d, *J* = 7.2 Hz, 1H, Ar–*H*), 7.40 (d, *J* = 6.5 Hz, 2H, Ar–*H*), 7.23–7.17 (m, 3H, Ar–*H*), 7.11 (t, *J* = 7.4 Hz, 1H, Ar–*H*), 7.04 (t, *J* = 7.5 Hz, 2H, Ar–*H*), 7.00–6.96 (t, *J* = 7.4 Hz, 1H, Ar–*H*), 2.82 (br m, 2H, C*H*$(CH_3)_2$), 2.50 (m, 2H, C*H*$(CH_3)_2$), 2.34 (m, 2H, C*H*$(CH_3)_2$), 1.33 (m, 6H, CH(C*H*$_3)_2$), 1.25 (m, 6H, CH(C*H*$_3)_2$), 1.11 (m, 6H, CH(C*H*$_3)_2$), 0.78–0.68 (m, 12H, CH(C*H*$_3)_2$), 0.59 (br s, 6H, CH(C*H*$_3)_2$), –11.18 (dt, *J* = 50 Hz, 1H, Os–*H*).

^{31}P{^{1}H} NMR (162 MHz, C_6D_6, 25 ^{o}C): δ(ppm) 38.3 (br, 2P), 36.1 (m, 1P).

^{31}P{^{1}H} NMR (202 MHz, toluene-*d*$_8$, –78 ^{o}C): δ(ppm) 56.5 (d, 1P), 39.6 (s, 1P), 28.8 (d, 1P).

IR (thin film from C_6D_6): *ν*(NN) = 2098 cm^{-1}.

E.A.: No combustion analysis data was obtained due to the lability of the dinitrogen ligand under vacuum.

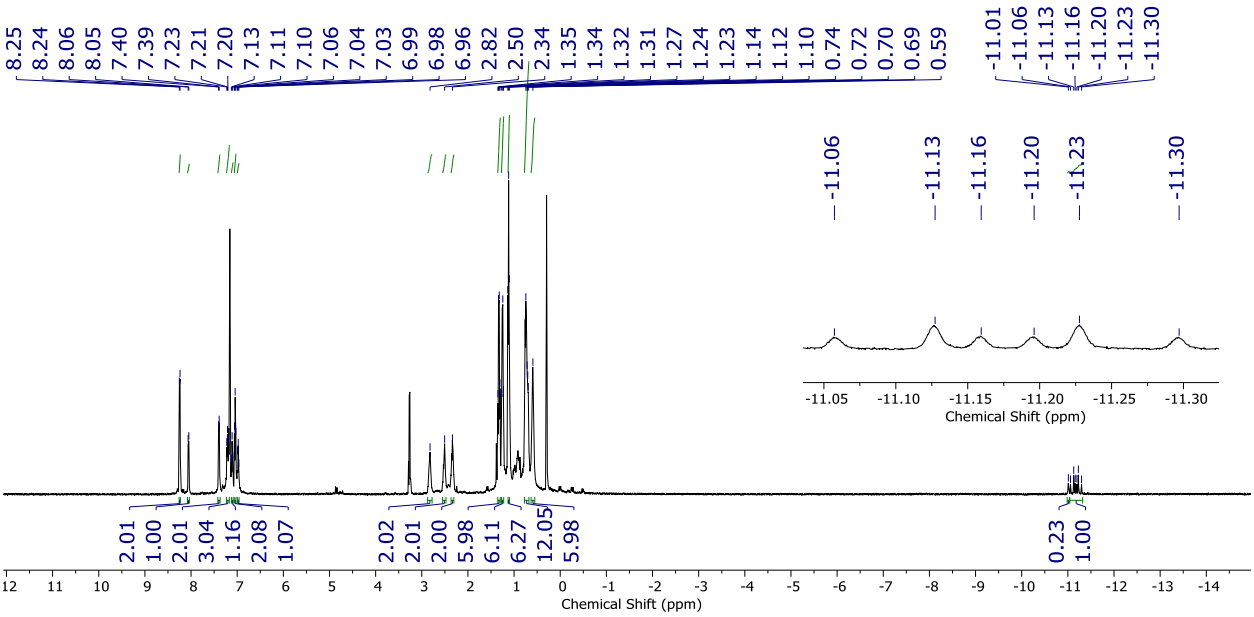

Figure 3.11. ^{1}H NMR spectrum (400 MHz, C_6D_6, 25 °C) of $P_3^{Si}Os(N_2)(H)$. The hydride resonance at –11.01 ppm corresponds to a small amount of $P_3^{Si}OsH_3$ present as an impurity.

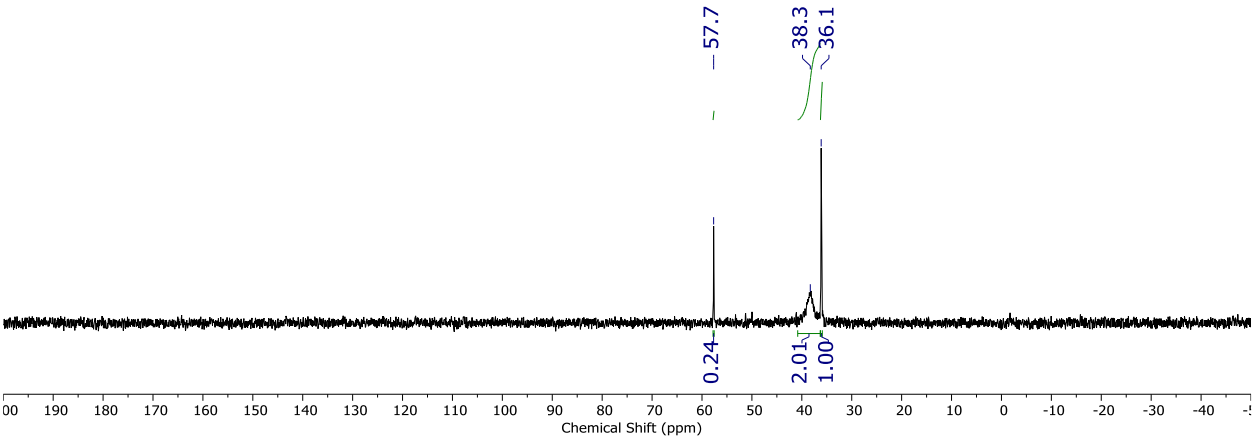

Figure 3.12. $^{31}P\{^{1}H\}$ NMR spectrum (162 MHz, C_6D_6, 25 °C) of $P_3^{Si}Os(N_2)(H)$. The ^{31}P resonance at 57.7 ppm corresponds to a small amount of $P_3^{Si}OsH_3$ present as an impurity.

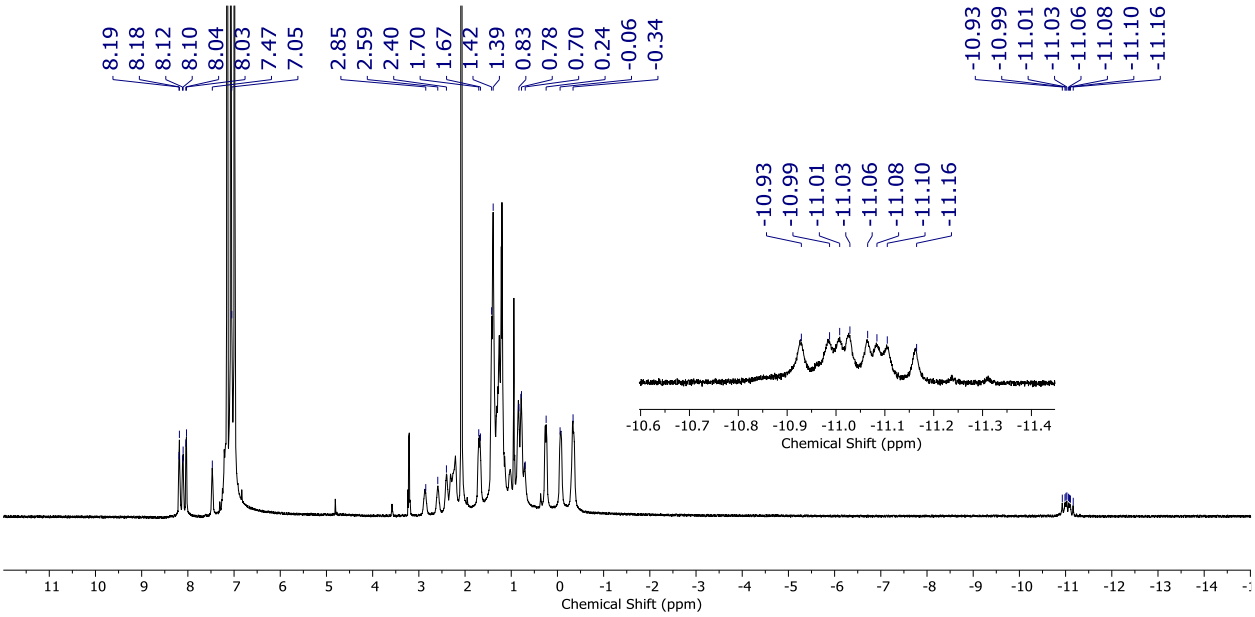

Figure 3.13. ^{1}H NMR spectrum (500 MHz, toluene-d_8, –78 °C) of $P_3{}^{Si}Os(N_2)(H)$. There is a small amount of $P_3{}^{Si}OsH_3$ present as an impurity.

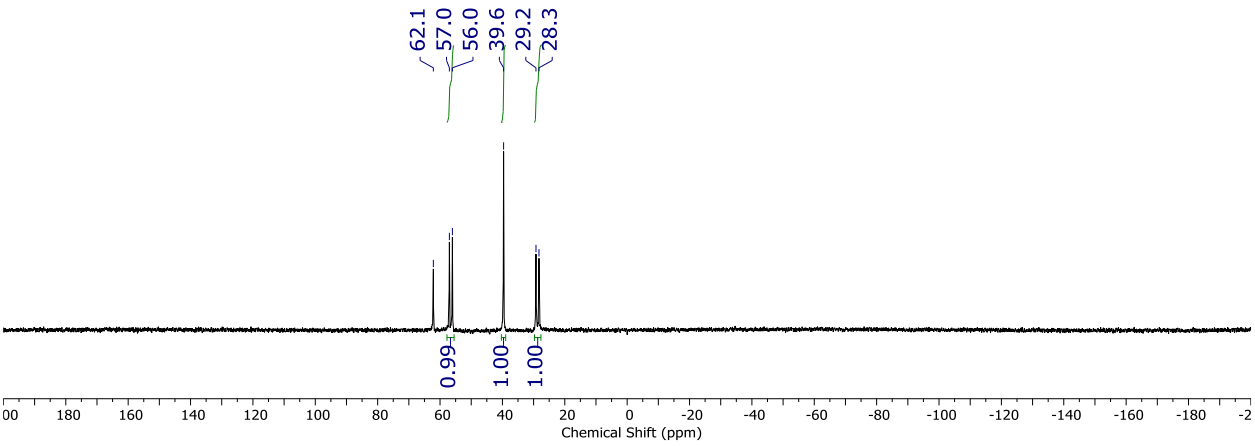

Figure 3.14. $^{31}P\{^{1}H\}$ NMR spectrum (202 MHz, toluene-d_8, –78 °C) of $P_3{}^{Si}Os(N_2)(H)$. The ^{31}P resonance at 62.1 ppm corresponds to a small amount of $P_3{}^{Si}OsH_3$ present as an impurity.

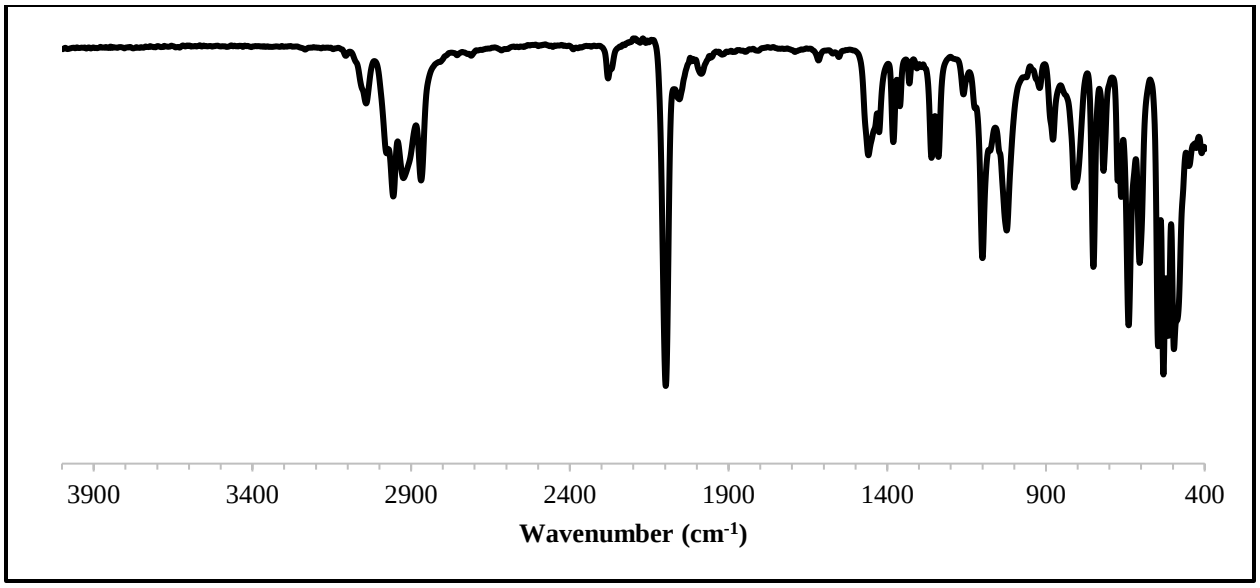

Figure 3.15. IR spectrum of $P_3^{Si}Os(N_2)(H)$ deposited as a thin film from C_6D_6.

$P_3^{Si}OsH_3$. $P_3^{Si}Os–Cl$ (0.0375 g, 0.0440 mmol) was dissolved in 3 mL of THF to give a brown solution. $LiEt_3BH$ (1.0 M in THF, 3.00 equiv, 0.135 mmol, 135 µL) was then added at room temperature via micropipette. The reaction was stirred vigorously for two days at room temperature, after which the color of the reaction had changed from brown to yellow. The THF was removed under vacuum, and the product was extracted into pentane (3 x 3 mL), filtered through celite, and dried under vacuum to yield $P_3^{Si}OsH_3$ as an off-white solid (0.0348 g, 0.0434 mmol) in 96% yield. Crystals suitable for XRD were obtained by slow concentration of a C_6H_6 solution of $P_3^{Si}OsH_3$ in a closed vessel containing HMDSO.

Alternatively, $P_3^{Si}OsH_3$ can be synthesized by addition of an atmosphere of H_2(g) to a degassed solution of $P_3^{Si}Os–N_2$ or $P_3^{Si}Os(N_2)(H)$ and stirring vigorously at room temperature. The reaction is shown to go to completion after 4 days or 12 hours, respectively, as determined by NMR and

IR spectroscopies.

^{1}H NMR (400 MHz, C_6D_6, 25 ^{o}C): δ(ppm) 8.24 (d, *J* = 7.2 Hz, 3H, Ar–*H*), 7.25–7.18 (m, 6H, Ar–*H*), 7.01 (t, *J* = 7.4 Hz, 3H, Ar–*H*), 2.41 (br s, 6H, C*H*(CH_3)$_2$), 1.05–0.80 (m, 24H, CH(C*H*$_3$)$_2$), 0.28 (br s, 12H, CH(C*H*$_3$)$_2$), –11.01 (t, *J* = 3.5 Hz, 3H, Os–*H*).

^{31}P{^{1}H} NMR (162 MHz, C_6D_6, 25 ^{o}C): δ(ppm) 57.6 (s).

^{1}H NMR (500 MHz, toluene-*d*$_8$, –78 ^{o}C): δ(ppm) δ 8.18 (d, *J* = 7.2 Hz, 3H, Ar–*H*), 7.25 (t, *J* = 7.0 Hz, 3H, Ar–*H*), 7.15–6.99 (remaining Ar–*H* signals overlap with toluene peaks), 2.40 (br s, 3H, C*H*(CH_3)$_2$), 2.21 (br s, 3H, C*H*(CH_3)$_2$), 1.37 (br s, 9H, CH(C*H*$_3$)$_2$), 1.02 (br s, 9H, CH(C*H*$_3$)$_2$), 0.71 (br s, 9H, CH(C*H*$_3$)$_2$), -0.32 (br s, 9H, CH(C*H*$_3$)$_2$), –10.79 to –11.18 (m, 3H, Os–*H*).

^{1}H{^{31}P} NMR (500 MHz, toluene-*d*$_8$, –78 ^{o}C): δ(ppm) δ 8.18 (d, *J* = 7.4 Hz, 3H, Ar–*H*), 7.25 (t, *J* = 6.7 Hz, 3H, Ar–*H*), 7.15–6.99 (remaining Ar–*H* signals overlap with toluene peaks), 2.40 (br m, 3H, C*H*(CH_3)$_2$), 2.21 (br m, 3H, C*H*(CH_3)$_2$), 1.38 (br s, 9H, CH(C*H*$_3$)$_2$), 1.02 (br s, 9H, CH(C*H*$_3$)$_2$), 0.71 (br s, 9H, CH(C*H*$_3$)$_2$), –0.32 (br s, 9H, CH(C*H*$_3$)$_2$), –10.37 (s, 3H, Os–*H*).

^{31}P{^{1}H} NMR (202 MHz, toluene-*d*$_8$, –78 ^{o}C): δ(ppm) 62.1 (s).

^{31}P NMR (202 MHz, toluene-*d*$_8$, –78 ^{o}C): δ(ppm) 62.1 (br s).

IR (thin film from C_6D_6): *ν*(OsH) = 1985 cm^{-1}.

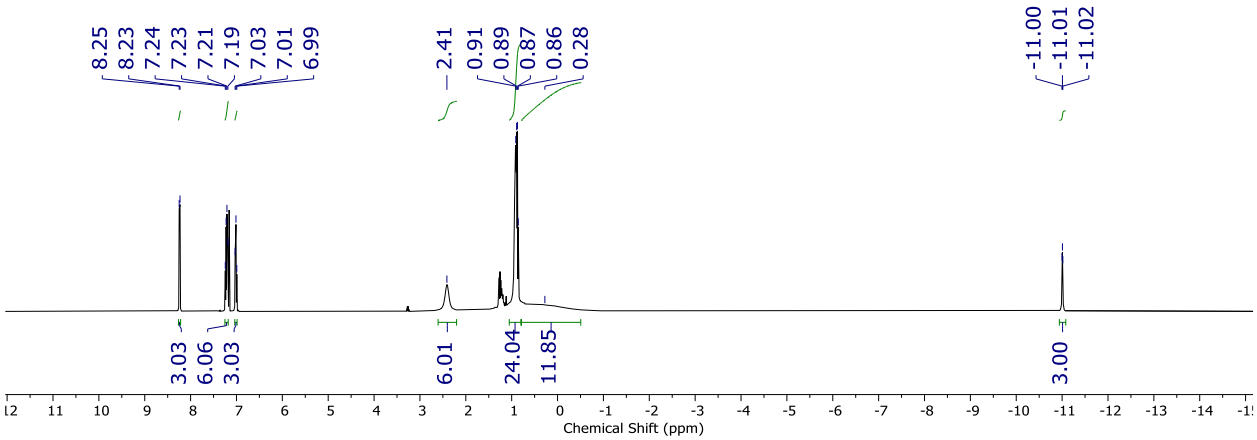

Figure 3.16. ^{1}H NMR spectrum (400 MHz, C_6D_6, 25 °C) of $P_3{}^{Si}OsH_3$.

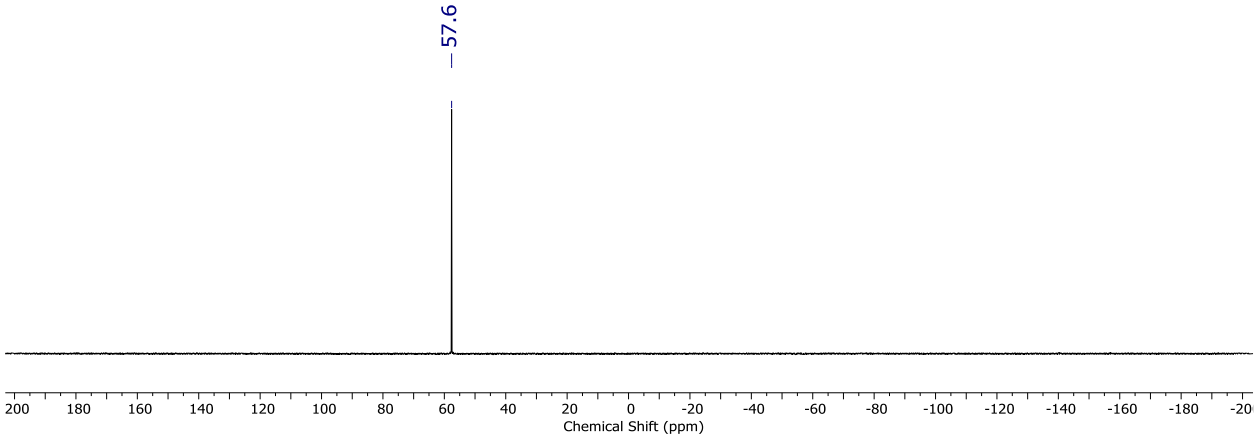

Figure 3.17. $^{31}P\{^{1}H\}$ NMR spectrum (162 MHz, C_6D_6, 25 °C) of $P_3{}^{Si}OsH_3$.

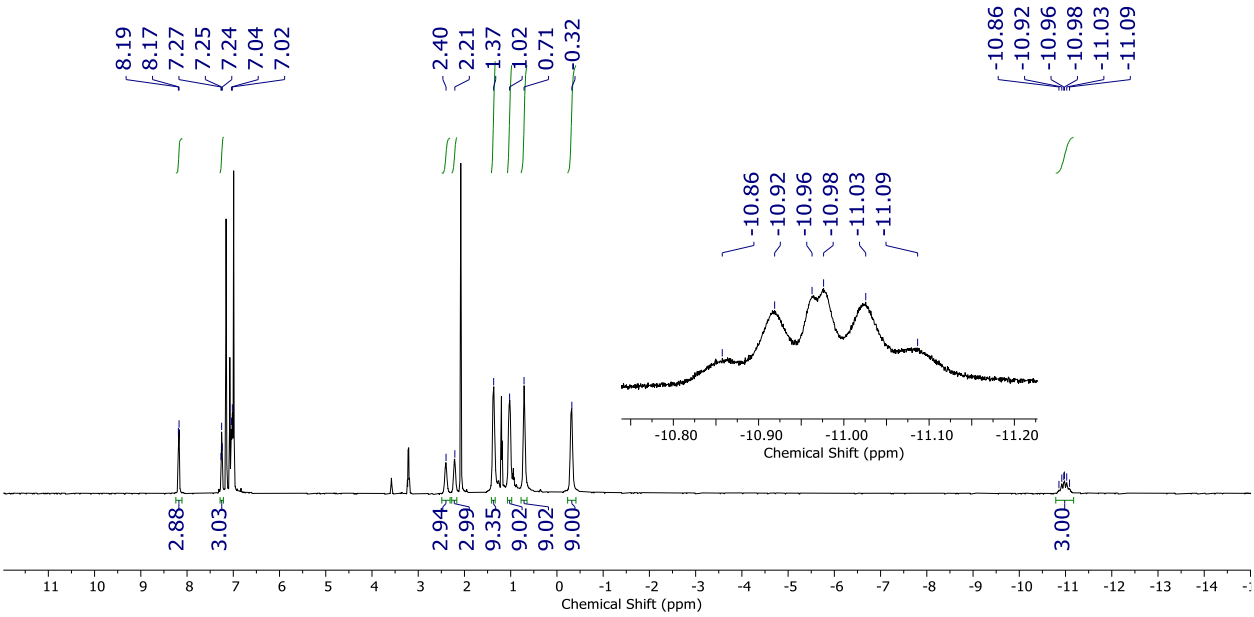

Figure 3.18. ^{1}H NMR spectrum (500 MHz, toluene-d_8, –78 °C) of $P_3{}^{Si}OsH_3$.

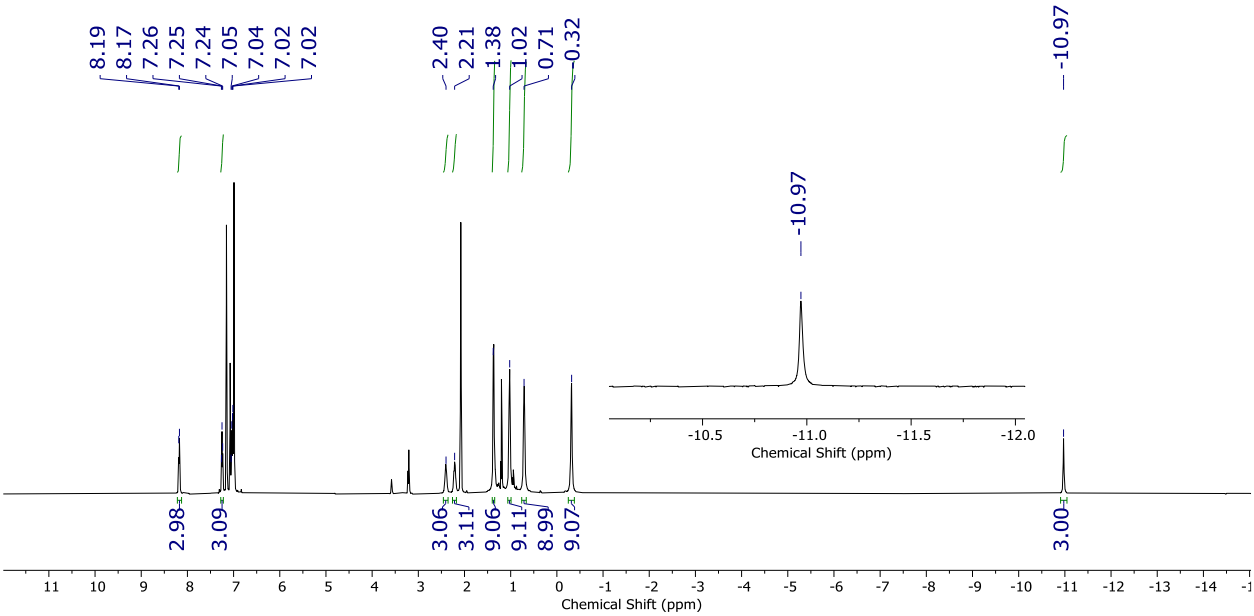

Figure 3.19. ^{1}H{^{31}P} NMR spectrum (500 MHz, toluene-d_8, –78 °C) of $P_3{}^{Si}OsH_3$.

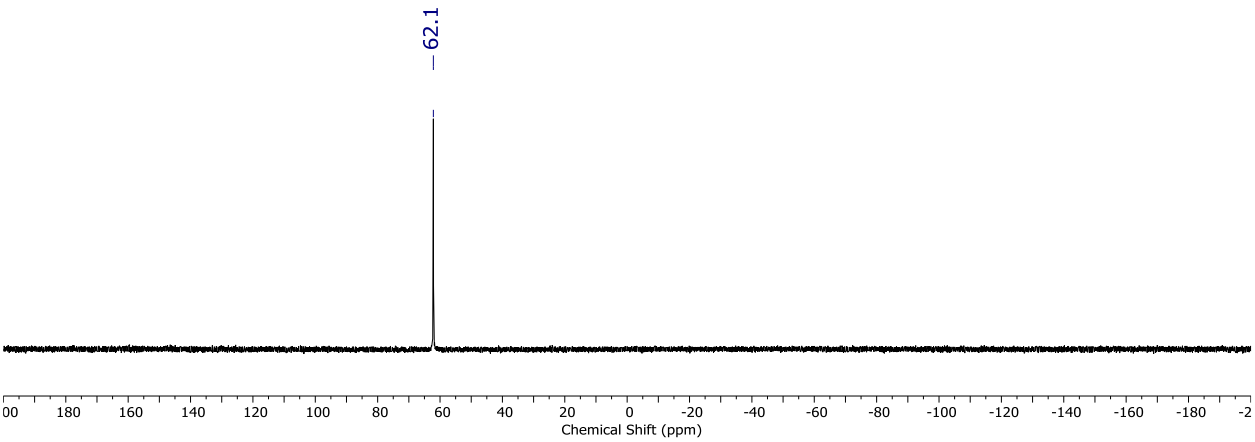

Figure 3.20. $^{31}P\{^{1}H\}$ NMR spectrum (202 MHz, toluene-d_8, –78 °C) of $P_3{}^{Si}OsH_3$.

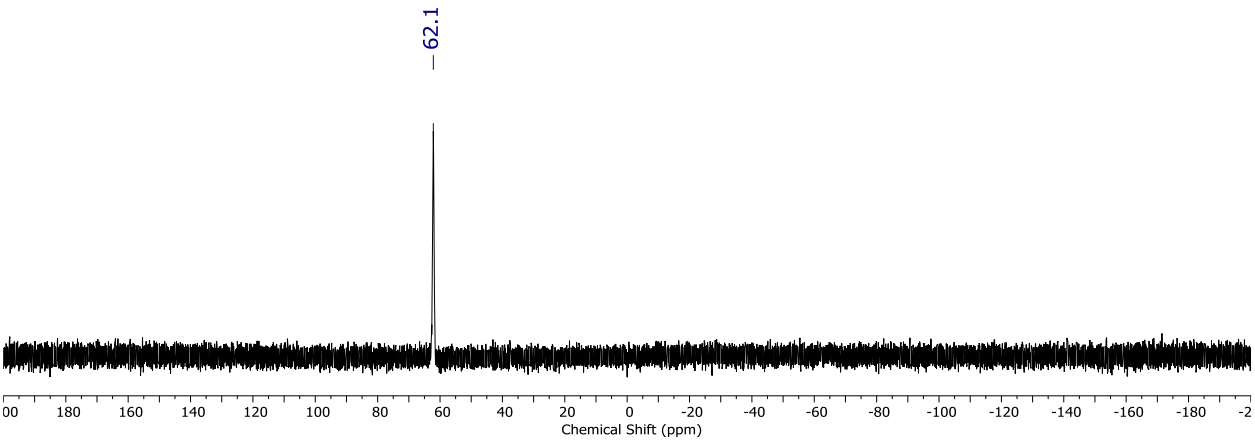

Figure 3.21. ^{31}P NMR spectrum (202 MHz, toluene-d_8, –78 °C) of $P_3{}^{Si}OsH_3$.

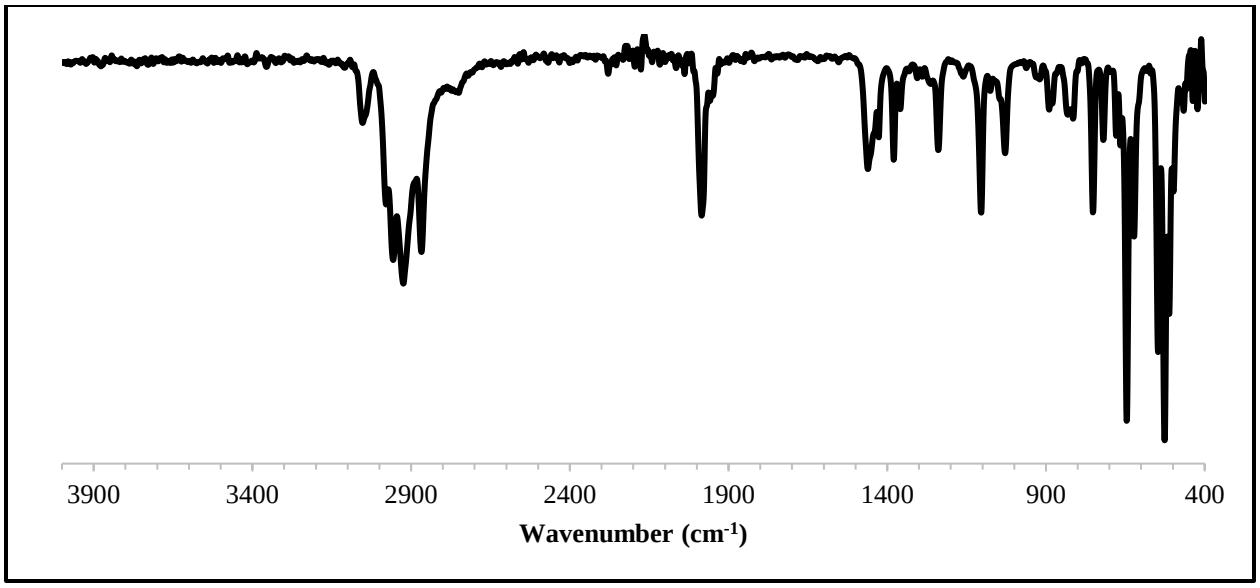

Figure 3.22. IR spectrum of $P_3^{Si}OsH_3$ deposited as a thin film from C_6D_6.

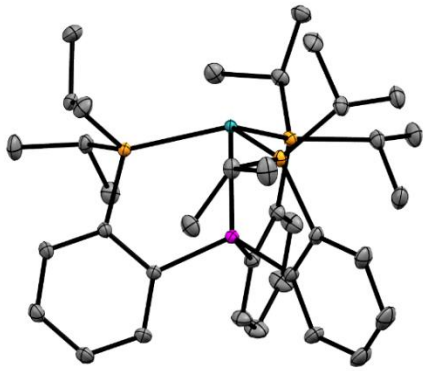

Figure 3.23. XRD structure of $P_3^{Si}OsH_3$ with thermal ellipsoids set at 50% probability. Hydrogen atoms are omitted for clarity. The terminal hydride ligands could not be located in the Fourier difference map. Color code: Os = teal, P = orange, Si = pink, C = gray.

$P_3^{Si}RuH_3$. P_3^{Si}Ru–Cl (0.0200 g, 0.0269 mmol) was dissolved in 2 mL of THF to give a red-brown solution. $LiEt_3BH$ (1.0 M in THF, 3.00 equiv, 0.806 mmol, 80.6 µL) was then added at room temperature via micropipette. The reaction was stirred vigorously for two days at room temperature, after which the color of the reaction had changed from red-brown to yellow. The THF

was removed under vacuum, and the product was extracted into pentane (3 x 3 mL), filtered through celite, and dried under vacuum to yield $P_3^{Si}RuH_3$ (0.0159 g, 0.0223 mmol) in 83% yield. While no combustion analysis data or XRD structure was obtained, $P_3^{Si}RuH_3$ features a nearly identical ^{1}H NMR spectrum to that of $P_3^{Si}OsH_3$.

^{1}H NMR (400 MHz, C_6D_6, 25 ^{o}C): δ(ppm) 8.16 (d, *J* = 7.3 Hz, 3H, Ar–*H*), 7.20–7.18 (m, 6H, Ar–*H*), 7.01 (t, *J* = 7.3 Hz, 3H, Ar–*H*), 2.31 (br s, 6H, C*H*$(CH_3)_2$), 0.91 (br s, 18H, CH$(CH_3)_2$), 0.57 (br s, 18H, CH$(CH_3)_2$), –8.44 (s, 3H, Ru–*H*).

^{31}P{^{1}H} NMR (162 MHz, C_6D_6, 25 ^{o}C): δ(ppm) 92.9 (s).

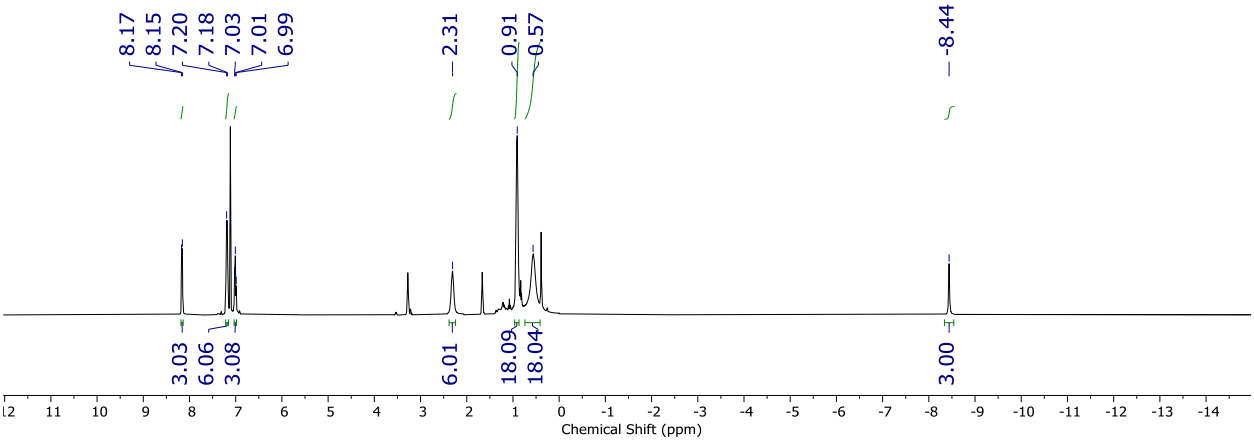

Figure 3.24. ^{1}H NMR spectrum (400 MHz, C_6D_6, 25 °C) of $P_3^{Si}RuH_3$.

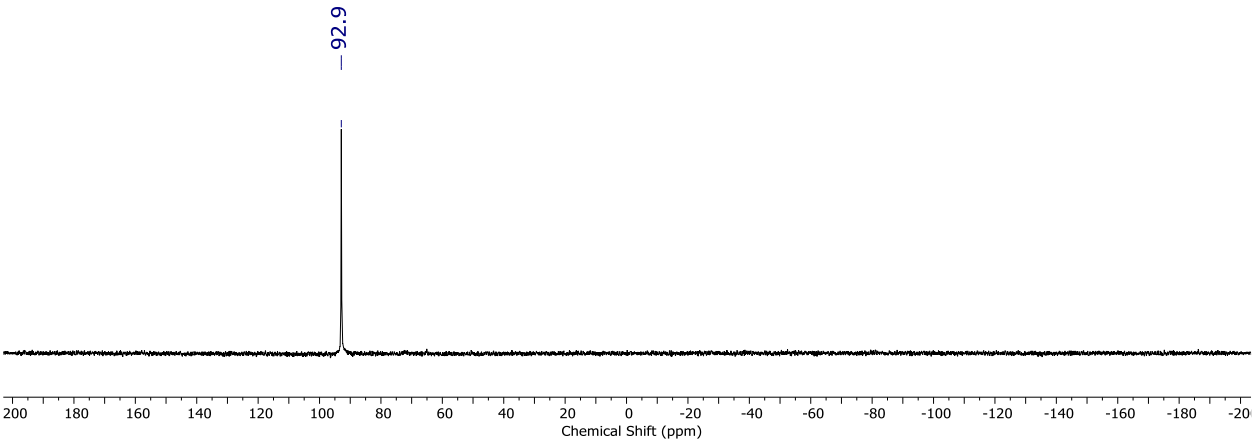

Figure 3.25. $^{31}P\{^{1}H\}$ NMR spectrum (162 MHz, C_6D_6, 25 °C) of $P_3{}^{Si}RuH_3$.

3.4.3. Ammonia Production and Quantification Studies

Standard NH_3 Generation Reaction Procedure

All solvents were stirred with Na/K for ≥ 1 hour and filtered prior to use. In a nitrogen-filled glovebox, the precatalyst (2.0 μmol) was weighed into a vial.* The precatalyst was then transferred quantitatively into a Schlenk tube as a suspension in Et_2O. The Et_2O was then evaporated to provide a solid layer (or thin film) of precatalyst at the bottom of the Schlenk tube. The acid and reductant were then added as solids and the tube was equipped with a stir bar. The tube was then cooled to 77 K in the coldwell. To the cold tube was added Et_2O to produce the desired concentration of precatalyst. The temperature of the system was allowed to equilibrate for 5 minutes and then the tube was sealed with a Teflon screw-valve. This tube was passed out of the box into a liquid nitrogen bath and transported to a fume hood. The tube was then transferred to a dry ice/acetone bath (–78 °C) where it thawed and was allowed to stir at –78 °C. For runs utilizing $HBAr^F{}_4$, reactions were stirred at –78 °C for 1 hour, followed by stirring at room temperature for 45 minutes. For all other runs, reactions were allowed to stir and gradually warm to room

temperature overnight. To ensure reproducibility, all experiments were conducted in 200 mL Schlenk tubes (51 mm OD) using 25 mm stir bars, and stirring was conducted at ~900 rpm.

*In cases where less than 2.0 μmol of precatalyst was used, stock solutions (in THF) were used to avoid having to weigh very small amounts.

Ammonia and Hydrazine Quantification

The catalytic reaction mixture was cooled to 77 K and allowed to freeze. The reaction vessel was then opened to atmosphere and to the frozen solution was added an excess (with respect to acid) solution of a NaO^{t}Bu solution in MeOH (0.25 mM) dropwise over 1–2 minutes. This solution was allowed to freeze, then the headspace of the tube was evacuated and the tube was sealed. The tube was then allowed to warm to room temperature and stirred at room temperature for at least 10 minutes. An additional Schlenk tube was charged with HCl (3 mL of a 2.0 M solution in Et_2O, 6 mmol) to serve as a collection flask. The volatiles of the reaction mixture were vacuum transferred at room temperature into this collection flask. After completion of the vacuum transfer, the collection flask was sealed and warmed to room temperature. Solvent was removed *in vacuo*, and the remaining residue dissolved in 1 mL of DI H_2O. A 20 μL aliquot of this solution was then analyzed for the presence of NH_3 (present as $[NH_4][Cl]$) by the indophenol method.[38] Quantification was performed with UV-visible spectroscopy by analyzing the absorbance at 635 nm. A further aliquot of this solution was analyzed for the presence of N_2H_4 (present as $[N_2H_5][Cl]$) by a standard colorimetric method.[39] Quantification was performed with UV-visible spectroscopy by analyzing the absorbance at 458 nm.

In the case of runs with [H_3NPh][OTf], [H_3N-2,5-$Cl_2C_6H_3$][OTf], [*N*-Me-H_2NPh][OTf], and [H_3NPh][$BAr^F{}_4$], it was found that the corresponding aniline derivative in the form of anilinium chloride was present in the receiving vessel. The anilinium chloride interfered with the indophenol and hydrazine detection methods. Therefore, quantification for NH_3 was performed by extracting the solid residue into 1 mL of DMSO-d_6 that had 1,4-dioxane as an internal standard. Integration of the ^{1}H NMR peak observed for [NH_4][Cl] against the peak of 1,4-dioxane was used to quantify the ammonium present. This ^{1}H NMR detection method was also used to differentiate [$^{14}NH_4$][Cl] and [$^{15}NH_4$][Cl] produced in the control reactions conducted with [$H_2{}^{15}NPh_2$][OTf] and [$H_3{}^{15}$NPh][OTf].

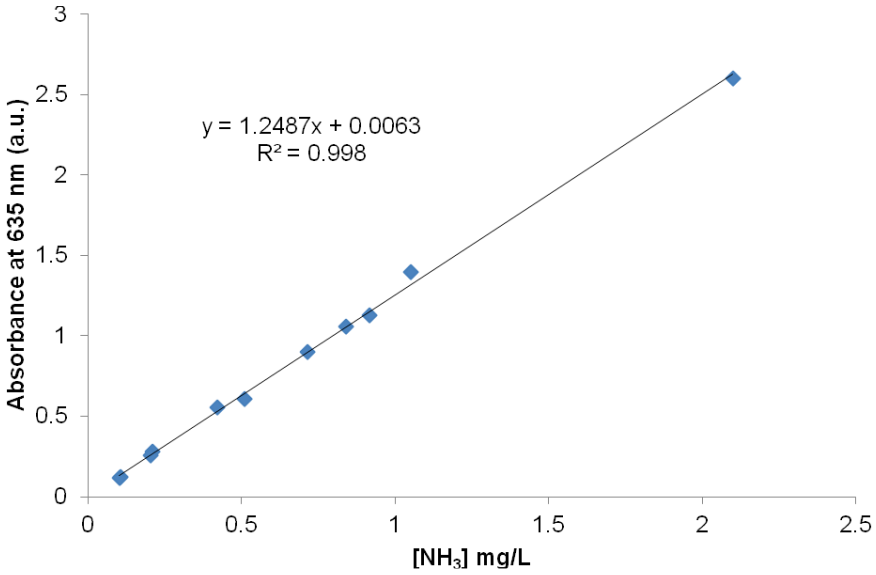

Figure 3.26. Calibration curve used for NH_3 quantification.

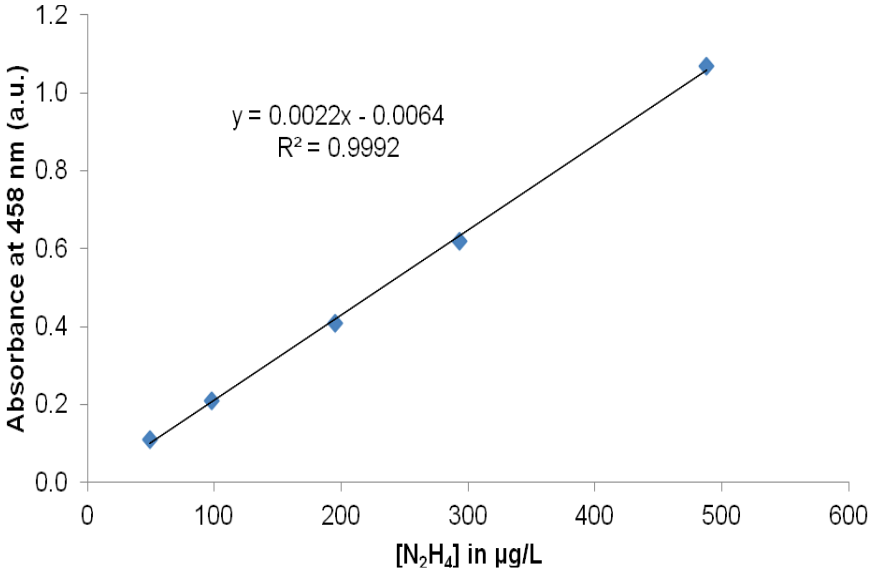

Figure 3.27. Calibration curve used for N_2H_4 quantification.

Table 3.3. UV-visible quantification results for standard NH_3 generation experiments with $[K(THF)_2][P_3^{Si}Os–N_2]$.

Entry	Total volume of Et_2O (mL)	[Os]–N_2^- (µmol)	Acid (equiv)	Reductant (equiv)	NH_4Cl (µmol)	NH_3/Os (equiv)	Yield NH_3/H^+ (%)
A	2.0	2.0	46[a]	50[b]	2.5	1.2	8.0
B	2.0	2.0	46[a]	50[b]	3.4	1.7	11.1
C	2.0	2.0	46[a]	50[b]	3.7	1.9	12.1
Avg.						1.6 ± 0.3	10 ± 2
D	2.0	2.0	46[c]	50[d]	12.7	6.4	41.9
E	2.0	2.0	46[c]	50[d]	13.5	6.8	44.0
F	2.0	2.0	46[c]	50[d]	14.7	7.4	48.5
G	2.0	2.0	46[c]	50[d]	15.4	7.8	50.8
Avg.						7.1 ± 0.6	46 ± 4
H	1.1	0.48	150[c]	180[d]	8.3	17.2	34.5
I	1.1	0.48	150[c]	180[d]	8.5	17.8	35.6
J	1.1	0.48	150[c]	180[d]	8.5	17.9	35.7
Avg.						18 ± 1	35 ± 1
K	1.5	0.19	500[c]	800[d]	9.1	47.9	28.7
L	1.5	0.19	500[c]	800[d]	9.9	52.5	31.5
Avg.						50 ± 3	30 ± 2
M	2.0	0.16	800[c]	960[d]	12.9	82.1	30.8

N	2.0	0.16	800[c]	960[d]	13.2	83.9	31.5
O	2.0	0.16	800[c]	960[d]	14.4	91.8	34.4
Avg.						86 ± 5	32 ± 2
P	2.8	0.12	1500[c]	1800[d]	13.1	110.4	22.1
Q	2.8	0.12	1500[c]	1800[d]	13.5	112.9	22.6
R	2.8	0.12	1500[c]	1800[d]	13.8	115.1	23.0
S	2.8	0.12	1500[c]	1800[d]	15.2	126.4	25.3
T	2.8	0.12	1500[c]	1800[d]	16.4	136.3	27.3
Avg.						120 ± 11	24 ± 2
U	2.0	2.0	46[e]	50[d]	15.3	7.7	50.3
V	2.0	2.0	46[e]	50[d]	16.0	8.1	52.7
Avg.						7.9 ± 0.3	52 ± 2
W	2.0	2.0	46[f]	50[d]	15.7	7.9	52
X	2.0	2.0	46[g]	50[d]	11.7	5.9	38.7
Y	2.0	2.0	46[g]	50[d]	13.2	6.6	43.2
Avg.						6.3 ± 0.5	41 ± 3
Z	2.0	2.0	46[h]	50[d]	0.2	0.1	0.7
AA	2.0	2.0	46[h]	50[d]	0.3	0.15	1.0
Avg.						0.1 ± 0.1	0.8 ± 0.2
BB	2.0	2.0	46[i]	50[d]	2.1	1.1	7.0
CC	2.0	2.0	46[i]	50[d]	2.5	1.3	8.2
Avg.						1.2 ± 0.1	7.6 ± 0.8
DD	2.0	2.0	46[j]	50[d]	1.2	0.6	4.1
EE	2.0	2.0	46[j]	50[d]	1.5	0.8	5.1
Avg.						0.7 ± 0.1	4.6 ± 0.7
FF**	2.0	2.0	46[c]	50[d]	12.3	6.2	40.4
GG	2.0	2.0	46[c]	50[k]	0	0	0
HH	2.0	2.0	46[c]	50[l]	0	0	0

[a]$HBAr^F_4$. [b]KC_8. [c]$[H_2NPh_2][OTf]$. [d]Cp^*_2Co. [e]$[H_3NPh][OTf]$. [f]$[H_3N\text{-}2,5\text{-}Cl_2C_6H_3][OTf]$. [g][*N*-Me-$H_2NPh$][OTf]. [h]$[H_2NPh_2][BAr^F_4]$. [i]$[H_3NPh][BAr^F_4]$. [j]HOTf. [k]$Cp_2Co$. [l]$Cp^*_2Cr$.

*N_2H_4 was not detected in the catalytic runs.

**Run at −40 °C instead of −78 °C.

Table 3.4. UV-visible quantification results for standard NH_3 generation experiments with $[K(THF)_2][P_3^{Si}Ru–N_2]$.

Entry	Total volume of Et_2O (mL)	$[Ru]–N_2^-$ (μmol)	Acid (equiv)	Reductant (equiv)	NH_4Cl (μmol)	NH_3/Ru (equiv)	Yield NH_3/H^+ (%)
A	2.0	2.0	46[a]	50[b]	7.8	4.0	25.8
B	2.0	2.0	46[a]	50[b]	8.8	4.3	27.7
C	2.0	2.0	46[a]	50[b]	8.9	4.6	29.7
Avg.						4.3 ± 0.3	28 ± 2
D	2.0	2.0	46[c]	50[d]	0.7	0.4	2.4
E	2.0	2.0	46[c]	50[d]	2.2	1.1	7.4
Avg.						0.8 ± 0.5	4.9 ± 3.5

[a]$HBAr^F_4$. [b]KC_8. [c]$[H_2NPh_2][OTf]$. [d]Cp^*_2Co.

*N_2H_4 was not detected in the catalytic runs.

Table 3.5. UV-visible quantification results for standard NH_3 generation experiments with $[Na(12\text{-crown-4})_2][P_3^{Si}Fe–N_2]$.

Entry	Total volume of Et_2O (mL)	$[Fe]–N_2^-$ (μmol)	Acid (equiv)	Reductant (equiv)	NH_4Cl (μmol)	NH_3/Fe (equiv)	Yield NH_3/H^+ (%)
A	2.0	2.0	46[a]	50[b]	2.2	1.1	7.3
B	2.0	2.0	46[a]	50[b]	2.9	1.5	9.8
C	2.0	2.0	46[a]	50[b]	3.4	1.7	10.8
Avg.						1.4 ± 0.3	9.3 ± 1.8

[a]$[H_2NPh_2][OTf]$. [b]Cp^*_2Co.

*N_2H_4 was not detected in the catalytic runs.

Table 3.6. UV-visible quantification results for standard NH_3 generation experiments with [Na(12-crown-4)$_2$][$P_3^BFe–N_2$].

Entry	Total volume of Et_2O (mL)	$P_3^BFe–N_2^-$ (μmol)	Acid (equiv)	Reductant (equiv)	NH_4Cl (μmol)	NH_3/Fe (equiv)	Yield NH_3/H^+ (%)
A	2.8	0.12	1500[a]	1800[b]	2.2	18.3	3.7
B	2.8	0.12	1500[a]	1800[b]	3.1	25.5	5.1
Avg.						22 ± 5	4.4 ± 1.0

[a][H_2NPh_2][OTf]. [b]Cp*$_2$Co.

*N_2H_4 was not detected in the catalytic runs.

Table 3.7. UV-visible quantification results for standard NH_3 generation experiments with $P_3^{Si}Os(N_2)(H)$.

Entry	Total volume of Et_2O (mL)	[Os](N_2)(H) (μmol)	Acid (equiv)	Reductant (equiv)	NH_4Cl (μmol)	NH_3/Os (equiv)	Yield NH_3/H^+ (%)
A	2.0	2.0	46[a]	50[b]	0	0	0
B	2.0	2.0	46[c]	50[d]	0	0	0

[a]$HBAr^F_4$. [b]KC_8. [c][H_2NPh_2][OTf]. [d]Cp*$_2$Co.

*N_2H_4 was not detected in the catalytic runs.

Table 3.8. UV-visible quantification results for standard NH_3 generation experiments with $P_3^{Si}OsH_3$.

Entry	Total volume of Et_2O (mL)	[Os]H_3 (μmol)	Acid (equiv)	Reductant (equiv)	NH_4Cl (μmol)	NH_3/Os (equiv)	Yield NH_3/H^+ (%)
A	2.0	2.0	46[a]	50[b]	0	0	0
B	2.0	2.0	46[c]	50[d]	0	0	0

[a]$HBAr^F_4$. [b]KC_8. [c][H_2NPh_2][OTf]. [d]Cp*$_2$Co.

*N_2H_4 was not detected in the catalytic runs.

Table 3.9. UV-visible quantification results for standard NH_3 generation experiments with $[P_3^{Si}Os{=}NNH_2][OTf]$.

Entry	Total volume of Et_2O (mL)	[Os]=NNH_2^+ (μmol)	Acid (equiv)	Reductant (equiv)	NH_4Cl (μmol)	NH_3/Os (equiv)	Yield NH_3/H^+ (%)
A	2.0	2.0	46[a]	50[b]	5.3	2.6	17

[a]$[H_2NPh_2][OTf]$. [b]Cp^*_2Co.

*N_2H_4 was not detected in the catalytic runs.

Table 3.10. UV-visible quantification results for standard NH_3 generation experiments with $P_3^{Si}Os–Cl$.

Entry	Total volume of Et_2O (mL)	[Os]–Cl (μmol)	Acid (equiv)	Reductant (equiv)	NH_4Cl (μmol)	NH_3/Os (equiv)	Yield NH_3/H^+ (%)
A	2.0	2.0	46[a]	50[b]	5.0	2.5	16

[a]$[H_2NPh_2][OTf]$. [b]Cp^*_2Co.

*N_2H_4 was not detected in the catalytic runs.

Table 3.11. UV-visible quantification results for standard NH_3 generation experiments with $[(\eta^6\text{-}C_6H_6)Os(Cl)(\mu\text{-}Cl)]_2$.

Entry	Total volume of Et_2O (mL)	Os-dimer (μmol)	Acid (equiv)	Reductant (equiv)	NH_4Cl (μmol)	NH_3/Os (equiv)	Yield NH_3/H^+ (%)
A	2.0	2.0	46[a]	50[b]	0	0	0

[a]$[H_2NPh_2][OTf]$. [b]Cp^*_2Co.

*N_2H_4 was not detected in the catalytic runs.

NH_3 Generation Reaction with Periodic Substrate Reloading – Procedure with $[K(THF)_2][P_3^{Si}Os–N_2]$

All solvents were stirred with Na/K for ≥ 1 hour and filtered prior to use. In a nitrogen-filled

glovebox, a stock solution of the precatalyst in THF was used to deliver the precatalyst to the Schlenk tube. The THF was then evaporated to provide a thin film of the precatalyst at the bottom of the Schlenk tube. The acid and reductant were then added as solids and the tube was equipped with a stir bar. The tube was then cooled to 77 K in the coldwell. To the cold tube was added Et_2O. The temperature of the system was allowed to equilibrate for 5 minutes and then the tube was sealed with a Teflon screw-valve. The coldwell cooling bath was switched from a liquid nitrogen bath to a dry ice/acetone bath (–78 °C). In the coldwell, the mixture in the sealed tube was stirred at –78 °C for 3 hours. Then, without allowing the tube to warm above –78 °C, the coldwell bath was switched from dry ice/acetone to a liquid nitrogen bath. After fifteen minutes the reaction mixture was observed to have frozen, and at this time the tube was opened. To the cold tube was added acid and reductant as solids. Then an additional fraction of Et_2O was added. The coldwell cooling bath was switched from a liquid nitrogen bath to a dry ice/acetone bath. In the coldwell, the mixture in the sealed tube was stirred at –78 °C for 3 hours. These reloading steps were repeated the desired number of times. Then the tube was allowed to stir and gradually warm to room temperature overnight.

Table 3.12. UV-visible quantification results for NH_3 generation experiments with $[K(THF)_2][P_3^{Si}Os–N_2]$, with reloading.

Entry	Number of Loadings	Total volume of Et_2O (mL)	[Os]–N_2^- (μmol)	Acid (equiv)	Reductant (equiv)	NH_4Cl (μmol)	NH_3/Os (equiv)	Yield NH_3/H^+ (%)
A	2	2.0 x 2	0.16	800[a] x 2	960[b] x 2	19.3	122	23.0

[a]$[H_2NPh_2][OTf]$. [b]Cp^*_2Co.

*N_2H_4 was not detected in the catalytic runs.

Control Experiments with $[H_2{}^{15}NPh_2][OTf]$ and $[H_3{}^{15}NPh][OTf]$

The procedure was the same as the standard NH_3 generation reaction procedure with 2.0 μmol of $[K(THF)_2][P_3{}^{Si}Os–N_2]$ catalyst, 46 equiv of $[H_2{}^{15}NPh_2][OTf]$ or $[H_3{}^{15}NPh][OTf]$, and 50 equiv of Cp^*_2Co. The product was analyzed by ^1H NMR and only the diagnostic triplet of $[^{14}NH_4][Cl]$ was observed.

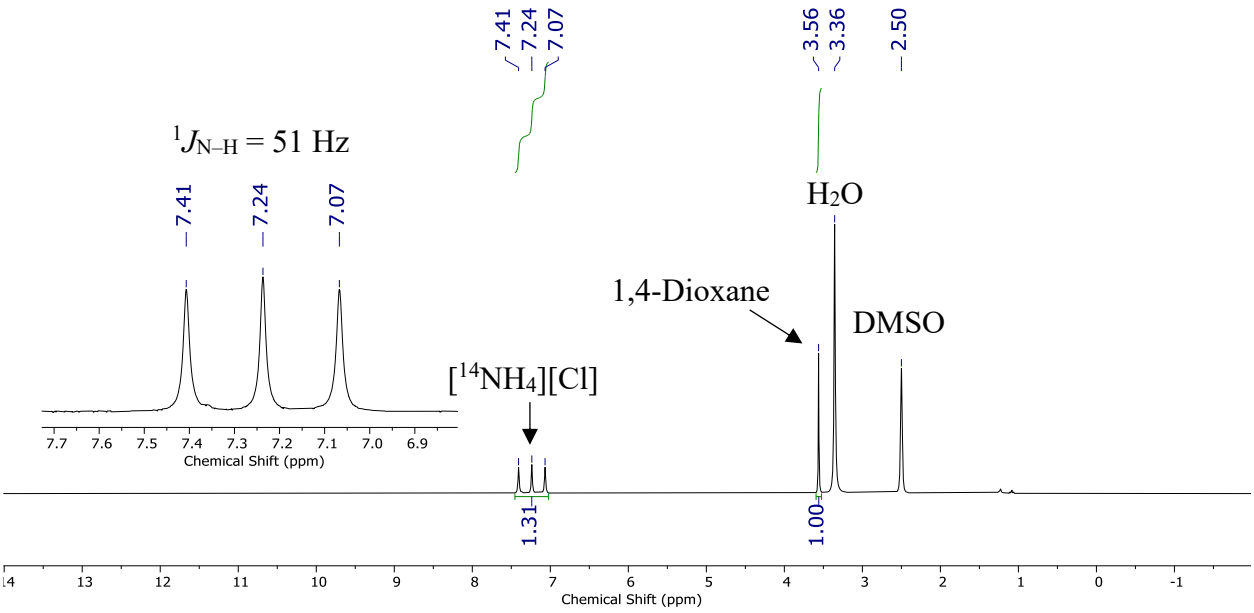

Figure 3.28. ^1H NMR spectrum (300 MHz, DMSO-d_6, 25 °C) of $[^{14}NH_4][Cl]$ produced from a catalytic reaction with $[K(THF)_2][P_3{}^{Si}Os–N_2]$ catalyst, 46 equiv of $[H_2{}^{15}NPh_2][OTf]$, and 50 equiv of Cp^*_2Co under an atmosphere of $^{14}N_2$.

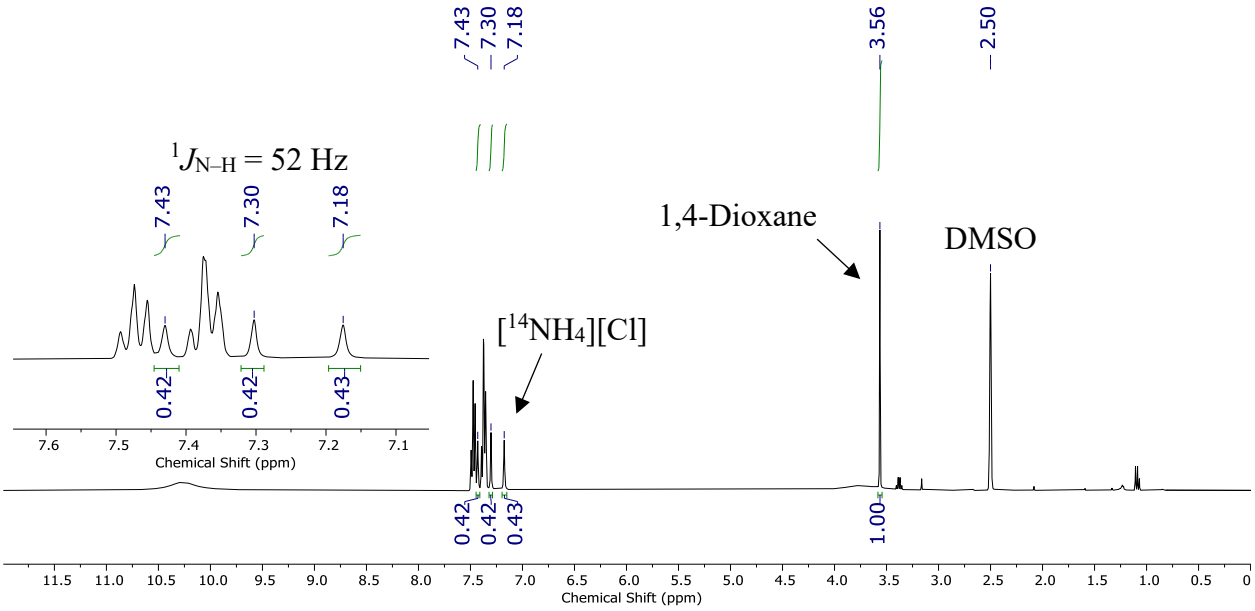

Figure 3.29. ^{1}H NMR spectrum (400 MHz, DMSO-d_6, 25 °C) of [$^{14}NH_4$][Cl] produced from a catalytic reaction with [K(THF)$_2$][P$_3^{Si}$Os–N$_2$] catalyst, 46 equiv of [H$_3$^{15}NPh][OTf], and 50 equiv of Cp*$_2$Co under an atmosphere of $^{14}N_2$.

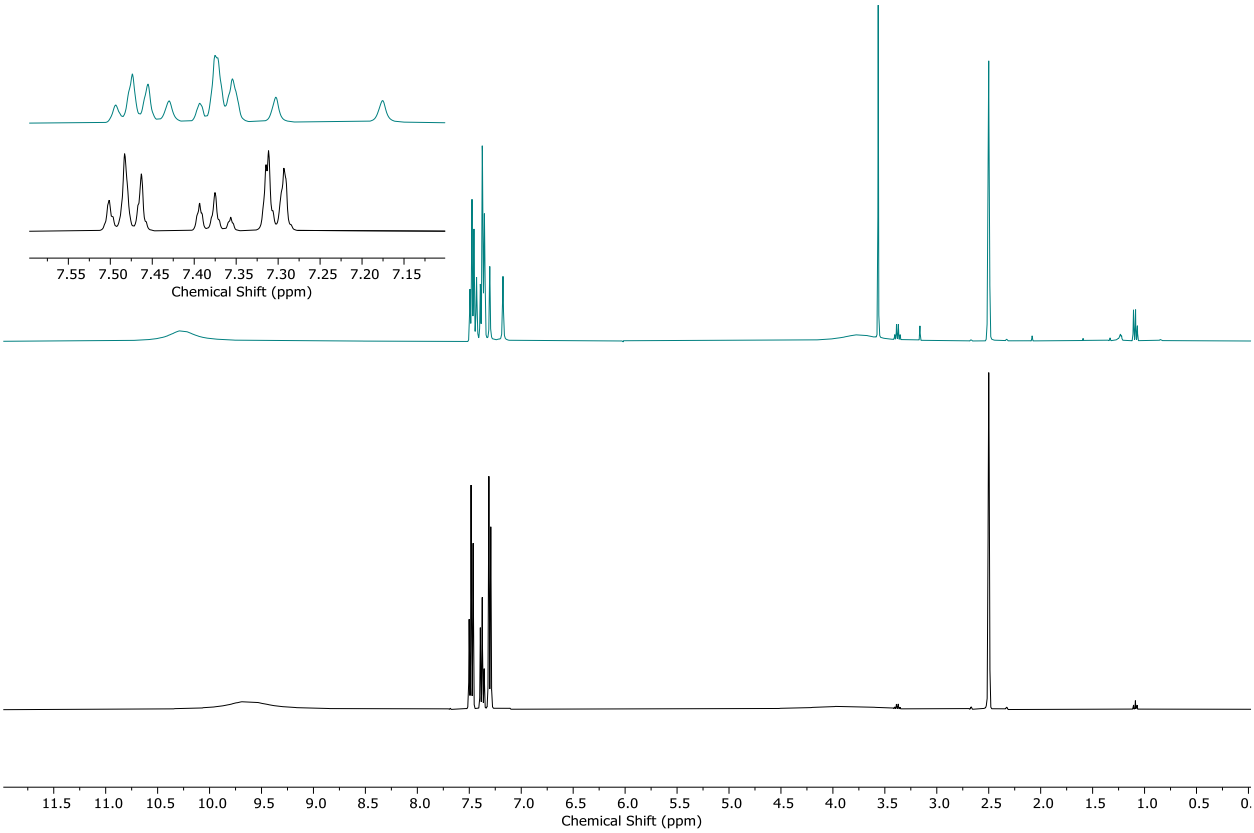

Figure 3.30. Stacked ^{1}H NMR spectra (400 MHz, DMSO-d_6, 25 °C) of the volatiles from the catalytic reaction described in Figure 3.29 (top) and an authentic sample of [H_3NPh][OTf] (bottom).

3.4.4. Miscellaneous Experiments

Treatment of [K(THF)$_2$][P$_3^{Si}$Os–N$_2$] with 10 equiv HBAr$^F_4$ and 12 equiv KC$_8$

In the glovebox, [K(THF)$_2$][P$_3^{Si}$Os–N$_2$] (0.0088 g, 8.7 x 10^{-3} mmol) was weighed out into a 20 mL scintillation vial, equipped with a stir bar, and cooled to 77 K inside the coldwell chilled with an external liquid nitrogen bath. 1 mL of Et_2O was added dropwise to the vial and allowed to freeze. A solution of HBAr$^F_4$ (10 equiv, 0.087 mmol, 0.088 g) in Et_2O (1 mL) was then layered dropwise. Residual acid was dissolved in Et_2O (0.5 mL) and added subsequently. This was allowed to chill

in the coldwell until the contents of the vial were frozen. Finally, KC_8 (12 equiv, 0.10 mmol, 0.014 g) was transferred as a suspension in Et_2O (1 mL) to the reaction vial. The vial was then sealed and its contents were cooled until the mixture was again frozen.

After thawing the mixture by replacing the liquid nitrogen bath with a dry ice/acetone bath (–78 °C), the reaction was stirred for 1 hour at –78 °C followed by 45 minutes at room temperature. The reaction mixture was then filtered through glass filter paper into a 20 mL vial containing triphenylphosphine (3.0 equiv, 0.026 mmol, 0.0068 g) as a ^{31}P NMR internal standard, concentrated to ½ the original volume, and transferred to an NMR tube. The integration of the ^{31}P resonances suggested the formation of $P_3^{Si}Os(N_2)(H)$ and $P_3^{Si}OsH_3$ in approximately 32% yield and 48% yield, respectively. The NMR solution was then transferred to a 20 mL vial in the glovebox, concentrated, redissolved in C_6D_6, and analyzed by ^1H and ^{31}P NMR spectroscopies. The data obtained matched the data reported above.

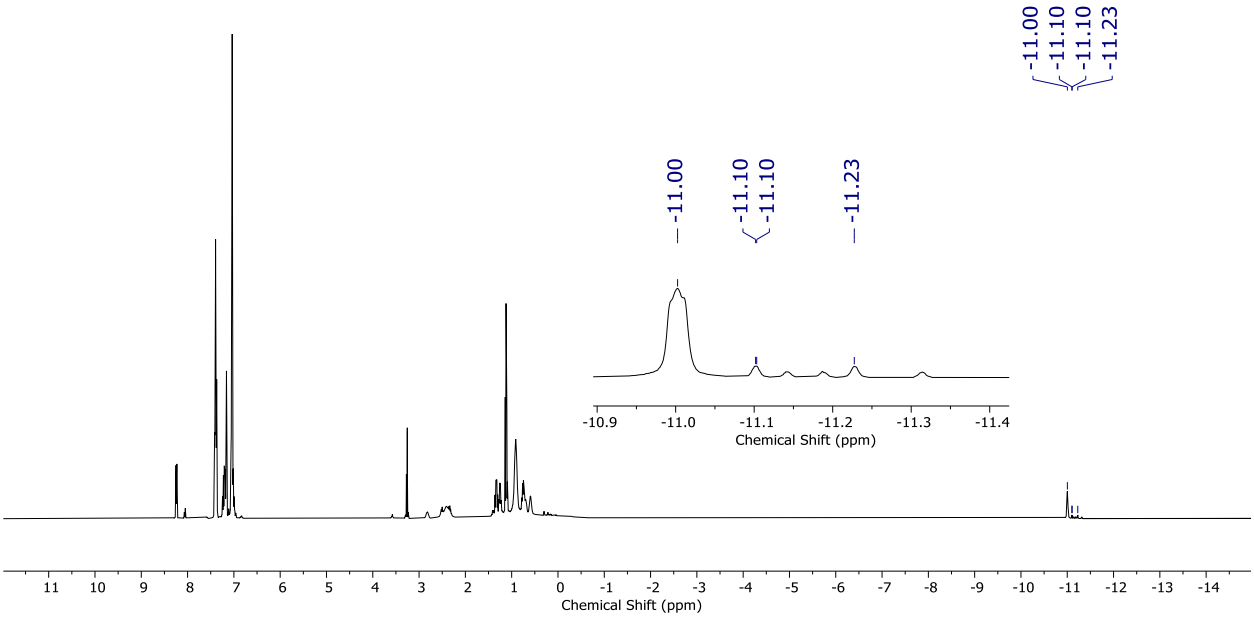

Figure 3.31. ^{1}H NMR spectrum (400 MHz, C_6D_6, 25 °C) for the addition of 10 equiv $HBAr^{F}_{4}$ and 12 equiv KC_8 to $[K(THF)_2][P_3{}^{Si}Os–N_2]$.

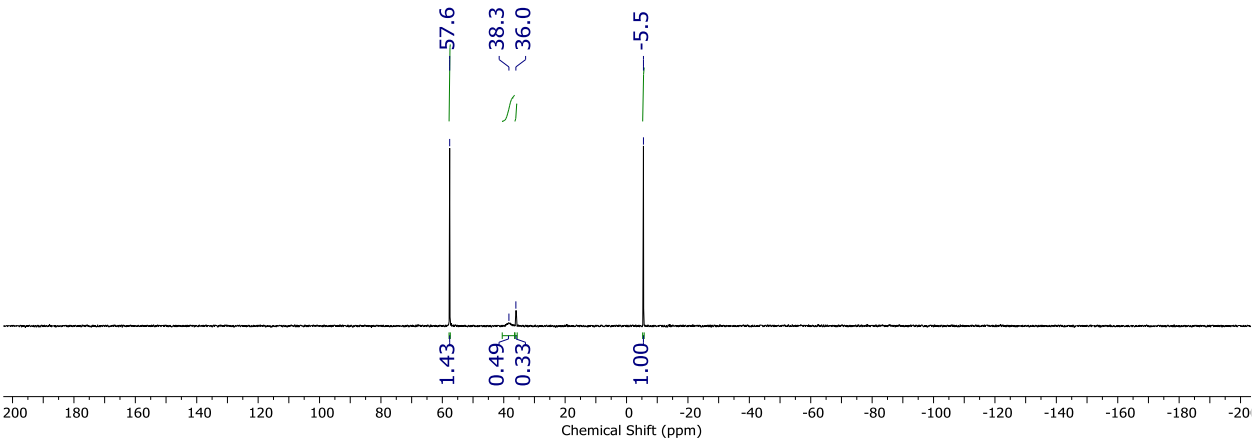

Figure 3.32. $^{31}P\{^{1}H\}$ NMR spectrum (162 MHz, C_6D_6, 25 °C) for the addition of 10 equiv $HBAr^{F}_{4}$ and 12 equiv KC_8 to $[K(THF)_2][P_3{}^{Si}Os–N_2]$.

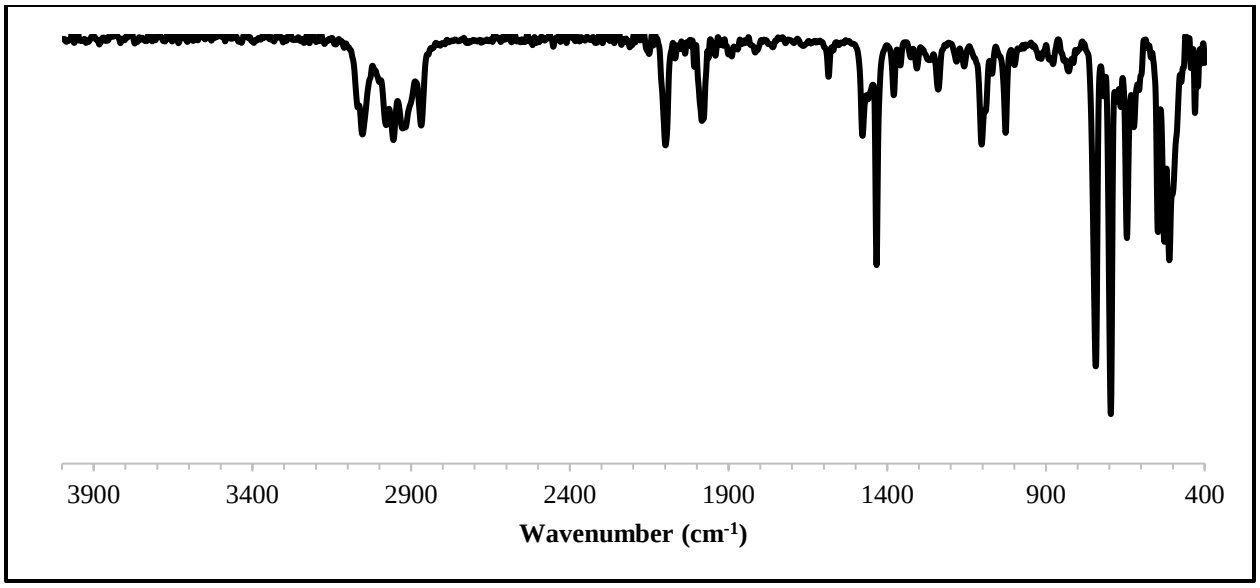

Figure 3.33. IR spectrum for the addition of 10 equiv $HBAr^F_4$ and 12 equiv KC_8 to $[K(THF)_2][P_3{}^{Si}Os–N_2]$; deposited as a thin film from C_6D_6.

Treatment of $[K(THF)_2][P_3{}^{Si}Ru–N_2]$ with 10 equiv $HBAr^F_4$ and 12 equiv KC_8

In the glovebox, $[K(THF)_2][P_3{}^{Si}Ru–N_2]$ (0.0088 g, 9.6 x 10^{-3} mmol) was weighed out into a 20 mL scintillation vial, equipped with a stir bar, and cooled to 77 K inside the coldwell chilled with an external liquid nitrogen bath. 1 mL of Et_2O was added dropwise to the vial and allowed to freeze. A solution of $HBAr^F_4$ (10 equiv, 0.096 mmol, 0.097 g) in Et_2O (1 mL) was then layered dropwise. Residual acid was dissolved in Et_2O (0.5 mL) and added subsequently. This was allowed to chill in the coldwell until the contents of the vial were frozen. Finally, KC_8 (12 equiv, 0.11 mmol, 0.016 g) was transferred as a suspension in Et_2O (1 mL) to the reaction vial. The vial was then sealed and its contents were cooled until the mixture was again frozen.

After thawing the mixture by replacing the liquid nitrogen bath with a dry ice/acetone bath (–

78 °C), the reaction was stirred for 1 hour at –78 °C followed by 45 minutes at room temperature. The reaction mixture was then filtered through glass filter paper into a 20 mL vial containing triphenylphosphine (3.0 equiv, 0.029 mmol, 0.0075 g) as a ^{31}P NMR internal standard, concentrated to ½ the original volume, and transferred to an NMR tube. The integration of the ^{31}P resonances suggested the formation of $P_3^{Si}Ru(N_2)(H)$ and $P_3^{Si}RuH_3$ in approximately 39% yield and 21% yield, respectively. The NMR solution was then transferred to a 20 mL vial in the glovebox, concentrated, redissolved in C_6D_6, and analyzed by ^1H and ^{31}P NMR spectroscopies. The data obtained matched the data reported above.

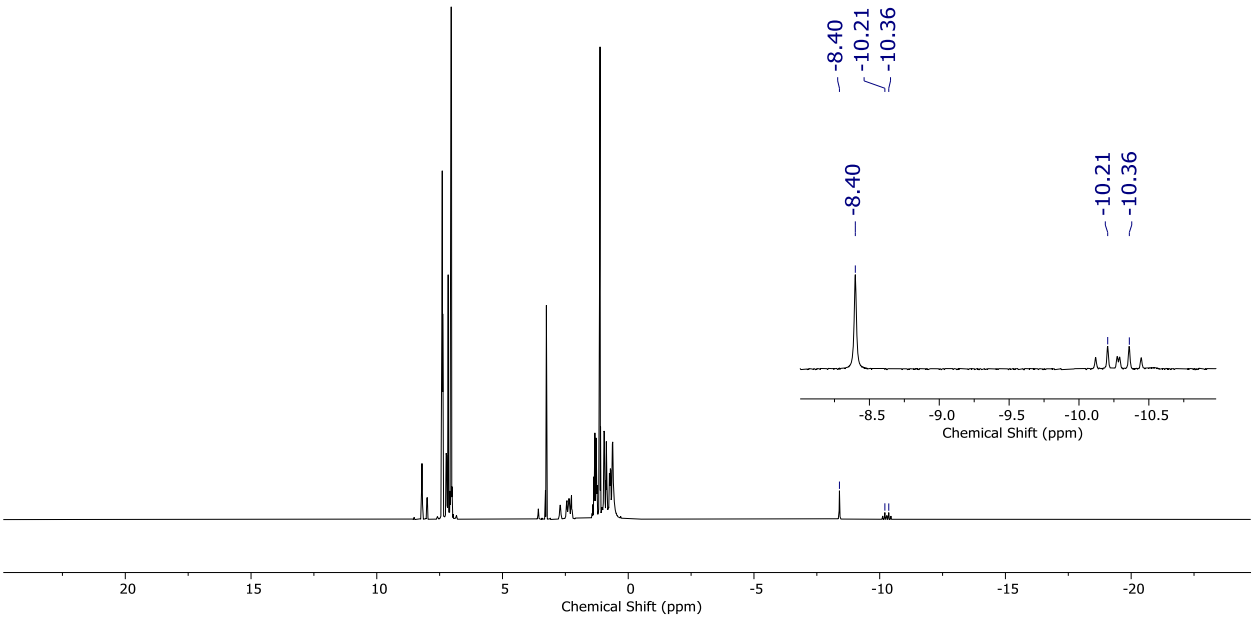

Figure 3.34. ^1H NMR spectrum (400 MHz, C_6D_6, 25 °C) for the addition of 10 equiv $HBAr^F_4$ and 12 equiv KC_8 to $[K(THF)_2][P_3^{Si}Ru–N_2]$.

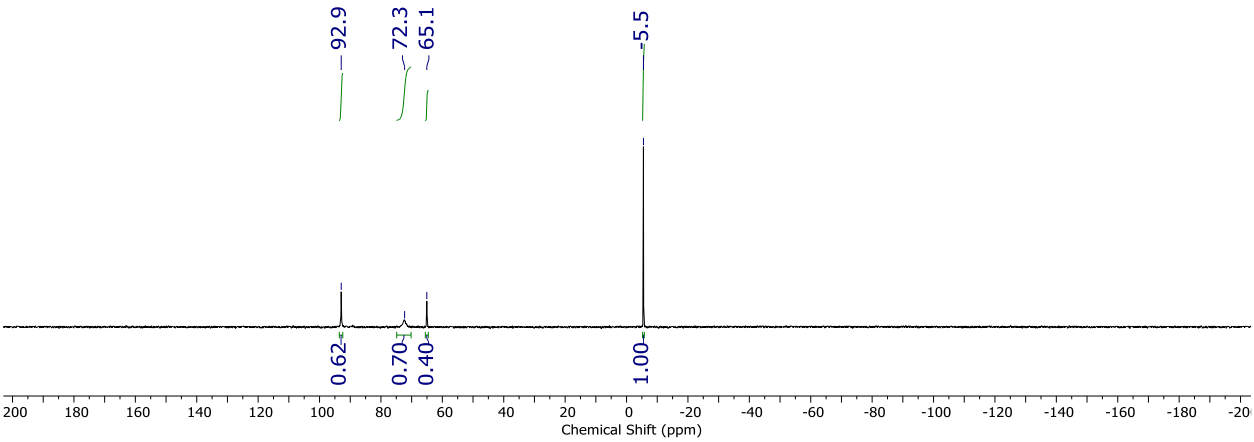

Figure 3.35. $^{31}P\{^{1}H\}$ NMR spectrum (162 MHz, C_6D_6, 25 °C) for the addition of 10 equiv $HBAr^F_4$ and 12 equiv KC_8 to $[K(THF)_2][P_3{}^{Si}Ru–N_2]$.

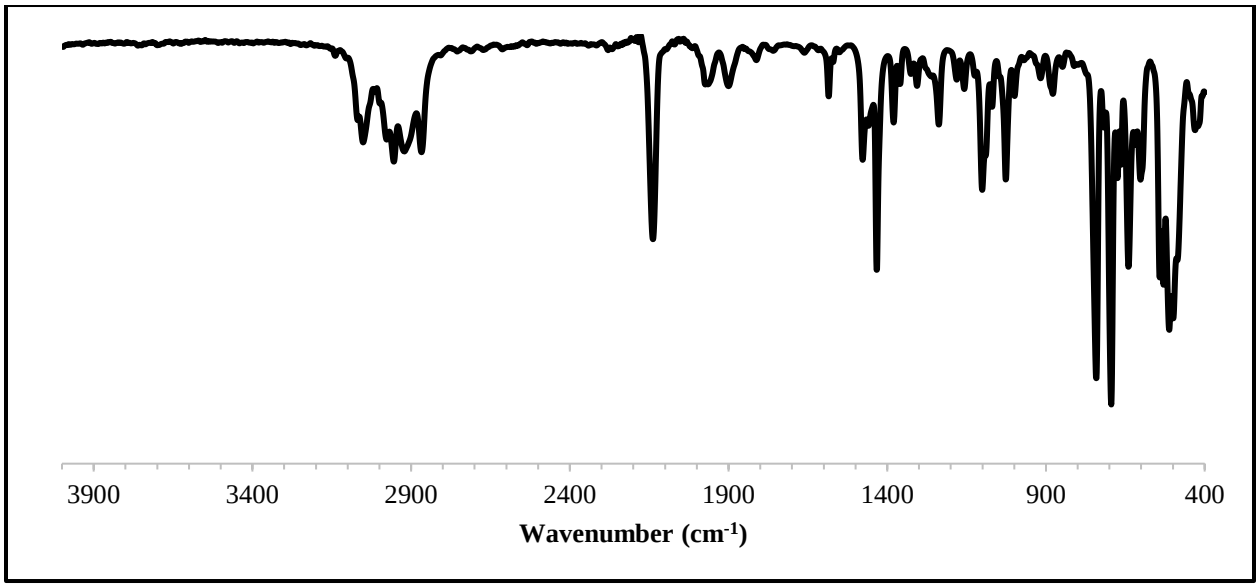

Figure 3.36. IR spectrum for the addition of 10 equiv $HBAr^F_4$ and 12 equiv KC_8 to $[K(THF)_2][P_3{}^{Si}Ru–N_2]$; deposited as a thin film from C_6D_6.

Treatment of $[K(THF)_2][P_3{}^{Si}Os–N_2]$ with 10 equiv $[H_2NPh_2][OTf]$ and 12 equiv Cp^*_2Co

In the glovebox, $[K(THF)_2][P_3{}^{Si}Os–N_2]$ (0.0091 g, 9.0 x 10^{-3} mmol) was weighed out into a 20 mL scintillation vial, equipped with a stir bar, and cooled to 77 K inside the coldwell chilled with an

external liquid nitrogen bath. 1 mL of Et_2O was added dropwise to the vial and allowed to freeze. A suspension of Cp^*_2Co (12 equiv, 0.11 mmol, 0.036 g) in Et_2O (1 mL) was then layered dropwise. This was allowed to chill in the coldwell until the contents of the vial were frozen. Finally, $[H_2NPh_2][OTf]$ (10 equiv, 0.090 mmol, 0.029 g) was transferred as a suspension in Et_2O (1 mL) to the reaction vial. The vial was then sealed and its contents were cooled until the mixture was again frozen.

After thawing the mixture by replacing the liquid nitrogen bath with a dry ice/acetone bath (–78 °C), the reaction was stirred for 3 hours at –78 °C followed by 1 hour at room temperature. The reaction mixture was then filtered through glass filter paper into a 20 mL vial containing triphenylphosphine (3.0 equiv, 0.027 mmol, 0.0071 g) as a ^{31}P NMR internal standard, concentrated to ½ the original volume, and transferred to an NMR tube. The integration of the ^{31}P resonances suggested the formation of $P_3{}^{Si}OsH_3$ in approximately 64% yield. The NMR solution was then transferred to a 20 mL vial in the glovebox, concentrated, redissolved in C_6D_6, and analyzed by ^1H and ^{31}P NMR spectroscopies. The data obtained matched the data reported above.

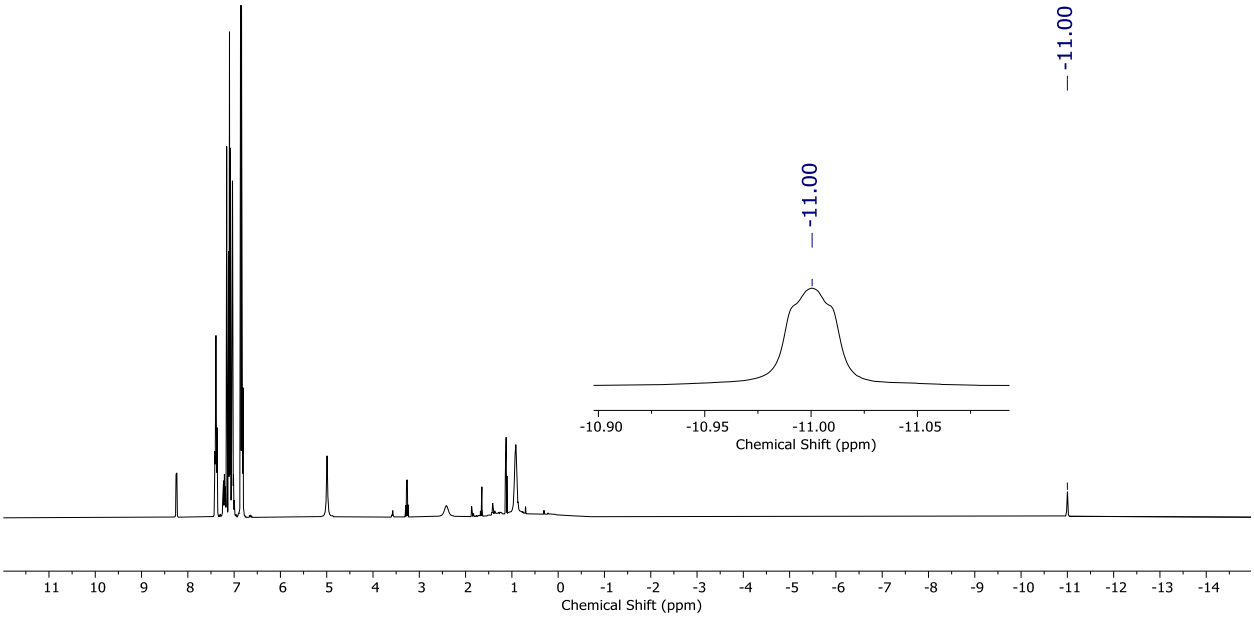

Figure 3.37. ^{1}H NMR spectrum (400 MHz, C_6D_6, 25 °C) for the addition of 10 equiv $[H_2NPh_2][OTf]$ and 12 equiv Cp^*_2Co to $[K(THF)_2][P_3^{Si}Os–N_2]$.

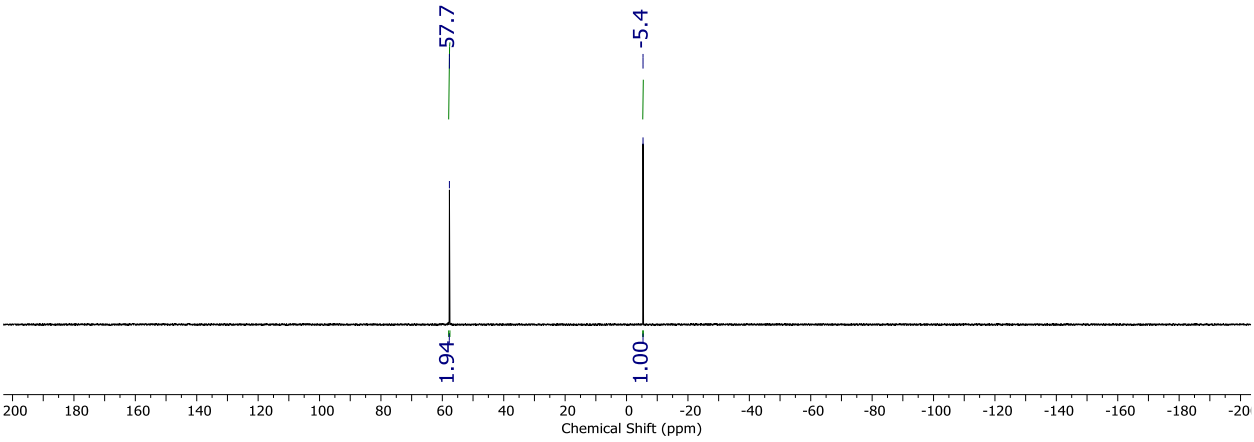

Figure 3.38. $^{31}P\{^{1}H\}$ NMR spectrum (162 MHz, C_6D_6, 25 °C) for the addition of 10 equiv $[H_2NPh_2][OTf]$ and 12 equiv Cp^*_2Co to $[K(THF)_2][P_3^{Si}Os–N_2]$.

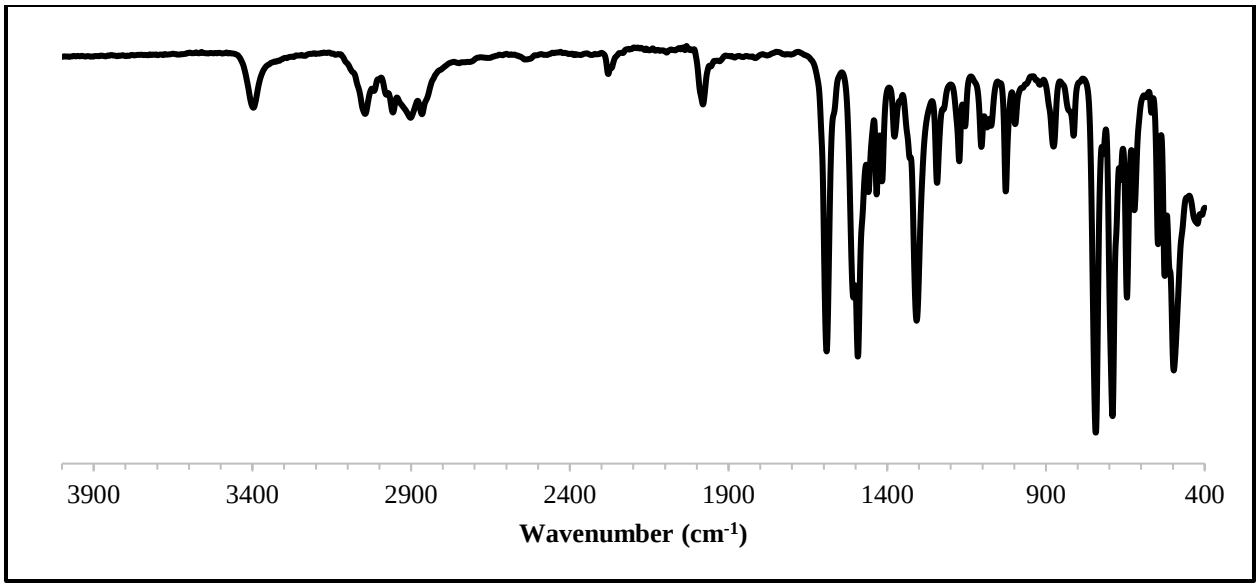

Figure 3.39. IR spectrum for the addition of 10 equiv $[H_2NPh_2][OTf]$ and 12 equiv Cp^*_2Co to $[K(THF)_2][P_3{}^{Si}Os–N_2]$; deposited as a thin film from C_6D_6.

Monitoring the Stability of $[P_3{}^{Si}Os{=}NNH_2][OTf]$ in THF Solution at Room Temperature

A sample of $[P_3{}^{Si}Os{=}NNH_2][OTf]$ was dissolved in THF-d_8 and filtered through glass filter paper into a J-Young NMR tube. The sample was allowed to sit at room temperature, and spectra were acquired at various time points.

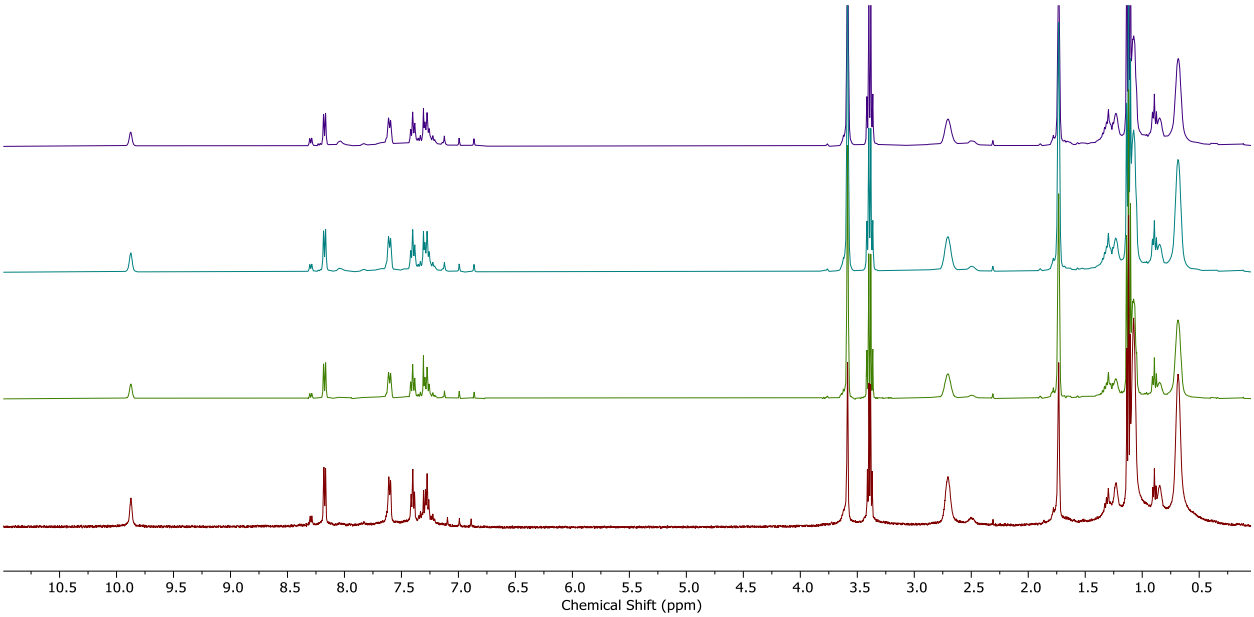

Figure 3.40. Stacked ^{1}H NMR spectra (400 MHz, THF-d_8, 25 °C) of [P_3^{Si}Os=NNH_2][OTf] after preparing the sample (red), 2 days (light green), 5 days (aqua), and 7 days (purple).

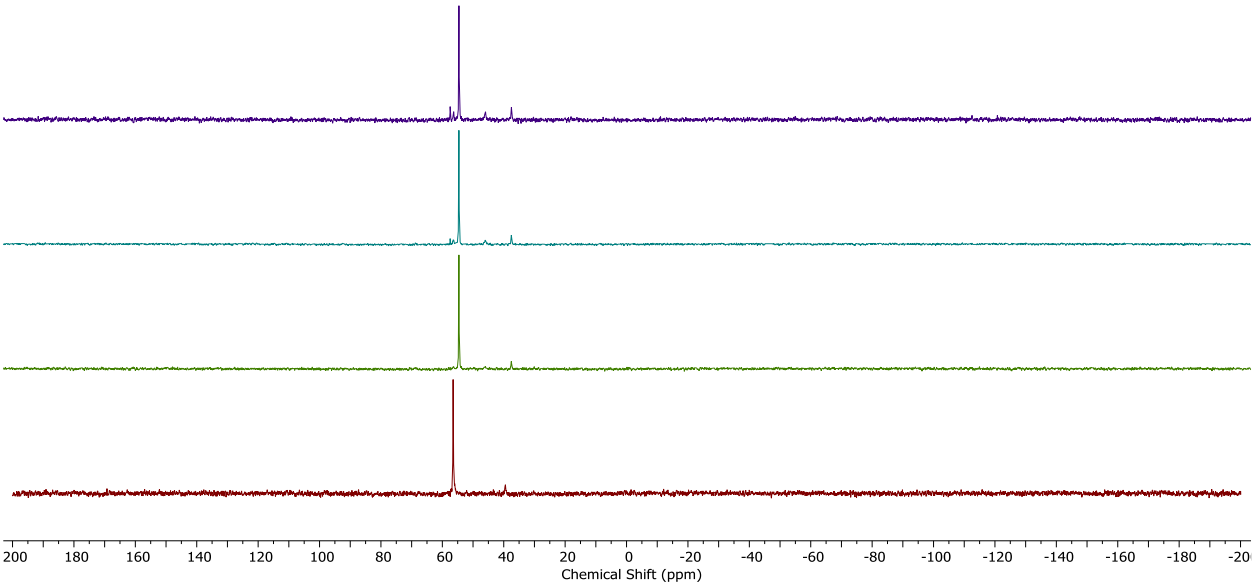

Figure 3.41. Stacked ^{31}P{^{1}H} NMR spectra (162 MHz, THF-d_8, 25 °C) of [P_3^{Si}Os=NNH_2][OTf] after preparing the sample (red), 2 days (light green), 5 days (aqua), and 7 days (purple).

Variable Temperature NMR Spectral Analysis of the Reaction of $[K(THF)_2][P_3^{Si}Os–N_2]$ with 1 equiv of $HBAr^F_4$ at –78 °C

In the glovebox, 0.0056 g (5.5 x 10^{-3} mmol) of $[K(THF)_2][P_3^{Si}Os–N_2]$ was dissolved in 400 µL of THF-d_8 to give a dark red solution that was cooled to –78 °C in the coldwell. In a separate vial, $HBAr^F_4$ (1.0 equiv, 5.5 x 10^{-3} mmol, 0.0056 g) was dissolved in 200 µL of THF-d_8 and similarly cooled. After allowing the temperature to equilibrate for 15 minutes, the $HBAr^F_4$ solution was added dropwise to the stirring solution of $[K(THF)_2][P_3^{Si}Os–N_2]$ inside the coldwell. The reaction was stirred for 15 minutes at –78 °C before being transferred to a pre-chilled J-Young NMR tube using a pre-chilled pipet. The sample was removed quickly from the glovebox and transferred to a waiting dry/ice acetone bath (–78 °C). The sample was analyzed by variable temperature NMR spectroscopy (beginning at –78 °C) on a Varian 500 MHz instrument, allowing the probe temperature to equilibrate for 5 minutes before acquiring the spectra.

After warming to room temperature, ^{1}H and ^{31}P NMR spectra, as well as an IR spectrum of a thin film from the THF-d_8 solution, were acquired. These analyses revealed the products to be $P_3^{Si}Os(N_2)(H)$ (major), $P_3^{Si}Os–N_2$ (minor), and $P_3^{Si}OsH_3$ (minor).

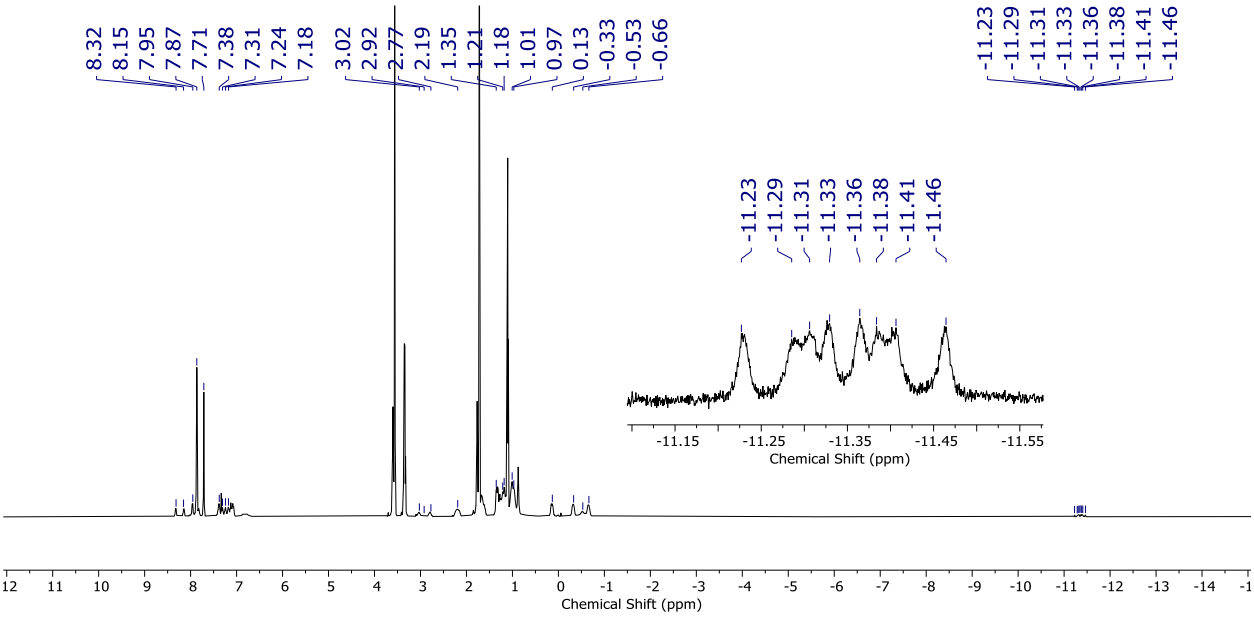

Figure 3.42. ^{1}H NMR spectrum (500 MHz, THF-d_8, –78 °C) for the reaction of [K(THF)$_2$][P$_3^{Si}$Os–N$_2$] with 1 equiv of HBAr$^F_4$.

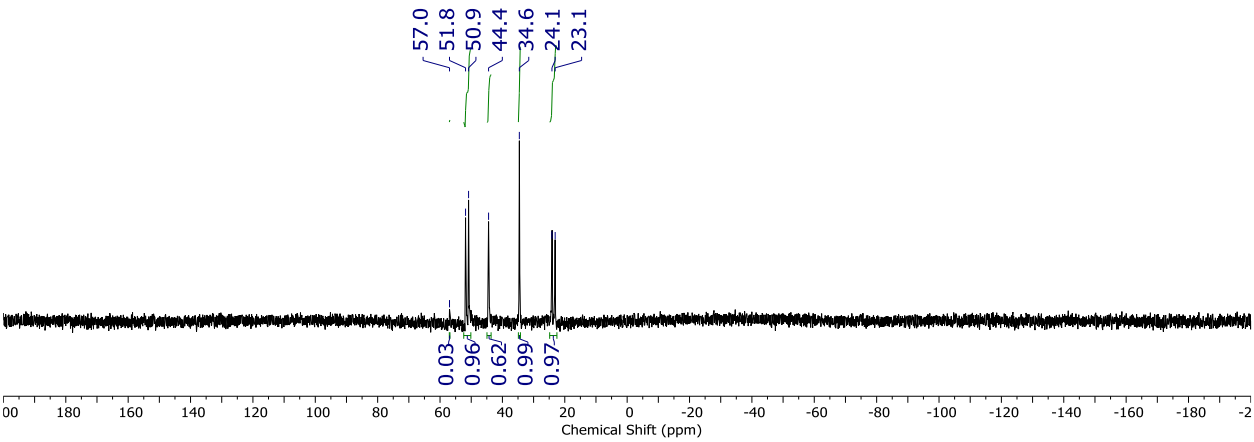

Figure 3.43. ^{31}P{^{1}H} NMR spectrum (202 MHz, THF-d_8, –78 °C) for the reaction of [K(THF)$_2$][P$_3^{Si}$Os–N$_2$] with 1 equiv of HBAr$^F_4$. The resonance at 44.4 ppm corresponds to a small amount of unreacted [K(THF)$_2$][P$_3^{Si}$Os–N$_2$]. The signals centered at 51.3 ppm, 34.6 ppm, and 23.6 ppm correspond to P$_3^{Si}$Os(N$_2$)(H), and the signal at 57.0 ppm corresponds to P$_3^{Si}$OsH$_3$ (see characterization data for authentic spectra of individual compounds).

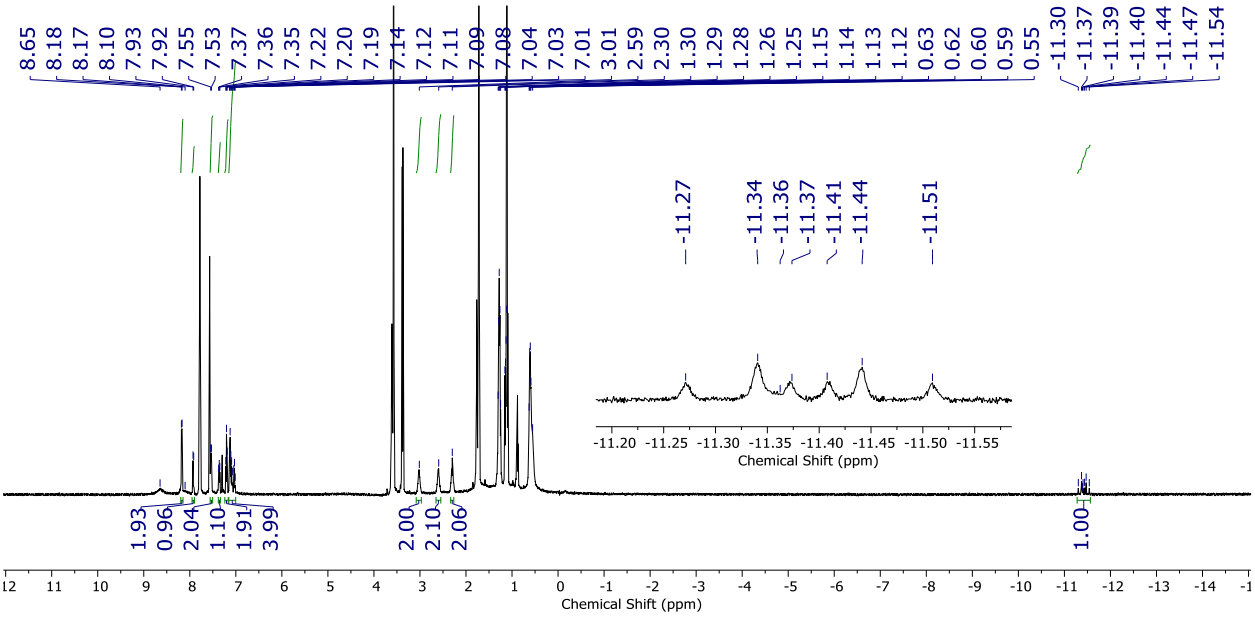

Figure 3.44. ^{1}H NMR spectrum (500 MHz, THF-d_8, 25 °C) for the reaction of $[K(THF)_2][P_3^{Si}Os–N_2]$ with 1 equiv of $HBAr^F_4$.

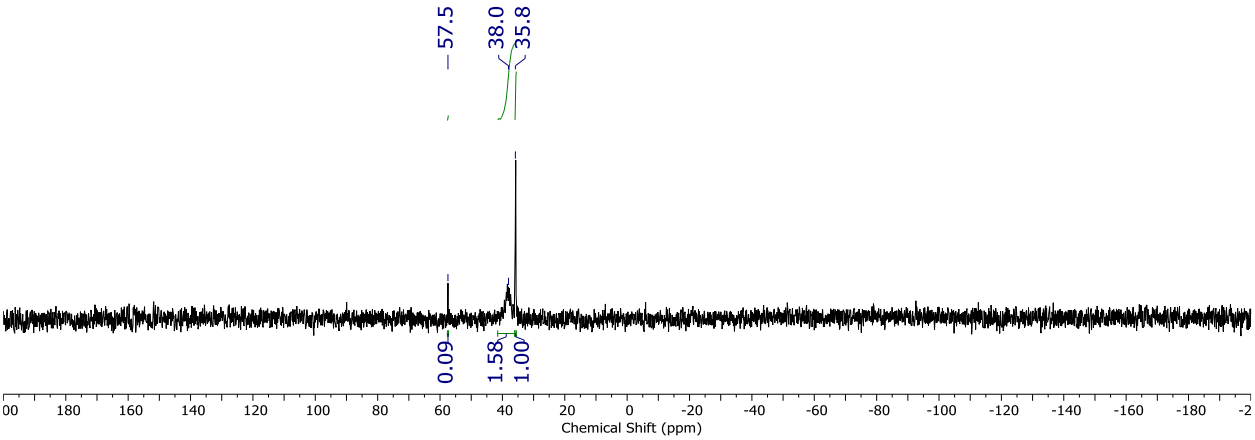

Figure 3.45. $^{31}P\{^{1}H\}$ NMR spectrum (202 MHz, THF-d_8, 25 °C) for the reaction of $[K(THF)_2][P_3^{Si}Os–N_2]$ with 1 equiv of $HBAr^F_4$.

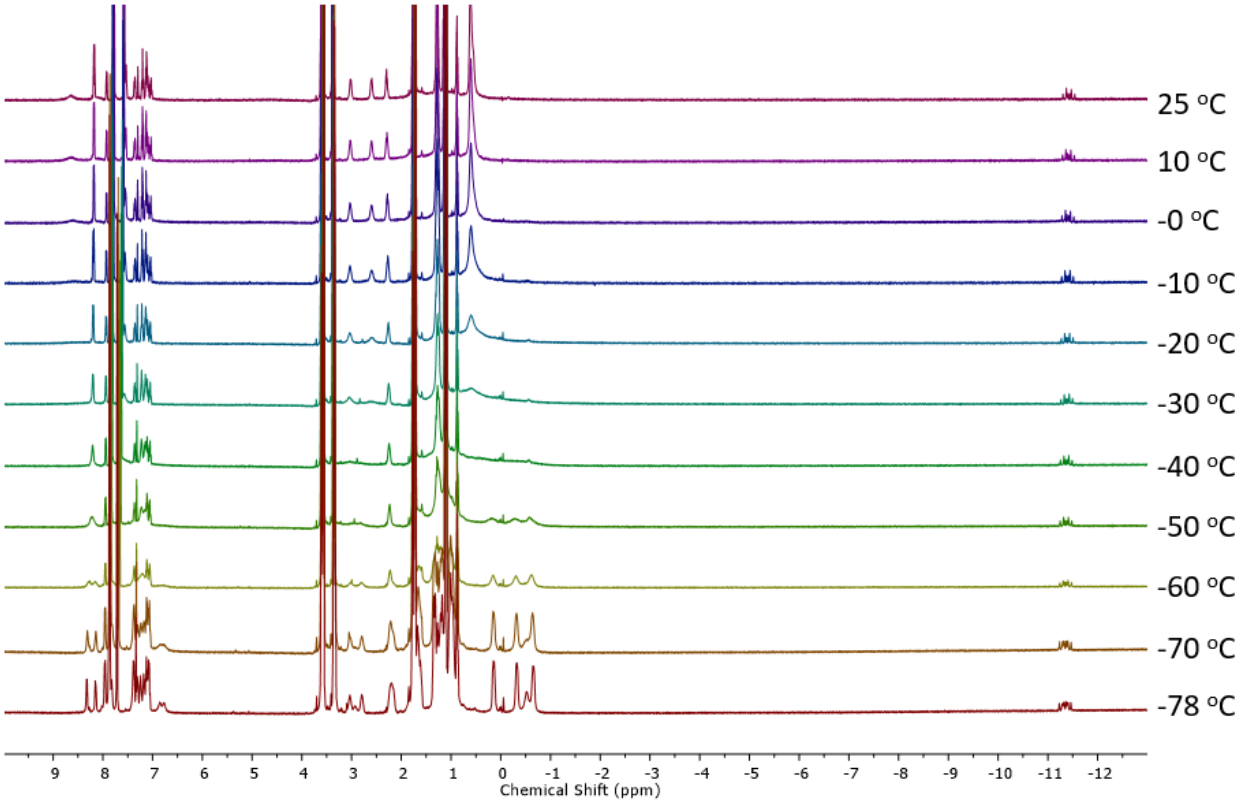

Figure 3.46. Variable temperature ^{1}H NMR spectra (500 MHz, THF-d_8) for the reaction of $[K(THF)_2][P_3{}^{Si}Os–N_2]$ with 1 equiv of $HBAr^F{}_4$.

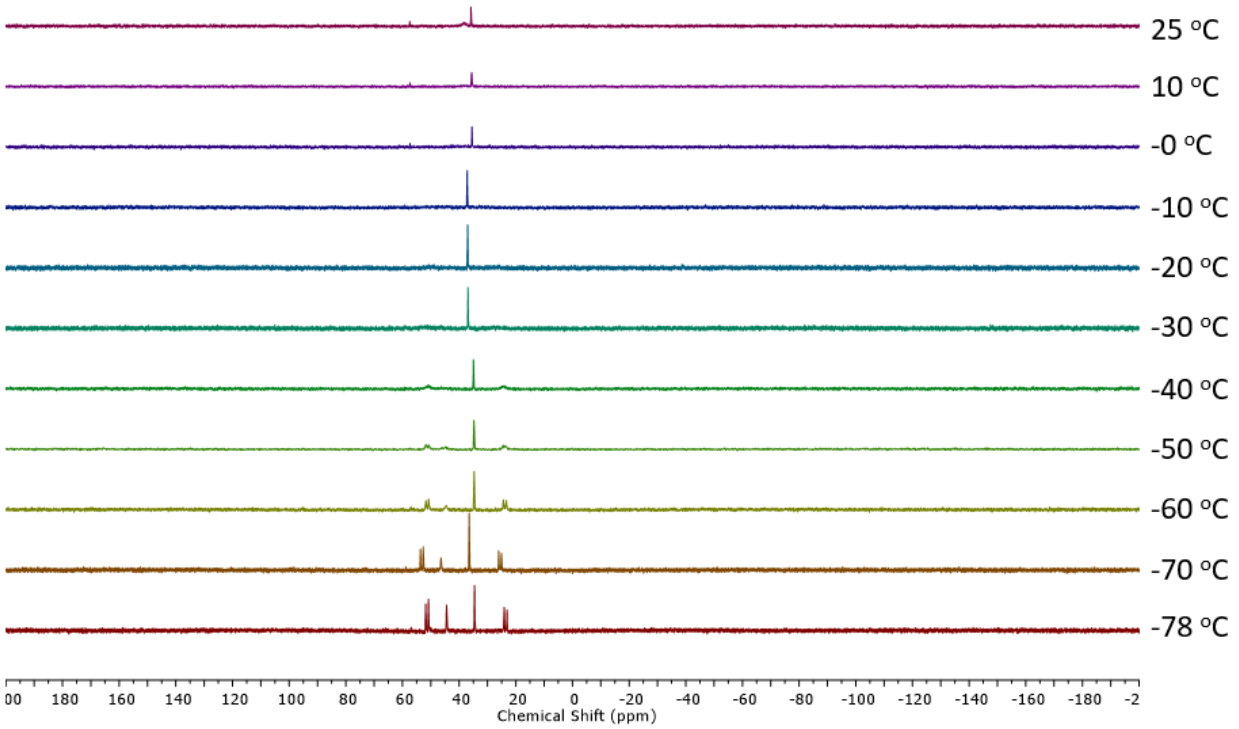

Figure 3.47. Variable temperature $^{31}P\{^{1}H\}$ NMR spectra (202 MHz, THF-d_8) for the reaction of $[K(THF)_2][P_3{}^{Si}Os–N_2]$ with 1 equiv of $HBAr^F{}_4$.

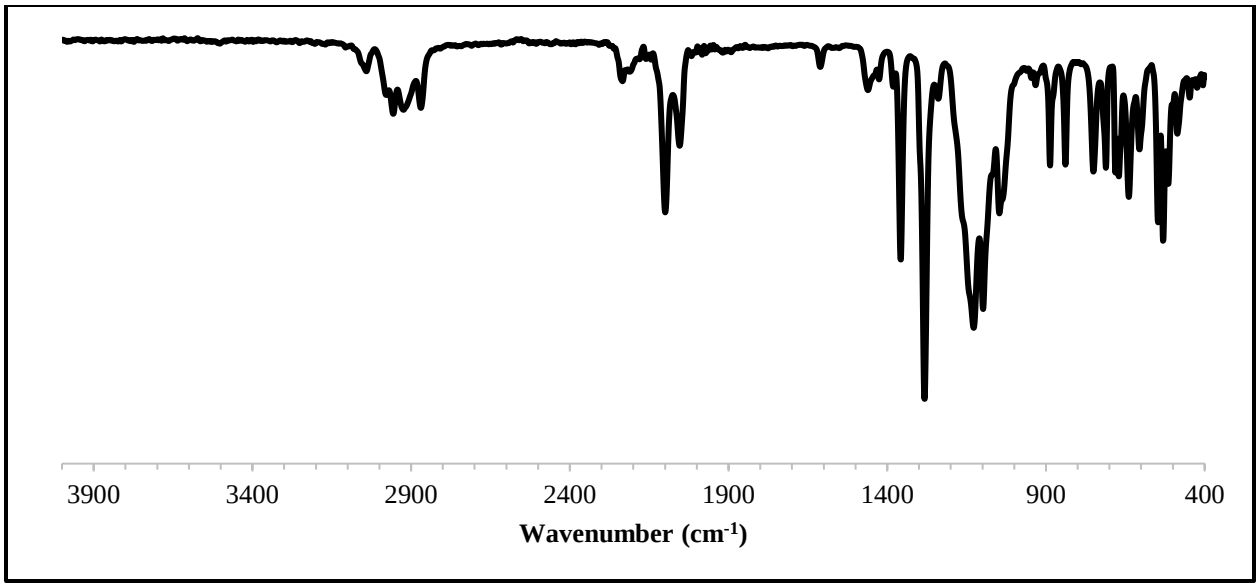

Figure 3.48. IR spectrum for the reaction of $[K(THF)_2][P_3^{Si}Os–N_2]$ with 1 equiv of $HBAr^F_4$; deposited as a thin film from THF-d_8.

General Procedure for the Variable Temperature NMR Spectral Analysis of the Reaction of $P_3^{Si}M–N_2$ (M = Os, Ru, Fe) with 5 equiv of Cp^*_2Co

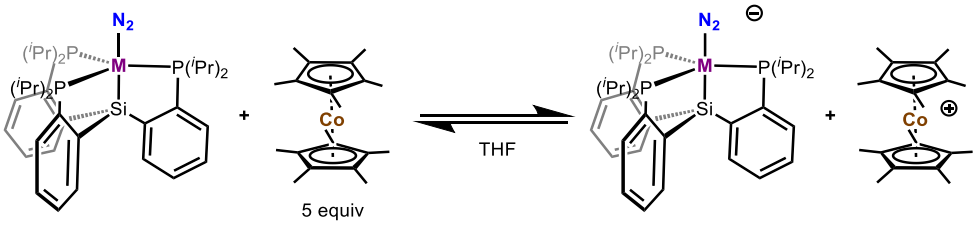

In the glovebox, $P_3^{Si}M–N_2$ and Cp^*_2Co (5 equiv with respect to $P_3^{Si}M–N_2$) were weighed out in separate vials. Both compounds were dissolved in THF-d_8, and then the solution of Cp^*_2Co was transferred to the vial containing $P_3^{Si}M–N_2$. The reaction was stirred at room temperature for 15 minutes before being filtered through glass filter paper into a J-Young NMR tube. Samples

prepared in this fashion were analyzed by variable temperature NMR spectroscopy on a Varian 500 MHz instrument, allowing the probe temperature to equilibrate for 5 minutes before acquiring the spectra.

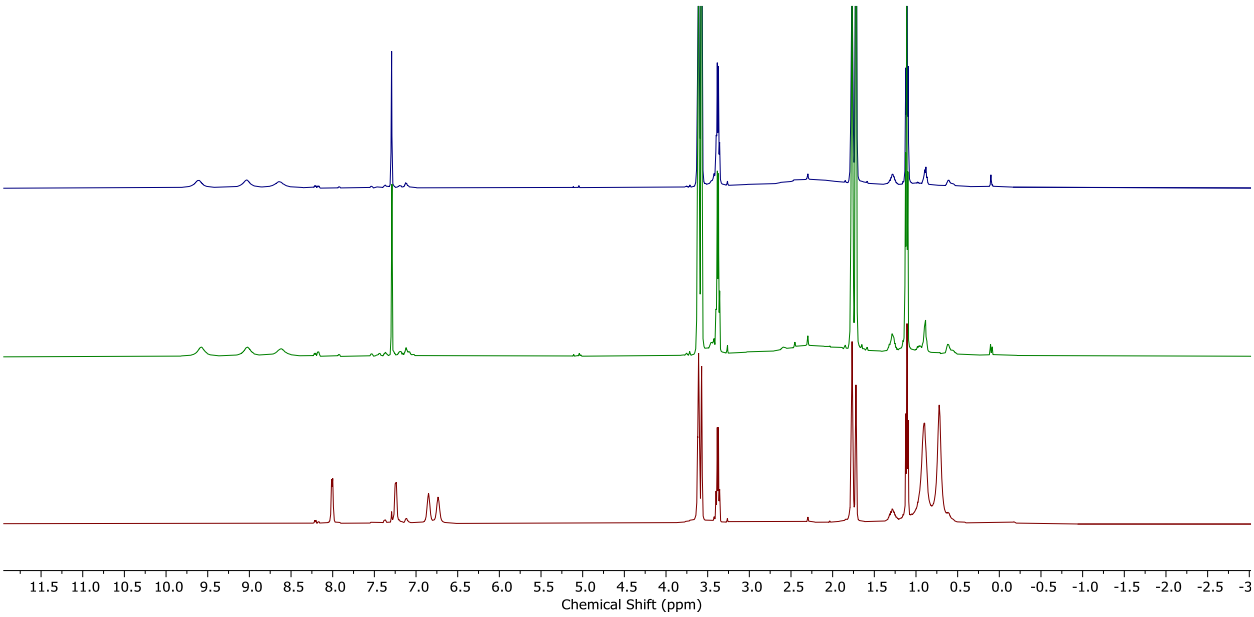

Figure 3.49. Stacked ^{1}H NMR spectra (500 MHz, THF-d_8, 25 °C) of an authentic sample of $P_3^{Si}Os–N_2$ (top, blue), the reaction of $P_3^{Si}Os–N_2$ with 5 equiv of Cp^*_2Co (middle, green), and an authentic sample of $[K(THF)_2][P_3^{Si}Os–N_2]$ (bottom, red). *Note:* $P_3^{Si}Os–N_2$ and $[K(THF)_2][P_3^{Si}Os–N_2]$ contain small amounts of $P_3^{Si}Os(N_2)(H)$ and $P_3^{Si}OsH_3$ present as impurities.

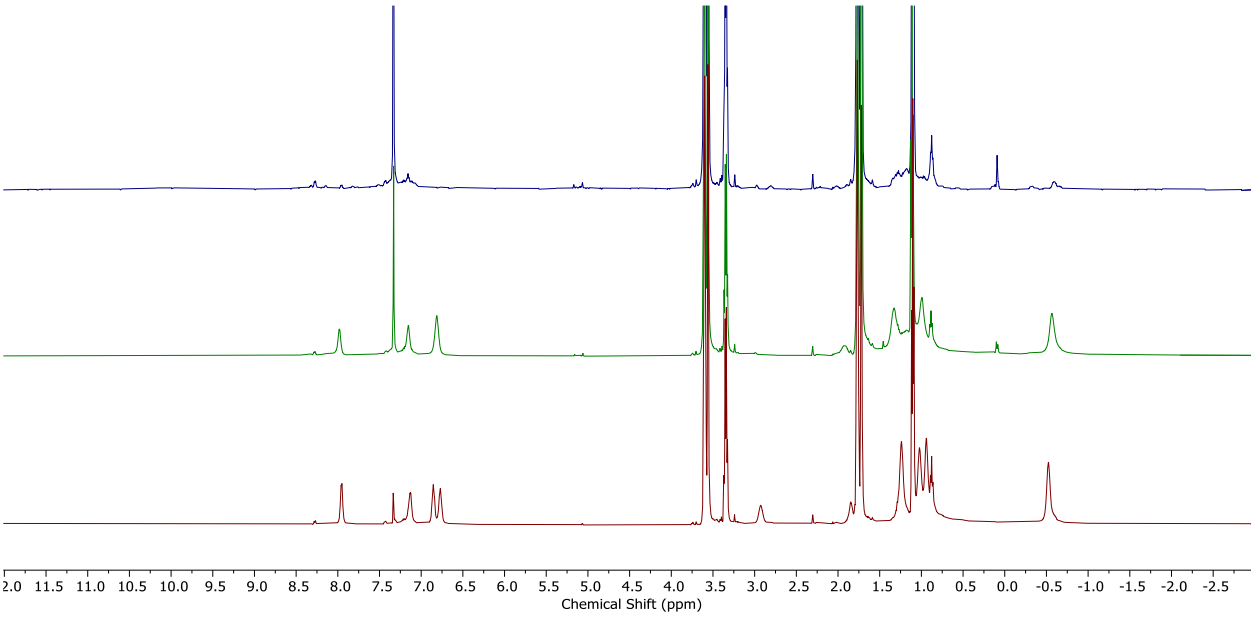

Figure 3.50. Stacked ^{1}H NMR spectra (500 MHz, THF-d_8, –78 °C) of an authentic sample of $P_3^{Si}Os–N_2$ (top, blue), the reaction of $P_3^{Si}Os–N_2$ with 5 equiv of Cp^*_2Co (middle, green), and an authentic sample of $[K(THF)_2][P_3^{Si}Os–N_2]$ (bottom, red). *Note:* $P_3^{Si}Os–N_2$ and $[K(THF)_2][P_3^{Si}Os–N_2]$ contain small amounts of $P_3^{Si}Os(N_2)(H)$ and $P_3^{Si}OsH_3$ present as impurities.

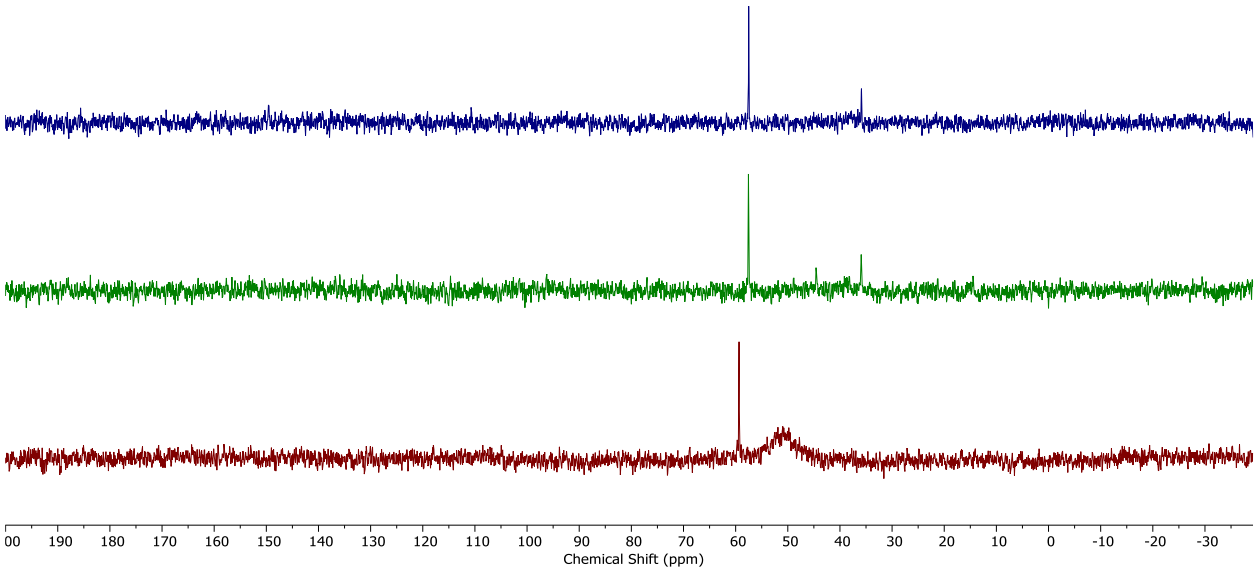

Figure 3.51. Stacked $^{31}P\{^{1}H\}$ NMR spectra (202 MHz, THF-d_8, 25 °C) of an authentic sample of $P_3^{Si}Os–N_2$ (top, blue), the reaction of $P_3^{Si}Os–N_2$ with 5 equiv of Cp^*_2Co (middle, green), and an authentic sample of $[K(THF)_2][P_3^{Si}Os–N_2]$ (bottom, red). *Note:* $P_3^{Si}Os–N_2$ and $[K(THF)_2][P_3^{Si}Os–N_2]$ contain small amounts of $P_3^{Si}Os(N_2)(H)$ and $P_3^{Si}OsH_3$ present as impurities that give rise to the peaks at ca. 35–40 ppm and ca. 59 ppm, respectively.

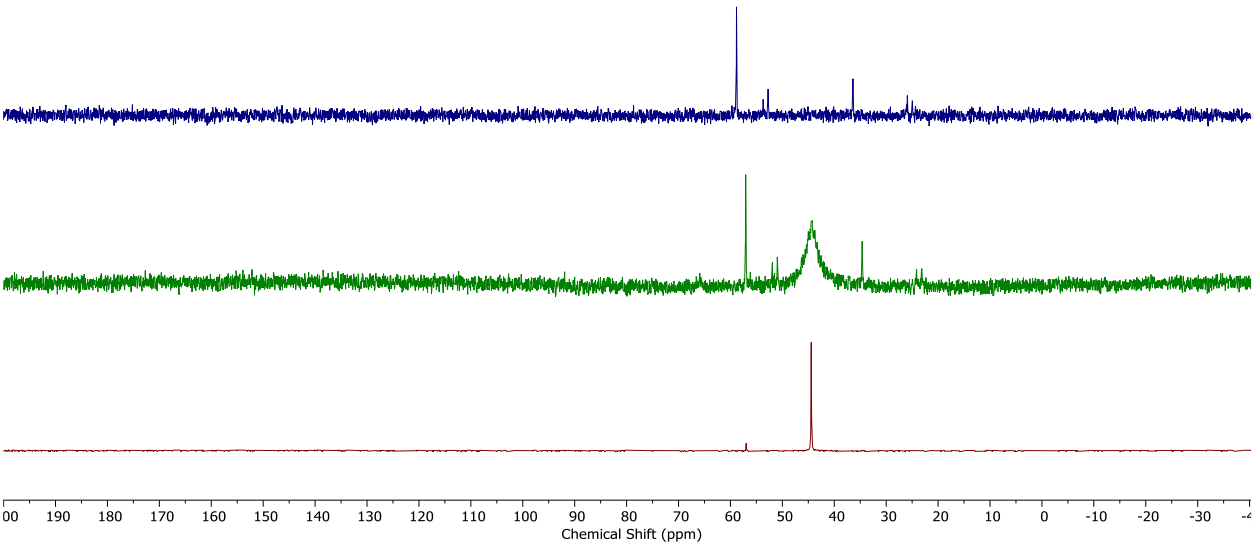

Figure 3.52. Stacked $^{31}P\{^{1}H\}$ NMR spectra (202 MHz, THF-d_8, –78 °C) of an authentic sample of $P_3^{Si}Os–N_2$ (top, blue), the reaction of $P_3^{Si}Os–N_2$ with 5 equiv of Cp^*_2Co (middle, green), and an authentic sample of $[K(THF)_2][P_3^{Si}Os–N_2]$ (bottom, red). *Note:* $P_3^{Si}Os–N_2$ and $[K(THF)_2][P_3^{Si}Os–N_2]$ contain small amounts of $P_3^{Si}Os(N_2)(H)$ and $P_3^{Si}OsH_3$ present as impurities. $P_3^{Si}Os(N_2)(H)$ gives rise to the doublets at ca. 54 ppm and ca. 24 ppm, and the singlet at ca. 35 ppm. $P_3^{Si}OsH_3$ gives rise to the singlet at ca. 59 ppm.

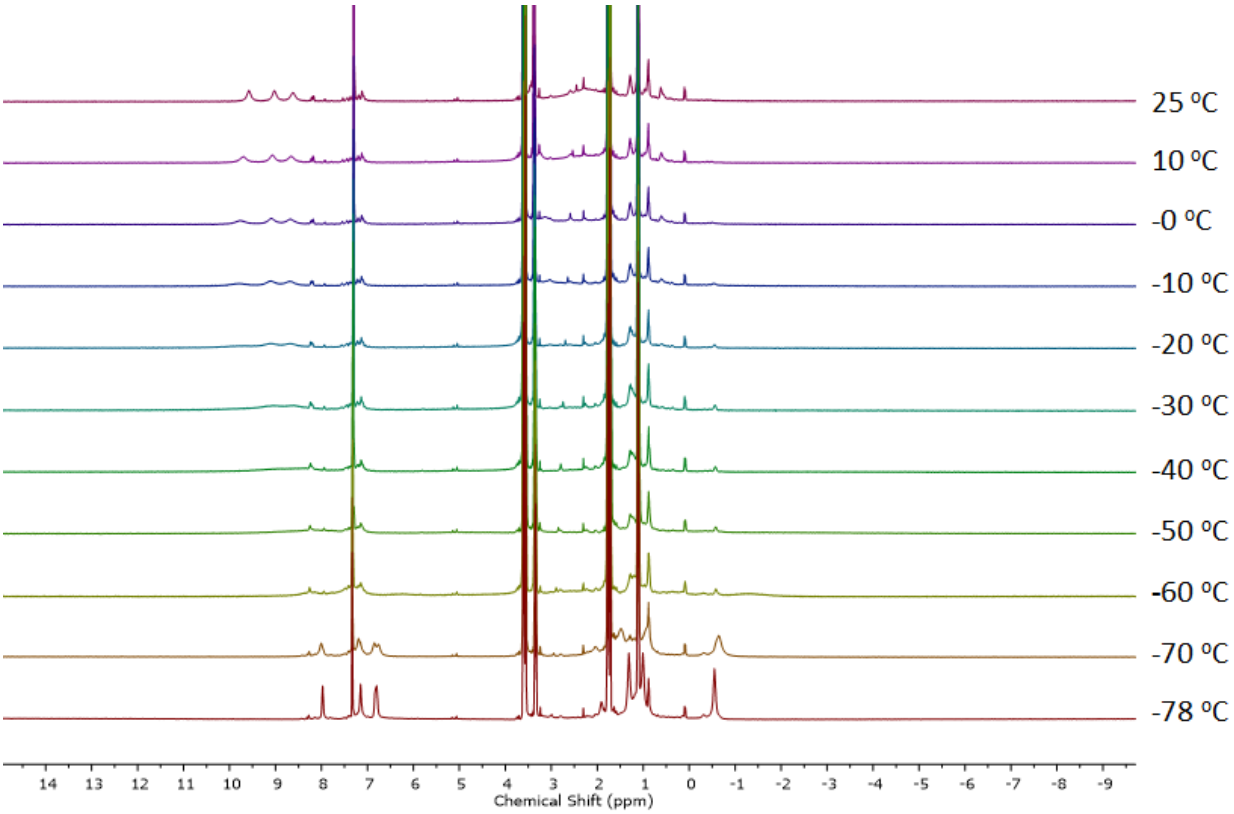

Figure 3.53. Variable temperature ^{1}H NMR spectra (500 MHz, THF-d_8) for the reaction of $P_3{}^{Si}Os–N_2$ with 5 equiv of Cp^*_2Co.

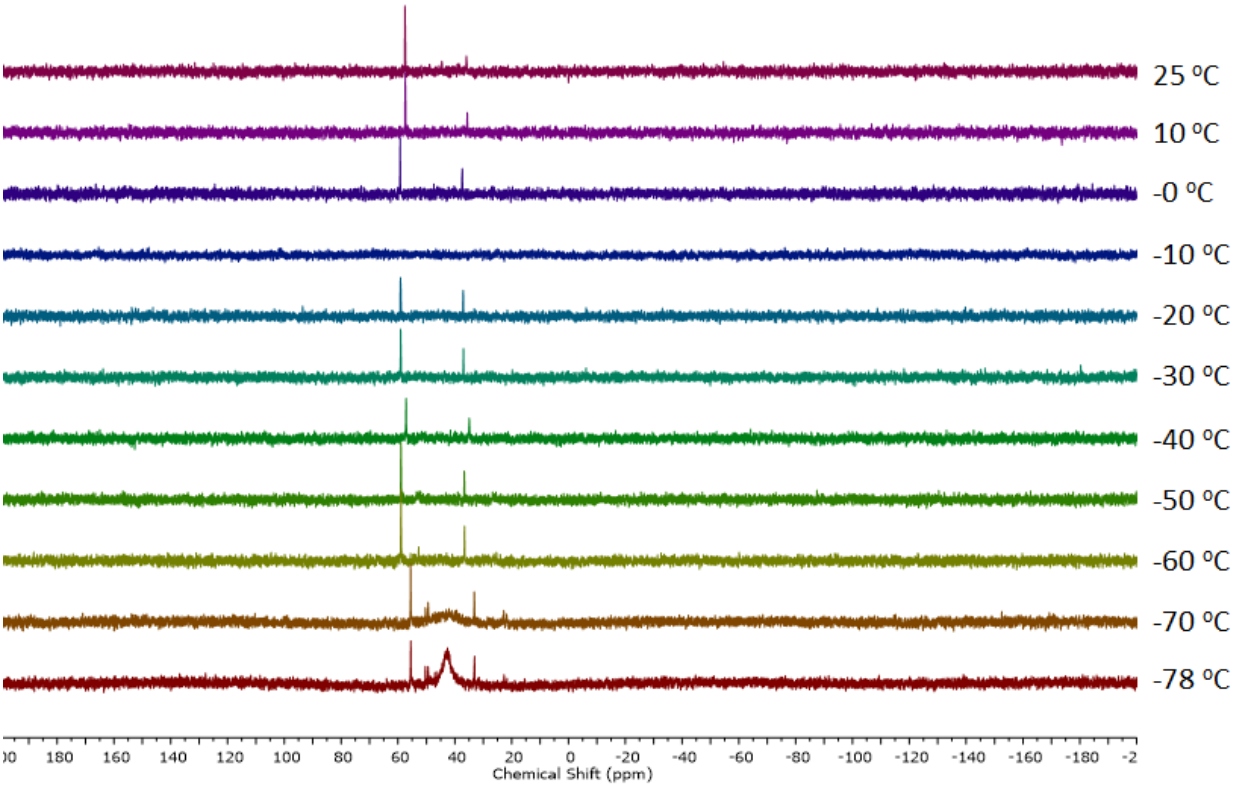

Figure 3.54. Variable temperature $^{31}P\{^{1}H\}$ NMR spectra (202 MHz, THF-d_8) for the reaction of $P_3{}^{Si}Os–N_2$ with 5 equiv of Cp^*_2Co.

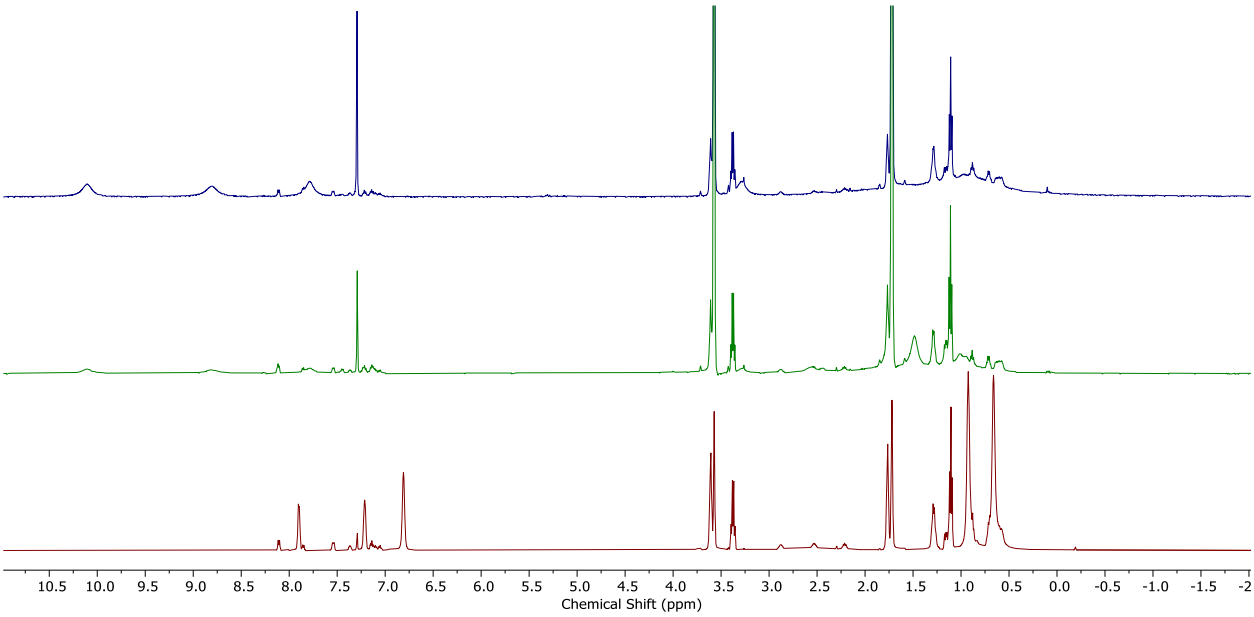

Figure 3.55. Stacked ^{1}H NMR spectra (500 MHz, THF-d_8, 25 °C) of an authentic sample of $P_3^{Si}Ru–N_2$ (top, blue), the reaction of $P_3^{Si}Ru–N_2$ with 5 equiv of Cp^*_2Co (middle, green), and an authentic sample of $[K(THF)_2][P_3^{Si}Ru–N_2]$ (bottom, red). *Note:* $P_3^{Si}Ru–N_2$ and $[K(THF)_2][P_3^{Si}Ru–N_2]$ contain a small amount of $P_3^{Si}Ru(N_2)(H)$ present as an impurity.

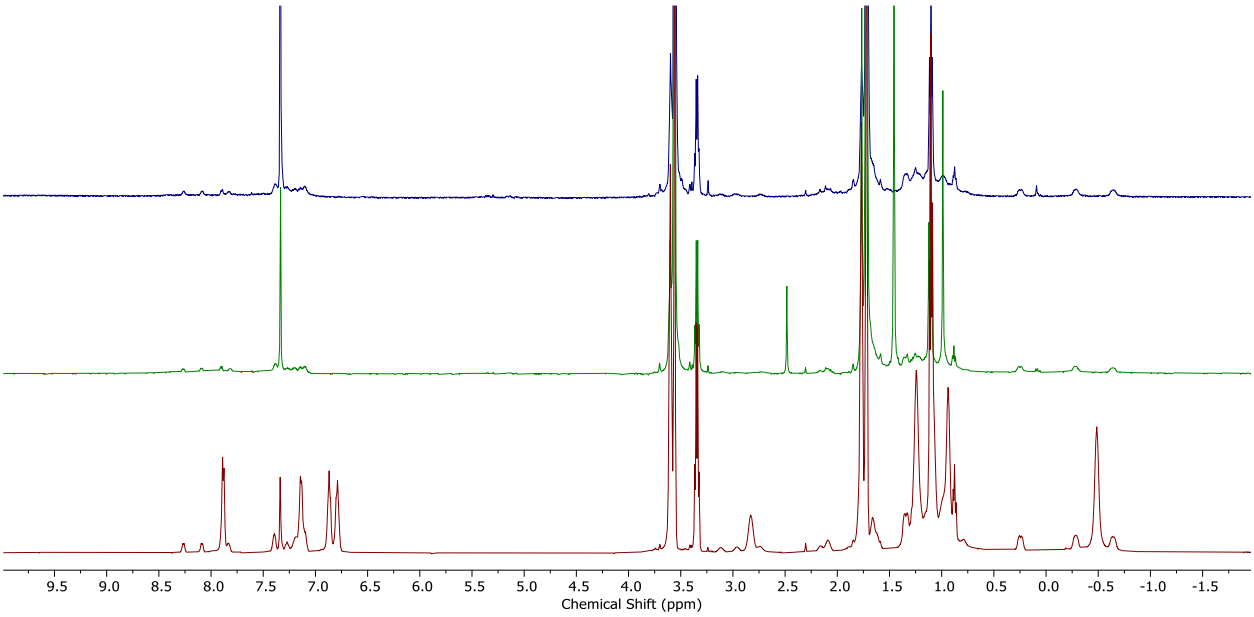

Figure 3.56. Stacked ^{1}H NMR spectra (500 MHz, THF-d_8, –78 °C) of an authentic sample of $P_3^{Si}Ru–N_2$ (top, blue), the reaction of $P_3^{Si}Ru–N_2$ with 5 equiv of Cp^*_2Co (middle, green), and an authentic sample of $[K(THF)_2][P_3^{Si}Ru–N_2]$ (bottom, red). *Note:* $P_3^{Si}Ru–N_2$ and $[K(THF)_2][P_3^{Si}Ru–N_2]$ contain a small amount of $P_3^{Si}Ru(N_2)(H)$ present as an impurity.

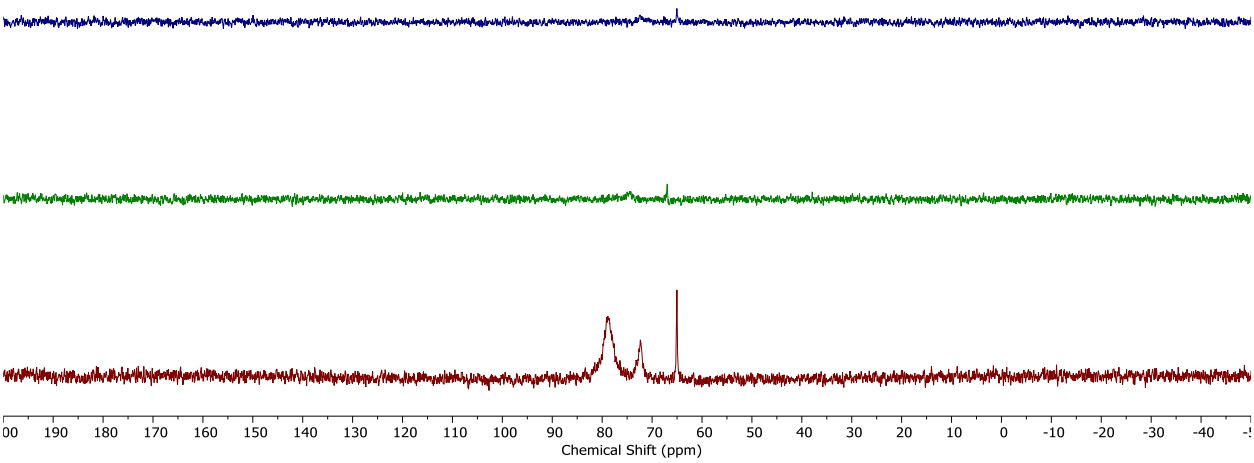

Figure 3.57. Stacked $^{31}P\{^{1}H\}$ NMR spectra (202 MHz, THF-d_8, 25 °C) of an authentic sample of $P_3^{Si}Ru–N_2$ (top, blue), the reaction of $P_3^{Si}Ru–N_2$ with 5 equiv of Cp^*_2Co (middle, green), and an authentic sample of $[K(THF)_2][P_3^{Si}Ru–N_2]$ (bottom, red). *Note:* $P_3^{Si}Ru–N_2$ and $[K(THF)_2][P_3^{Si}Ru–N_2]$ contain a small amount of $P_3^{Si}Ru(N_2)(H)$ present as an impurity that gives rise to the peaks at ca. 65 ppm and ca. 73 ppm.

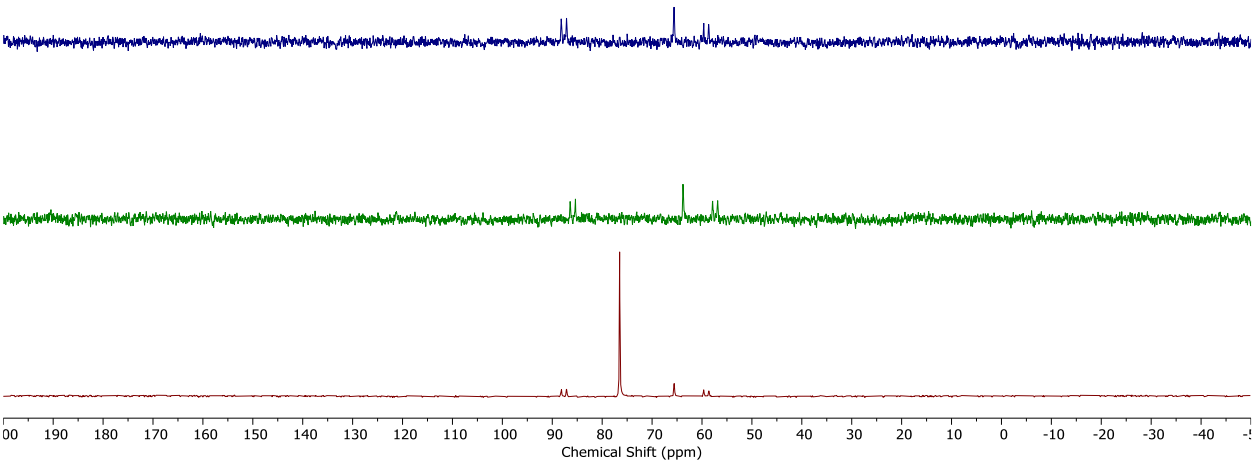

Figure 3.58. Stacked $^{31}P\{^{1}H\}$ NMR spectra (202 MHz, THF-d_8, –78 °C) of an authentic sample of $P_3^{Si}Ru–N_2$ (top, blue), the reaction of $P_3^{Si}Ru–N_2$ with 5 equiv of Cp^*_2Co (middle, green), and an authentic sample of $[K(THF)_2][P_3^{Si}Ru–N_2]$ (bottom, red). *Note:* $P_3^{Si}Ru–N_2$ and $[K(THF)_2][P_3^{Si}Ru–N_2]$ contain a small amount of $P_3^{Si}Ru(N_2)(H)$ present as an impurity that gives rise to the doublets at ca. 59 ppm and ca. 88 ppm, and the singlet at ca. 65 ppm.

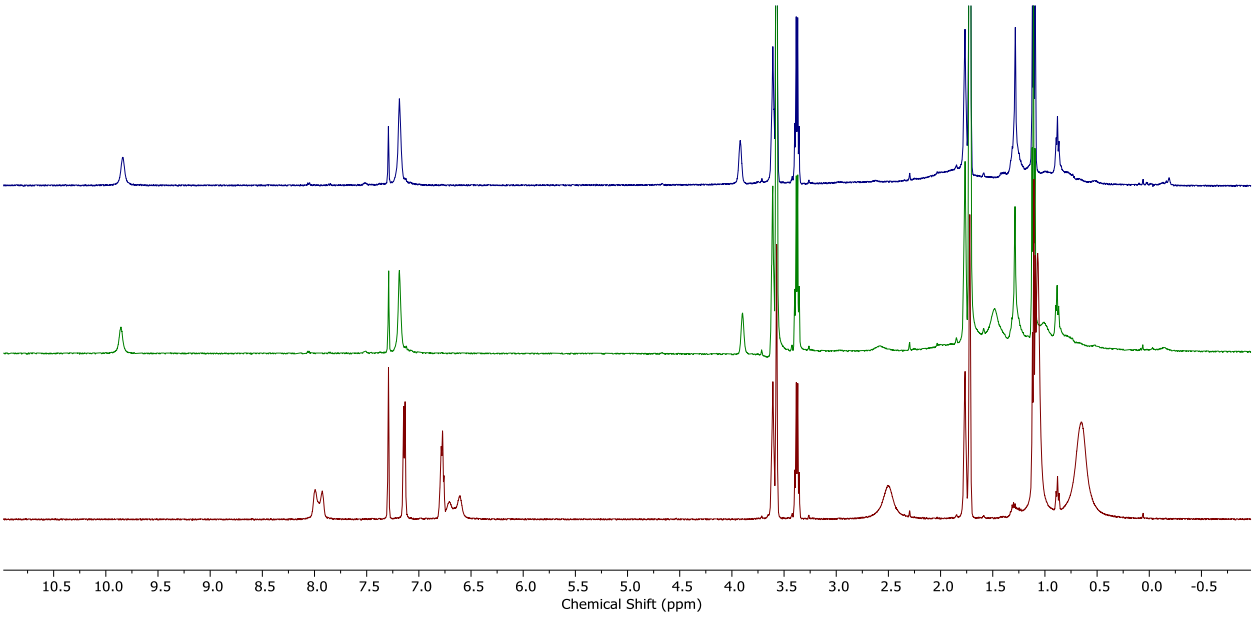

Figure 3.59. Stacked ^{1}H NMR spectra (500 MHz, THF-d_8, 25 °C) of an authentic sample of $P_3^{Si}Fe–N_2$ (top, blue), the reaction of $P_3^{Si}Fe–N_2$ with 5 equiv of Cp^*_2Co (middle, green), and an authentic sample of $[K(DME)_x][P_3^{Si}Fe–N_2]$ (bottom, red).

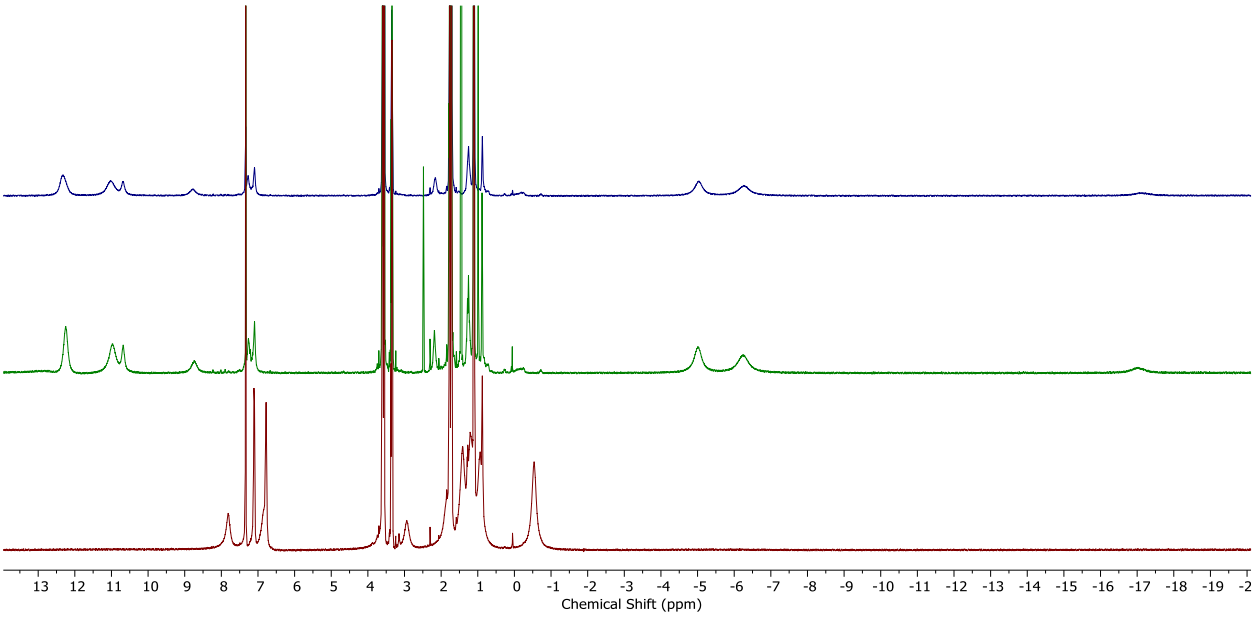

Figure 3.60. Stacked ^{1}H NMR spectra (500 MHz, THF-d_8, –78 °C) of an authentic sample of $P_3^{Si}Fe–N_2$ (top, blue), the reaction of $P_3^{Si}Fe–N_2$ with 5 equiv of Cp^*_2Co (middle, green), and an authentic sample of $[K(DME)_x][P_3^{Si}Fe–N_2]$ (bottom, red).

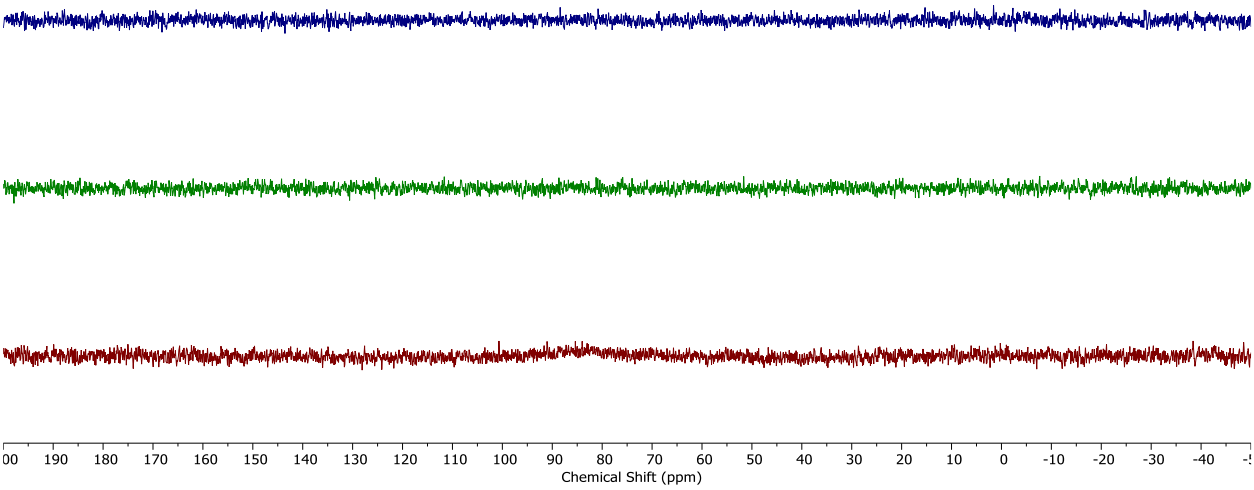

Figure 3.61. Stacked $^{31}P\{^{1}H\}$ NMR spectra (202 MHz, THF-d_8, 25 °C) of an authentic sample of $P_3^{Si}Fe–N_2$ (top, blue), the reaction of $P_3^{Si}Fe–N_2$ with 5 equiv of Cp^*_2Co (middle, green), and an authentic sample of $[K(DME)_x][P_3^{Si}Fe–N_2]$ (bottom, red).

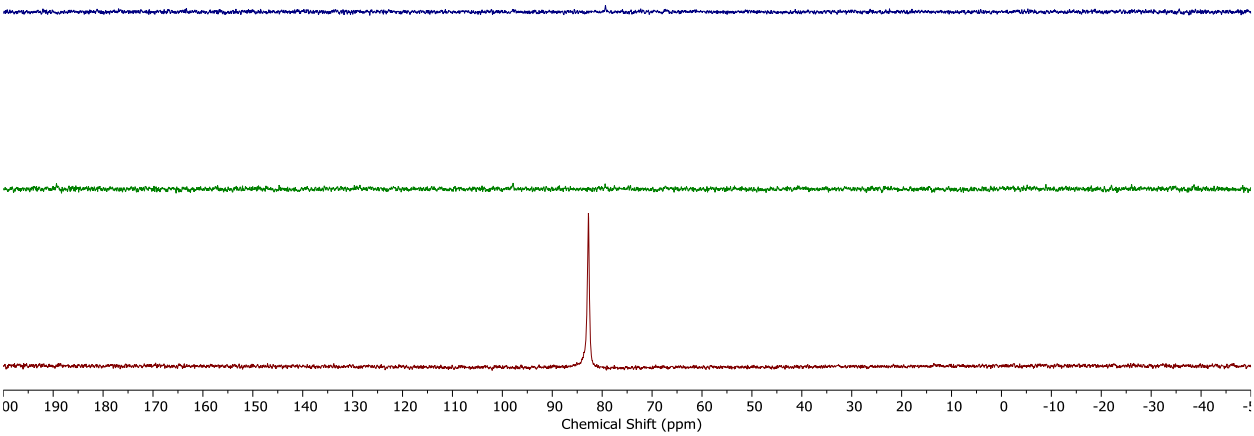

Figure 3.62. Stacked $^{31}P\{^{1}H\}$ NMR spectra (202 MHz, THF-d_8, –78 °C) of an authentic sample of $P_3^{Si}Fe–N_2$ (top, blue), the reaction of $P_3^{Si}Fe–N_2$ with 5 equiv of Cp^*_2Co (middle, green), and an authentic sample of $[K(DME)_x][P_3^{Si}Fe–N_2]$ (bottom, red).

UV-Visible Spectral Analysis of the Reaction of $P_3^{Si}Os–N_2$ with 5 equiv of Cp^*_2Co

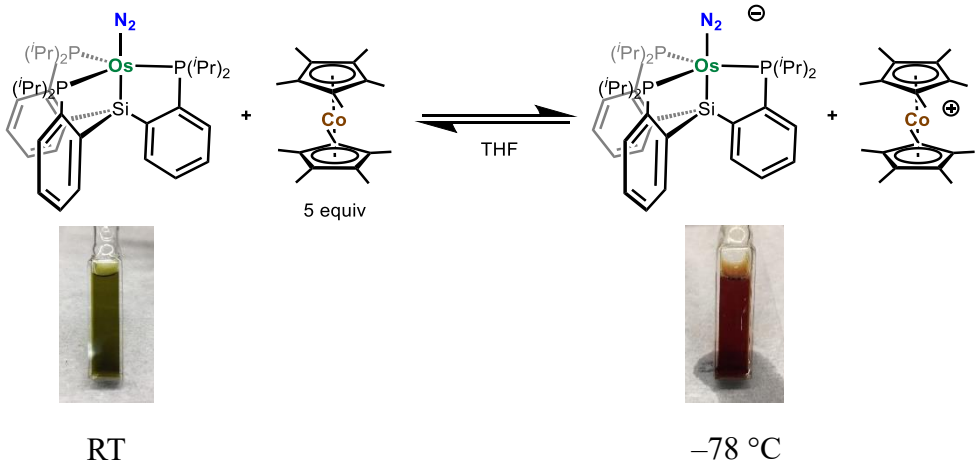

In the glovebox, $P_3^{Si}Os–N_2$ (0.0040 g, 4.8 x 10^{-3} mmol) and Cp^*_2Co (5.0 equiv, 0.024 mmol,

0.0079 g) were weighed out in separate vials. Both compounds were dissolved in 1.5 mL of THF, and then both solutions were transferred to a UV-visible cuvette. The volume of the resulting solution was then diluted to 4 mL with additional THF. The cuvette was sealed with a Teflon screw-valve, removed from the glovebox, and analyzed by variable temperature optical spectroscopy. At each temperature, the system was allowed to equilibrate for 5 minutes before collecting the spectrum.

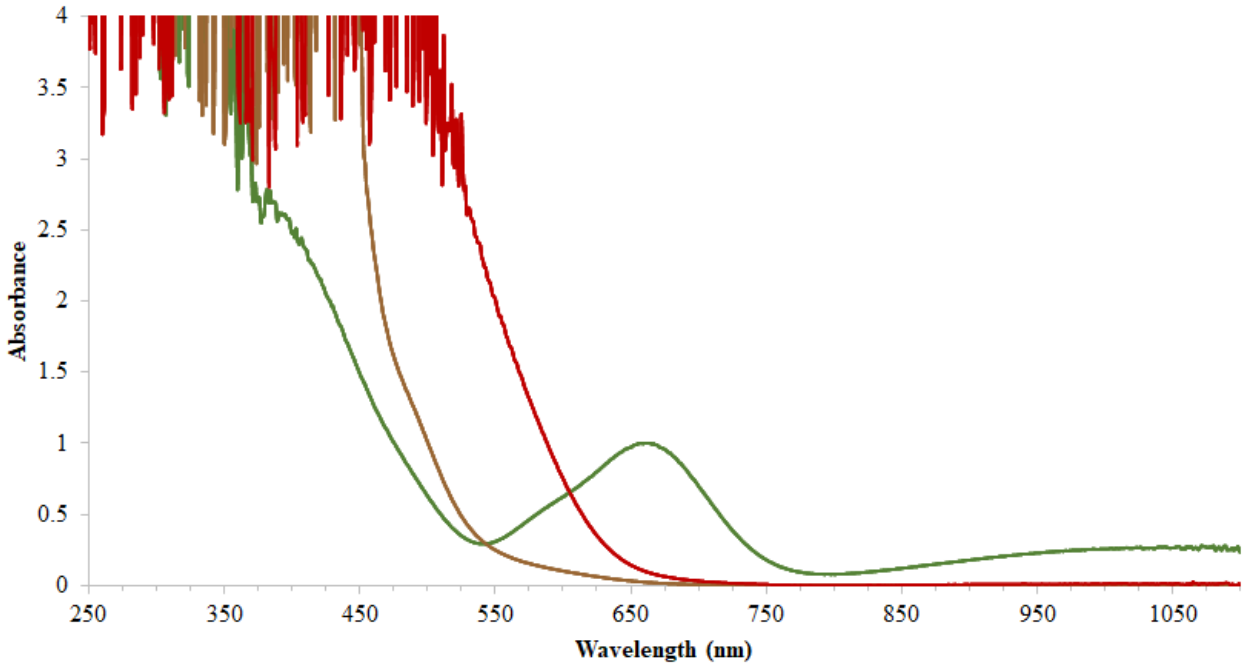

Figure 3.63. Overlaid UV-visible absorbance spectra (THF, –78 °C) of $P_3^{Si}Os–N_2$ (green, 1.2 mM), Cp^*_2Co (brown, 6.0 mM), and $[K(THF)_2][P_3^{Si}Os–N_2]$ (red, 1.2 mM).

3.4.5. X-Ray Data Tables

Table 3.13. Crystal data and structure refinement for $[P_3{}^{Si}Os{=}NNH_2][OTf]$.

Empirical formula	$C_{37}H_{56}N_2O_3F_3SiP_3SOs$
Formula weight	977.09
Temperature/K	99.98
Crystal system	orthorhombic
Space group	$P2_12_12_1$
a/Å	22.2348(15)
b/Å	12.2611(7)
c/Å	15.1377(9)
α/°	90
β/°	90
γ/°	90
Volume/Å^3	4126.9(4)
Z	4
ρ_{calc}g/cm^3	1.573
μ/mm^{-1}	3.337
F(000)	1976.0
Crystal size/mm^3	0.154 × 0.134 × 0.077
Radiation	MoKα (λ = 0.71073)
2Θ range for data collection/°	4.652 to 62.04
Index ranges	$-23 \leq h \leq 32$, $-17 \leq k \leq 17$, $-21 \leq l \leq 21$
Reflections collected	59454
Independent reflections	13119 [R_{int} = 0.0438, R_{sigma} = 0.0560]
Data/restraints/parameters	13119/0/481
Goodness-of-fit on F^2	0.998
Final R indexes [I>=2σ (I)]	R_1 = 0.0291, wR_2 = 0.0479
Final R indexes [all data]	R_1 = 0.0367, wR_2 = 0.0497
Largest diff. peak/hole / e Å^{-3}	1.34/-1.20
Flack parameter	0.009(4)

Table 3.14. Crystal data and structure refinement for $P_3{}^{Si}OsH_3$.

Empirical formula	$C_{36}H_{54}SiP_3Os$
Formula weight	797.99
Temperature/K	100.06
Crystal system	triclinic
Space group	P-1
a/Å	11.1667(18)
b/Å	11.2875(18)
c/Å	16.677(3)
α/°	100.081(6)
β/°	94.097(6)
γ/°	118.576(5)
Volume/Å^3	1788.0(5)
Z	2
ρ_{calc}g/cm^3	1.482
μ/mm^{-1}	3.757
F(000)	810.0
Crystal size/mm^3	0.201 × 0.16 × 0.145
Radiation	MoKα (λ = 0.71073)
2Θ range for data collection/°	4.792 to 95.518
Index ranges	$-23 \leq h \leq 23$, $-23 \leq k \leq 23$, $-34 \leq l \leq 34$
Reflections collected	426246
Independent reflections	33848 [R_{int} = 0.0727, R_{sigma} = 0.0286]
Data/restraints/parameters	33848/0/382
Goodness-of-fit on F^2	1.068
Final R indexes [I>=2σ (I)]	R_1 = 0.0205, wR_2 = 0.0483
Final R indexes [all data]	R_1 = 0.0247, wR_2 = 0.0499
Largest diff. peak/hole / e Å^{-3}	3.09/-1.50

3.5. References

(1) For representative examples of synthetic Mo catalysts for N_2RR, see: (a) Yandulov, D. V.; Schrock, R. R. *Science* **2003**, *301*, 76. (b) Arashiba, K.; Miyake, Y.; Nishibayashi, Y. *Nat. Chem.* **2011**, *3*, 120. (c) Arashiba, K.; Kinoshita, E.; Kuriyama, S.; Eizawa, A.; Nakajima, K.; Tanaka, H.; Yoshizawa, K.; Nishibayashi, Y. *J. Am. Chem. Soc.* **2015**, *137*, 5666. (d) Eizawa, A.; Arashiba, K.; Tanaka, H.; Kuriyama, S.; Matsuo, Y.; Nakajima, K.; Yoshizawa, K.; Nishibayashi, Y. *Nat. Commun.* **2017**, *8*, 14874. (e) Wickramasinghe, L. A.; Ogawa, T.; Schrock, R. R.; Müller, P. *J. Am. Chem. Soc.* **2017**, *139*, 9132. (f) Arashiba, K.; Eizawa, A.; Tanaka, H.; Nakajima, K.; Yoshizawa, K.; Nishibayashi, Y. *Bull. Chem. Soc. Jpn.* **2017**, *90*, 1111.

(2) For representative examples of synthetic Fe catalysts forN_2RR, see: (a) Anderson, J. S.; Rittle, J.; Peters, J. C. *Nature* **2013**, *501*, 84. (b) Creutz, S. E.; Peters, J. C. *J. Am. Chem. Soc.* **2014**, *136*, 1105. (c) Ung, G.; Peters, J. C. *Angew. Chem. Int. Ed.* **2015**, *54*, 532. (d) Del Castillo, T. J.; Thompson, N. B.; Peters, J. C. *J. Am. Chem. Soc.* **2016**, *138*, 5341. (e) Kuriyama, S.; Arashiba, K.; Nakajima, K.; Matsuo, Y.; Tanaka, H.; Ishii, K.; Yoshizawa, K.; Nishibayashi, Y. *Nat. Commun.* **2016**, *7*, 12181. (f) Chalkley, M. J.; Del Castillo, T. J.; Matson, B. D.; Roddy, J. P.; Peters, J. C. *ACS Cent. Sci.* **2017**, *3*, 217.

(3) (a) Howard, J. B.; Rees, D. C. *Chem. Rev.* **1996**, *96*, 2965. (b) Rittle, J.; Peters, J. C. *Proc. Natl. Acad. Sci. U. S. A.* **2013**, *110*, 15898. (c) MacLeod, K. C.; Holland, P. L. *Nat. Chem.* **2013**, *5*, 559. (d) Hoffman, B. M.; Lukoyanov, D.; Yang, Z.-Y.; Dean, D. R.; Seefeldt, L. C. *Chem. Rev.* **2014**, *114*, 4041.

(4) (a) Del Castillo, T. J.; Thompson, N. B.; Suess, D. L. M.; Ung, G.; Peters, J. C. *Inorg. Chem.* **2015**, *54*, 9256. (b) Kuriyama, S.; Arashiba, K.; Tanaka, H.; Matsuo, Y.; Nakajima, K.; Yoshizawa, K.; Nishibayashi, Y. *Angew. Chem. Int. Ed.* **2016**, *55*, 14291.

(5) Maxwell, G. R. Synthetic Nitrogen Products - A Practical Guide to the Products and Processes; Springer: Boston, MA, 2005.

(6) Allen, A. D.; Senoff, C. V. *Chem. Commun.* **1965**, 621.

(7) For select Os examples, see: (a) Buhr, J. D.; Taube, H. *Inorg. Chem.* **1979**, *18*, 2208. (b) Che, C.-M.; Lam, H.-W.; Tong, W.-F.; Lai, T.-F.; Lau, T.-C. *J. Chem. Soc., Chem. Commun.* **1989**, 1883. (c) Ware, D. C.; Taube, H. *Inorg. Chem.* **1991**, *30*, 4605. (d) Demadis, K. D.; Meyer, T. J.; White, P. S. *Inorg. Chem.* **1997**, *36*, 5678.

(8) For a Ru example, see: (a) Man, W.-L.; Tang, T.-M.; Wong, T.-W.; Lau, T.-C.; Peng, S.-M.; Wong, W.-T. *J. Am. Chem. Soc.* **2004**, *126*, 478. For a recent review, see: (b) Man, W.-L.; Lam, W. W. Y.; Lau, T.-C. *Acc. Chem. Res.* **2014**, *47*, 427.

(9) Kunkely, H.; Vogler, A. *Angew. Chem. Int. Ed.* **2010**, *49*, 1591.

(10) (a) Pipes, D. W.; Bakir, M.; Vitols, S. E.; Hodgson, D. J.; Meyer, T. J. *J. Am. Chem. Soc.* **1990**, *112*, 5507. (b) Schendzielorz, F. S.; Finger, M.; Volkmann, C.; Würtele, C.; Schneider, S. *Angew. Chem. Int. Ed.* **2016**, *55*, 11417. (c) Lindley, B. M.; Bruch, Q. J.; White, P. S.; Hasanayn, F.; Miller, A. J. M. *J. Am. Chem. Soc.* **2017**, *139*, 5305.

(11) Collman, J. P.; Hutchison, J. E.; Lopez, M. A.; Guilard, R.; Reed, R. A. *J. Am. Chem. Soc.* **1991**, *113*, 2794.

(12) Khoenkhoen, N.; de Bruin, B.; Reek, J. N. H.; Dzik, W. I. *Eur. J. Inorg. Chem.* **2015**, *2015*, 567.

(13) Zero-valent Ru and Os systems have been known for decades when stabilized by π-acidic ligands. For early examples, see: (a) Abel, E. W. *Q. Rev., Chem. Soc.* **1963**, *17*, 133. (b) Collman, J. P.; Roper, W. R. *J. Am. Chem. Soc.* **1965**, *87*, 4008. (c) Collman, J. P.; Roper, W. R. *J. Am. Chem. Soc.* **1966**, *88*, 3504.

(14) For relevant literature, see: (a) Takaoka, A.; Gerber, L. C. H.; Peters, J. C. *Angew. Chem. Int. Ed.* **2010**, *49*, 4088. (b) Poli, R. *Angew. Chem. Int. Ed.* **2011**, *50*, 43. (c) Yang, X.; Gianetti, T. L.; Harbort, J.; Wörle, M. D.; Tan, L.; Su, C.-Y.; Jurt, P.; Harmer, J. R.; Grützmacher, H. *Angew. Chem. Int. Ed.* **2016**, *55*, 11999. (d) Bianchini, C.; Laschi, F.; Peruzzini, M.; Zanello, P. *Gazz. Chim. Ital.* **1994**, *124*, 271. (e) Angelici, R. J.; Zhu, B.; Fedi, S.; Laschi, F.; Zanello, P. *Inorg. Chem.* **2007**, *46*, 10901.

(15) (a) Anderson, J. S.; Cutsail, G. E.; Rittle, J.; Connor, B. A.; Gunderson, W. A.; Zhang, L.; Hoffman, B. M.; Peters, J. C. *J. Am. Chem. Soc.* **2015**, *137*, 7803. (b) Rittle, J.; Peters, J. C. *J. Am. Chem. Soc.* **2016**, *138*, 4243. (c) Matson, B. D.; Peters, J. C. *ACS Catal.* **2018**, *8*, 1448.

(16) (a) Field, L. D.; Guest, R. W.; Vuong, K. Q.; Dalgarno, S. J.; Jensen, P. *Inorg. Chem.* **2009**, *48*, 2246. (b) Gilbert-Wilson, R.; Field, L. D.; Colbran, S. B.; Bhadbhade, M. M. *Inorg. Chem.* **2013**, *52*, 3043.

(17) Hill, P. J.; Doyle, L. R.; Crawford, A. D.; Myers, W. K.; Ashley, A. E. *J. Am. Chem. Soc.* **2016**, *138*, 13521.

(18) Lee, Y.; Mankad, N. P.; Peters, J. C. *Nat. Chem.* **2010**, *2*, 558.

(19) Buscagan, T. M.; Oyala, P. H.; Peters, J. C. *Angew. Chem. Int. Ed.* **2017**, *56*, 6921.

(20) Rittle, J.; Peters, J. C. *J. Am. Chem. Soc.* **2017**, *139*, 3161.

(21) Fong, H.; Moret, M.-E.; Lee, Y.; Peters, J. C. *Organometallics* **2013**, *32*, 3053.

(22) **[Ru]**(N_2)(H) and **[Ru]**H_3 form as catalytically inactive species in the corresponding Ru-system. See Experimental Section for details.

(23) Analogous experiments produce none of either **[Ru]**–N_2^- or **[Fe]**–N_2^-, as probed by ^{1}H and ^{31}P NMR spectroscopies.

(24) The generation of **[Os]**–N_2^- during catalysis does not preclude the possibility of productive PCET pathways.[2f]

(25) Coia, G. M.; White, P. S.; Meyer, T. J.; Wink, D. A.; Keefer, L. K.; Davis, W. M. *J. Am. Chem. Soc.* **1994**, *116*, 3649.

(26) Coia, G. M.; Devenney, M.; White, P. S.; Meyer, T. J.; Wink, D. A. *Inorg. Chem.* **1997**, *36*, 2341.

(27) Huynh, M. H. V.; El-Samanody, E.-S.; Demadis, K. D.; Meyer, T. J.; White, P. S. *J. Am. Chem. Soc.* **1999**, *121*, 1403.

(28) Moret, M.-E.; Peters, J. C. *Angew. Chem. Int. Ed.* **2011**, *50*, 2063.

(29) Brookhart, M.; Grant, B.; Volpe, A. F. *Organometallics* **1992**, *11*, 3920.

(30) Weitz, I. S.; Rabinovitz, M. *J. Chem. Soc., Perkin Trans. 1* **1993**, 117.

(31) Vicente, J.; Chicote, M.-T.; Guerrero, R.; Jones, P. G. *J. Chem. Soc., Dalton Trans.* **1995**, 1251.

(32) Melzer, M. M.; Mossin, S.; Dai, X.; Bartell, A. M.; Kapoor, P.; Meyer, K.; Warren, T. H. *Angew. Chem. Int. Ed.* **2010**, *49*, 904.

(33) Robbins, J. L.; Edelstein, N.; Spencer, B.; Smart, J. C. *J. Am. Chem. Soc.* **1982**, *104*, 1882.

(34) (a) Carvajal, C.; Tölle, K. J.; Smid, J.; Szwarc, M. *J. Am. Chem. Soc.* **1965**, *87*, 5548. (b) Metz, D. J.; Glines, A. *J. Phys. Chem.* **1967**, *71*, 1158.

(35) Dolomanov O. V.; Bourhis, L. J.; Gildea, R. J.; Howards, J. A. K.; Puschmann, H. *J. Appl. Cryst.* **2009**, *42*, 339.

(36) Sheldrick, G. M. *Acta Cryst. A.* **2015**, *71*, 3.

(37) Sheldrick, G. M. *Acta Cryst. A.* **2008**, *64*, 112.

(38) Weatherburn, M. W. *Anal. Chem.* **1967**, *39*, 971.

(39) Watt, G.W.; Crisp, J. D. *Anal Chem.* **1952**, *24*, 2006.

Chapter 4

Third Generation $W(CNAr)_6$ Photosensitizers Supported by Fused-Ring and Alkynyl-Bridged Arylisocyanides

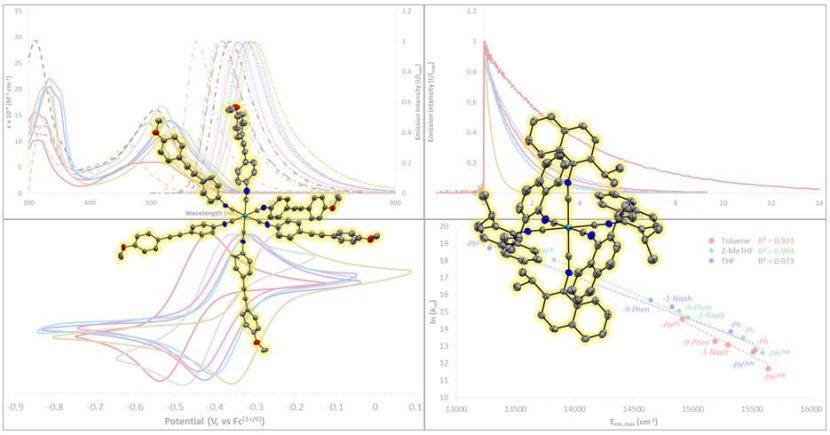

Abstract

Homoleptic tungsten(0) arylisocyanide complexes of the form $W(CNAr)_6$ possess photophysical and photochemical properties that rival those of archetypal Ru(II) polypyridine and cyclometalated Ir(III) photoactive complexes. Previous studies have established that extending the π-system of CNDipp by coupling of aryl substituents *para* to the isocyanide functionality leads to $W(CNDippAr)_6$ oligoarylisocyanide complexes with greatly enhanced excited-state properties relative to $W(CNDipp)_6$. To expand on such types of electronic modifications, herein we report a novel series of $W(CNAr)_6$ photoactive coordination compounds supported by fused-ring (CN-1-(2-^{i}Pr)-Naph) or alkynyl-bridged ($CNDipp^{CC}Ar$) arylisocyanide ligands. Systematic electronic variations of the $CNDipp^{CC}Ar$ platform provide a straightforward method by which to rationally modulate the photophysical properties of $W(CNDipp^{CC}Ar)_6$ complexes, allowing access to a complementary range of absorption/luminescence profiles and excited-state reduction potentials. $W(CN\text{-}1\text{-}(2\text{-}^i Pr)\text{-}Naph)_6$ exhibits the longest excited-state lifetimes of all $W(CNAr)_6$ complexes explored thus far, highlighting the potential benefits of utilizing fused-ring arylisocyanide ligands in the design of this class of photosensitizers.

4.1. Introduction

Photoactive coordination complexes are utilized in a variety of valuable applications ranging from dye-sensitized solar cells[1] and photoredox catalysis[2,3] to luminescent devices[4] and biological imaging.[5] As a result of such breadth, the development of photosensitizers with readily tailorable photophysical and photochemical properties is of great interest. Ru(II) polypyridine[6,7] and cyclometalated Ir(III) 2-phenylpyridine[8,9] octahedral coordination compounds with low-spin $4d^6$ and $5d^6$ electronic configurations represent a privileged and highly modular category of molecular photosensitizers. Because $Ru(bpy)_3^{2+}$- and *fac*-$Ir(ppy)_3$-type coordination compounds can undergo visible light-induced metal-to-ligand charge transfer (MLCT) [$d\pi(M) \rightarrow \pi^*$(ligand)] transitions that generate long-lived, strongly luminescent, and photoredox-active ^{3}MLCT states,[10] they currently dominate many photonic applications.

There is a long-standing interest in replacing these precious metal-based photosensitizers with similarly tunable earth-abundant photoactive complexes.[11] In this regard, isoelectronic group 6 homoleptic arylisocyanide (CNAr) transition metal complexes have recently emerged as a novel class of low-spin d^6 photosensitizers with photophysical and photochemical properties that rival those of Ru(II) and Ir(III) coordination compounds.[12,13] For instance, tris(*meta*-terphenyl diisocyanide)molybdenum(0) complexes of the form $Mo(CN^RAr_3NC)_3$ (R = Me, ^{t}Bu), explored by Wenger and co-workers, are remarkably photostable and can achieve room temperature solution ^{3}MLCT lifetimes (τ) and photoluminescence quantum yields (ϕ_{PL}) of up to 1 μs and 0.2, respectively.[14] Notably, these compounds are more powerful photoreductants (E (Mo^+/*Mo^0) ≈ –2.6 V vs $Fc^{[1+/0]}$; * denotes the lowest energy excited state) than *fac*-$Ir(ppy)_3$ (E (Ir^{4+}/*Ir^{3+}) = –2.1 V vs $Fc^{[1+/0]}$), and thus are efficient visible light photoredox catalysts for the rearrangement of acyl

cyclopropanes to 2,3-dihydrofurans and the base-promoted homolytic aromatic substitution of aryl iodides.[14,15] Similarly, $Cr(CN^{tBu}Ar_3NC)_3$ is emissive in deaerated room temperature THF solution with $\tau(^3MLCT)$ = 2.2 ns, representing the first example of a $3d^6$ ^3MLCT room temperature photoluminescent analogue of $Fe(bpy)_3^{2+}$, and has been used as an excited-state energy transfer agent for triplet-triplet annihilation upconversion.[16]

Related studies by our group have established that the sterically encumbered tungsten(0) hexakis(2,6-diisopropylphenylisocyanide) complex $W(CNDipp)_6$ is also a photo-robust, long-lived ($\tau(^3MLCT)$ = 75 ns in THF), strong excited-state reductant (E ($W^+/{}^*W^0$) = –3.0 V vs $Fc^{[1+/0]}$) capable of triggering one-electron reduction of challenging substrates, including anthracene, cobaltocenium, benzophenone, and acetophenone, upon visible light excitation.[17-20] Notably, electronic modification of CNDipp by coupling of aryl substituents *para* to the isocyanide functionality (Figure 4.1) leads to $W(CNDippAr)_6$ oligoarylisocyanide complexes with greatly enhanced excited-state properties. Compared to $W(CNDipp)_6$, $W(CNDippPh)_6$, $W(CNDippPh^{OMe2})_6$, $W(CNDippPh^{OMe3})_6$, and $W(CNDippPh^{Ph})_6$ feature more intense and red-shifted MLCT absorption and emission profiles, $\tau(^3MLCT)$ up to 1.8 μs, and ϕ_{PL} up to 0.4, while retaining comparable excited-state reduction potentials.[21,22] More recently, we also found that $W(CNDippAr)_6$ complexes exhibit exceptionally high two-photon absorption (TPA) cross sections (δ) in the range 1000–2000 GM (GM = Goeppert-Mayer; 1 GM = 10^{-50} cm^4 s $photon^{-1}$ $molecule^{-1}$) at 812 nm,[23] making them attractive platforms to investigate in the context of two-photon imaging[24] and two-photon near-infrared light photoredox catalysis.[25]

Because the photophysical properties of $W(CNDippAr)_6$ photosensitizers are strongly dependent on the identity of the appended aryl group, we became interested in further interrogating

the effect of extension of the aromatic π-system on the one- and two-photon properties of these complexes. Herein we report a third generation of homoleptic tungsten(0) photoactive coordination compounds supported by fused-ring (CN-1-(2-^{i}Pr)-Naph) or alkynyl-bridged (CNDipp^{CC}Ar)$_6$ arylisocyanide ligands (Figure 4.1). Through systematic variation of the ligand electronics, we demonstrate that simple substitutions on the CNDipp^{CC}Ar platform provide a straightforward method by which to rationally modulate the ground- and excited-state properties of W(CNDipp^{CC}Ar)$_6$ complexes. Alternatively, W(CN-1-(2-^{i}Pr)-Naph)$_6$ exhibits the longest excited-state lifetimes of all W(CNAr)$_6$ complexes explored thus far, highlighting the potential benefits of utilizing fused-ring arylisocyanide ligands in the design of this class of photosensitizers.

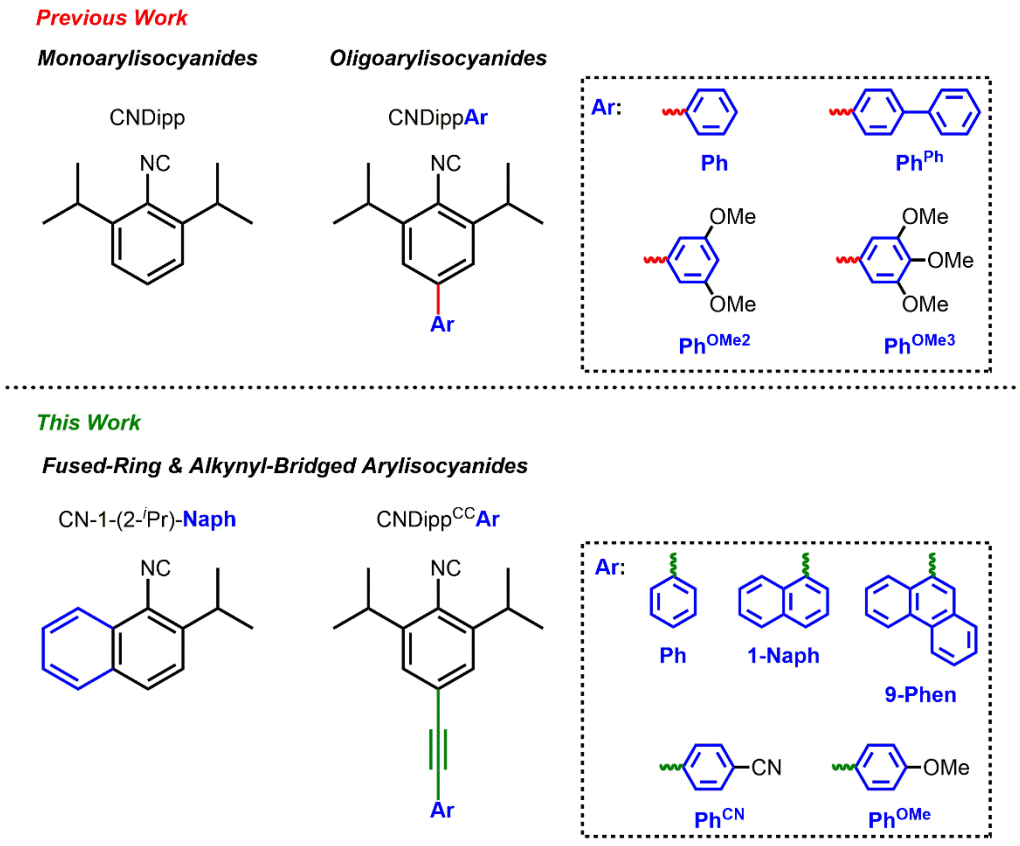

Figure 4.1. The arylisocyanide ligands of relevance to this work.

4.2. Results and Discussion

4.2.1. Synthesis and Characterization of Alkynyl-Bridged and Fused-Ring Arylisocyanide Ligands

The alkynyl-bridged and fused-ring arylisocyanide ligands of interest for this work are depicted in Figure 4.1. The CNDipp and CNDippAr ligands previously employed by our group for the construction of homoleptic tungsten(0) mono- and oligoarylisocyanide complexes are also shown. Alkynyl-bridged arylisocyanides (CNDipp^{CC}Ar) were prepared according to modified literature procedures.[21,26,27] Like their CNDippAr counterparts, all CNDipp^{CC}Ar ligands can be prepared from the same readily accessible synthetic intermediate, *N*-formyl-4-iodo-2,6-diisopropylaniline. Sonogashira coupling of this reagent with phenylacetylene, 1-naphthylacetylene, 9-phenanthrenylacetylene, 4-methoxyphenylacetylene, or 4-cyanophenylacetylene, followed by dehydration of the resulting formamide with $OPCl_3$, yields the

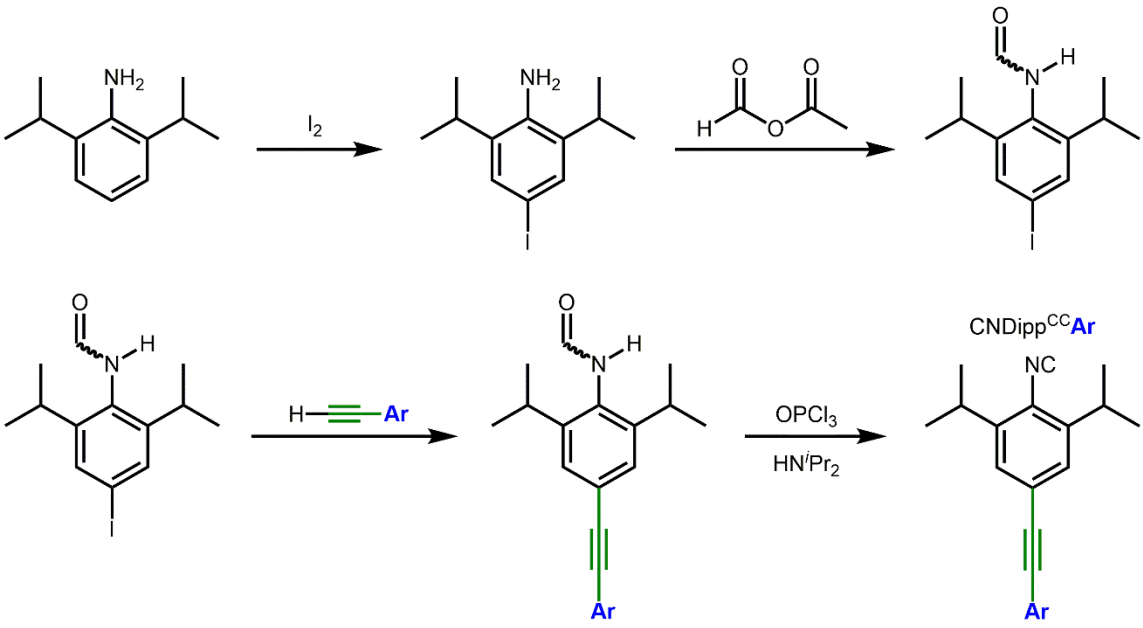

Scheme 4.1. Synthesis of CNDipp^{CC}Ar ligands. See Figure 4.1 for Ar groups.

isocyanide ligands CNDipp^{CC}Ph, CNDipp^{CC}-1-Naph, CNDipp^{CC}-9-Phen, CNDipp^{CC}Ph^{OMe}, and CNDipp^{CC}Ph^{CN}, respectively, in moderate to high yield (Scheme 4.1). These ligands display sharp, strong infrared (IR) *ν*(CN) isocyanide absorption bands in the narrow range 2109–2114 cm^{-1}, as well as similar isocyanide (173.3–174.0 ppm) and alkyne (88.5–94.4 ppm) ^{13}C NMR chemical shifts. Their *ν*(CC) alkyne stretching frequencies also span a small range (2203–2213 cm^{-1}), but vary from weak (CNDipp^{CC}Ph, CNDipp^{CC}-1-Naph, CNDipp^{CC}-9-Phen) to medium (CNDipp^{CC}Ph^{OMe}, CNDipp^{CC}Ph^{CN}) intensity. A strong *ν*(CN) nitrile absorption band is observed for CNDipp^{CC}Ph^{CN} at 2228 cm^{-1}.

Fused-ring 2-isopropyl-1-naphthylisocyanide (CN-1-(2-^{i}Pr)-Naph) was prepared according to the multistep synthesis in Scheme 4.2. Nitration of 2-isopropylnaphthalene occurs unselectively, requiring separation of the desired 2-isopropyl-1-nitronaphthalene isomer by column chromatography. Subsequent reduction of the nitro group with H_2(g) and Pd/C yields the key intermediate (2-isopropyl-1-naphthyl)amine.[28,29] Formylation, followed by dehydration, then yields CN-1-(2-^{i}Pr)-Naph, which exhibits a sharp *ν*(CN) stretching frequency at 2114 cm^{-1} with a

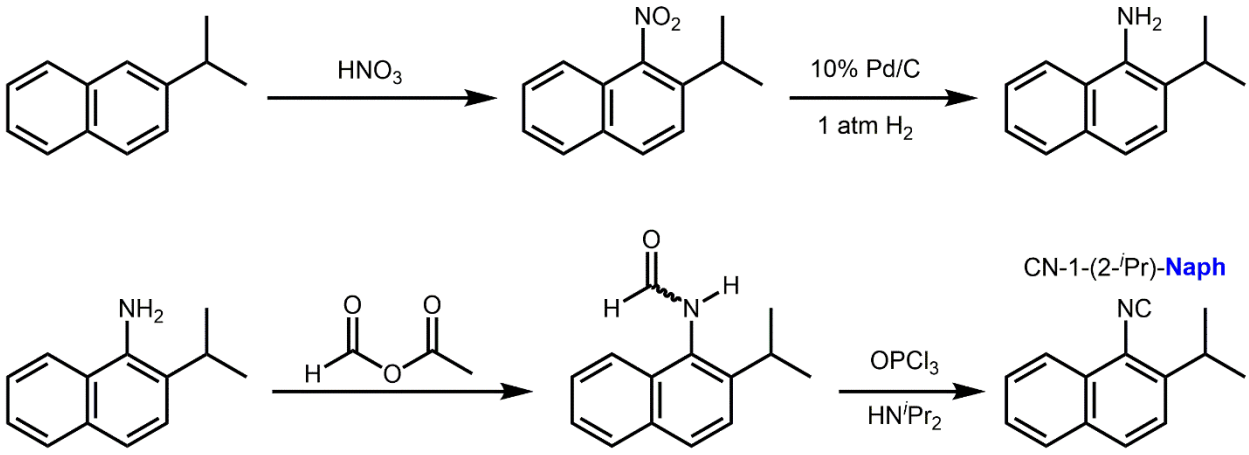

Scheme 4.2. Synthesis of the fused-ring arylisocyanide ligand CN-1-(2-^{i}Pr)-Naph.

shoulder at 2092 cm^{-1}, and a diagnostic ^{13}C NMR chemical shift at 172.7 ppm for the isocyanide carbon.

4.2.2. Synthesis and Characterization of W(CNDipp^{CC}Ar)$_6$ and W(CN-1-(2-^{i}Pr)-Naph)$_6$ Complexes

Reductive metalation of CNDipp^{CC}Ar ligands with $WCl_4(THF)_2$ and sodium amalgam (Na(Hg)) in the dark proceeds smoothly in room temperature THF solution over the course of several hours to yield magenta W(CNDipp^{CC}Ar)$_6$ (Scheme 4.3; Ar = Ph, 1-Naph, 9-Phen). Use of CNDipp^{CC}Ph^{OMe} instead affords W(CNDipp^{CC}Ph^{OMe})$_6$ as red needles after crystallization from pentane/C_6H_6. Interestingly, THF solutions of CNDipp^{CC}Ph^{CN} appear to be reductively unstable

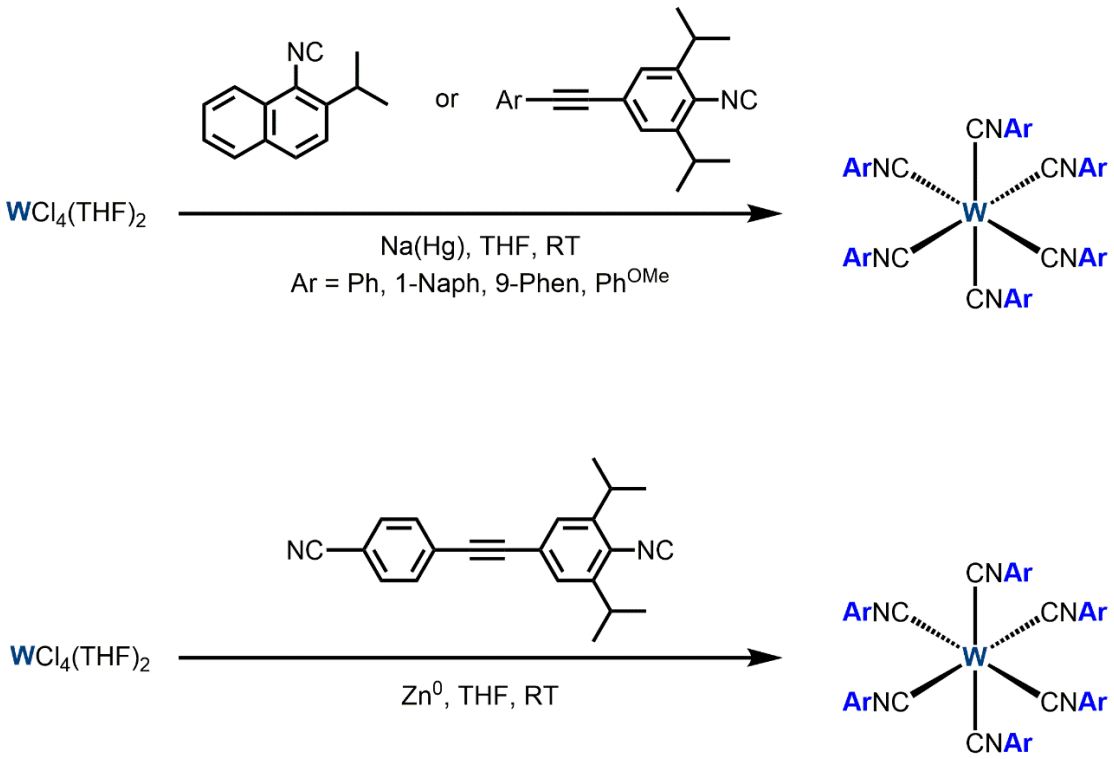

Scheme 4.3. Synthesis of W(CNDipp^{CC}Ar)$_6$ and W(CN-1-(2-^{i}Pr)-Naph)$_6$ complexes.

towards Na(Hg), and W(CNDipp^{CC}Ph^{CN})$_6$ is not observed to form under these conditions. Instead, reduction of a mixture of CNDipp^{CC}Ph^{CN} and $WCl_4(THF)_2$ in THF with Zn^0 affords W(CNDipp^{CC}Ph^{CN})$_6$ as a dark violet solid after purification (Scheme 4.3).

Attempts to prepare homoleptic tungsten(0) fused-ring arylisocyanide complexes using 2-naphthylisocyanide (CN-2-Naph) and 1-naphthylisocyanide (CN-1-Naph) under analogous reaction conditions were largely unsuccessful. While W(CN-2-Naph)$_6$ and W(CN-1-Naph)$_6$ could be observed to form at early time points (ca. 15–30 minutes) by IR analysis of crude reaction mixtures, upon prolonged stirring the diagnostic broad, intense *ν*(CN) assigned to the complex was no longer present. Scouring milder reductant/solvent combinations (e.g., Na(Hg)/C_6H_6, Zn^0/THF, Zn^0/C_6H_6, etc.) led to only minor improvements- W(CN-2-Naph)$_6$ and W(CN-1-Naph)$_6$ were present after longer reaction times, as confirmed by ^{1}H NMR spectroscopy, IR spectroscopy, and single crystal X-ray diffraction (XRD; *vide infra*), but could not be isolated in significant quantity. Control experiments established that THF solutions of CN-2-Naph and CN-1-Naph are stable towards Na(Hg) for extended periods of time. Therefore, we attribute the instability of W(CN-2-Naph)$_6$ and W(CN-1-Naph)$_6$ under the reductive synthetic conditions to tungsten-mediated isocyanide coupling. Intramolecular coupling of coordinated isocyanides has been observed in related low-valent molybdenum and tungsten isocyanide complexes.[30]

Reduction of $WCl_4(THF)_2$ by Na(Hg) in the presence of more sterically hindered CN-1-(2-^{i}Pr)-Naph instead yields W(CN-1-(2-^{i}Pr)-Naph)$_6$ as red needles in high isolated yield following crystallization from room temperature pentane/C_6H_6 solution (Scheme 4.3). The greater stability of W(CN-1-(2-^{i}Pr)-Naph)$_6$ versus W(CN-2-Naph)$_6$ and W(CN-1-Naph)$_6$ is consistent with the presence of sterically demanding substituents at both positions *ortho* to the isocyanide, which

preclude inter- and intramolecular CNAr coupling due to steric clashing. This is reflected in the corresponding solid-state structures (*vide infra*). The behavior of W(CN-1-(2-^{i}Pr)-Naph)$_6$ is also in line with previous findings from our group that incorporation of increasingly bulky groups at the 2 and 6 positions of monoarylisocyanides leads to more effective protection of the tungsten center and overall greater stability for W(CNAr)$_6$ complexes (Ar = Dipp > Xy > Ph; Xy = 2,6-dimethylphenyl).[18-20]

W(CN-1-(2-^{i}Pr)-Naph)$_6$ and all W(CNDipp^{CC}Ar)$_6$ complexes display a single set of ^{1}H and ^{13}C NMR resonances for the isocyanide ligands in C_6D_6, indicating high symmetry in solution. While the isocyanide (CN-1-(2-^{i}Pr)-Naph: 179.6 ppm; CNDipp^{CC}Ar: 176.3–177.1 ppm) and alkyne (88.4–95.8 ppm) ^{13}C NMR resonances of the complexes do not shift significantly from their corresponding free ligands, they display diagnostic broad, intense ν(CN) at lower energies (1934–1944 cm^{-1}), consistent with significant π-back-donation from the W(0) center to the arylisocyanides upon coordination.

Single crystal X-ray diffraction studies confirmed the identity of the W(CN-Naph)$_6$ and W(CNDipp^{CC}Ar)$_6$ complexes, and their solid-state structures are illustrated in Figure 4.2. W(CNDipp^{CC}Ar)$_6$ compounds (Ar = 1-Naph, 9-Phen, Ph^{OMe}, Ph^{CN}) invariably suffer from poor resolution and/or disorder, and only the major component of the disorder is shown. Attempts to obtain higher quality structures by growing crystals under different sets of conditions were unsuccessful. Thus, the disorder and poor resolution of the W(CNDipp^{CC}Ar)$_6$ molecular structures preclude a detailed comparative discussion of their structural metrics. Single crystals suitable for XRD analysis could not be obtained for W(CNDipp^{CC}Ph)$_6$ despite significant efforts.

In contrast, W(CN-1-(2-^{i}Pr)-Naph)$_6$ crystallizes in the space group $P\bar{1}$ without any disorder

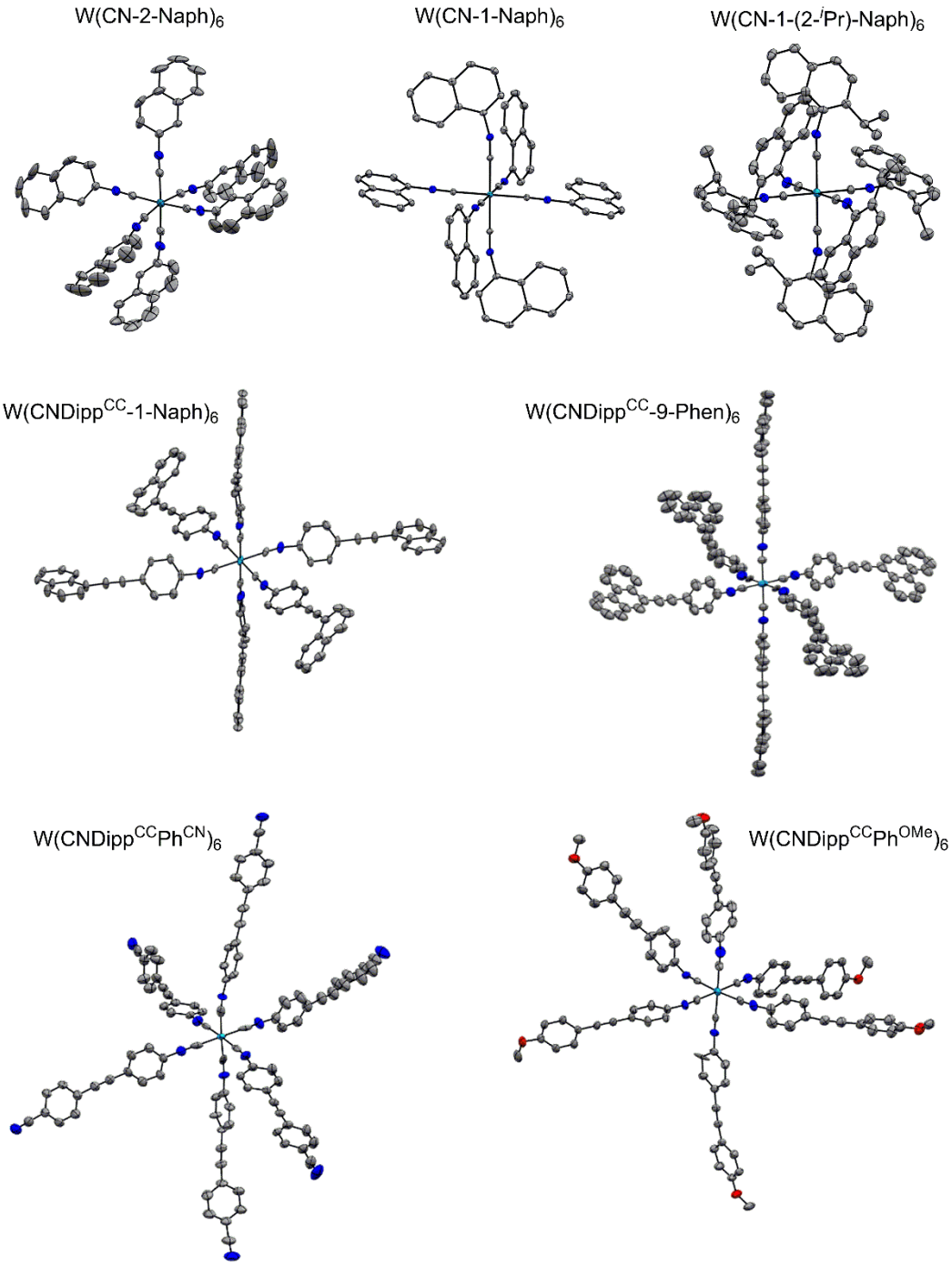

Figure 4.2. Solid-state structures of $W(CN\text{-}Naph)_6$ and $W(CNDipp^{CC}Ar)_6$ complexes with thermal ellipsoids set at 50% probability. Isopropyl groups, co-crystallized solvents, hydrogen atoms, and the minor component of the disorder are omitted for clarity. Color code: W = teal, N = blue, O = red, C = gray.

(Figure 4.2). This complex displays W–C (2.068, 2.070, 2.084 Å) and C≡N (1.171, 1.170, 1.164 Å) bond lengths, as well as C_{iso}–N–C_{aryl} bond angles (159.7°, 159.7°, 166.7°), comparable to those of W(CNDipp)$_6$ and W(CNDippAr)$_6$ compounds (Ar = Ph, Ph^{OMe2}, Ph^{OMe3}, Ph^{Ph}) previously structurally characterized by our group.[20,21] The geometry around the tungsten center is close to octahedral, with C–W–C angles of 88.3°, 89.7°, and 92.3°. W(CNDipp^{CC}-1-Naph)$_6$ and W(CNDipp^{CC}Ph^{OMe})$_6$, which only feature minor disorder in their W(C≡N–C_{aryl})$_6$ core, also display similar bond lengths and angles.

Further inspection of the solid-state structure of W(CN-1-(2-^{i}Pr)-Naph)$_6$ reveals that, in addition to effectively shielding the metal center, the sterics afforded by the naphthyl and isopropyl groups flanking the isocyanide functionality significantly constrain the ligands, and thus likely impart considerable rigidity to the complex. Steric clashing also impedes close approach between adjacent C≡N–Ar units, disfavoring potential decomposition by an intramolecular isocyanide coupling pathway. In contrast, the structure of W(CN-1-Naph)$_6$, which is nearly identical to that of W(CN-1-(2-^{i}Pr)-Naph)$_6$, but where the ligands lack sterics at one of the *ortho* positions, suggests each naphthylisocyanide has two neighboring ligands to which it can potentially couple (Figure 4.2). Such possibility is even greater in W(CN-2-Naph)$_6$, which features only hydrogen atoms *ortho* to the isocyanide. Thus, this trend is consistent with the greater stability of W(CN-1-(2-^{i}Pr)-Naph)$_6$ over W(CN-1-Naph)$_6$ and W(CN-2-Naph)$_6$ under the reductive metalation conditions employed.

Despite the marginal quality of the molecular structures of W(CNDipp^{CC}Ar)$_6$ complexes, they are sufficiently adequate to provide critical information regarding the orientation of the π-systems present. We have previously established that the conformation of the *trans* arylisocyanide

aromatic systems determines the degree of conjugation along the three distinct molecular axes, and consequently, the location of the lowest energy MLCT absorption maximum.[22] Importantly, the use of bulky *ortho* isopropyl groups in $W(CNDipp)_6$ and $W(CNDippAr)_6$ (Ar = Ph, Ph^{OMe2}, Ph^{OMe3}, Ph^{Ph}) has been observed to enforce coplanar *trans* CNDipp π-systems, resulting in the fully conjugated orientation being the lowest energy conformation.[20,21] $W(CN\text{-}1\text{-}(2\text{-}^{i}Pr)\text{-}Naph)_6$ and $W(CNDipp^{CC}\text{-}1\text{-}Naph)_6$, $W(CNDipp^{CC}\text{-}9\text{-}Phen)_6$, and $W(CNDipp^{CC}Ph^{CN})_6$ follow this trend, displaying nearly coplanar *trans* naphthyl- and 2,6-diisopropylphenylisocyanide aromatic systems, respectively (Figure 4.2). Interestingly, the CNDipp π-systems of $W(CNDipp^{CC}Ph^{OMe})_6$ are instead closer to orthogonal, despite the presence of isopropyl substituents at both *ortho* positions. However, the electronic absorption spectrum of this complex closely resembles that of its $W(CNDippAr)_6$ and $W(CNDipp^{CC}Ar)_6$ congeners rather than that of $W(CNXy)_6$, where the *trans* CNXy ligands are approximately orthogonal to each other.[31] We tentatively ascribe this discrepancy to crystal packing effects; one molecule of C_6H_6 co-crystallizes in the vicinity of two CNDipp fragments. It is also worth noting that for $W(CNXy)_6$, $W(CNDipp)_6$, and $W(CNDippAr)_6$ both orthogonal and coplanar conformers are present in solution, albeit with appreciably different populations.[22]

In addition to the CNDipp π-systems proximal to the tungsten center, the orientation of the peripheral aromatic systems in the alkynyl-bridged $W(CNDipp^{CC}Ar)_6$ complexes will also influence the degree of conjugation along a given molecular axis, and as a result the observed spectroscopic and photophysical properties. With relation to the CNDipp fragment for a given individual ligand, the 1-Naph, 9-Phen, Ph^{CN}, and Ph^{OMe} secondary π-systems adopt a distribution of conformations ranging from nearly coplanar to nearly orthogonal, as determined by the dihedral

angle between the mean planes defined by the corresponding aryl rings ($\varphi_{Ar1–Ar2}$; Ar1 = Dipp). The average $\varphi_{Ar1–Ar2}$ in the series of W(CNDipp^{CC}Ar)$_6$ compounds are 37.7° (Ar2 = 1-Naph), 34.6° (Ar2 = 9-Phen), 31.5° (Ar2 = Ph^{OMe}), and 56.1° (Ar2 = Ph^{CN}). While these angles are calculated using the major component of the disordered structure, the dihedral angles for the minor component do not differ appreciably. The distribution of conformations observed for these compounds in the solid state, despite featuring an alkynyl π-bridge, are not entirely surprising given the low rotational barrier for related diphenylacetylene. For comparison, the average dihedral angle for W(CNDippPh)$_6$, W(CNDippPh^{Ph})$_6$, and W(CNDippPh^{OMe2})$_6$ is ca. 35°, and that of W(CNDippPh^{OMe3})$_6$ is 51°.

4.2.3. Absorption and Steady-State Emission of W(CNDipp^{CC}Ar)$_6$ and W(CN-1-(2-*i*Pr)-Naph)$_6$ Complexes

Previous studies from our group established that W(CNAr)$_6$ compounds (Ar = Ph, Xy, Dipp) display intense MLCT [dπ(W) → π*(CNAr)] absorption bands in the visible region,[17-20,22] as anticipated for isoelectronic analogues of Ru(bpy)$_3^{2+}$. Gratifyingly, the employment of CNDippAr in place of CNDipp leads to both a bathochromic shift and increase in intensity of the lowest energy MLCT absorption maximum for W(CNDippAr)$_6$.[21] For example, the MLCT transition shifts from $\lambda_{abs,max}$ = 465 nm with ε_{465} = 9.5 x 10^4 M^{-1} cm^{-1} for the base complex W(CNDipp)$_6$ to $\lambda_{abs,max}$ = 495 nm with ε_{495} = 1.3 x 10^5 M^{-1} cm^{-1} for the biarylisocyanide complexes W(CNDippPh)$_6$, W(CNDippPh^{OMe2})$_6$, and W(CNDippPh^{OMe3})$_6$ (Figure 4.3, Table 4.1). Further red-shifting ($\lambda_{abs,max}$ = 506 nm) and increased MLCT band intensity (ε_{506} = 1.6 x 10^5 M^{-1} cm^{-1}) is observed for W(CNDippPh^{Ph})$_6$, supported by more conjugated terarylisocyanides.

Given these observations, we reasoned that replacing the biaryl C(sp^2)–C(sp^2) linkage in CNDippAr, which limits the degree of coplanarity that can be achieved, with an alkyne π-bridge would lead to increased conjugation and more favorable optical properties. In accordance with its deep magenta color in solution, the lowest energy MLCT absorption maximum for W(CNDipp^{CC}Ph)$_6$ occurs at $\lambda_{abs,max}$ = 521 nm in toluene, which is bathochromically shifted by 26 nm from that of its biphenylisocyanide analogue W(CNDippPh)$_6$ (Figure 4.3, Table 4.1). Satisfyingly, this maximum also occurs at a longer wavelength than that of the most conjugated oligoarylisocyanide complex studied previously, W(CNDippPh^{Ph})$_6$.

Increasing the peripheral aromatic system of W(CNDipp^{CC}Ar)$_6$ from Ar = Ph to Ar = 1-Naph or 9-Phen leads further red-shifts in the MLCT absorption maximum; these occur at $\lambda_{abs,max}$ = 531 and 533 nm for W(CNDipp^{CC}-1-Naph)$_6$ and W(CNDipp^{CC}-9-Phen)$_6$, respectively. Addition of a nitrile group at the 4-position of the phenyl group (Ar = Ph^{CN}) results in an even greater shift to lower energy, with W(CNDipp^{CC}Ph^{CN})$_6$ displaying its MLCT absorption band at $\lambda_{abs,max}$ = 544 nm. In contrast, W(CNDipp^{CC}Ph^{OMe})$_6$, incorporating an electron-donating methoxy group, leads to a slight blue-shift relative to W(CNDipp^{CC}Ph)$_6$ (Figure 4.3, Table 4.1). These measurements correlate well with the increasing electron-withdrawing nature of the secondary aromatic system in the order Ph^{OMe} < Ph < 1-Naph < 9-Phen < Ph^{CN}, as gauged by their Hammett parameters (taking Ph as the base complex; *vide infra*),[32] and are consistent with the MLCT nature of the transition. Importantly, these W(CNDipp^{CC}Ar)$_6$ complexes maintain extinction coefficients of similar intensity (ε = 1.1–1.6 x 10^5 M^{-1} cm^{-1}) to their oligoarylisocyanide relatives (Table 4.1). It is also worth noting that the absorption traces of all W(CNDipp^{CC}Ar)$_6$ complexes resemble those of the W(CNDippAr)$_6$ variants. This suggests that in solution the *trans* CNDipp π-systems of

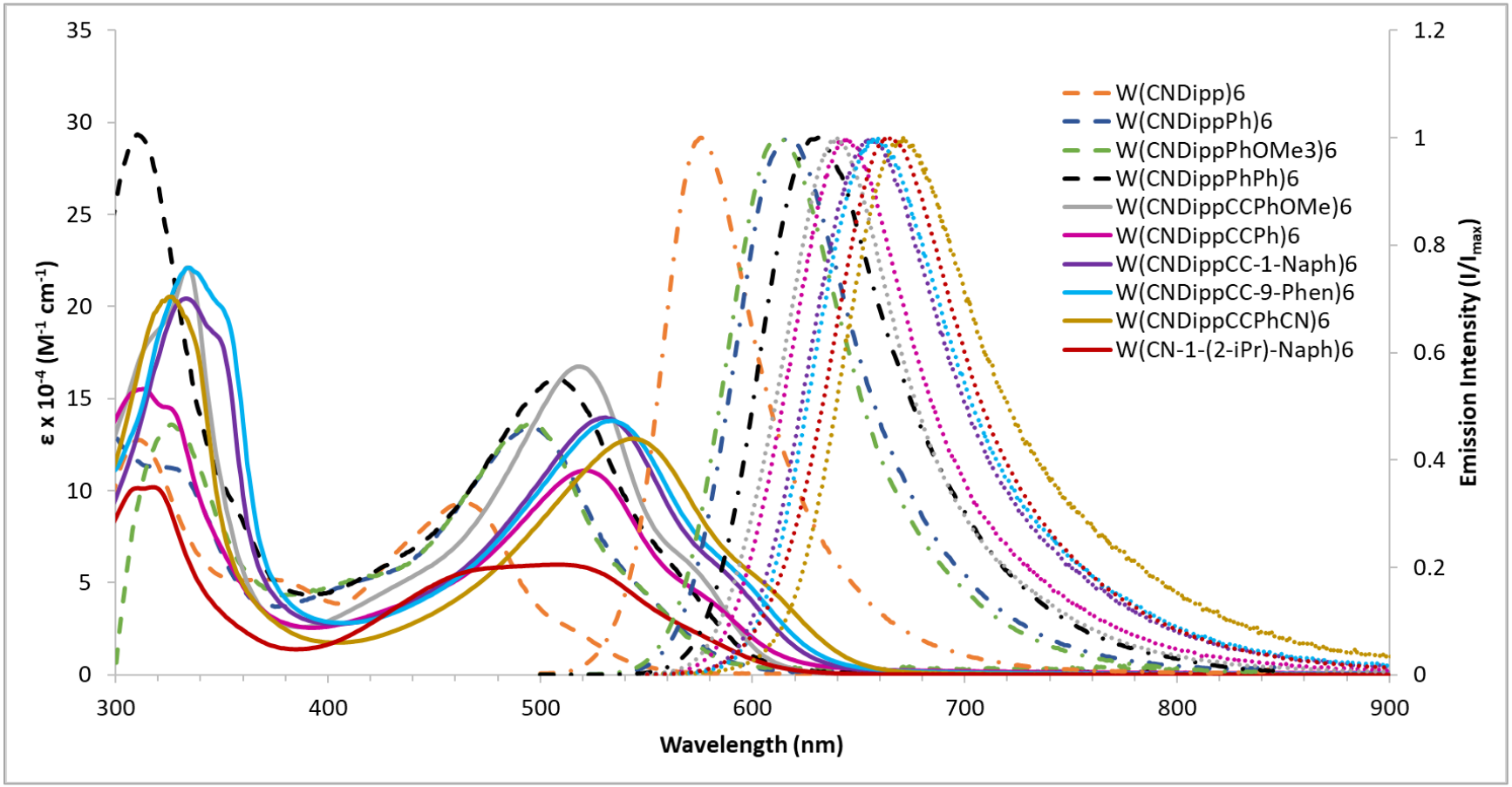

Figure 4.3. Absorption (dashed, solid) and emission (dotted-dashed, dotted) spectra of $W(CNDipp)_6$,[a] $W(CNDippAr)_6$ (Ar = Ph, Ph^{OMe3}, Ph^{Ph}),[a] $W(CNDipp^{CC}Ar)_6$ (Ar = Ph^{OMe}, Ph, 1-Naph, 9-Phen, Ph^{CN}), and $W(CN\text{-}1\text{-}(2\text{-}^{i}Pr)\text{-}Naph)_6$ in room temperature toluene solution. [a]Data taken from ref. 21.

Table 4.1. Absorption maxima, extinction coefficients, emission maxima, and FWHM values for W(CNDipp)$_6$, W(CNDippAr)$_6$, W(CNDipp^{CC}Ar)$_6$, and W(CN-1-(2-^{i}Pr)-Naph)$_6$ complexes in room temperature toluene, 2-MeTHF, and THF solution.

		Toluene		2-MeTHF		THF	
Compound	$\varepsilon_{\lambda,max}$[b] {$\lambda_{abs,max}$}[c]	$\lambda_{em,max}$[c] {$\tilde{\nu}_{em,max}$}[d]	**FWHM**[d]	$\lambda_{em,max}$[c] {$\tilde{\nu}_{em,max}$}[d]	**FWHM**[d]	$\lambda_{em,max}$[c] {$\tilde{\nu}_{em,max}$}[d]	**FWHM**[d]
W(CNDipp)$_6$[a]	9.5 x 10^4 {465}	575 {17300}	1610	-----	-----	577 {17300}	1750
W(CNDippPh)$_6$[a]	1.3 x 10^5 {495}	617 {16200}	1880	-----	-----	626 {15900}	2250
W(CNDippPh^{OMe2})$_6$[a]	1.3 x 10^5 {495}	618 {16100}	1890	-----	-----	627 {15800}	2280
W(CNDippPh^{OMe3})$_6$[a]	1.3 x 10^5 {495}	612 {16300}	1850	-----	-----	623 {16000}	2180
W(CNDippPh^{Ph})$_6$[a]	1.6 x 10^5 {506}	629 {15800}	1970	-----	-----	656 {15200}	2670
W(CNDipp^{CC}Ph^{OMe})$_6$	1.6 x 10^5 {518}	640 {15600}	1610	642 {15600}	1780	645 {15500}	1850
W(CNDipp^{CC}Ph)$_6$	1.1 x 10^5 {521}	644 {15500}	1670	648 {15400}	1880	653 {15300}	1980
W(CNDipp^{CC}-1-Naph)$_6$	1.4 x 10^5 {531}	653 {15300}	1780	669 {15000}	2120	675 {14800}	2300
W(CNDipp^{CC}-9-Phen)$_6$	1.4 x 10^5 {533}	658 {15200}	1780	672 {14900}	2150	683 {14600}	2350
W(CNDipp^{CC}Ph^{CN})$_6$	1.3 x 10^5 {544}	671 {14900}	1770	723 {13800}	2990	753 {13300}	3510
W(CN-1-(2-^{i}Pr)-Naph)$_6$	5.7 x 10^4 {509}	664 {15100}	1680	670 {14900}	1910	671 {14900}	1990

[a]Data taken from ref. 21. [b]In M^{-1} cm^{-1}. [c]In nm. [d]In cm^{-1}.

$W(CNDipp^{CC}Ph^{OMe})_6$ predominantly adopt a coplanar conformation, in contrast to what is observed in the solid state.

The fused-ring arylisocyanide CN-1-(2-*i*Pr)-Naph provides an orthogonal approach to increasing the conjugation in the parent complex $W(CNDipp)_6$, whereby rather than attachment of a second phenyl group to CNDipp via a C(sp^2)–C(sp^2) or C(*sp*)–C(*sp*) linkage, it is fused to this fragment. In toluene solution, $W(CN\text{-}1\text{-}(2\text{-}^{i}Pr)\text{-}Naph)_6$ absorbs equally strongly in the region 460–520 nm, with a very slight maximum at 509 nm (Figure 4.3). Interestingly, the extinction coefficient at this wavelength (ε_{509} = 5.7 x 10^4 M^{-1} cm^{-1}) is roughly half that of $W(CNDippAr)_6$ and $W(CNDipp^{CC}Ar)_6$ complexes at their corresponding maxima (Table 4.1).

As for $W(CNDippAr)_6$ complexes, the absorption profiles of $W(CN\text{-}1\text{-}(2\text{-}^{i}Pr)\text{-}Naph)_6$ and $W(CNDipp^{CC}Ar)_6$ compounds are unchanged in the more polar solvents 2-MeTHF and THF. The extinction coefficients measured in the latter are similar to those in toluene. This is consistent with the high octahedral symmetry of the complexes, which only results in a small net dipole moment despite significant charge delocalization in the ground state.[21,22]

Normalized luminescence spectra of $W(CNDipp^{CC}Ar)_6$ and $W(CN\text{-}1\text{-}(2\text{-}^{i}Pr)\text{-}Naph)_6$ complexes acquired in dilute toluene solutions under an inert N_2 atmosphere are presented in Figure 4.3. For comparison, the emission spectra of parent $W(CNDipp)_6$ and oligoarylisocyanides $W(CNDippAr)_6$ (Ar = Ph, Ph^{OMe3}, Ph^{Ph}) are also included. As can be seen, the luminescence traces of all these $W(CNAr)_6$ complexes are similar in shape. In toluene solution, the emission profiles of $W(CNDipp^{CC}Ar)_6$ compounds mirror the trend observed in their absorption spectra. For instance, the emission maximum of $W(CNDipp^{CC}Ph)_6$ at $\lambda_{em,max}$ = 644 nm is red-shifted from that of $W(CNDippPh)_6$ at $\lambda_{em,max}$ = 617 nm ($\Delta\lambda_{em,max}$ = 27 nm) by the same amount as their respective

lowest energy MLCT absorption maxima ($\Delta\lambda_{abs,max}$ = 26 nm). Similarly, within the W(CNDipp^{CC}Ar)$_6$ series, movement of the emission maximum to longer wavelength in the order Ph^{OMe} < Ph < 1-Naph < 9-Phen < Ph^{CN} occurs with $\Delta\lambda_{em,max} \approx \Delta\lambda_{abs,max}$ (Figure 4.3, Table 4.1). Structurally unique W(CN-1-(2-^{i}Pr)-Naph)$_6$ does not follow this pattern, and instead luminesces with $\lambda_{em,max}$ = 664 nm. Thus, the absorption and emission profiles of W(CNAr)$_6$ complexes in toluene can readily be tuned by 80–100 nm through appropriate choice of arylisocyanide ligand.

Measurements of the photoluminescence quantum yields of W(CNDipp^{CC}Ar)$_6$ compounds in toluene solution also reveal they are highly emissive. W(CNDipp^{CC}Ph)$_6$ possesses ϕ_{PL} = 0.37, comparable to ϕ_{PL} = 0.41 for its biarylisocyanide analogue W(CNDippPh)$_6$. Interestingly, increasing the π-accepting ability of the secondary aryl system in W(CNDipp^{CC}Ar)$_6$ results in systematic decrease of ϕ_{PL}, with Ar = 1-Naph, 9-Phen, and Ph^{CN} variants displaying photoluminescence quantum yields of 0.30, 0.26, and 0.23, respectively. These values are lower and cover a larger range than those of W(CNDippAr)$_6$ complexes (0.41–0.44) in the same solvent. Surprisingly, addition of a methoxy substituent to CNDipp^{CC}Ph has an even more substantial effect, doubling the measured quantum yield to ϕ_{PL} = 0.78 for W(CNDipp^{CC}Ph^{OMe})$_6$. Meanwhile, W(CN-1-(2-^{i}Pr)-Naph)$_6$ features a respectable value of ϕ_{PL} = 0.25. These photoluminescence quantum yields are still high compared to those of W(CNDipp)$_6$ (ϕ_{PL} = 0.03) and Ru(bpy)$_3^{2+}$ (ϕ_{PL} = 0.062 in MeCN).

In contrast to their absorption properties, the luminescence profiles of W(CNDipp^{CC}Ar)$_6$ and W(CN-1-(2-^{i}Pr)-Naph)$_6$ complexes are highly dependent on the polarity of the solvent. In general, their behavior in 2-MeTHF and THF parallels that of their W(CNDippAr)$_6$ relatives. For example, upon moving to 2-MeTHF, the emission bands of W(CNDipp^{CC}Ar)$_6$ and W(CN-1-(2-

^{i}Pr)-Naph)$_6$ compounds red-shift and broaden (Table 4.1). These changes are more prominent in THF, which has a higher dielectric constant. Comparison of the differences in $\lambda_{em,max}$ and the full-width at half-maximum (FWHM) for the luminescence traces in toluene versus THF solution suggests W(CN-1-(2-^{i}Pr)-Naph)$_6$ ($\Delta\lambda_{em,max}$ = 7 nm; ΔFWHM = 310 cm^{-1}) and W(CNDipp^{CC}Ph)$_6$ ($\Delta\lambda_{em,max}$ = 9 nm; ΔFWHM = 310 cm^{-1}) behave most similar to the biarylisocyanide complexes W(CNDippAr)$_6$ (Ar = Ph, Ph^{OMe2}, Ph^{OMe3}; $\Delta\lambda_{em,max}$ = 9–11 nm; ΔFWHM = 330–390 cm^{-1}). In turn, the changes are greater for W(CNDipp^{CC}1-Naph)$_6$ and W(CNDipp^{CC}-1-Phen)$_6$, with $\Delta\lambda_{em,max}$ = 22 and 25 nm, and ΔFWHM = 520 and 570 cm^{-1}, respectively. These values imply that the more extended aromatic systems promote larger excited-state dipoles, which are able to relax and be stabilized to a greater degree in more polar media. This is consistent with DFT investigations on the lowest triplet excited states of W(CNDipp)$_6$ and W(CNDippPh^{OMe2})$_6$.[22]

W(CNDipp^{CC}Ph^{CN})$_6$ exhibits the most drastic shifts in $\lambda_{em,max}$ and FWHM upon moving from toluene to THF. Notably, the emission maximum red-shifts by 82 nm and the FWHM increases by 1740 cm^{-1} (Table 4.1). These changes are substantially greater than those for W(CNDipp^{CC}-1-Naph)$_6$, W(CNDipp^{CC}-9-Phen)$_6$, and W(CNDippPh^{Ph})$_6$ ($\Delta\lambda_{em,max}$ = 27 nm; ΔFWHM = 700 cm^{-1}). We attribute this to the greater electron-withdrawing capacity of the Ph^{CN} group and its ability to interact with solvent via the nitrile functionality. Intriguingly, the luminescence of W(CNDipp^{CC}Ph^{OMe})$_6$ is only minimally perturbed by the polarity of the solvent ($\Delta\lambda_{em,max}$ = 5 nm; ΔFWHM = 240 cm^{-1}; Table 4.1).

As with W(CNDipp)$_6$ and W(CNDippAr)$_6$ complexes, the photoluminescence quantum yields of W(CNDipp^{CC}Ar)$_6$ and W(CN-1-(2-^{i}Pr)-Naph)$_6$ compounds are also observed to diminish in more polar solvents (Table 4.2). Compared to toluene solution, ϕ_{PL} drops by 30% for

W(CNDipp^{CC}Ph^{OMe})$_6$, 57% for W(CNDipp^{CC}Ph)$_6$ and W(CN-1-(2-^{i}Pr)-Naph)$_6$, 83% for W(CNDipp^{CC}-1-Naph)$_6$, 88% for W(CNDipp^{CC}-9-Phen)$_6$, and >96% for W(CNDipp^{CC}Ph^{CN})$_6$ in THF. For comparison, ϕ_{PL} for W(CNDippPh)$_6$, W(CNDippPh^{OMe2})$_6$, W(CNDippPh^{OMe3})$_6$, and W(CNDippPh^{Ph})$_6$ decreases by 49, 50, 39, and 84%, respectively. These values are in line with the magnitude of charge transfer and subsequent excited-state relaxation expected for the different complexes as described above.

4.2.4. Excited-State Dynamics and Reduction Potentials of W(CNDipp^{CC}Ar)$_6$ and W(CN-1-(2-^{i}Pr)-Naph)$_6$ Complexes

The overlaid time-resolved luminescence traces for *W(CNDipp^{CC}Ar)$_6$ and *W(CN-1-(2-^{i}Pr)-Naph)$_6$ complexes in toluene, 2-MeTHF, and THF are shown in Figure 4.4. These measurements show that the excited-state lifetimes of these complexes highly depend on the solvent polarity, with τ(^{3}MLCT) decreasing on progression from toluene to THF for a given complex. This is in agreement with the greater distortion observed for *W(CNDipp^{CC}Ar)$_6$ or *W(CN-1-(2-^{i}Pr)-Naph)$_6$ in THF versus toluene solution (*vide supra*), and the trend exhibited by *W(CNDippAr)$_6$ complexes.

Like *W(CNDippAr)$_6$ complexes, the excited-state dynamics of *W(CNDipp^{CC}Ar)$_6$ compounds are governed by nonradiative decay. Whereas the radiative decay rate constant (k_r) remains relatively constant for a given complex in all three solvents, the nonradiative decay constant (k_{nr}) increases upon progression to more polar THF and can vary by over an order of magnitude (Table 4.2). As a result, the lifetimes of *W(CNDipp^{CC}Ar)$_6$ and *W(CN-1-(2-^{i}Pr)-Naph)$_6$ in general decrease in the order toluene > 2-MeTHF > THF. In alignment with their other

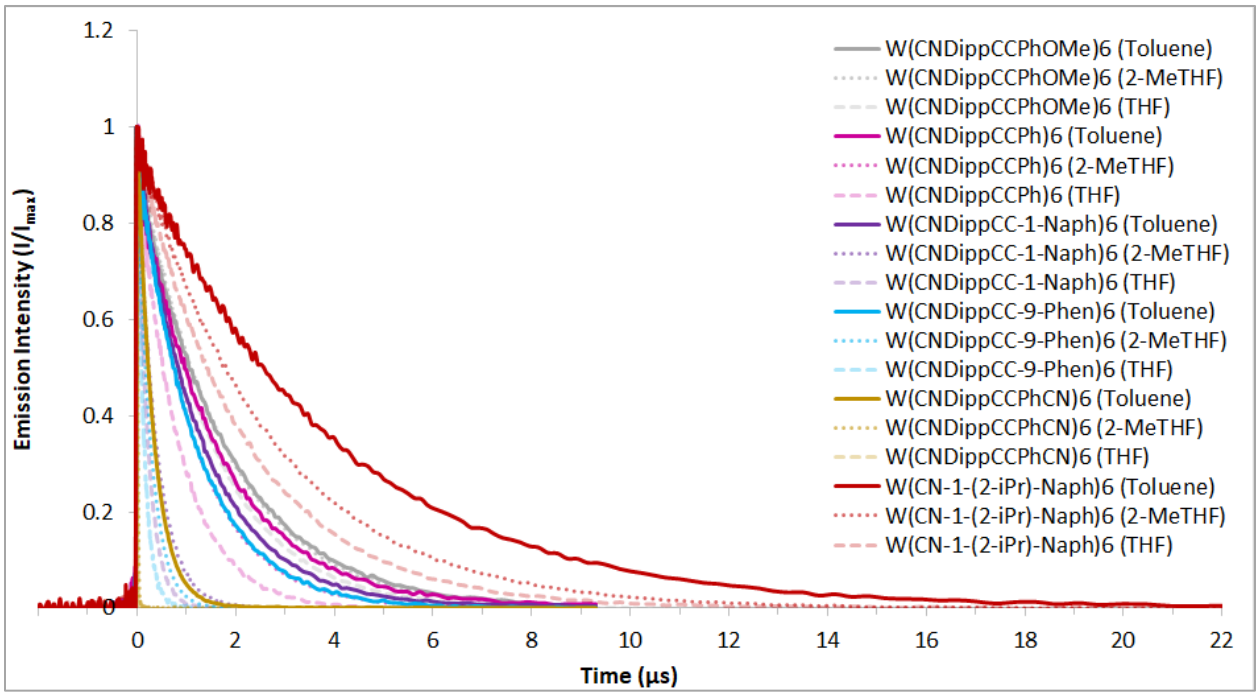

Figure 4.4. Time-resolved luminescence traces for W(CNDipp^{CC}Ar)$_6$ and W(CN-1-(2-^{i}Pr)-Naph)$_6$ complexes in room temperature toluene, 2-MeTHF, and THF solution.

photophysical properties, the drop in τ(*W(CNDipp^{CC}Ar)$_6$) is more drastic in the order Ph^{OMe} < Ph < 1-Naph < 9-Phen < Ph^{CN}, with corresponding k_{nr}(THF)/k_{nr}(toluene) ratios of 2.6 < 2.8 < 9.0 < 10.7 < 59, respectively. For W(CN-1-(2-^{i}Pr)-Naph)$_6$, k_{nr}(THF)/k_{nr}(toluene) = 2.1.

Because of the relatively small ratios of k_{nr}(THF)/k_{nr}(toluene) for W(CNDipp^{CC}Ph^{OMe})$_6$ and W(CN-1-(2-^{i}Pr)-Naph)$_6$, the excited-state lifetimes of these compounds are long in both solvents: τ(*W(CNDipp^{CC}Ph^{OMe})$_6$) = 1.82/1.45 µs and τ(*W(CN-1-(2-^{i}Pr)-Naph)$_6$) = 3.83/2.15 µs in toluene/THF. Notably, ϕ_{PL} = 0.55 in THF is comparatively high for W(CNDipp^{CC}Ph^{OMe})$_6$. Such a fortuitous combination of photophysical properties in solvents of different polarity make these complexes uniquely appealing for applications such as photoredox catalysis (*vide infra*).

That W(CN-1-(2-^{i}Pr)-Naph)$_6$ exhibits longer τ(^{3}MLCT) than all W(CNDippAr)$_6$ and

Table 4.2. Excited-state decay parameters for $W(CNDipp)_6$, $W(CNDippAr)_6$, $W(CNDipp^{CC}Ar)_6$, and $W(CN\text{-}1\text{-}(2\text{-}^{i}Pr)\text{-}Naph)_6$ complexes in room temperature toluene, 2-MeTHF, and THF solution.

	Toluene				2-MeTHF				THF			
Compound	τ^b	ϕ_{PL}	$k_r{}^c$	$k_{nr}{}^c$	τ^b	ϕ_{PL}	$k_r{}^c$	$k_{nr}{}^c$	τ^b	ϕ_{PL}	$k_r{}^c$	$k_{nr}{}^c$
$W(CNDipp)_6$[a]	0.12	0.03	2.3×10^5	8.0×10^6	-----	-----	-----	-----	0.08	0.01	1.6×10^5	1.3×10^7
$W(CNDippPh)_6$[a]	1.73	0.41	2.4×10^5	3.4×10^5	-----	-----	-----	-----	1.32	0.21	1.6×10^5	6.0×10^5
$W(CNDippPh^{OMe2})_6$[a]	1.65	0.42	2.6×10^5	3.5×10^5	-----	-----	-----	-----	1.20	0.21	1.8×10^5	6.6×10^5
$W(CNDippPh^{OMe3})_6$[a]	1.83	0.41	2.2×10^5	3.2×10^5	-----	-----	-----	-----	1.56	0.25	1.6×10^5	4.8×10^5
$W(CNDippPh^{Ph})_6$[a]	1.53	0.44	2.9×10^5	3.7×10^5	-----	-----	-----	-----	0.35	0.07	1.9×10^5	2.7×10^6
$W(CNDipp^{CC}Ph^{OMe})_6$	1.82	0.78	4.3×10^5	1.2×10^5	1.69	0.49	2.9×10^5	3.0×10^5	1.45	0.55	3.8×10^5	3.1×10^5
$W(CNDipp^{CC}Ph)_6$	1.75	0.37	2.1×10^5	3.6×10^5	1.07	0.21	2.0×10^5	7.3×10^5	0.80	0.16	2.0×10^5	1.0×10^6
$W(CNDipp^{CC}\text{-}1\text{-}Naph)_6$	1.45	0.30	2.0×10^5	4.8×10^5	0.38	0.09	2.3×10^5	2.4×10^6	0.22	0.05	2.1×10^5	4.3×10^6
$W(CNDipp^{CC}\text{-}9\text{-}Phen)_6$	1.24	0.26	2.1×10^5	6.0×10^5	0.27	0.06	2.3×10^5	3.5×10^6	0.15	0.03	2.2×10^5	6.4×10^6
$W(CNDipp^{CC}Ph^{CN})_6$	0.36	0.23	6.3×10^5	2.2×10^6	0.015	< 0.01	6.6×10^5	6.8×10^7	0.008	< 0.01	7.5×10^5	1.3×10^8
$W(CN\text{-}1\text{-}(2\text{-}^{i}Pr)\text{-}Naph)_6$	3.83	0.25	6.5×10^4	2.0×10^5	2.57	0.14	5.6×10^4	3.3×10^5	2.15	0.11	5.3×10^4	4.1×10^5

[a]Data taken from ref. 21. [b]In μs. [c]In s^{-1}.

$W(CNDipp^{CC}Ar)_6$ complexes in all three solvents is also noteworthy. We credit these observations to the greater rigidity of the former system. In contrast to $W(CNDippAr)_6$ and $W(CNDipp^{CC}Ar)_6$ complexes, which have radially extended aromatic systems that can enable a number of nonradiative decay pathways owing to their ability to rotate to a great extent in solution and interact more readily with solvent in the MLCT excited state, the expanded π-system in W(CN-1-(2-^{i}Pr)-Naph)$_6$ remains within the primary coordination sphere and is less accessible. In addition to helping protect the tungsten center in the excited state, the sterics resulting from the use of a 2-isopropylnaphthyl- rather 2,6-diisopropylphenylisocyanide appear to lock the ligands well in place (see XRD structure in Figure 4.2). This increased rigidity should favour longer *W(CN-1-(2-^{i}Pr)-Naph)$_6$ lifetimes. A similar increase in framework rigidity has been proposed to account for the more favorable photophysical properties, including increased $\tau(^3MLCT)$ and ϕ_{PL}, observed upon augmenting the sterics from $Mo(CN^{Me}Ar_3NC)_3$ to $Mo(CN^{tBu}Ar_3NC)_3$.[14,33]

In addition to the dependence of $*W(CNDipp^{CC}Ar)_6$ lifetimes on the polarity of the solvent, another trend can be gleaned from their photophysical data. For a given solvent, $\tau(^3MLCT)$ for these complexes decreases in the order Ph^{OMe} > Ph > 1-Naph > 9-Phen > Ph^{CN}. On the other hand, both $\lambda_{em,max}$ and k_{nr} increase along this progression, suggesting this class of chromophores may follow the energy-gap law.[34] This law predicts that for a set of related excited-state complexes, nonradiative decay becomes exponentially favorable as the energy gap between the ground and excited state decreases. Plots of $\ln(k_{nr})$ versus the energy of the emission maxima ($E_{em,max}$ in cm^{-1}) for $W(CNDipp^{CC}Ar)_6$ complexes have linear fits with R^2 values of 0.924, 0.994, and 0.973 in toluene, 2-MeTHF, and THF, respectively, confirming they abide by the energy-gap law (Figure 4.5). Because $E_{em,max}$ also correlates with the Hammett parameters, in principle this provides a

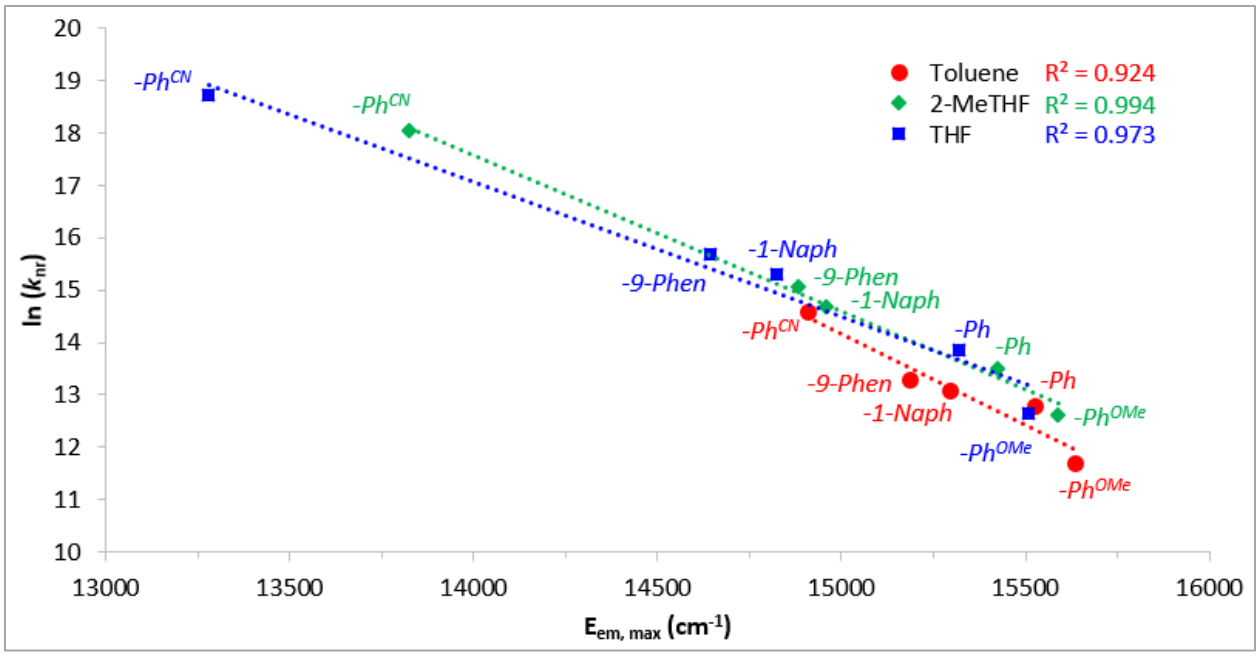

Figure 4.5. Plots of ln(k_{nr}) versus $E_{em,max}$ for W(CNDipp^{CC}Ar)$_6$ complexes.

rational method for constructing W(CNDipp^{CC}Ar)$_6$ photoactive complexes with desired photophysical properties for targeted applications.

Plots of ln(k_{nr}) versus $E_{em,max}$ for W(CNDippAr)$_6$ oligoarylisocyanide complexes display linear fits with R^2 values of 0.811 and 0.996 in toluene and THF, respectively, implying they may also follow the energy-gap law. This is not surprising given W(CNDippAr)$_6$ and W(CNDipp^{CC}Ar)$_6$ behave very similarly. However, it is worth mentioning that despite the strong correlation observed in THF, W(CNDippPh)$_6$, W(CNDippPh^{OMe2})$_6$, and W(CNDippPh^{OMe3})$_6$ share similar values of k_{nr} and $E_{em,max}$, so that these data points provide a closely spaced cluster in a plot consisting of four compounds. In contrast, W(CNDipp^{CC}Ar)$_6$ complexes cover a wider range of ln(k_{nr}) and $E_{em,max}$ values.

Encouraged by the promising combination of photophysical properties for W(CN-1-(2-

^{i}Pr)-Naph)$_6$ and W(CNDipp^{CC}Ar)$_6$ complexes, and the highly reducing excited-state potentials of their W(CNDipp)$_6$ and W(CNDippAr)$_6$ relatives, we next explored their electrochemistry by cyclic voltammetry. The full voltammograms of these complexes recorded at a scan rate of 100 mV/s in THF with 0.1 M [^{n}Bu$_4$N][PF$_6$] supporting electrolyte under an N_2 atmosphere are presented in Figure 4.6. Like their predecessors, W(CN-1-(2-^{i}Pr)-Naph)$_6$ and W(CNDipp^{CC}Ar)$_6$ complexes exhibit reversible W$^{[1+/0]}$ couples in the narrow range –0.47 to –0.30 V vs Fc$^{[1+/0]}$ (Fc = ferrocene). Only irreversible oxidation events are observed at more positive potentials. Alternatively, upon scanning cathodically of the W$^{[1+/0]}$ wave for W(CNDipp^{CC}-1-Naph)$_6$, W(CNDipp^{CC}-9-Phen)$_6$, and W(CNDipp^{CC}Ph^{CN})$_6$, a quasi-reversible reduction event is observed. Because the current passed

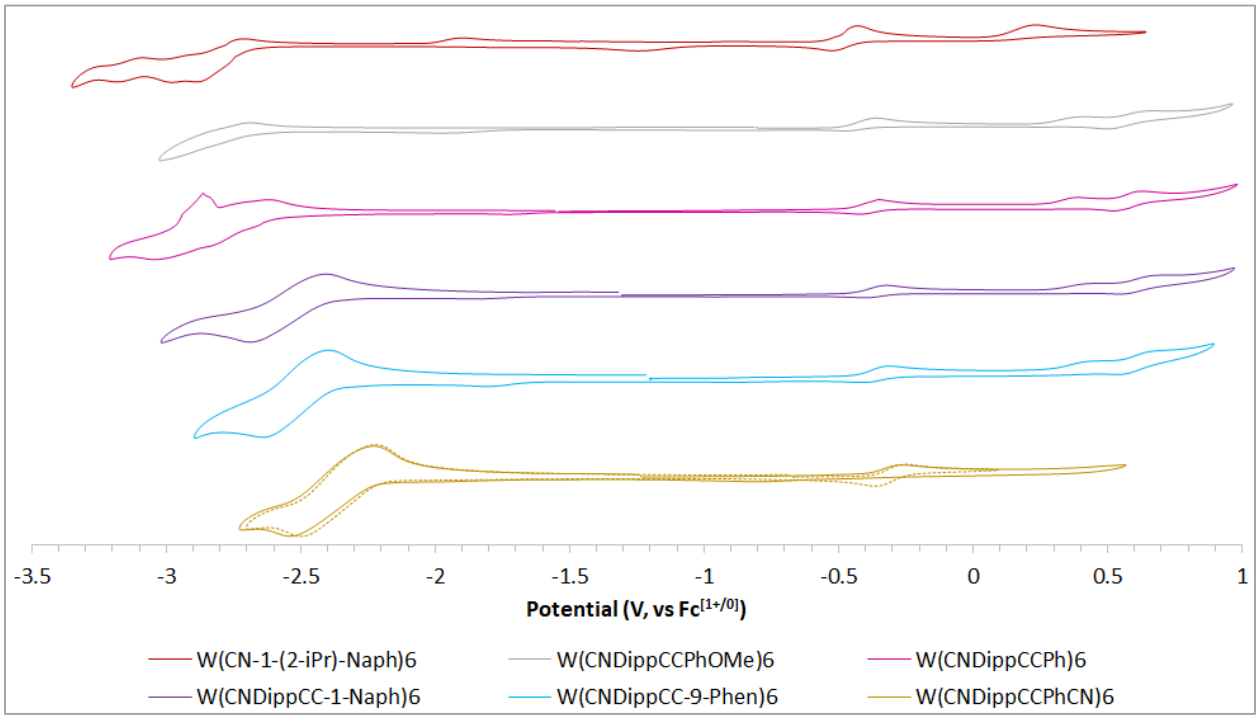

Figure 4.6. Cyclic voltammograms for W(CNDipp^{CC}Ar)$_6$ and W(CN-1-(2-^{i}Pr)-Naph)$_6$ complexes at a scan rate of 100 mV/s in THF with 0.1 M [^{n}Bu$_4$N][PF$_6$] supporting electrolyte (referenced vs Fc$^{[1+/0]}$).

during this redox event is much larger than that of the $W^{[1+/0]}$ couple, and the formal potential of the wave is highly sensitive to the identity of the CNDipp^{CC}Ar ligand, we assign this as a ligand-centered reduction rather than a $W^{[0/1-]}$ couple. Consistent with this, *E* (CNDipp^{CC}Ar$^{[0/1-]}$) shifts to more negative potentials and becomes less reversible as the electron-withdrawing nature of the secondary aromatic group decreases according to Ph^{CN} > 1-Naph > 9-Phen > Ph > Ph^{OMe}.

The $W^{[1+/0]}$ couples also depend on the nature of the secondary aromatic system in the CNDipp^{CC}Ar framework, albeit to a lesser extent. Notably, *E* ($W^{[1+/0]}$) are found to correlate well with the Hammett parameters[32] (σ; R^2 = 0.992) when W(CNDipp^{CC}Ph)$_6$ is taken as the base complex (σ = 0) and the other W(CNDipp^{CC}Ar)$_6$ coordination compounds (Ar = Ph^{OMe}, 1-Naph, 9-Phen, Ph^{CN}) are considered as arising from addition of the appropriate substituent to this complex (Figure 4.7). Thus, W(CNDipp^{CC}Ph^{CN})$_6$, having the largest σ value (e.g., the 4-nitrile substituent is the most electron-withdrawing), features the most anodic $W^{[1+/0]}$ wave (*E* = –0.30 V vs $Fc^{[1+/0]}$) from this series of compounds. This redox couple shifts cathodically as the electron-withdrawing capability of the peripheral aromatic system dwindles in the order 9-Phen (–0.36 V) > 1-Naph (–0.37 V) > Ph (–0.39 V) > Ph^{OMe} (–0.42 V; Table 4.3). That *E* ($W^{[1+/0]}$) only varies by ca. 120 mV over this set of W(CNDipp^{CC}Ar)$_6$ complexes is consistent with the electronic variations taking place at remote sites far removed from the tungsten center.

The E_{00} energies of W(CN-1-(2-^{i}Pr)-Naph)$_6$ and W(CNDipp^{CC}Ar)$_6$ complexes estimated from the onset of emission in their 77 K steady-state luminescence spectra in 2-MeTHF also span a small range (0.13 eV; Table 4.3). As expected, these energies are smaller than those of W(CNDippAr)$_6$ complexes. Combination of the ground-state $W^{[1+/0]}$ couples with the E_{00} energies yields the excited-state reduction potentials listed in Table 4.3. In agreement with the

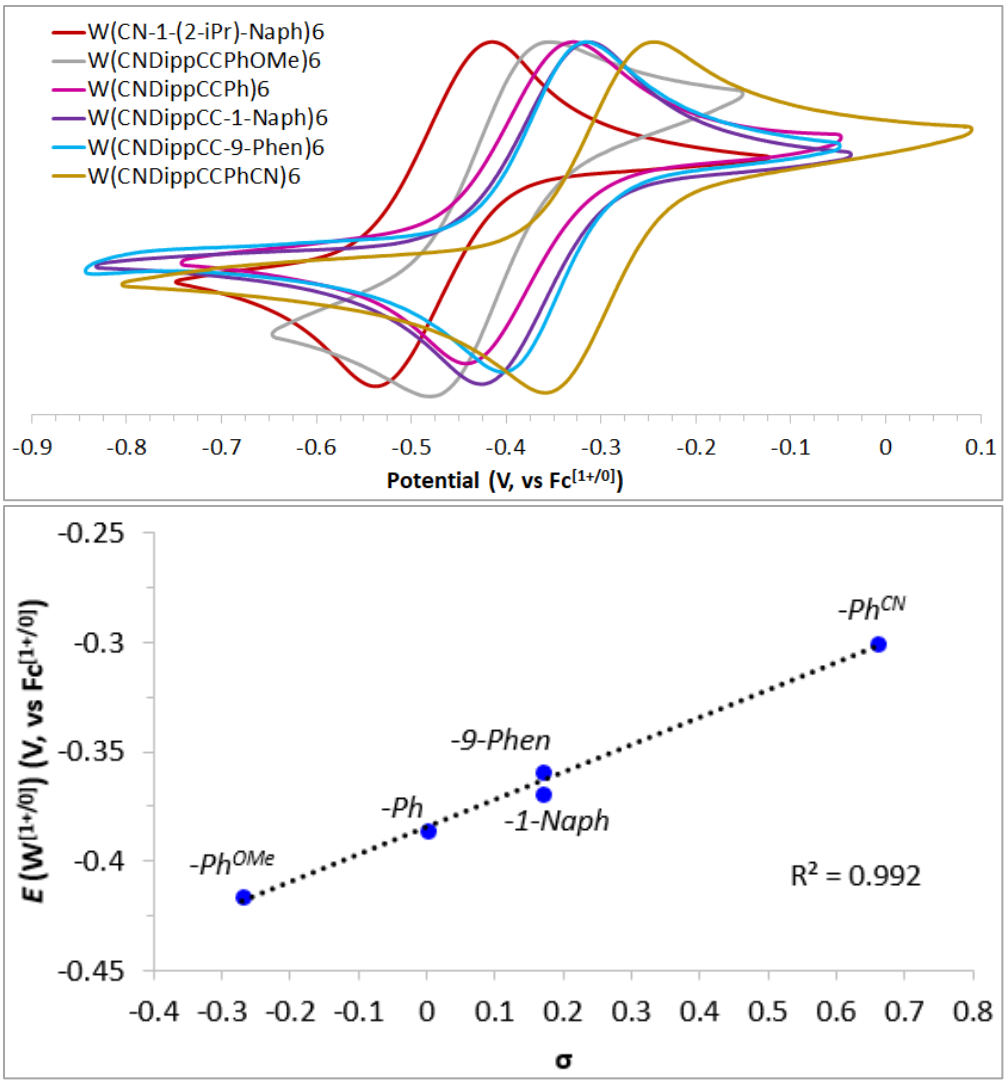

Figure 4.7. (Top) Cyclic voltammograms for W(CNDipp^{CC}Ar)$_6$ and W(CN-1-(2-^{i}Pr)-Naph)$_6$ complexes depicting the isolated W$^{[1+/0]}$ redox couple at a scan rate of 100 mV/s in THF with 0.1 M [^{n}Bu$_4$N][PF$_6$] supporting electrolyte (referenced vs Fc$^{[1+/0]}$). (Bottom) Plot of E (W$^{[1+/0]}$) versus the Hammett parameter for W(CNDipp^{CC}Ar)$_6$ complexes (setting σ(Ph) = 0).

photophysical and electrochemical data discussed above, E (W^{+}/*W^{0}) for W(CN-1-(2-^{i}Pr)-Naph)$_6$ and W(CNDipp^{CC}Ar)$_6$ complexes are attenuated with respect to W(CNDipp)$_6$ and W(CNDippAr)$_6$. However, their excited-state reduction potentials are slightly more tunable than

Table 4.3. Ground-state and excited-state reduction potentials of $W(CNAr)_6$ complexes.

Compound	E (W^{1+}/W^0)	E_{00}	E ($W^+/{*}W^0$)
$W(CNDipp)_6$	–0.53[a] (–0.72[b])	2.28	–2.81 (–3.00)
$W(CNDippPh)_6$	–0.68[b]	2.12	–2.80
$W(CNDippPh^{OMe2})_6$	–0.65[b]	2.14	–2.79
$W(CNDippPh^{OMe3})_6$	–0.65[b]	2.15	–2.80
$W(CNDippPh^{Ph})_6$	–0.67[b]	2.08	–2.75
$W(CNDipp^{CC}Ph^{OMe})_6$	–0.42	2.01	–2.43
$W(CNDipp^{CC}Ph)_6$	–0.39	1.99	–2.38
$W(CNDipp^{CC}$-1-Naph$)_6$	–0.37	1.94	–2.31
$W(CNDipp^{CC}$-9-Phen$)_6$	–0.36	1.93	–2.29
$W(CNDipp^{CC}Ph^{CN})_6$	–0.30	1.89	–2.19
W(CN-1-(2-^{i}Pr)-Naph$)_6$	–0.47	2.02	–2.49

[a]Electrochemical measurements performed in THF with 0.1 M [^{n}Bu$_4$N][PF$_6$] supporting electrolyte. Reported vs $Fc^{[1+/0]}$. Data taken from ref. 20. [b]Electrochemical measurements performed in DCM with 0.5 M [^{n}Bu$_4$N][PF$_6$] supporting electrolyte. Reported vs $Fc^{[1+/0]}$. Data taken from ref. 21.

the latter and are still more negative than *[*fac*-Ir(ppy)$_3$]. That $W(CNDipp^{CC}Ph^{OMe})_6$ and W(CN-1-(2-^{i}Pr)-Naph$)_6$ have E ($W^+/{*}W^0$) ≈ –2.5 V vs $Fc^{[1+/0]}$, long τ(^{3}MLCT), and in the case of the former, a high quantum yield (ϕ_{PL} = 0.55) in THF, suggests these complexes may be promising photoredox reagents.

4.3. Conclusion

In conclusion, we have reported a novel set of homoleptic tungsten(0) fused-ring and alkynyl-bridged arylisocyanide photoactive complexes with photophysical properties that

complement those of previously reported oligoarylisocyanide variants. The excited-state properties of W(CNDipp^{CC}Ar)$_6$ are highly dependent on the identity of the secondary aromatic system, providing a facile route by which they can be tuned. Alternatively, W(CN-1-(2-^{i}Pr)-Naph)$_6$ features the longest room temperature solution lifetimes observed to date for photoactive complexes of this type, demonstrating the potential benefits of employing fused-ring arylisocyanide ligands in the design of this class of photosensitizers. Ongoing work is aimed at elucidating whether W(CNDipp^{CC}Ph^{OMe})$_6$ and W(CN-1-(2-^{i}Pr)-Naph)$_6$ can serve as competent visible light photoredox catalysts for organic transformations. Preliminary results show that W(CN-1-(2-^{i}Pr)-Naph)$_6$ and W(CNDipp^{CC}Ar)$_6$ complexes possess δ_{800} = 500–2000 GM, potentially enabling substrate reduction utilizing lower energy near-infrared light and the development of important design principles for W(CNAr)$_6$ TPA dyes.

4.4. References

(1) Hagfeldt, A.; Boschloo, G.; Sun, L.; Kloo, L.; Pettersson, H. *Chem. Rev.* **2010**, *110*, 6595.

(2) Prier, C. K.; Rankic, D. A.; MacMillan, D. W. C. *Chem. Rev.* **2013**, *113*, 5322.

(3) Glaser, F.; Wenger, O. S. *Coord. Chem. Rev.* **2020**, *405*, 213129.

(4) Yersin, H.; Rausch, A. F.; Czerwieniec, R.; Hofbeck, T.; Fischer, T. *Coord. Chem. Rev.* **2011**, *255*, 2622.

(5) Zhao, Q.; Huang, C.; Li, F. *Chem. Soc. Rev.* **2011**, *40*, 2508.

(6) Juris, A.; Balzani, V.; Barigelletti, F.; Campagna, S.; Belser, P.; von Zelewsky, A. *Coord. Chem. Rev.* **1988**, *84*, 85.

(7) Campagna, S.; Puntoriero, F.; Nastasi, F.; Bergamini, G.; Balzani, V. *Photochemistry and Photophysics of Coordination Compounds: Ruthenium*; Springer, Berlin, Heidelberg: Berlin, 2007.

(8) Lowry, M. S.; Bernhard, S. *Chem. Eur. J.* **2006**, *12*, 7970.

(9) Flamigni, L.; Barbieri, A.; Sabatini, C.; Ventura, B.; Barigelletti, F. *Photochemistry and Photophysics of Coordination Compounds: Iridium*; Springer, Berlin, Heidelberg: Berlin, 2007.

(10) Arias-Rotondo, D. M.; McCusker, J. K. *Chem. Soc. Rev.* **2016**, *45*, 5803.

(11) Wenger, O. S. *J. Am. Chem. Soc.* **2018**, *140*, 13522.

(12) Büldt, L. A.; Wenger, O. S. *Dalton Trans.* **2017**, *46*, 15175.

(13) Büldt, L. A.; Wenger, O. S. *Angew. Chem. Int. Ed.* **2017**, *56*, 5676.

(14) Herr, P.; Glaser, F.; Büldt, L. A.; Larsen, C. B.; Wenger, O. S. *J. Am. Chem. Soc.* **2019**, *141*, 14394.

(15) Büldt, L. A.; Guo, X.; Prescimone, A.; Wenger, O. S. *Angew. Chem. Int. Ed.* **2016**, *55*, 11247.

(16) Büldt, L. A.; Guo, X.; Vogel, R.; Prescimone, A.; Wenger, O. S. *J. Am. Chem. Soc.* **2017**, *139*, 985.

(17) Mann, K. R.; Cimolino, M.; Geoffroy, G. L.; Hammond, G. S.; Orio, A. A.; Albertin, G.; Gray, H. B. *Inorg. Chim. Acta* **1976**, *16*, 97.

(18) Mann, K. R.; Gray, H. B.; Hammond, G. S. *J. Am. Chem. Soc.* **1977**, *99*, 306.

(19) Gray, H. B.; Mann, K. R.; Lewis, N. S.; Thich, J. A.; Richman, R. M. *Inorganic and Organometallic Photochemistry* **1978**, *168*, 44.

(20) Sattler, W.; Ener, M. E.; Blakemore, J. D.; Rachford, A. A.; LaBeaume, P. J.; Thackeray, J. W.; Cameron, J. F.; Winkler, J. R.; Gray, H. B. *J. Am. Chem. Soc.* **2013**, *135*, 10614.

(21) Sattler, W.; Henling, L. M.; Winkler, J. R.; Gray, H. B. *J. Am. Chem. Soc.* **2015**, *137*, 1198.

(22) Kvapilová, H.; Sattler, W.; Sattler, A.; Sazanovich, I. V.; Clark, I. P.; Towrie, M.; Gray, H. B.; Záliš, S.; Vlček, A. *Inorg. Chem.* **2015**, *54*, 8518.

(23) Takematsu, K.; Wehlin, S. A. M.; Sattler, W.; Winkler, J. R.; Gray, H. B. *Dalton Trans.* **2017**, *46*, 13188.

(24) Chen, Y.; Guan, R.; Zhang, C.; Huang, J.; Ji, L.; Chao, H. *Coord. Chem. Rev.* **2016**, *310*, 16.

(25) Li, H.; Yang, Y.; He, C.; Zeng, L.; Duan, C. *ACS Catal.* **2019**, *9*, 422.

(26) Favale, J. M.; Danilov, E. O.; Yarnell, J. E.; Castellano, F. N. *Inorg. Chem.* **2019**, *58*, 8750.

(27) Dong, Y.; Jv, J.-J.; Wu, X.-W.; Kan, J.-L.; Lin, T.; Dong, Y.-B. *Chem. Commun.* **2019**, *55*, 14414.

(28) Belcher, R.; Lyle, S. J.; Stephen, W. I. *J. Chem. Soc.* **1958**, 3243.

(29) Davalli, S.; Lunazzi, L.; Macciantelli, D. *J. Org. Chem.* **1991**, *56*, 1739.

(30) Carnahan, E. M.; Protasiewicz, J. D.; Lippard, S. J. *Acc. Chem. Res.* **1993**, *26*, 90.

(31) Lockwood, M. A.; Fanwick, P. E.; Rothwell, I. P. *Organometallics* **1997**, *16*, 3574.

(32) Hansch, C.; Leo, A.; Taft, R. W. *Chem. Rev.* **1991**, *91*, 165.

(33) Herr, P.; Wenger, O. S. *Inorganics* **2020**, *8*, 14.

(34) Caspar, J. V.; Kober, E. M.; Sullivan, B. P.; Meyer, T. J. *J. Am. Chem. Soc.* **1982**, *104*, 630.